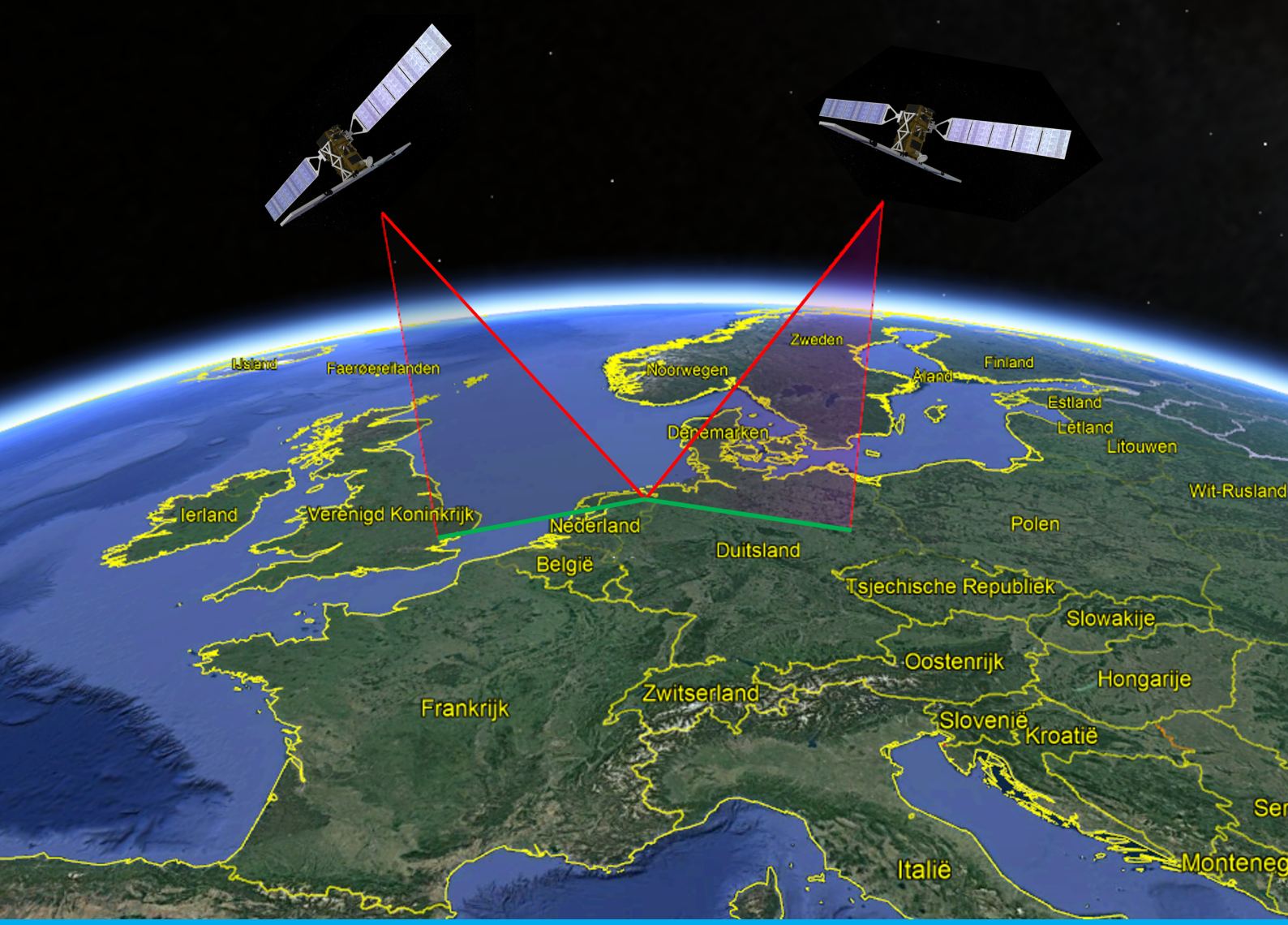

Delft University of Technology

An analysis of the InSAR displacement vector decomposition

InSAR fallacies and the strap-down solution

Wietske Brouwer

TU Delft

An analysis of the InSAR displacement vector decomposition

InSAR fallacies and the strap-down solution

by

Wietske Brouwer

to obtain the degree of Master of Science
at the Delft University of Technology,
to be defended publicly on Wednesday September 22, 2021 at 10:00 AM.

Student number:	4385314	
Project duration:	September 23, 2020 – September 22, 2021	
Thesis committee:	Prof. dr. ir. R. F. Hanssen,	TU Delft, chair of the committee, daily supervisor
	Prof. dr. ir. P. J. G. Teunissen,	TU Delft, supervisor
	dr. ir. P. López Dekker,	TU Delft, supervisor
	dr. G. Giardina	TU Delft, supervisor

An electronic version of this thesis is available at http://repository.tudelft.nl/.

TU Delft

Preface

At many times, doing this research was like climbing a huge mountain. The tension, because you have no idea what climb lies ahead and sometimes, a bit of suffering (for example, getting everything right on paper). At times, there seemed to be no end in sight because it seemed like I had chosen the wrong path. But fortunately, after these difficult steps, there was always a fantastic view. I also noticed that during the climbing, I started to enjoy it more and more. One of my highlights was presenting my research at two conferences, Fringe and IGARSS.

Part of this thesis is about how displacement results should be communicated to the public. I think it is still quite unimaginable that it is possible to obtain millions of displacement observations at millimeter scale from satellites that orbit at a height of 700km. I do not think this will diminish in the future. Probably, there will be more and more earth observation satellites in the future. Therefore, it remains important that results are communicated properly. In this thesis I have chosen to take a strict stand on how results are communicated in common literature. I think this will help to open up the discussion on how results should be communicated. I would like to stress that the aim is not to "blame" authors and that I do not want to imply any position on the level of their understanding. In the end, I'm very proud that I reached the summit, which not only marks the end of my thesis but also the period of being a student at the TU Delft.

All the work presented in this thesis would not have been possible without the help of a lot of people. First of all, a big thanks to Ramon, your excellent guidance and support made it a great climb. When I lost track, you helped me out. Also, thanks for the nice discussions we had on the findings and how you always placed them in a good perspective. Furthermore, I would like to express my gratitude to Giorgia, Paco and Peter. Your constructive feedback and critical questions helped me further. Also, thanks to Max, Marc, Phil, Simon, John and Freek for the nice daily huddles we had in the past year. I would also take the opportunity to thank SkyGeo for providing the data.

But also the support from my family and friends was very welcome. Amber, Sita and Vita, working with you from our home was (almost) always fun. And finally, a big thanks to my father, mother, and two sisters. You always make sure that I keep on climbing and, not unimportantly, that I take time to enjoy it too.

Wietske Brouwer
Delft, September 2021

Abstract

Satellite radar interferometry (InSAR) is a powerful technique for monitoring deformation phenomena. While deformation phenomena occur in a three-dimensional (3D) world, one of the limitations of the InSAR phase observations is that they are only sensitive to the projection of the 3D displacement vector onto the radar line-of-sight (LoS) direction. To uniquely estimate the three displacement components, we would require at least three sets of spatiotemporally coinciding independent (STCI) LoS observations, (i.e., scatterers on an object that is not subject to internal deformations, observed at the same time) available over the same Region of Uniform Motion (RUM). More importantly, the system of equations needs to have a full rank coefficient matrix. Unfortunately, in most practical situations at most two sets of STCI LoS observations are available, resulting in an underdetermined system with an infinite amount of possible solutions.

Within the InSAR literature we encounter different approaches to address the underdeterminancy problem, unfortunately often with either mathematical or semantic flaws. Their impact reaches from quantitative errors in the reported studies, mismatches in comparative studies with other geodetic techniques, a lack of trust in the technology by end users, to plain confusion. We concluded that the InSAR community has no uniform way of addressing the underdeterminancy problem. A recurring problem is the lack of distinction between a 'projection' and a 'decomposition'. We developed a taxonomy for the different fallacious approaches that can help by evaluating InSAR results and reviewing InSAR papers.

Moreover, using the east-north-up (ENU) reference frame for decomposing the LoS observations provides results that are not tuned to the needs of the end-user of an InSAR product. Therefore, developed an alternative solution to the underdetermined problem, in the form of a 'strap-down' approach, which uses a local strap-down reference system that is fixed to the deformation phenomenon with transversal, longitudinal, and normal (TLN) components. For many practical cases, such as line-infrastructure, landslides, or subsidence bowls, analysis of the main driving forces supports the assumption that significant deformations in the longitudinal direction are unlikely.

We found that using the strap-down approach gives physically more relevant estimates. Moreover, it results in more relevant estimates since it properly includes all uncertainties. We can further conclude that the conventional way of communicating (PS)-InSAR results by means of a 'dot distribution map' is sub-optimal when considering the quality of the estimates, in particular for products with a decomposition in two (or three) orthogonal directions. For such InSAR information products, 'vector arrow maps', or traditional geodetic vector-based visualizations, including error ellipses are a viable and more optimal alternative.

List of Acronyms

1D	one-Dimensional
2D	two-Dimensional
3D	three-Dimensional
DEM	Digital Elevation Model
DRaMA	Delft Radar Modelling and performance Analysis
DP	Detectability Power
DS	Distributed Scatterer
ENU	East, North, Up
EU plane	East-Up Plane
EW	East-West
InSAR	Interferometric Synthetic Aperture Radar
LoS	Line of Sight
MDD	Minimal Detectable Displacement
MC	Monte Carlo
NAF	North Anatolian Fault
NS	North-South
PDF	Probability Density Function
PS	Persistent Scatterer
radar	Radio detection and ranging
RUM	Region of Uniform Motion
SAF	San Andreas Fault
SAR	Synthetic Aperture Radar
SD	Standard Deviation
SNR	Signal to Noise Ratio
STCI	Spatio-Temporally Coinciding Independent
TLN	Transversal, Longitudinal, Normal
UD	Up-Down
ZDP	Zero-Doppler Plane

Contents

1

Introduction

1.1. Background

Satellite radar interferometry (InSAR) is a powerful technique for monitoring deformation phenomena [1], [2]. With deformation phenomena, one can think of deformations due to natural hazards such as landslides, earthquakes and volcanic eruptions but also deforming infrastructure, residential areas, or water defense structures. The analysis of InSAR time series enables the estimation of millimeter level surface motions with a high spatial resolution [3], [4].

The large amount of available data, frequently acquired, with high precision at relatively low costs, makes InSAR observations valuable. Fig. 1.1 shows an example of the results of an InSAR study. Such results are often presented as colored dots on a map, where the colors represent a particular displacement rate for a specific location.

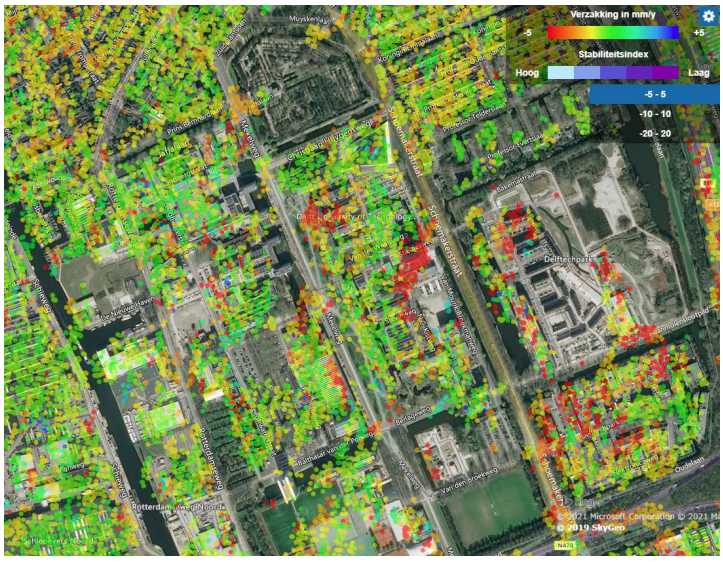

Figure 1.1: InSAR time series results for the TU Delft campus area. The colored dots on the map represent estimated displacement rates into the line-of-sight direction of the radar. Given observations from a single satellite viewing geometry, the full 3D displacement cannot be estimated. From [5].

However, a defining characteristic of the InSAR observations is that they are not tuned to a specific problem, unlike conventional geodetic observations, which are generally only performed given a particular signal of interest. Stakeholders related to deformation phenomena are usually interested in the full three-dimensional (3D) displacements. Yet, one of the characteristics of the InSAR phase obser-

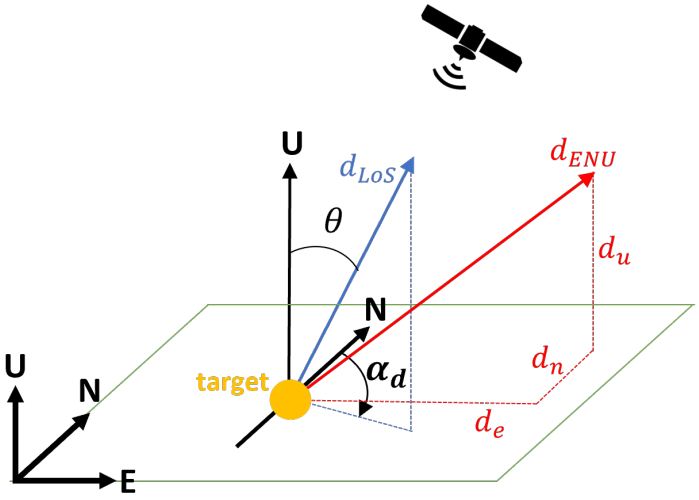

Figure 1.2: Geometric configuration of the 3D displacement vector, the LoS vector, the incidence angle θ, and the azimuth of the zero-Doppler plane α_d at the position of the target.

vations is that they are only sensitive to the projection of the 3D displacement vector onto the radar line-of-sight (LoS) direction, along a plane orthogonal to the LoS [6]. Thus, the LoS projection d_{LoS} in a local Cartesian east, north, up (ENU) coordinate system is given by

$$d_{\mathrm{LoS}} = p_{\mathrm{LoS}}\, d_{\mathrm{ENU}}, \tag{1.1}$$

where $p_{\mathrm{LoS}} = [\sin\theta \sin\alpha_d, \sin\theta \cos\alpha_d, \cos\theta]$ is the orthogonal projector onto the line of sight, and the 3D displacement vector in east, north and up direction is $d_{\mathrm{ENU}} = [d_e, d_n, d_u]^T$. The angle θ is the incidence angle of the radar, and α_d is the azimuth of the zero-Doppler plane of the radar, at the position of the target. See Fig. 1.2 for an overview of the geometry.

From observations from one viewing geometry only, see Fig. 1.1, it remains unclear what happens in the real world. For example, the red dots can be due to subsidence, to horizontal displacements, or a combination of both. Uniquely estimating (disentangling) the three displacement components would require at least three independent LoS observations from different viewing geometries. Unfortunately, in most practical situations, only two LoS observation geometries are available, resulting in an underdetermined system with an infinite amount of possible solutions.

Different approaches to interpret the InSAR observations
While the underdeterminancy problem is rather trivial and straightforward, a systematic review of InSAR literature (section 2.5) reveals that approaches to address it often have either mathematical or semantic flaws. The impact of these flaws reaches from (i) quantitative errors in the reported studies, (ii) mismatches in comparative studies with other geodetic techniques, (iii) a lack of trust in the technology by end-users, to (iv) problems in the interpretation.

In several studies the LoS observations are directly (but erroneously) interpreted as vertical displacements. For example, in [7] the following statement can be found: *"A comprehensive image of the ground vertical displacements affecting the Venice region has been drawn […] using the available data."* The authors show Fig. 1.3a, stating that the LoS observations are presented as vertical displacements. In chapter 2 we will show that this can cause an underestimation of the vertical displacements of up to 40%.

There are also studies that claim that the vertical displacement component is derived by computing the (oblique) projection of the LoS observations onto the vertical direction without explicitly stating assumptions on the potential horizontal components. A quote from [8]: *"We converted the LoS displacements […] to vertical displacements using* $d_u = d_{LoS}/\cos\theta$*"*, see Fig. 1.3b. In other words, the contribution of

a potential horizontal component to the LoS observations is simply ignored, which is unsubstantiated.

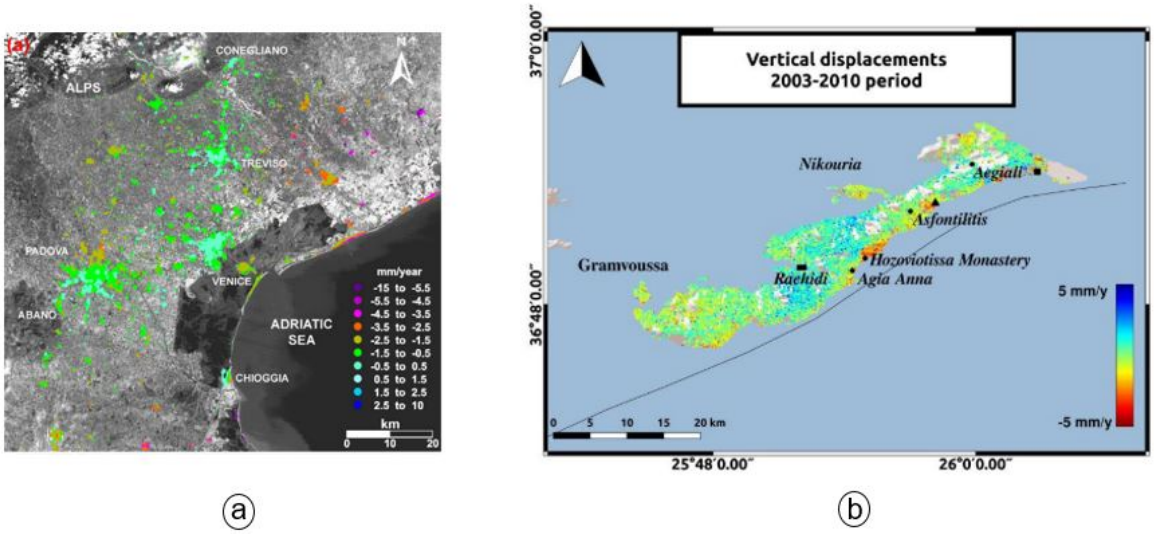

Figure 1.3: a), published by [7], shows the InSAR results from a study where the LoS observations are directly interpreted as vertical displacements. In [7], the figure title states that the results are *vertical displacements* whereas the results are in fact LoS displacements. Hence, this is erratic by up to 40%. b) published by [8], shows the vertical displacements, which are obtained by computing the (oblique) projection of the LoS observations onto the vertical direction without stating any assumption on the horizontal components. Without such an explicit assumption, the results are not substantiated.

As a final example, [9] state *"It is possible to decompose the LoS measurements to horizontal and vertical products in certain areas of interest where two LoS observations are available"*, followed by *"Consequently, we add the additional constraint that the north-south (d_n) motion is assumed to be zero"*, see Fig. 1.4. While such an assumption is theoretically possible, it is unsubstantiated, as it is an assumption on the physical signal, not on the observations. The mistake the authors make is that they confuse the lack of sensitivity of an observation (to a particular displacement direction) with the absence of the physical signal. While the former can be valid, the latter would need to be substantiated, and requires a geophysical argumentation.

The three examples above demonstrate that there are different ways to interpret and present InSAR LoS observations, with mathematical or semantic flaws. In chapter 2, we will describe and categorize all approaches we have found.

Quality description of the unknown parameters

Stakeholders and end-users of InSAR data need to know the quality of the estimated parameters, i.e., the unknown displacements in the east, north, and up direction: d_e, d_n, and d_u. The quality of the estimates follows from the precision (noise level) of the observations, and potential biases of the estimates. The approaches mentioned above all result in quantitatively incorrect estimates for the displacement parameters, i.e., there is a bias between the estimated displacement and the actual displacement, independent of the precision of the LoS observations. Obviously, this bias is often undesirable. For example, when a stakeholder wants to use InSAR to monitor a particular deformation phenomenon, e.g., a landslide-prone area, the magnitude of a displacement that needs to be detected can be predefined. Often this magnitude is related to the maximum allowable displacement to still ensure the safety of the surroundings. However, when the estimated displacements are biased, they result in displacements not being detected at all, or in false warnings being sent out, which are both undesirable [10].

The considerations above lead to the following two research questions. (i) How large is the bias for the estimated parameters? And, (ii) is the variance-covariance matrix of the estimated parameters sufficient to describe the quality of the estimates?

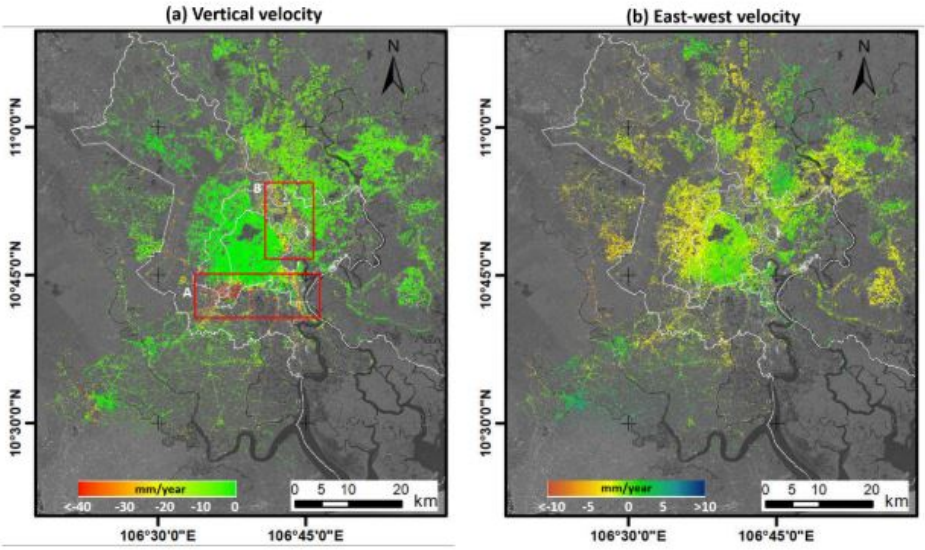

Figure 1.4: Results from [9]: decomposed displacement results obtained with LoS observations from only two viewing geometries. (Physical) displacements in the north direction are assumed to be zero and are therefore removed from the decomposition equation (Eq. (2.7)).

Parameterization for the decomposition
In almost all InSAR studies where the LoS observations are 'decomposed', this is done in the ENU reference frame. We are interested in investigating whether this choice of reference frame is always optimal. For example for a deforming dike. Physically, it would be the most useful to know how much the dike deforms along the slope or how large the displacements are in the normal direction. Therefore, a research question is (i) is the decomposition in the ENU reference frame always the most optimal, or (ii) is it better to decompose the LoS observations in other directions?

1.2. Problem statement

The introduction above shows that there is a need for further unification in how InSAR results are computed and communicated and for insight into the consequences of particular choices in terms of accuracy and precision. Within the InSAR community, there is no authoritative documentation on the full problem description and no analysis of the consequences of particular choices. Moreover, it is unclear which semantics should be used, and there is a need for clear recommendations on how the underdetermined nature of the estimation problem should be handled.

These problems will be addressed in this study.

1.3. Different problem perspectives

InSAR investigations are typically complex, and we can distinguish different factors that are all related and affect the final result. Here, we define different perspectives on how we can 'look' at the InSAR problem.

1.3.1. The stakeholder's perspective

The first perspective to look at the problem is the perspective of the end-user. For example, suppose an asset manager wants to use InSAR to monitor a deformation phenomenon of a bridge. While the asset manager has minimal knowledge about satellites, radars, and the InSAR technology in general, he should still make difficult decisions, e.g., on what satellite mission(s) to use. The question of the stakeholder then is: *"What can InSAR do for me in this situation?"* and *"is InSAR able to detect displacements of a particular size in a particular direction for my bridge with InSAR?"* After the choice for

a particular satellite mission is made, this will lead to particular product requirements, i.e., *"how precise can we estimate the unknown displacement parameters and can we disentangle (estimate) the three displacement parameters?"* But also *"what is the magnitude of the displacement that can be detected in a particular direction?"* It is desirable to be able to answer the stakeholder questions before starting with the InSAR study because the answer to these questions determine whether it is worth investing in using the InSAR technology, or whether conventional geodetic techniques should be deployed.

1.3.2. User of a pre-existing InSAR information product

Within this perspective, the InSAR information product does already exist. This is different from the first perspective, in which the information product still needs to be acquired or computed. Suppose the end user has access to a particular information product, e.g., a displacement map that shows colored dots, where the colored dots represent the LoS displacement rates, as in Fig. 1.1. The user is not particularly interested in the colored dots. Most probably, he is interested in what happens with a particular deformation phenomenon that he should monitor. He wants to know what the product tells him about the deformation phenomenon. So the question related to this perspective is: *"What can we get from the product?"*, or, in other words: *"What deformation phenomenon can be significantly estimated from the product?"*

1.3.3. The InSAR service provider

The last perspective reviews the problem from the space segment. On the one hand, the stakeholders within this perspective can be 'value-adding service' providers. These are companies that are using InSAR data to create end products that stakeholders can use. These companies have to meet the product requirements set by their customers. The question that such parties typically ask is *"with which (combination) of satellite mission(s) can we meet the product requirements asked by the client?"*

Another category of stakeholders are the data providers, such as space agencies. Space agencies and other space companies providing InSAR satellites want to create missions (or systems) that deliver what is needed and have highest added value. As they want to know what the viewing geometry of a new InSAR satellite should be, they may ask: *"what should be the viewing geometry of a new operating satellite to deliver an InSAR product that has a high added value?"*

1.4. Research objective

As discussed above, InSAR studies are often complex studies with many possibilities. Moreover, there are different perspectives on the problem, all accompanied by specific questions. Therefore, the aim of this research is to provide a full and complete description of the problem and an analysis of the consequences of particular choices. Moreover, we want to come with clear recommendations on how the underdetermined nature of the estimation problem should be handled. Furthermore, as the decomposition in the ENU system is not tuned for the problem we want to develop a new approach that provides physically more relevant estimates.

The main research question of this research is therefore defined as follows:

> **Can a better geometrical insight lead to a more optimal way of computing and communicating InSAR results?**

To be able to answer this question, the research is divided into the following subquestions:

1. What conditions need to be satisfied to fully solve for the 3D displacement vector in the East-North-Up reference frame from InSAR LoS observations?
2. What are current approaches within the literature to address the underdeterminancy problem, and what are potential mathematical and semantic flaws?

3. Can we find a better solution to the underdeterminancy problem?
4. What are different perspectives to study the InSAR decomposition and what are corresponding approaches?

1.5. Outline

First, in chapter 2 we discuss the relevant InSAR geometry and conditions that need to be satisfied to solve for the full 3D displacement vector. We end the second chapter with an analysis of the different approaches we encounter in InSAR literature. In the third chapter we introduce an alternative solution to the underdeterminancy problem, in the form of a 'strap-down' approach, which uses a local strap-down reference system that is fixed to the deformation phenomenon. We also discuss the effect of the uncertainty of the frame on the final estimates. In chapter 4, we describe the different InSAR perspectives to review the decomposition problem and we discuss the related questions. Then, in chapter 5 we present the results of some case studies related to the different InSAR perspectives. Finally, in chapter 6, the main findings and recommendations of this study are presented.

2

InSAR LoS observations and current approaches to address the undeterminancy problem

InSAR (Interferometric Synthetic Aperture Radar) has become an established and efficient tool to monitor deformations of the Earth's surface. However, to solve for the full 3D displacement vector, several conditions (necessary but individually not sufficient) need to be satisfied. In section 2.1, we first review the relevant InSAR geometry. The forward model is discussed in section 2.2, and the inverse model, including the necessary conditions in section 2.3. In section 2.4 we discuss the rank deficiency generally encountered in InSAR and the necessary conditions. Subsequently, in section 2.5 we analyze the different approaches we encounter in InSAR literature and finally, in section 2.6 we show the correct approaches.

2.1. InSAR viewing geometry

Within this research, we assume that we always start with already 'processed' data, i.e., time series estimates of displacements in the LoS direction. It is further assumed that this input data is provided with an a priori standard deviation. We now first discuss the basic principles of InSAR. For a more detailed description of the InSAR technique the reader is referred to [6] and [11].

2.1.1. InSAR basics

InSAR is a technique that can be used to estimate displacements of the ground or the objects on it. The initial measurements are obtained by a radar on board of a satellite which sends out electromagnetic pulses. A part of the pulse is reflected back to the sensor by the Earth's surface and arrives with a delay due to the two-way travel time of the signal. While orbiting over the Earth, the satellite illuminates a certain area on the Earth's surface, with a width which is defined as the swath width. For each resolution cell, a complex measurement is recorded, which can be transformed into a phase and an amplitude. The amplitude A, or intensity of the signal, contains information on the slope, roughness and electrical properties of the reflecting surface. The phase ψ gives information on the travel time and is also dependent on the complex interaction of the electromagnetic wave with the Earth's surface. Both properties are combined in the complex phasor P [6, 11]

$$P = Ae^{i\psi}. \tag{2.1}$$

A SAR image consists of a two-dimensional array of pixels in the azimuth and range direction. The azimuth direction is defined parallel to the velocity vector of the satellite, the range direction is per-

Table 2.1: Taxonomy of classes of scatterers, [12], based on coherence, including their acronyms, amplitude PDF's and expected normalized amplitude dispersion (NAD).

	Continuously Coherent	Temporary Coherent	Incoherent
Distributed Scatterers	**CCDS**	**TCDS**	**IDS**
	Rice (low SNR)	Rice (low SNR) & Rayleigh	Rayleigh,
	NAD low	NAD high	NAD medium
Point Scatterers	**CCPS**	**TCPS**	unlikely
	Rice (high SNR), [13]	Rice (high SNR) & Rayleigh	
	NAD lowest	NAD highest	
	CCS	**TCS**	

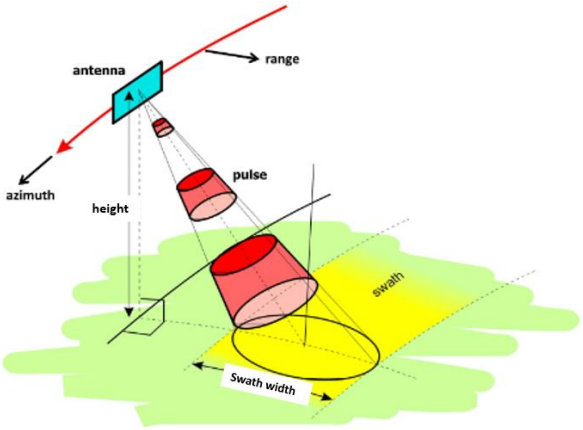

Figure 2.1: While orbiting the Earth, the radar sends out electromagnetic pulses that are reflected bu the Earth surface. The area that is covered on the ground surface is called the swath of the satellite [14]

pendicular to the azimuth direction. The width of the image is referred to as the swath, see Fig. 2.1. Every pixel in the SAR image has its own value for the phasor P, where P is the coherent sum of all reflections on the Earth's surface that fall within that specific image resolution cell. We can distinguish two extreme cases for signal reflections, following the taxonomy of Hu et al., [12], see table 2.1. The first is Point Scattering (PS), where the measurement of the pixel is dominated by one strong reflecting object, such as a corner reflector, which can be considered as a point source at a fixed 3D position. The other one is Distributed Scattering (DS), where a large number of scattering objects, distributed within the entire resolution cell, form the measurement, this is the case for for instance farmlands or forests [11]. Note that in this taxonomy, the acronym PS does not refer to 'persistent' scatterers, as used by the wider InSAR community.

As already described, the phase, ψ, holds information on the time delay of the signal when travelling in the range direction. One phase measurement ψ_P itself cannot give any information about a displacement. However, if (i) a phase measurement at a different location is also available ψ_Q, and (ii) it is possible to repeat those measurements when the satellite passes over during a subsequent acquisition, it is possible to compute the double-difference. This is the phase difference in space and time and is also called the interferometric phase,

$$\phi = (\psi_P - \psi_Q)_{t_2} - (\psi_P - \psi_Q)_{t_1}. \tag{2.2}$$

When a point moves between the times of the first satellite acquisition and the second acquisition, a phase difference will be measured, see Fig. 2.2. All interferometric phases together form an interferogram [6]. The phase differences are measured as changes in range in the Line of Sight (LoS) of a satellite, which is the vector from the phase center of the SAR antenna on the satellite at zero-Doppler towards the point scatterer (PS), or the center of the DS resolution cell on the Earth's surface. The

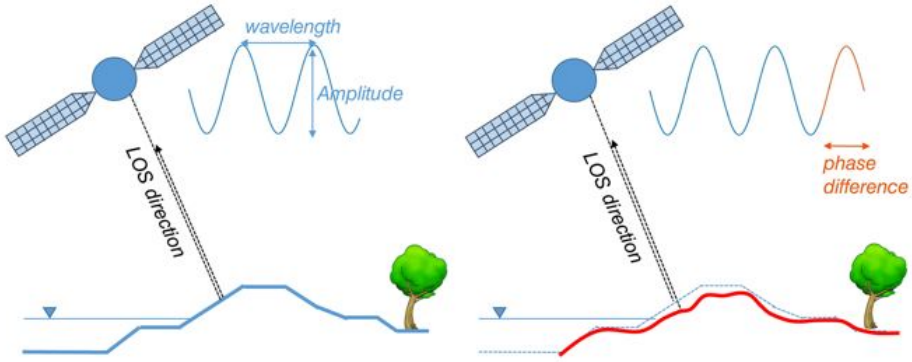

Figure 2.2: Two InSAR LoS measurements, one before and one after a displacement occurs, for this situation on a dike. The image-plane coincides with the zero-Doppler plane. Both the deformation and the different position of the satellite cause a phase difference, due to the longer two-way travel time of the radar signal between the first and the second acquisition of the satellite, assuming sufficient temporal coherence and identical atmospheric conditions. From this phase difference, the displacement in the LoS direction of the satellite can be determined (Image from [16]).

relation between the interferometric phase and a displacement in the LoS direction is given by

$$\phi = -\frac{4\pi}{\lambda}\delta_{\mathrm{LoS}} \tag{2.3}$$

where λ is the radar wavelength and δ_{LoS} the displacement in the LoS direction. Typically, considering only instrumental noise, the double differences have a precision of about 0.45 mm [15].

The interferometric phase does not only contain information about displacements but also contains information on several other components, such as the Earth's curvature, the topography, atmospheric delay, orbital errors, scattering mechanisms at the Earth's surface, and measurement noise. It is therefore needed to separate the displacement signal from these other signals. In general, the separation of the displacement signal is done by using time-series of many satellite acquisitions. Yet, one of the most important conditions for separation is that the signal between the satellite acquisitions remains coherent [6].

Using multiple satellite acquisitions results in radar interferometric data of hundreds of radar images, each with billions of image pixels. There are various time-series processing techniques for estimating the displacement signal from the data. Here we give a short explanation of the the PS-InSAR method that uses PS points which are expected to have a coherent phase behavior over a longer time. The method roughly consists of three main steps. (i) Creating multiple interferometric combinations from complex data, (ii) identifying the PS points and estimating the displacement phase (also called the 'PSI analysis'), and (iii) assessing the quality of the results. The PSI analysis is very valuable since it aims to detect scatterers with a coherent phase behavior. The result of the PS-InSAR approach is often a space-time matrix that consists of PS points and their location on Earth. For each PS point a displacement time-series is estimated in the LoS direction. For a description of the PS-InSAR method the reader is referred to [11].

2.1.2. Geometry

The estimated displacements resulting from the radar image processing are one-dimensional displacements towards the satellite. This direction, whcih is the line-of-sight direction at the target, depends of the viewing geometry to the satellite, that can be described using two angles: the azimuth of the zero-Doppler plane at the Earth surface α_d and the incidence angle θ.

2.1.3. Heading angle and azimuth of the zero-Doppler plane

Most radar satellites orbit in retrograde sun-synchronous near-polar orbits. Thus, the satellite passes a location on Earth in the *north by west* direction (ascending) and in the *south by west* direction (descend-

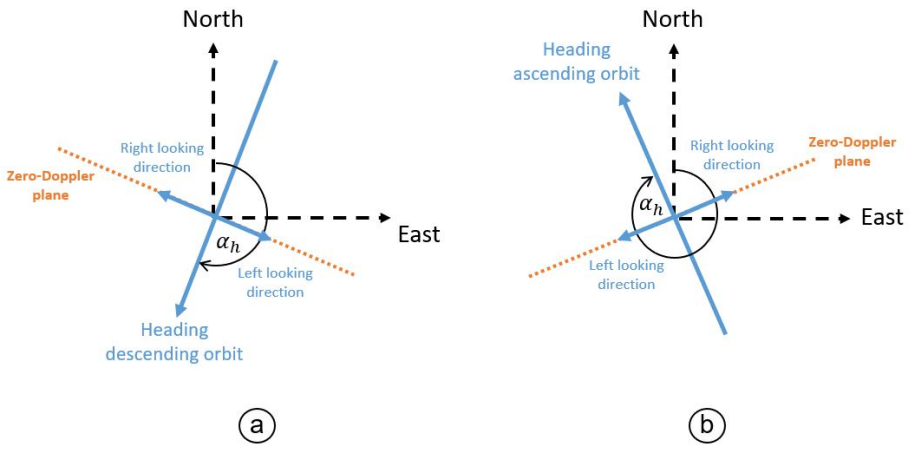

Figure 2.3: The viewing geometry to (a) a descending satellite acquisition and (b) an ascending acquisition shown in the horizontal plane. The orbit heading α_h is the angle between the velocity vector of the satellite with respect to the geometrical north and changes as a function of the longitude

ing). While the orbital plane of the satellite has a fixed inclination, both the ascending and descending track have a varying orbital heading α_h, which is the angle between the velocity vector of the satellite with respect to the geometrical north, see Figs. 2.3a and b and Fig. 2.9. Most SAR satellites are right-looking satellites, and in most cases the observations are taken at zero-Doppler, the zero-Doppler plane (ZDP) is perpendicular to the heading of the satellite[1].

The heading of the satellite α_h, and consequently the orientation of the ZDP from a satellite-centered coordinate frame, are different from the direction of the velocity vector and the azimuth of the ZDP α_d in a target-centered coordinate frame on the Earth's surface, see Fig.2.4. This effect is the largest near the poles and is caused by the non-parallel nature (convergence) of the Earth meridians. For a satellite in an ascending acquisition at a higher latitude, considering the zero-Doppler plane at the moment of the satellite acquisition, the satellite has a lower latitude in space compared to the latitude at the Earth's surface. Due to the meridian convergence, the azimuth of the ZDP of the satellite at the Earth surface, α_d, is greater than the heading of the satellite (in space), $\alpha_h - 90°$. This effect should be taken into account while computing the viewing geometry since the difference can be significant, especially at higher latitudes.

Note, however, that the effect is also present near the equator. When at the moment of the acquisition a descending satellite is positioned exactly at the equator, the satellite 'looks' at a point which is located at a higher latitude $> 0°$. The heading of a satellite corresponds to a latitude of the location of the satellites in space, and consequently a (slight) difference between the heading angle of the satellite and the orientation of the ZDP. Thus, to obtain the correct azimuth angle of the ZDP for a target on the Earth's surface, these effects need to be accounted for.

Finally it is important to mention that not all observations are taken at zero-Doppler, consider e.g., Sentinel-1 in TOPS mode. Strictly, for such cases the azimuth of the zero-Doppler plane cannot be used to express the orientation of the LoS direction at the target. Instead, it is the azimuth of the plane spanned by the LoS vector and the gravity vector pointing from the Earth to the satellite that should be considered. Yet, for many satellites modes, the zero-Doppler plane is a good approximation to describe the orientation of the LoS vector. In the following, we therefore consider the standard 'stripmap' viewing geometry since the potential errors are minimal.

2.1.4. Incidence angle

Within this study, the incidence angle, θ, refers to the nominal (ellipsoidal) incidence angle, i.e., the angle between the normal vector on the local ellipsoid, at the position of the target, and the Line-of-

[1]Note that the ZDP is an approximation for the zero-Doppler. Actually, we have to do with iso-doppler lines which can be curved

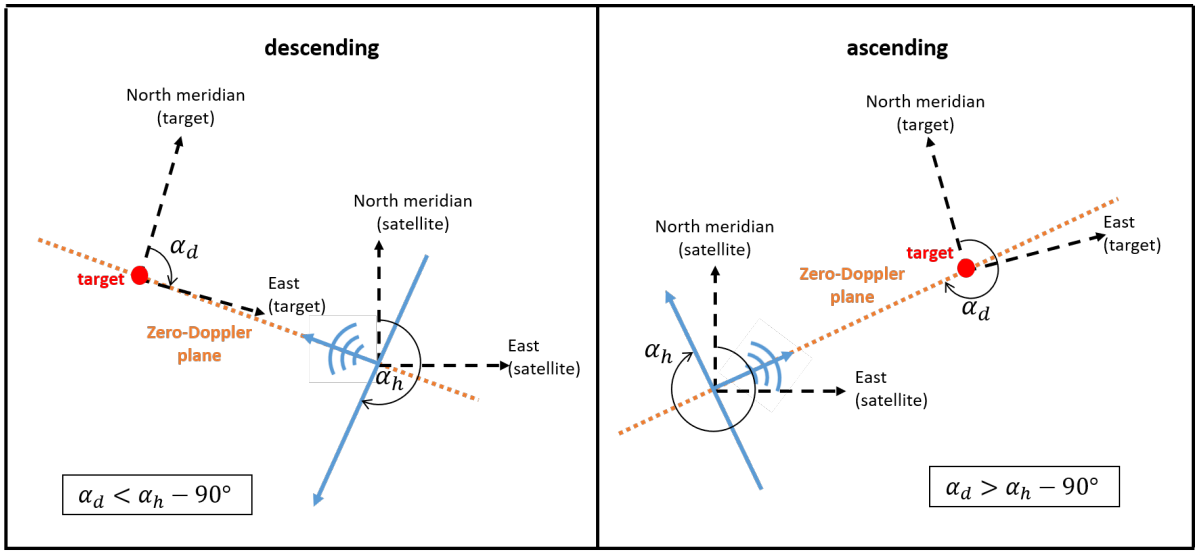

Figure 2.4: A satellite observes a location on Earth (target) from a particular latitude in space. The velocity vector of the satellite has azimuth angle α_h with respect to the geographical north. For the Northern Hemisphere, the satellite is observing the target on Earth (red dot) which is located at a higher latitude compared to the latitude of the satellite. Due to the meridian convergence, the azimuth of the zero-Doppler plane on Earth (α_d) differs from $\alpha_h - 90°$. For an ascending acquisition $\alpha_d > \alpha_h - 90°$ and for a descending acquisition, the opposite is true: $\alpha_d < \alpha_h - 90°$

Sight towards the satellite in the ZDP, see Fig. 2.5a [17]. The incidence angle should not be confused with the satellite look angle θ_l, which is the angle between the LoS direction and the nadir of the satellite sensor. Due to the curved surface of the Earth the incidence angle is always greater than the look angle ($\theta > \theta_l$). Moreover, the nominal incidence angle varies with the range direction. Therefore, the incidence angle is different for every pixel in an InSAR image. For example the swath width of the Sentinel-1 radar is 250 km, therefore the incidence angle varies from 29.1° at the near range to 46° at the far range [18]. The difference between the near-range and far-range incidence angles should be taken into account when performing a decomposition or projection of the LoS displacements.

We can also define a topographic incidence angle θ_{topo}. This is the angle between the LoS vector towards the satellite and the normal at the surface at the point of interest, see Fig. 2.5c. The topographic incidence angle determines for a great part whether a displacement is observable by a satellite, especially at steep slopes, where it can be expected that the main displacements occur parallel to the slope. For small topographic incidence angles, the LoS direction is almost perpendicular to the expected dis-

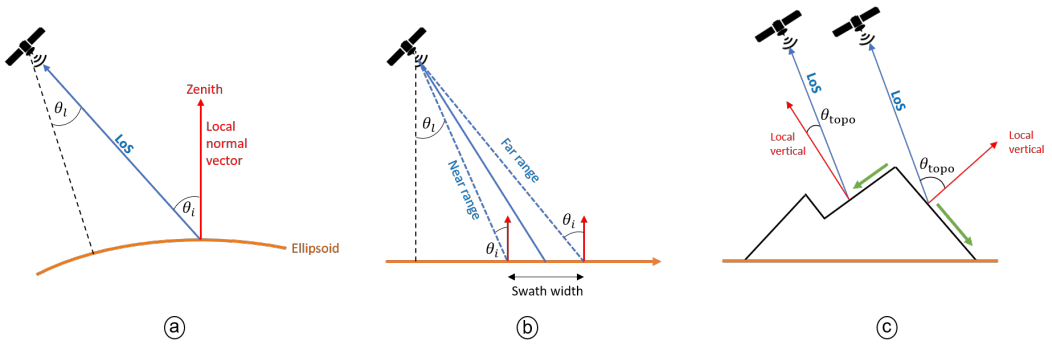

Figure 2.5: (a) The incidence angle θ is the angle between the LoS vector and the local zenith at the surface. The incidence differs from the satellite look angle θ_l. (b) shows that the incidence angle varies over an InSAR image. The near-range incidence angles can be significantly smaller than the far-range incidence angles. In (c) the topographic incidence angles are shown. θ_{topo} determines whether a displacement can be observed by a satellite. Larger topographic incidence angles will result in better observable displacements.

placement direction, resulting in the fact that only a part of the occurring displacement is mapped to the LoS direction. For large topographic incidence angles, the LoS direction can almost be parallel to the slope and up to the full deformation signal will be mapped to the LoS.

From now on, we will use θ to indicate the nominal incidence angle which we will call the incidence angle for short. A complete overview of the viewing geometry to the satellite is given in Fig. 2.6.

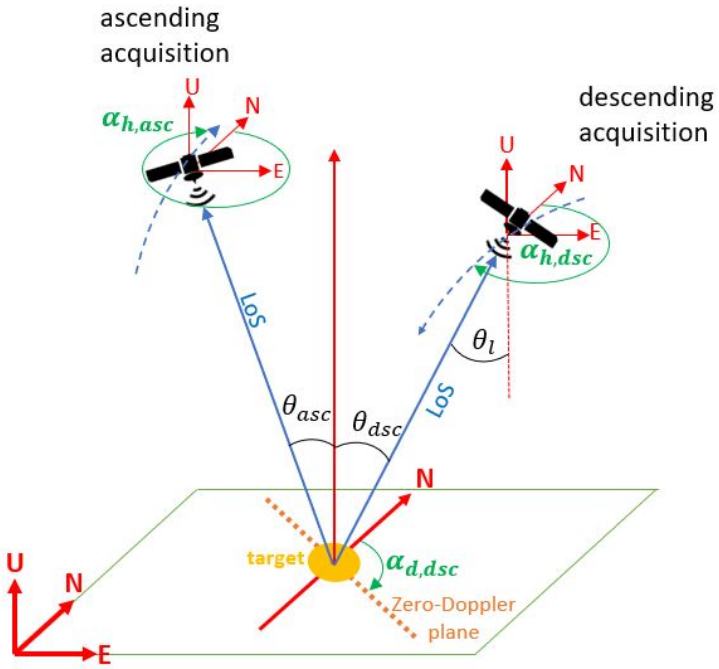

Figure 2.6: Schematic overview of the viewing geometry to a satellite in an ascending and a descending acquisition. The heading angles $\alpha_{h,asc}$ and $\alpha_{h,dsc}$ are the azimuth angles of the velocity vectors of the satellites with respect to the geometrical north. The azimuth angle of the ZDP at the Earth surface $\alpha_{d,dsc}$ is shown for the descending acquisition. The incidence angle is the angle between the LoS vector and the local zenith and differs from the satellite look angle θ_l.

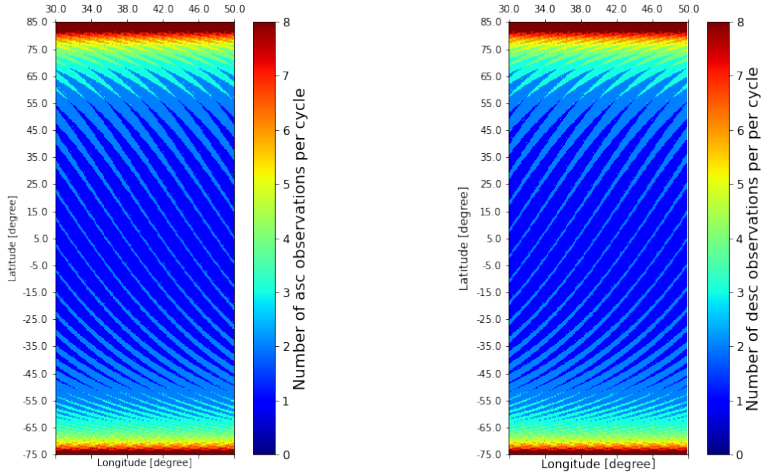

Figure 2.7: Number of observations per cycle per location on Earth. Due to the convergence of the meridians, different tracks overlap at higher and lower latitudes. Around the equator, at most one ascending and one descending acquisition are available. Whereas at high latitudes some locations are observed by up to eight different ascending and descending acquisitions.

2.1.5. Correlation incidence angle and azimuth of the ZDP

Due to the convergence of the meridians, different tracks overlap at higher and lower latitudes. As a result, the number of observations per cycle per location on Earth differs, see Fig. 2.7. For locations on Earth observed by multiple acquisitions, the geometric configuration of the observations differs since the range distance between the different satellite positions and the target is unique. Consequently, the incidence angles differ, but the azimuth of the ZDP varies as well.

Using DRaMA, the Delft Radar Modelling and performance Analysis toolbox[2] [19], we estimated the viewing geometries of all available acquisitions for all locations on Earth. In Fig. 2.8, we show the maximum and minimum values for the azimuth of the ZDP for the available acquisitions. This shows that

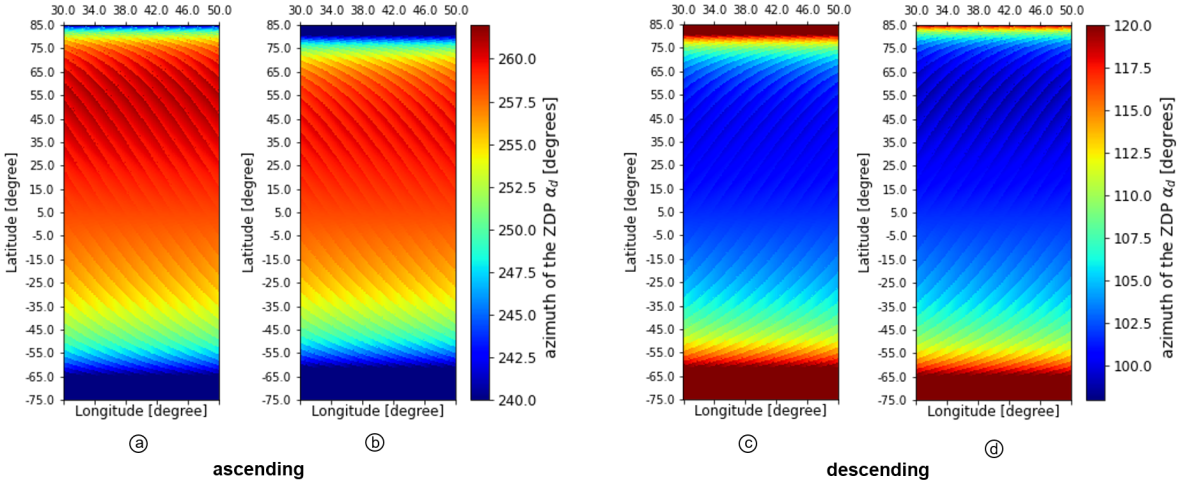

Figure 2.8: Minimum and maximum azimuth angle of the ZDP, α_d, as a function of location on Earth. In (a) and (b), the minimum and maximum values for α_d for all ascending acquisitions are shown, and (c) and (d) show the minimum and maximum α_d for the descending acquisitions.This shows that α_d varies more than 20° over the earth, and that this is both latitude as well as longitude dependent.

the values for α_d can differ per acquisition. Around the equator, the minimum and maximum azimuth

[2]DRaMA can be downloaded from: https://gitlab.tudelft.nl/drama/drama

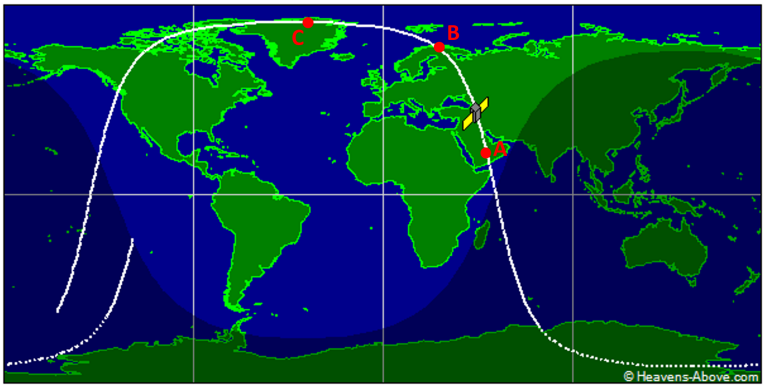

Figure 2.9: The ground track for Sentinel-1.It can be seen that the heading of the satellite changes with latitude. At the equator, the heading is almost NS directed (at location A) whereas, for a satellite in an ascending orbit around the poles, the heading is almost westward (location C), source: Heavens Above [20].

of the ZDP are equal, which is trivial since there is typically only one ascending or one descending acquisition. For the ascending acquisitions, we find $\alpha_d \approx 260°$, and for the descending acquisitions, we find $\alpha_d \approx 100°$. At high latitudes, α_d increases for the ascending acquisitions and decreases for the descending acquisitions. Note that there is also a difference between the minimum and maximum value for α_d. Finally, it can be observed that there is also a longitude-dependent variability of the minimum and maximum azimuth angles, particularly at mid-latitudes.

We will explain this behavior first geographically. For an ascending satellite, seen from the Earth's surface, the heading of the satellite α_h shifts more and more to the west while the satellite heads for the poles, see Fig. 2.9. Therefore, α_d shifts more north and becomes smaller compared to α_d around the equator (at the poles we find $\alpha_d < 260°$). As already mentioned, the incidence angle varies with range. But from Fig. 2.10 it can be seen that also α_d varies with range. In blue, the position of the satellite is given, imaging two targets—indicated in red—at different ranges. As the range to the target increases, due to the meridian convergence the azimuth of the ZDP, α_d increases. Thus, for ascending acquisitions, $\alpha_{d,\mathrm{nr}} < \alpha_{d,\mathrm{fr}}$ where $\alpha_{d,\mathrm{nr}}$ is the azimuth of the ZDP at the near range and $\alpha_{d,\mathrm{fr}}$ the azimuth of the ZDP at the far range. This implies that there is a positive correlation between the incidence angle and the azimuth of the ZDP. For the descending satellite, the opposite is true—with $\alpha_{d,\mathrm{nr}} > \alpha_{d,\mathrm{fr}}$ and a negative correlation between θ and α_d, see Appendix B at p. 103 for a visualization.

We tested whether these correlations were also visible in the viewing geometry from Sentinel-1 as estimated with DRaMA. In Fig. 2.11, the correlation between θ and α_d for all available ascending (left) and descending (right) acquisitions for a location at 81° latitude and 40° longitude can be seen. This shows that there is a clear positive (linear) $\theta - \alpha_d$ correlation for the ascending acquisitions and a negative (linear) $\theta - \alpha_d$ correlation for the descending acquisitions. These relations are described by

$$\theta_{\mathrm{asc}} = c_{a1}\alpha_{d,\mathrm{asc}} + c_{a2} \tag{2.4}$$

$$\theta_{\mathrm{desc}} = c_{d1}\alpha_{d,\mathrm{desc}} + c_{d2} \tag{2.5}$$

where c_{a1} and c_{a2} are constants related to the ascending acquisitions and c_{d1} and c_{d2} are the constants related to the descending acquisitions.

For locations on Earth between $-75°$ and $+85°$ latitude and between 30° and 50° longitude we estimated the constants c_{a1}, c_{a2}, c_{d1} and c_{d2}, plotted in Fig. 2.12. This demonstrates that there is indeed a positive correlation ($c_{a1} > 0$) between θ and α_d for the ascending acquisitions for the Northern Hemisphere and a negative correlation ($c_{a1} < 0$) for the descending acquisitions. Moreover, it can be seen that c_{a1} and c_{d1} change sign when going from the northern to the Southern Hemisphere. Near the equator, we expect to see large values for c_{a1} and c_{d1} since the incidence angles vary from near to far range. In contrast, the azimuth of the ZDP's only have a minor difference since the meridian convergence is minimal.

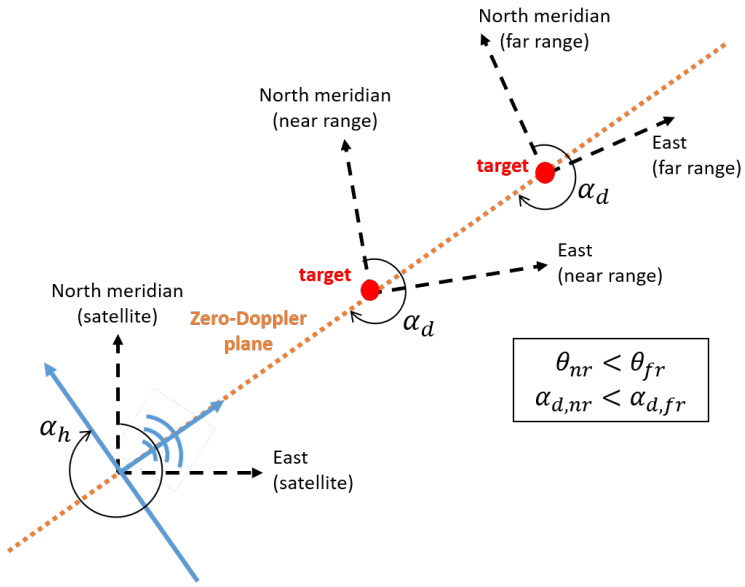

Figure 2.10: Range dependency of the azimuth of the ZDP. In blue, the position and heading of the satellite. In red, two targets on the ground at different ranges. For the near range (nr), the north meridians at the Earth surface have a different orientation then the north meridians at the far range (fr). Therefore, for ascending acquisitions, $\alpha_{d,\mathrm{nr}} < \alpha_{d,\mathrm{fr}}$. As the incidence angle also varies with range, this results in a positive correlation between α_d and θ.

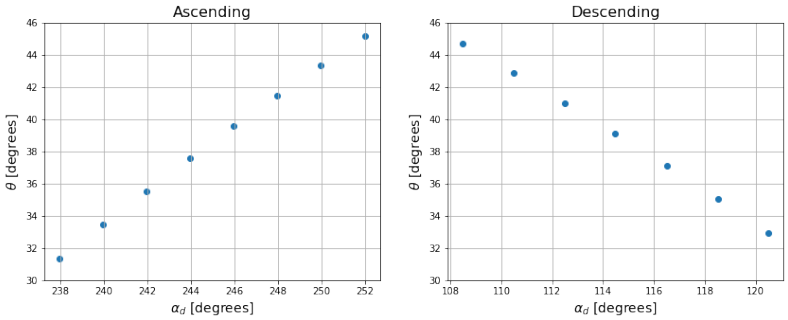

Figure 2.11: For a location at 81° latitude and 40° longitude, the left figure shows the positive correlation between α_d and θ for ascending acquisitions. For descending acquisitions there is a negative correlation

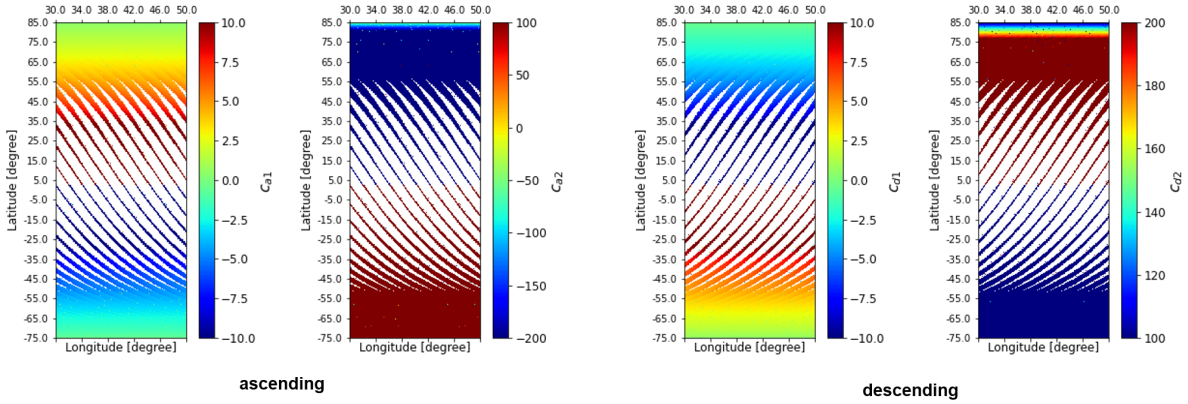

Figure 2.12: For locations on Earth where multiple acquisitions were available, we computed the linear relation between the incidence angles and azimuth values of the ZDP's for both the ascending, (a) and (b) and the descending (c) and (d) acquisitions. The figures show the estimated constants in Eqs. (2.4) and (2.5)

We also observe a very strong relation between the different constants c_{a1} and c_{d1} and c_{a2} and c_{d2}. In fact, in Appendix B we find that $c_{a1} = -c_{d1}$. Moreover, we found that there is also a strong relation between the latitudinal coordinate and the four constants, see also the Appendix B.

2.2. The forward model: LoS observations

Deformation phenomena, i.e., the displacements of objects represented by infinitesimally small points, occur in a 3D world and their displacement can be described by a 3D vector with displacement components in the east, north and up direction: $d_{\mathrm{ENU}} = [d_e, d_n, d_u]^T$. This displacement is observed by the satellite as the orthogonal projection of d_{ENU} onto the LoS direction. We refer to this as a *forced* projection, as it is an implicit autonomous operation.[3] For a SAR satellite with an azimuth angle of the ZDP, α_d, the LoS projection d_{LoS} in a Cartesian east, north, up (ENU) coordinate system is given by

$$d_{\mathrm{LoS}} = -\sin\theta\,[-d_e\ \sin\alpha_d - d_n\ \cos\alpha_d] + d_u\ \cos\theta. \tag{2.6}$$

We refer to this as the forward problem, which can be written as the multiplication of a row and column vector by

$$d_{\mathrm{LoS}} = \begin{bmatrix}\sin\theta\ \sin\alpha_d & \sin\theta\ \cos\alpha_d & \cos\theta\end{bmatrix}\begin{bmatrix}d_e\\ d_n\\ d_u\end{bmatrix} = P_{\mathrm{LoS}}\, d_{\mathrm{ENU}}, \tag{2.7}$$

where $P_{\mathrm{LoS}} = [\sin\theta\sin\alpha_d, \sin\theta\cos\alpha_d, \cos\theta]$ is the orthogonal projector onto the LoS. It is crucial to note that the unit vector spanning the LoS direction has its origin at the scatterer (i.e., the target), and not at the satellite. Consequently, the signs of the projector elements make sense when looking from the scatterers perspective. The reference is the scatterer position at t_0 and a motion upward ($+$, positive d_u) would yield a decrease ($-$) in slant range, i.e. the distance between the satellite and the scatterer will be shorter. This can also be seen in Eq. (2.7), where the signs of the projector are $[+,+,+]$ as measured from the scatterer (the up-component is positive, indicating that upward motion corresponds with an increasing LoS (the objects moves towards the satellite), hence, a decreasing total slant range. A detailed derivation of the signs of the projector is given in Appendix A.

The alternative choice is to use the satellite as the reference point. In that case, the unit vector spanning the LoS direction is pointing in the opposite direction, and the signs of the projector in Eq. (2.7) would be the opposite resulting in $[-,-,-]$, a choice made by other authors, e.g., [9]. This way, a positive LoS displacement is a (positive) range increase, but if we then look at the up-component, this will result in the scatterer moving downward. Here we propose to use the more straightforward convention from the target's perspective.

Since d_{LoS} is the orthogonal projection of the 3D displacement vector onto the LoS direction, displacements that have a direction which is orthogonal to the LoS, i.e., displacements that are directed in the solution plane or null space, result in $d_{\mathrm{LoS}} = 0$. This is visualized in Fig. 2.13 where the red arrow represents the LoS direction and the blue surface is the null space. Therefore, displacements represented by the blue arrows (which are in the null space) result in $d_{\mathrm{LoS}} = 0$, i.e., the radar has no sensitivity for displacements in that direction. Moreover, any displacement vector from the target to a location somewhere on the solution plane (the orange arrows) result in the same orthogonal projection onto the LoS direction and therefore in the same LoS observation.

2.3. The inverse model: decomposition of the LoS displacements

The LoS displacements itself are one-dimensional and are hard to interpret for end users without a substantial radar knowledge. Moreover, end users are mostly interested in the 'real' 3D displacements. Therefore it is required to decompose the LoS displacements, d_{LoS}, into 'real' 3D displacements, d_e, d_n

[3] Later, in section 2.4.2 we will compare the forced projection with a voluntary projection.

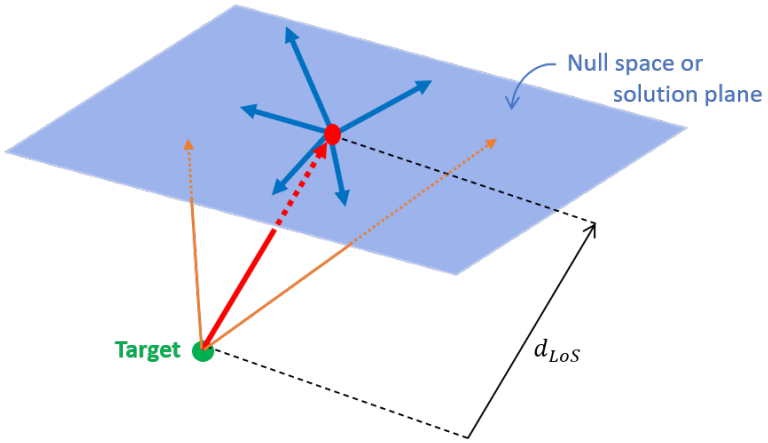

Figure 2.13: d_{LoS} is the orthogonal projection of the 3D displacement vector (the orange vectors) onto the LoS direction of the satellite. The blue plane orthogonal to the LoS direction is the null space or solution plane. Displacements into this plane (blue arrows) have no projection onto the LoS and therefore $d_{\mathrm{LoS}} = 0$. Moreover, all displacement vectors from the target with the end point at a location somewhere in the solution plane result in the same projection onto the LoS direction.

and d_u, which we call the inverse problem. To uniquely estimate the three displacement components, we require at least three spatio-temporally coinciding independent (STCI) LoS observations (i.e., of the same scatterer, observed at the same time), discussed in section 2.3.1, which are all stemming from the same Region of Uniform Motion (RUM), discussed in section 2.3.2, and a full-rank system of equations, meaning that the observations need to have sufficiently angular diversity. The mathematical model of Eq. (2.7) is then extended to

$$\underbrace{E\{\begin{bmatrix} \underline{d}_{\mathrm{LoS}}^{(1)} \\ \underline{d}_{\mathrm{LoS}}^{(2)} \\ \vdots \\ \underline{d}_{\mathrm{LoS}}^{(m)} \end{bmatrix}\}}_{\underline{y}} = \underbrace{\begin{bmatrix} \sin\theta_1 & \sin\alpha_{d,1} & \sin\theta_1 & \cos\alpha_{d,1} & \cos\theta_1 \\ \sin\theta_2 & \sin\alpha_{d,2} & \sin\theta_2 & \cos\alpha_{d,2} & \cos\theta_2 \\ & \vdots & & \vdots & \vdots \\ \sin\theta_m & \sin\alpha_{d,m} & \sin\theta_m & \cos\alpha_{d,m} & \cos\theta_m \end{bmatrix}}_{A} \underbrace{\begin{bmatrix} d_e \\ d_n \\ d_u \end{bmatrix}}_{x}, \tag{2.8}$$

$$\underbrace{D\{\begin{bmatrix} \underline{d}_{\mathrm{LoS}}^{(1)} \\ \underline{d}_{\mathrm{LoS}}^{(2)} \\ \vdots \\ \underline{d}_{\mathrm{LoS}}^{(m)} \end{bmatrix}\}}_{\underline{y}} = \underbrace{\begin{bmatrix} Q_{\mathrm{LoS},1} & 0 & \dots & 0 \\ 0 & Q_{\mathrm{LoS},2} & \dots & 0 \\ \vdots & \vdots & \ddots & \vdots \\ 0 & 0 & \dots & Q_{\mathrm{LoS},m} \end{bmatrix}}_{Q_{yy}}, \tag{2.9}$$

where vectors $\underline{d}_{\mathrm{LoS}}^{(1)}$ until $\underline{d}_{\mathrm{LoS}}^{(m)}$ are sets of STCI LoS displacement observations. Each vector $\underline{d}_{\mathrm{LoS}}^{(i)}$ represents an independent viewing geometry, i.e., the set of all observation points (scatterers) observed from a particular satellite orbit. The size of each displacement vector can be different since the number of available scatterers can differ. From now on, we refer to all observations from one viewing geometry as a 'set'. $E\{.\}$ expresses the expectation operator. This system of equations can be solved with at least three sets of STCI LoS observations, i.e. $\underline{d}_{\mathrm{LoS}}^{(1)}$, $\underline{d}_{\mathrm{LoS}}^{(2)}$ and $\underline{d}_{\mathrm{LoS}}^{(3)}$. The first row in the design matrix A, for $\underline{d}_{\mathrm{LoS}}^{(1)}$, is the projection of the 3D displacements onto the LoS vector towards the first satellite position. We assume that for the observations within one set, the incidence angle θ and azimuth of the ZDP α_d are the same within the RUM. $D\{.\}$ is the dispersion of the model, where $Q_{\mathrm{LoS},i}$ is the variance-covariance matric of an independent observation set. When $\underline{d}_{\mathrm{LoS}}^{(i)}$ has size $p \times 1$, the size of $Q_{\mathrm{LoS},i}$ is $p \times p$. It is a diagonal matrix with the variances of the STCI LoS observations on the diagonal. The off-diagonal elements are equal to zero. It can be safely assumed that the different LoS observations are uncorrelated since they all represent different physical scatterers, i.e., with different reflective characteristics of the imaged objects.

When $m > 3$, the unknown displacement parameters can be estimated by using the Best Linear Unbi-

ased Estimator (BLUE),

$$\underline{\hat{x}} = (A^T Q_{yy}^{-1} A)^{-1} A^T Q_{yy}^{-1} \underline{y}, \tag{2.10}$$

and when $m = 3$ and matrix A has rank 3 (full rank), the displacement parameters follow from inverting the system of equations, as

$$\underline{\hat{x}} = A^{-1} \underline{y}. \tag{2.11}$$

In the following sections, we will first explain the concepts STCI LoS observations and RUM in sections 2.3.1 and 2.3.2, respectively. Afterwards, in section 2.3.3, we explain why we require three different sets of STCI observations and why it remains difficult to have a full rank system of equations.

2.3.1. Spatio-temporally coinciding independent LoS observations

The mathematical discussion above would be valid only if all observations y from different radar geometries would be unambiguously linked to the same physical displacement signal, x. In reality, this is almost never exactly true. Therefore, using the concept of spatio-temporally coinciding independent (STCI) LoS observations, we mean that (i) the same scatterers, (ii) on an object that is not subject to internal deformation, are observed (iii) simultaneously by different viewing geometries. Thus, the following three conditions should be fulfilled:

1. The observations from the different viewing geometries should observe the same deformation signal or phenomenon.
2. This only works if the same (position of an) object would be measured by the different viewing geometries
3. Added to condition 1 and 2, the deformation phenomenon should be observed at the same moments in time (epochs).

Condition 1 is trivial. When the first satellite only observes targets that move in the vertical plane, while the other satellites observe different points that move both vertically and horizontally, the estimates for the displacements components will be wrong. For example, this may hold when ascending and descending viewing geometries observe the opposite sides of a house. In such cases the observations of the different viewing geometries are related to different functional models and combining them in one model would obviously cause errors in the estimated parameters.

The second condition is related to the spatial part of the STCI LoS observations and is essential since scatters close to each other are not per definition stemming from the same object. Added to this, different objects (or parts of objects) can show different deformation phenomena. An example would be a road with at one side a building. Due to soft soils , the road close to the building may show large vertical displacements, while the building is stable. Two scatterers may be spatially near, but showing a totally different deformation behavior.

The third condition is related to the temporal part, which is required since by definition deformation phenomena change over time. The observations from the different acquisitions are never taken at the same moment. E.g., in the Netherlands, there is a time difference of three days between the ascending en descending acquisition from Sentinel-1. For rapid changing deformation phenomena such as landslides, it may be tricky to assume that observations from different epochs represent the same behavior. When the different observations are indeed representing different signals, the observations belong to different functional models, which will cause errors when the observations are combined in the same functional model. However, to be still able to use observations from different viewing geometries, we need to assume that it is possible to interpolate the observations in time, which is only possible when the deformation phenomenon has a smooth behavior in time and is not rapidly changing.

The last term of importance from the STCI LoS observations in the 'independent' part, where the different observations need to be independent, to ensure the diagonal variance-covariance matrix in Eq. (2.9).

Thus, we need to explicitly make the STCI assumption when we attempt to solve the inverse problem and estimate the displacement components.

2.3.2. Region of Uniform Motion

Unfortunately, the three conditions described in section 2.3.1 are hardly ever fulfilled for a single target. This would only be the case when point scatterers (PS) observed with one satellite would exactly match the PS of the other satellites, as e.g., with lamp posts [21, 22] or integrated geodetic reference stations (IGRS) [23]. Thus, more in general, the decomposition of the LoS observations should be based on the following assumption:

Points that fall within one Region of Uniform Motion (RUM) are stemming from the same object and behave according to the same deformation phenomenon

So only after (i) defining a RUM, (ii) aligning the different data sets in time, and (iii) ensuring that the data sets are all referenced to one common reference point, it will be possible to decompose the LoS observations into the unknown displacements parameters. However, defining a RUM can be tricky since it is likely to fail. For example, when one would be interested in the deformation of a road and a RUM is defined, it may be that scatterers from the side of the road or the crash barrier fall within the RUM. However, those points may behave according to different deformation phenomena and should not end up in the same RUM as scatterers on the road.

Reference point

Apart from the STCI and RUM conditions, it is also essential that the different LoS observations are referenced to the same reference point. Typically PS displacements are acquired by taking double-differences with respect to a stable reference point. If the reference point is not as stable as expected, e.g., subsiding, the LoS displacements for the other scatterers are biased with an uplift signal. Obviously, there are different reference points for the observations from different viewing geometries, which results in erroneous results for the decomposed displacement parameters. Thus, if the different LoS observation sets are referenced to other reference points, they are not observing the 'same' deformation phenomenon anymore.

There are several ways to correct this problem. One approach relies on the assumption that for larger areas (significantly wider than one RUM), the average displacement of all PS points within this wider area is zero. When the average displacement of a complete LoS data set is not zero, it can be the case that the LoS displacements are referenced to a moving reference point. It is possible to subtract this average displacement signal from all PS points separately. Now, on average, the complete data set is assumed to have zero displacements. When this procedure is executed for all data sets used for the decomposition, all data sets are referenced to the same virtual reference point.

2.3.3. Full rank system

To unambiguously solve for the three unknown displacement components we require at least three sets of STCI observations from different viewing geometries, yielding a unique solution. Multiple observations from one set would not be sufficient since the observations within one RUM all belong to the same viewing geometry and the same deformation phenomena. This can be explained by analyzing the solution space for different cases. With only one LoS observation set, the solution space is the plane orthogonal to the LoS displacement vector that contains the end point of d_{LoS}, see Fig. 2.14a. All points located in the null space (red surface) are a possible solution to the inverse problem. The solution plane for one LoS observation is defined by the LoS unit vector $\mathrm{u}_{\mathrm{LoS}}$ which is normal to the solution plane, and can be written as

$$\mathrm{u}_{\mathrm{LoS}} = \begin{bmatrix} \mathrm{u}_1 \\ \mathrm{u}_2 \\ \mathrm{u}_3 \end{bmatrix} = \begin{bmatrix} \sin\theta \sin\alpha_d \\ \sin\theta \cos\alpha_d \\ \cos\theta \end{bmatrix}. \tag{2.12}$$

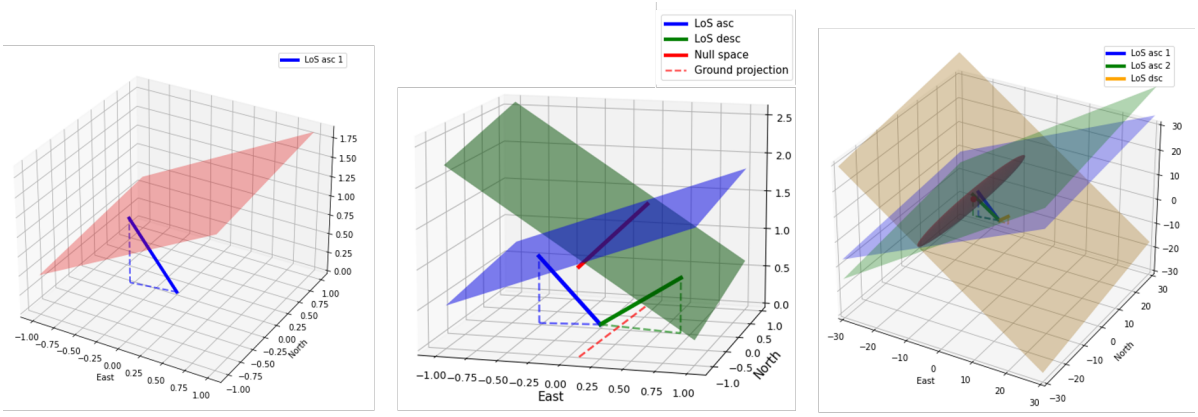

Figure 2.14: The solution space for the inverse problem. With only one LoS observation set this is the red plane shown in (a). When two LoS observation sets are available, the two solution planes (blue and green plane) intersect, where the intersection is a line. All points located on the null line, the red line in (b), are a possible solution to the inverse problem. Only with three observation sets, the displacement components can be solved unambiguously. The solution is the intersection point of the three solution planes in (c). When precisions are available for the observations, the precision of the solution is described by an error ellipsoid, shown in red in (c).

The solution plane further contains point $p_0 = (d_{\mathrm{LoS,e}}, d_{\mathrm{LoS,n}}, d_{\mathrm{LoS,u}})$, where $d_{\mathrm{LoS,e}}$, $d_{\mathrm{LoS,n}}$ and $d_{\mathrm{LoS,u}}$ are the coordinates of the LoS vector in the east, north and up direction and are defined as: $d_{\mathrm{LoS,e}} = d_{\mathrm{LoS}} \sin\theta \sin\alpha_d$, $d_{\mathrm{LoS,n}} = d_{\mathrm{LoS}} \sin\theta \cos\alpha_d$ and $d_{\mathrm{LoS,u}} = d_{\mathrm{LoS}} \cos\theta$. The equation of the plane is defined as

$$\mathrm{u}_1(x - d_{\mathrm{LoS,e}}) + \mathrm{u}_1(y - d_{\mathrm{LoS,n}}) + \mathrm{u}_1(z - d_{\mathrm{LoS,u}}) = 0. \tag{2.13}$$

When two LoS observation sets are available, the solution space is a line: the *null line*. This is visualized in Fig. 2.14b, where the blue and green lines are the LoS unit vectors corresponding to an ascending and a descending observation, the blue and green planes are the solution planes, and the red line is the solution space (or null space) for the two observations. This null line contains the endpoint of the unknown 3D displacement vector. However, the actual (correct) solution remains unknown since all points on the line are a potential solution to the underdetermined problem.

When the viewing geometry for both acquisitions is known, it is possible to describe the orientation of the null line with two angles, ϕ and ζ, where ϕ is the azimuth of the line and ζ the elevation angle. The direction of the null line is given by the cross product of the two normal vectors of the solution planes, which are the LoS unit vectors. Therefore the direction vector of the null line equals

$$\begin{aligned} n = \mathrm{u}_{\mathrm{LoS}}^{(1)} \times \mathrm{u}_{\mathrm{LoS}}^{(2)} &= \begin{bmatrix} \sin\theta_1 \sin\alpha_{d,1} \\ \sin\theta_1 \cos\alpha_{d,1} \\ \cos\theta_1 \end{bmatrix} \times \begin{bmatrix} \sin\theta_2 \sin\alpha_{d,2} \\ \sin\theta_2 \cos\alpha_{d,2} \\ \cos\theta_2 \end{bmatrix} \\ &= \begin{bmatrix} n_1 \\ n_2 \\ n_3 \end{bmatrix} = \begin{bmatrix} \sin\theta_1 \cos\alpha_{d,1} \cos\theta_2 - \cos\theta_1 \sin\theta_2 \cos\alpha_{d,2} \\ -\sin\theta_1 \sin\alpha_{d,1} \cos\theta_2 + \cos\theta_1 \sin\theta_2 \sin\alpha_{d,2} \\ \sin\theta_1 \sin\alpha_{d,1} \sin\theta_2 \cos\alpha_{d,2} - \sin\theta_1 \cos\alpha_{d,1} \sin\theta_2 \sin\alpha_{d,2} \end{bmatrix}, \end{aligned} \tag{2.14}$$

where n is the direction of the null line, θ_1 and $\alpha_{d,1}$ correspond to the first viewing geometry and θ_2 and $\alpha_{d,2}$ to the second viewing geometry. From s it is possible to compute ϕ and ζ with

$$\phi = \tan^{-1}\left(\frac{n_1}{n_2}\right) \text{ and} \tag{2.15}$$

$$\zeta = \tan^{-1}\left(\frac{n_3}{\sqrt{n_1^2 + n_2^2}}\right), \tag{2.16}$$

where n_1, n_2, and n_3 are the first, second, and third component of n respectively. Displacements that are directed in n have a projection into both LoS directions which is zero, i.e., both satellites are not

sensitive for displacements into that direction. Note that with ϕ and ζ we only have the direction of the null line and not the exact position.

Only with three or more sets of LoS observations, it is possible to solve for the 3D displacement vector unambiguously. With three viewing geometries, there is one unique point where the three solution planes intersect, see Fig. 2.14. This location is the unique solution to the (well-determined) problem.

Moreover, the quality of the solution for Eq. (2.11) is found with the error propagation law as

$$Q_{\hat{x}} = (A^T Q_{yy}^{-1} A)^{-1} = \begin{bmatrix} \sigma_e^2 & \sigma_{en} & \sigma_{eu} \\ \sigma_{en} & \sigma_n^2 & \sigma_{nu} \\ \sigma_{eu} & \sigma_{nu} & \sigma_u^2 \end{bmatrix}, \tag{2.17}$$

where the diagonal elements of $Q_{\hat{x}}$ give the precision for $\hat{d}_e, \hat{d}_n$, and $\hat{d}_u$ respectively. Within Fig. 2.14c we also showed the error ellipsoid for the solution, which is uniquely defined by $Q_{\hat{x}}$ It can be seen that, especially for the northern direction, the precision of the estimated displacement is ~30 times worse compared to the eastern and vertical direction. This is caused by the limited angular diversity of the observations on which we elaborate more on in the next section.

Angular diversity

The requirement of three STCI LoS observations sets stemming from the same RUM is a *necessary but insufficient* requirement. The three STCI LoS observations also need to have sufficiently different angular diversity. Only then, the solution to the underdetermined problem will result in reliable estimates for the three displacement components. For example, if only observations would be available from three ascending satellite orbits, with only small differences in the azimuth of the ZDP α_d and incidence angle θ, the angular diversity is too small to give reliable estimates for the unknown displacement parameters resulting in large condition numbers of the design matrix A.

2.3.4. Ill-posed problem

Because all SAR satellites are right-looking and orbiting the Earth in near-polar retrograde orbits, they all have very similar viewing geometries, and there is limited angular diversity between different SAR missions. So even with LoS observations from three viewing geometries, the inverse problem solution is extremely unstable—a small difference in the LoS observations can lead to an enormous change in the estimated displacement components. The inverse problem described by Eqs. (2.8) and (2.9) is therefore often an ill-posed problem. A part of the ill-posed problem comes from to the near-polar orbits of the SAR satellites. For an ascending acquisition, with an incidence angle of $23°$ and an azimuth angle of the ZDP of $256°$, Eq. (2.7) is

$$d_{LoS} = \begin{bmatrix} -0.38 & -0.09 & 0.92 \end{bmatrix} \begin{bmatrix} d_e \\ d_n \\ d_u \end{bmatrix}. \tag{2.18}$$

This means that only ~10% of the displacement in the north direction is mapped to the LoS, while the vertical (up) direction is captured for 92% by the LoS observation. Thus, as only a small part of the north component is mapped to the observation, it is difficult to estimate the north component. Therefore, SAR satellites are less 'sensitive' for displacements in the north direction, and it is more difficult to solve for the north component compared to the east and up components [24, 25].

Variance-covariance matrix of the estimates

With the variance-covariance matrix, we can show that it is indeed difficult to give reliable results for d_n. When simulating three different viewing geometries, consisting of two ascending acquisitions and one descending acquisition, it is possible to estimate the precision for the estimated displacement parameters with the error propagation law:

$$Q_{\hat{x}} = (A^T Q_{yy}^{-1} A)^{-1} = \begin{bmatrix} \sigma_e^2 & \sigma_{en} & \sigma_{eu} \\ \sigma_{en} & \sigma_n^2 & \sigma_{nu} \\ \sigma_{eu} & \sigma_{nu} & \sigma_u^2 \end{bmatrix}. \tag{2.19}$$

Table 2.2: Characteristics of the simulated viewing geometries to estimate $Q_{\hat{x}}$

Geometry type	Incidence angle θ	Azimuth ZDP α_d
ascending (right looking)	31°	261°
ascending (right *or* left looking)	41°	260°
descending (right looking)	44°	100°

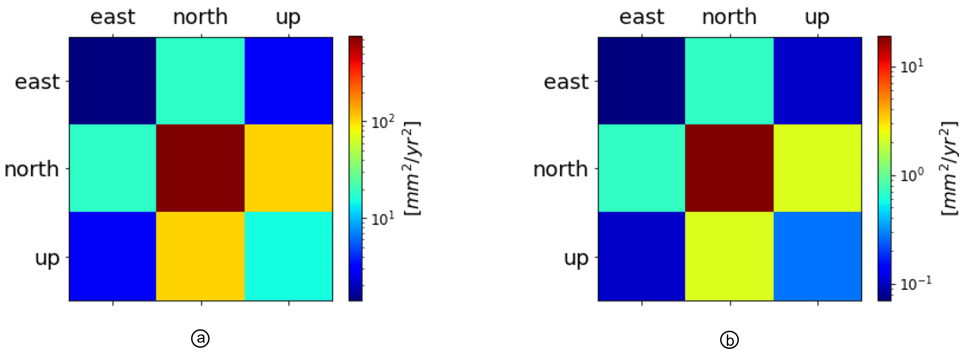

Figure 2.15: The full variance-covariance matrix for the estimates for the three displacement components shown in a logarithmic scale. a) shows the situation where all observations are stemming from right-looking satellites. In b) there are two right looking satellites and one left looking satellite. It can be seen that there is a significant improvement on retrieving d_n, but also the other displacement components benefit from the addition of a left-looking radar acquisition.

Here, A is the design matrix from Eq. (2.8) and Q_{yy} is the variance-covariance matrix from Eq. (2.9). With the characteristics of the three viewing geometries as presented in Tab. 2.2, simulating one scatterer per viewing geometry, and using $\sigma^2_{\text{LoS}} = 1$ mm/yr for all three observations, we estimated $Q_{\hat{x}}$, see Fig. 2.15a. The diagonal of $Q_{\hat{x}}$ shows the variances of $\hat{d}_e, \hat{d}_n$ and $\hat{d}_u$. The precision (σ) with which we can estimate the north component is 27.6 mm/yr, which is way larger than the simulated σ's of the LoS observations. The estimates for the east and up components are more precise and are 1.2 mm/yr and 3.9 mm/yr, respectively.

In Fig. 2.16a, the three null spaces for the three observations are shown, as well as the LoS unit vectors. It can be seen that for the three-unit vectors, the component in the north direction is small, resulting in the low sensitivity for north-south displacements. Furthermore, the intersection of one ascending and one descending solution plane results in the null line running almost from north to south. When a third ascending satellite is added, it only adds limited additional information since the geometry is much like the other ascending satellite. This also explains why the quality of the solution in Fig. 2.14c was described by an ellipsoid that was elongated in the Northern direction.

Left and right looking acquisitions

One solution to improve on retrieving d_n is to add a left-looking observation as Rocca [25] suggested. In Fig. 2.15b, the variance-covariance matrix for the unknown displacement components can be seen for the case where we changed the second ascending acquisition to a left looking acquisition. The precisions of the unknown parameters are now 1.1 mm/yr, 6.0 mm/yr, and 0.8 mm/yr for d_e, d_n, and d_u respectively, which is an improvement for all components. However, the σ for d_n is still large, especially when we consider that the σ for the LoS observations was 1 mm/yr. This can also be seen in Fig. 2.16b, where we see the three solution spaces. Still, there is limited angular diversity.

2.4. The underdetermined problem

Summarizing what we have discussed so far, we can state that uniquely estimating the three displacement components would require at least three sets of STCI LoS observations, all stemming from the

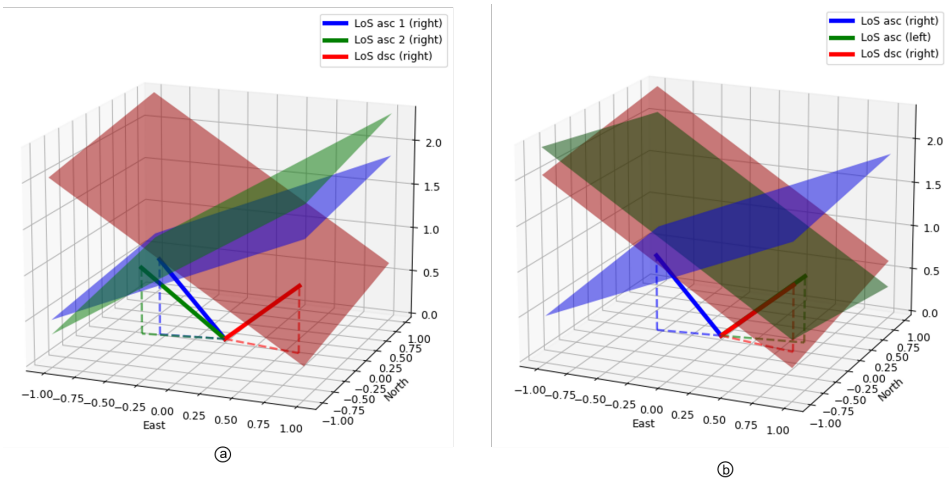

Figure 2.16: The solution spaces for the three observations used for the decomposition. In a) we see the case where only observations from right looking satellites are available. In b) there are two observations from right looking satellites and one observation from a left looking satellite.

Table 2.3: Characteristics of the simulated viewing geometries for one ascending and one descending satellite. Note that the azimuths of the ZDP are indicated *towards* the satellite.

Geometry type	Incidence angle θ	Azimuth ZDP α_d
ascending	30°	260°
descending	45°	100°

same RUM and with sufficiently angular diversity. Unfortunately, in many practical situations, at most two sets of STCI LoS observations (one ascending and one descending) are available, resulting in an underdetermined system with an infinite amount of possible solutions.

2.4.1. Orientation of the null line

In section 2.3.3 we have seen that the orientation of the null line from the RUM's perspective could be described by azimuth angle ϕ and elevation angle ζ. Intuitively, it may seem obvious that $\phi = 0°$ because the heading angles of the ascending and descending acquisition are symmetrical relative to the north. This is also the prevailing premise in the InSAR community, based on common sense: 'ascending and descending orbits are inclined but symmetrical with respect to the poles, so therefore the orientation of the solution space (line) is north-south'. However, in the following we argue that this premise is wrong in itself: it cannot be considered independently from the incidence angle.

Given the exact (nominal) orbital geometries of an ascending acquisition and a descending acquisition as in Tab.2.3, we computed $\phi = 2.7°$ and $\zeta = 7.2°$. This immediately shows that the premise above is incorrect, as $\phi \neq 0°$ despite the symmetric azimuths of the ZDP's ($+100°$ and $-100°$[4]). Thus, apparently, the fact that ϕ deviates from zero is caused by the difference in incidence angles between the ascending and descending acquisitions.

It is intuitively easier to understand that $\phi \neq 0°$ in case the azimuths of the ZDP's of the ascending and descending track are not symmetrical. Moreover, we have seen in section 2.1.5 that the azimuth of the ZDP varies with range. Consequently, the azimuth of the ZDP's for the ascending and descending track are hardly ever symmetrical. For locations on earth that can be viewed from multiple ascending and/or descending acquisitions, the extent of this asymmetry differs per combination. However, we find that the asymmetry is maximal when, for all locations, the acquisitions are chosen that have the maximal α_d, see Fig. 2.8. When we combine those two acquisitions, it is possible to estimate the orientation of

[4]The $-100°$ follows from the 260° azimuth of the ZDP minus 360°.

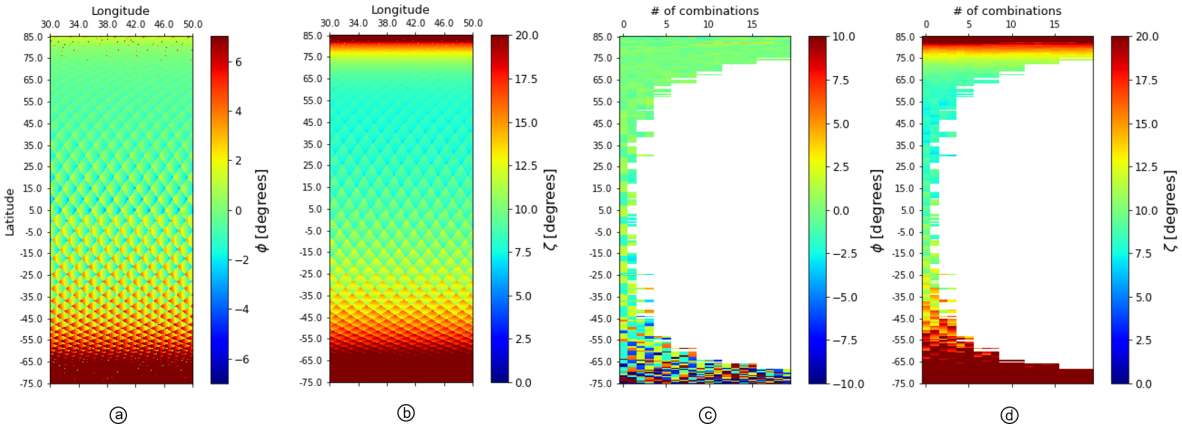

Figure 2.17: Orientation of the solution space line, defined by ϕ and ζ. In (a) and (b), we show ϕ and ζ respectively, estimated by combining the ascending and descending observations that had a maximum azimuth of the ZDP, for each location on earth, considering the maximal asymmetry between the two ZDP's. However, this demonstrates that it still results in $\phi = 0°$ for the Northern Hemisphere due to the difference in incidence angles. In (c) and (d), we estimated per location different ϕ and ζ values for all combinations that we could make between ascending and descending acquisitions. Again, we see at the Northern Hemisphere that $\phi = 0°$. Moreover, we can conclude that $\zeta \neq 0°$

the null line for all locations on earth. These results can be seen in Fig. 2.17a and b, where the values for ϕ and ζ are shown. A remarkable result is that $\phi \approx 0°$ for the Northern Hemisphere, whereas the azimuths of the ZDP's are often not symmetrical. So only considering the asymmetric azimuth of the ZDP's, the null line would have a $\phi \neq 0°$. However, the two corresponding incidence angles (which are not the same) are counteracting this result and 'steer back' to $\phi = 0°$. It is important to note that for the Southern Hemisphere, we find ϕ often not equal to 0°.

From section 2.1.5 we have seen that there is a correlation between α_d and θ, see, e.g., Fig. 2.11. Therefore, it is relevant to investigate whether $\phi = 0°$ can be considered as a 'general rule' for the Northern Hemisphere for Sentinel-1. We compute ϕ and ζ for all possible combinations between ascending and descending acquisitions for different locations. Since the viewing geometry changes with latitude, we defined different locations, all with the same longitudinal coordinate (set to 30°) but varying latitude (between $-75°$ and $+85°$). Around the equator, there are often only one, two, or four combinations to make since there are at most two ascending and two descending acquisitions available. However, for higher latitudes, with up to eight ascending and descending acquisitions, there are more combinations to make. In Fig. 2.17c and d, we show values for ϕ and ζ for different combinations that we could make at a particular latitude. We show up to 20 combinations per location. It can be seen that for the Northern Hemisphere, all combinations result in $\phi = 0°$. So the result for one particular case shown in Fig. 2.17a and b was not coincidental. Also, we found that for the higher southern latitudes, different combinations result in $\phi \neq 0°$. Moreover, for the elevation angle ζ, we find that it increases when approaching the poles.

In Appendix B we have shown that there is a relationship between the latitude and the azimuth of the ZDP with the corresponding incidence angle. In the appendix, we use this relation to show that $\phi = 0°$ for the Northern Hemisphere.

2.4.2. Neglecting the NS displacement component

In the previous section, we found that for the Northern Hemisphere the orientation for the null line is described by $\phi = 0°$, while ζ varies with latitude. Therefore, the unit vector spanning this null line has no component in the east direction. Thus, for any displacement into that direction of the line, the two acquisitions are not sensitive. The results of Fig. 2.17 are therefore in line with the ill-posed problem described in section 2.3.4. Now, the question can be asked whether it is allowable to simply remove

Table 2.4: Characteristics of the Sentinel-1 geometry at Sappemeer, the Netherlands.

	ascending	descending 1	descending 2
θ	32.2°	32.0°	40.5°
α_d	258.5°	101.5°	99.8 °

d_n from Eq. (2.8) resulting in the functional part of the mathematical model being:

$$E\{\underbrace{\begin{bmatrix} d_{\text{LoS}}^{(1)} \\ d_{\text{LoS}}^{(2)} \\ \vdots \\ d_{\text{LoS}}^{(m)} \end{bmatrix}}_{y}\} = \underbrace{\begin{bmatrix} \sin\theta_1 & \sin\alpha_{d,1} & \cos\theta_1 \\ \sin\theta_2 & \sin\alpha_{d,2} & \cos\theta_2 \\ & \vdots & \\ \sin\theta_m & \sin\alpha_{d,m} & \cos\theta_m \end{bmatrix}}_{A} \underbrace{\begin{bmatrix} d_e \\ d_u \end{bmatrix}}_{x}. \tag{2.20}$$

We can demonstrate that this leads to biased estimates for d_e and d_u (in the case that $d_n \neq 0$). We simulate a displacement signal of $d_e = 4$ mm, $d_n = 10$ mm, and $d_u = 4$ mm, and simulate two LoS observations using the forward model of Eq. (3.7). Then, we use the inverse model with Eq. (2.20), see Eq. (2.11), and the two LoS observations to estimate d_e and d_u. We compare the estimated displacements with the simulated values and compute the relative error as a percentage.

We performed the simulation on the viewing geometry of the available acquisitions at Sappemeer, The Netherlands, where we can use one ascending and two descending acquisitions, see Tab. 2.4. Combining the ascending acquisition with the first descending acquisition yields symmetrical azimuths of the ZDP's. We first consider this case in Fig. 2.18. In Fig. 2.18a, we fixed the azimuth of the ZDP to the descending orbit to 101.5° and we varied the incidence angle. We plotted both the relative error (in colored lines with the percentage on the left axis) as well as the orientation of the null line (black lines and right axis). In Fig. 2.18b, we fixed the incidence angle of the descending acquisition to 35° (which is the same as for the ascending acquisition), and we varied the azimuth of the ZDP. It can be seen that

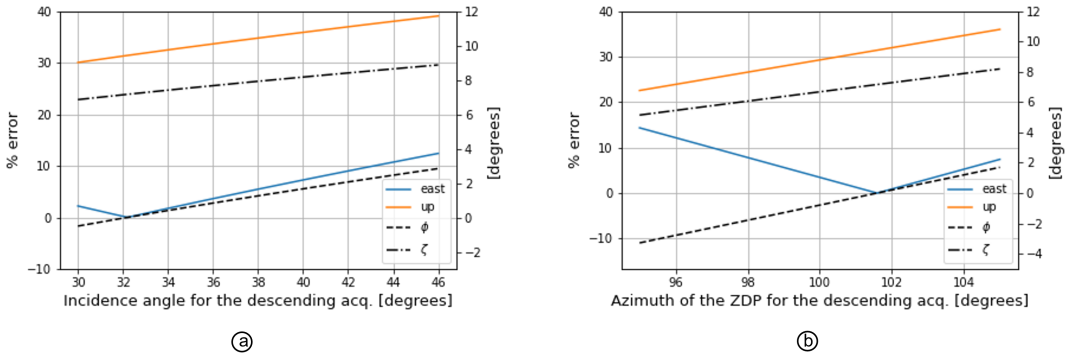

Figure 2.18: Relative error for the estimated east and up displacement components when the north component is simply removed and Eq. (2.20) is solved. It can be seen that both d_e and d_u (colored lines) are biased. In (a) we show the results when the azimuth angles of the ZDP for the ascending and descending acquisition are symmetrical and we vary the incidence angle of the descending acquisition. In (b) we fixed the incidence angle of the descending acquisition and varied the azimuth of the ZDP. Only for the case that the azimuths of the ZDP's are symmetrical *and* the incidence angles are equal, there is no bias for the east component. It can also be seen that the size of the biases are related to the variation in ϕ and ζ.

only if the azimuth of the ZDP's are symmetrical around the north-south direction *and* both incidence angles are equal, the bias for d_e is zero. In all other cases, there is a bias in the estimate of the vertical component. Moreover, it can be seen that the bias is not only caused due to non-symmetrical azimuths of the ZDP's but also due to differences in incidence angles, see Fig. 2.18a.

At Sappemeer, we can also combine the ascending acquisition with the second descending acquisition, which yields azimuths of the ZDP's that are not symmetric. The results for this case can be seen in

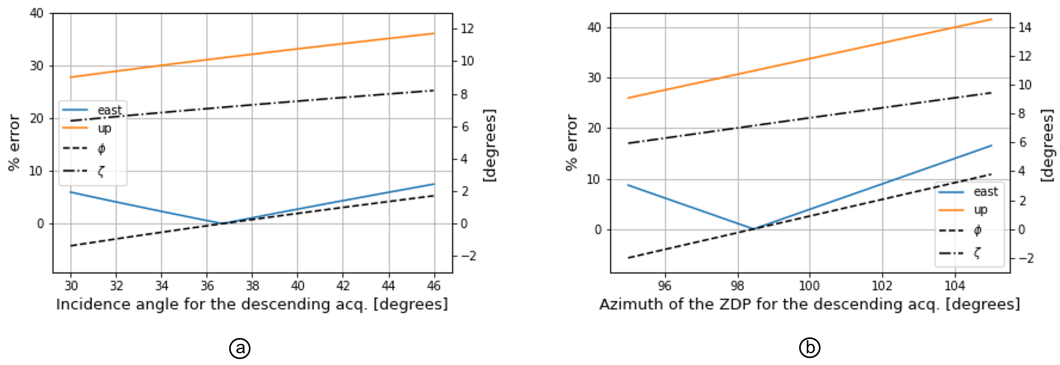

Figure 2.19: Relative error for the estimated east and up displacement components when the north component is removed and Eq. (2.20) is solved for a case where the azimuths of the ZDP's are non-symmetrical. Still, there are combinations of θ and α_d that result in $\phi = 0°$ and a non biased result for d_e. In (a), we fix the azimuth of the ZDP of the descending acquisition to 99.8°, and we varied the incidence angle and in (b), we varied the azimuth of the ZDP and fixed the incidence angle to 40.5°.

Fig. 2.19. In Fig. 2.19a, we fix the azimuth of the ZDP to 99.8°, and we varied the incidence angle. In Fig. 2.19b, we varied the azimuth of the ZDP and fixed the incidence angle to 40.5°. In both Figs. 2.19a and b we only find one combination of θ and α_d that results in a unbiased estimate for d_e.

The results from Fig. 2.18 and 2.19 can be understood by reviewing the orientation of the solution space (line) of the underdetermined problem. Since the two satellites are not sensitive for displacements into the direction of the null line, described by orientation angles ϕ and ζ, it is possible to do a 2D decomposition in the plane orthogonal to the null line that results in unbiased estimates. So if and only if $\phi = 0°$ and $\zeta = 0°$, the east-up plane (EU plane) is orthogonal to the null line and only then it is possible to give an unbiased estimate for d_e and d_u. Only in that case, the *forced* projection of d_n onto both LoS directions would always be zero and it is allowed to remove it from the decomposition equation.

By simply removing d_n from the decomposition equation, both LoS observations are implicitly projected onto the EU plane. Note that this is a 'voluntary' projection, and not a 'forced' projection, as introduced in section 2.1.5. Within this EU-plane, a solution is found for d_e and d_u. When we have the null line in 3D, this line also has a projection onto the EU plane, which is a line that we refer to as k, see Fig. 2.20. Line k is described by an angle Θ, which is the (elevation) angle between the east axis and k. As long

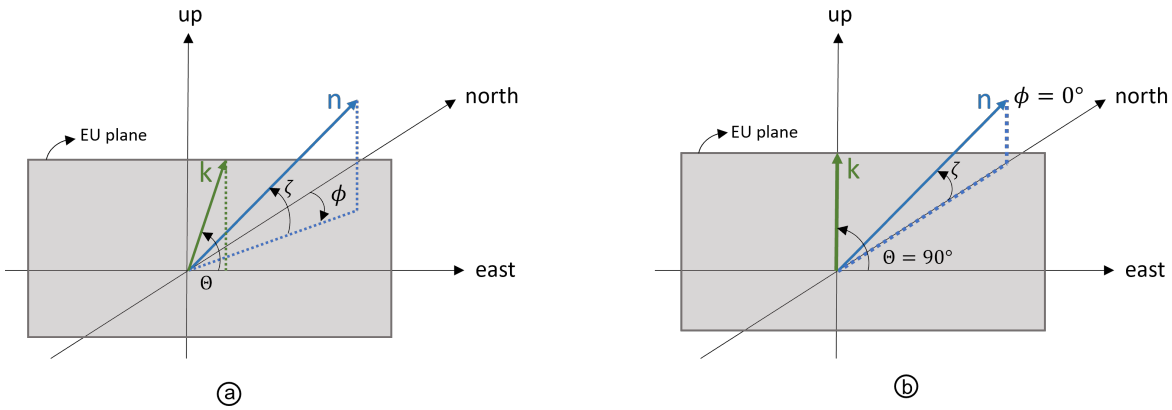

Figure 2.20: The orientation of the null line n in the ENU reference frame is given by azimuth angle ϕ and elevation angle ζ. The projection of n onto the EU plane is line k which has elevation angle Φ. In (a), the $\phi \neq 0°$ and $\zeta \neq 0°$ and therefore k as a component in the east and up direction, further $\Phi \neq 90°$. In (b), $\phi = 0°$ and therefore $\Phi = 90°$, k only has a component in the up direction, the component in the east direction is zero.

as $0° \geq \Theta \leq 90°$ the null line projected onto the EU plane has both a component in the up directed as well as in the east direction, meaning that k contains infinitely many combinations of d_e and d_u. So it is not possible to solve unambiguously for d_e and d_u. If and only if $\phi = 0°$, line k has no component in the east direction and $\Phi = 90°$. Only then, it is possible to solve unambiguously for d_e, and only d_u is biased. This can also be seen in Figs. 2.18 and 2.19, where we indeed see that the relative error for d_e equals 0% when $\phi = 0°$.

The elaboration above also shows that when ζ and ϕ increase, the biases for d_e and d_u increase accordingly. So the answer to the question whether it is allowed to remove d_n from the decomposition equation should simply be no. In Fig. 2.17 we have seen that the orientation of the null line is never parallel to the north-south axis. Therefore, we will always have biased results. However, it can be seen that for the Northern Hemisphere, $\phi = 0°$, so we can unambiguously solve for d_e, and only d_u will be biased. The bias for d_u will be more significant for higher latitudes since ζ increases for higher latitudes.

2.4.3. Discussion

It can be argued whether an unbiased estimator should always be preferred over a biased estimator. From a probabilistic view, one would prefer an estimator with the highest probability of being correct. For this reason, we need to consider the complete probability distribution of the estimator, as approximated by its expectation, $E\{\underline{\hat{x}}\}$, and spread (or variance), $D\{\underline{\hat{x}}\} = \sigma^2_{\hat{x}}$. In case of a biased estimator the expected value is not equal to the true value, i.e., $E\{\underline{\hat{x}}\} \neq x$. Thus, one could argue that a (slightly) biased estimator with a high precision should be preferred over an unbiased estimator with low precision. Unfortunately, for the InSAR estimators under evaluation here, we do not have the luxury of choosing an estimator with a higher precision, which makes biasedness a property that should be avoided, if possible. We can influence the bias (or expectation) of the estimator by changing the mathematical model, as proposed in this study, see chapter 3. Another reason why an unbiased estimator is preferred is the fact that, when a set of LoS observations consists of multiple scatterers, the observations from one viewing geometry are averaged over the RUM. This results in a higher precision for the estimator, while the bias will not disappear.

The statement that it is possible to give an unbiased estimate for the east-west component on the Northern Hemisphere with observations from two viewing geometries is currently only validated for Sentinel-1, since we only computed these viewing geometries. Other SAR missions have their own orbital parameters, and therefore, the relation between the incidence angle θ and azimuth of the ZDP α_d may be different. Yet, we provided the conceptual framework for this evaluation, as it is the relation between the two angles that is responsible for $\phi = 0°$. Even when the two α_d values of the two acquisitions are not symmetrical, the relation between θ and α_d results in $\phi = 0°$. So we need to know per mission what the exact relationship is between the two angles.

The computations of the viewing geometries are performed with DRaMA, which is discussed in more detail in Appendix B. Here, we also encounter some potential limitations. The first step DRaMA carries out is the computation of the LoS direction in the satellite-centered reference system, for which the look angle is used, see 2.5 on p. 11. However, the range of the look angle, θ_l, is estimated based on the near and far range incidence angles, θ_i, as described in the Sentinel-1 specification [26] and with:

$$\theta_l = \sin^{-1}\left(\frac{\sin\theta_i}{R_e + h} R_e\right), \tag{2.21}$$

where R_e is the radius of the Earth and h is the altitude of the spacecraft. This approach is not perfectly accurate since it does not provide the exact look angles, however it is good approximation.

Moreover, DRaMA can estimate the incidence angles and azimuths of the ZDP up to a particular resolution that is larger than the resolution for which we desired to estimate the two angles. A linear interpolation is used to obtain results at the specified resolution, which is not entirely correct, certainly around the poles.

2.4.4. Projecting the LoS displacement vector

We have discussed that with only two LoS observations it is not possible to decompose the observations into the 3D displacement vector. What is possible, however, is to project the two LoS observations on any arbitrary plane, e.g., the EU-plane spanned by the vertical and east axis, and then solve for d_e and d_u in that plane. Alternatively, when only one LoS observation is available, it is possible to project onto one direction, e.g., the vertical. We will refer to this as 'voluntary' projections, as it is up to the end-user on whether such a projection contains intelligible information. This differs from a 'forced' projection, such as the orthogonal projection of the 3D displacement onto the LoS direction, which is a necessary projection, i.e., we cannot influence it.

Projecting two LoS observations onto an arbitrary plane

The two available Los observations can be projected onto any arbitrary plane by a multiplication of the LoS displacement vector with a projection matrix P. When the LoS displacements are projected onto the plane spanned by the east and up axis, i.e., the EU plane, we have

$$d'_{\mathrm{EU}} = \underbrace{\begin{bmatrix} 1 & 0 & 0 \\ 0 & 0 & 0 \\ 0 & 0 & 1 \end{bmatrix}}_{P} \mathrm{u}_{\mathrm{LoS}} d_{\mathrm{LoS}}, \tag{2.22}$$

where d'_{EU} is the projection of d_{LoS} onto the EU plane and $\mathrm{u}_{\mathrm{LoS}}$ the LoS unit vector (see Eq. (2.12)). When this projection is performed for the two LoS observations it is possible to transform the observations into east and up components with Eq. (2.20). However, it should be stressed that the results of the voluntary projection are not the same as the unknown displacement components. This is because projecting the LoS onto a plane, such as the EU plane, and consequently 'solving' for the two components in that plane (such as the east and up components) is similar to neglecting the NS component, as described in section 2.4.2, where we found that the results are biased as long as $\phi \neq 0°$ and $\zeta \neq 0°$.

Projecting one LoS observation onto the vertical direction

When there is only one LoS observation available, it is possible to project that observation onto one direction. Usually, d_{LoS} is projected onto the vertical direction using

$$d'_{\mathrm{up}} = P_{\mathrm{up},(\mathrm{LoS})^{\perp}}\, d_{\mathrm{LoS}} = (\cos\theta)^{-1} d_{\mathrm{LoS}}, \tag{2.23}$$

which is an oblique projection of the LoS observations onto the vertical axis, along a plane orthogonal to the LoS unit vector. It is important to stress that Eq (2.23) is an *oblique* projection. When the LoS observations would be projected orthogonally onto the vertical, along a plane orthogonal to the 'up' unit vector, that would result in

$$P_{\mathrm{up},(\mathrm{up})^{\perp}}\, d_{\mathrm{LoS}} = \underbrace{\begin{bmatrix} 0 & 0 & 0 \\ 0 & 0 & 0 \\ 0 & 0 & 1 \end{bmatrix}}_{P} \mathrm{u}_{\mathrm{LoS}} d_{\mathrm{LoS}}, \tag{2.24}$$

which becomes

$$P_{\mathrm{up},(\mathrm{up})^{\perp}}\, d_{\mathrm{LoS}} = \cos\theta\; d_{\mathrm{LoS}}, \tag{2.25}$$

which differs from Eq. (2.23). Thus, both $P_{\mathrm{up},(\mathrm{LoS})^{\perp}}$ and $P_{\mathrm{up},(\mathrm{up})^{\perp}}$ are allowable voluntary projectors, albeit with a completely different result.

Note the the oblique projection in Eq. (2.23) may be counterintuitive as the result (d'_{up}) can be larger than the vector that is projected (d_{LoS}). For the orthogonal projection, the absolute value of the result will always be smaller than the vector that is projected. To avoid a misinterpretation we therefore recommend to write, for the case of an oblique projection: "The LoS observations are projection onto the vertical *along* ...", to make clear that it is not an orthogonal projection.

2.5. InSAR fallacies in literature

The inverse problem described by Eq. (2.7) is in fact a *"not possible, unless…"* case. If additional information is available, on which it is possible to make additional assumptions, then estimating the full 3D displacement vector may be possible. However, there is not one standard approach. Within InSAR literature, we encounter different approaches to address the underdeterminancy problem, yet often with either mathematical or semantic flaws. The impact of these flaws ranges from quantitative errors in the reported studies, mismatches in comparative studies with other geodetic techniques, to a lack of confidence in the technology by end-users. In this section, we report on an in-depth literature review of InSAR studies, with the main goal to classify the main categories of InSAR fallacies and to analyze their impact. We distinguish four different types of InSAR fallacies: on the attribution, projection, decomposition, and on assumptions.

Note that the review below is not intended to "blame" authors and that we do not want to imply any position on the level of their understanding. Instead, we respectfully assume that the majority of authors is well-aware of the geometric limitations of InSAR. Yet, we do observe that many of the different fallacies that are cited have a rather loose usage of semantics. For the general public, loose and non-strict communication may easily lead to misinterpretation, misunderstanding or confusion, which can have a high impact in several cases. Therefore, we chose to communicate our statements on the fallacious approaches quit strictly and firmly, as we believe that this will stimulate discussion on how InSAR results should be communicated.

2.5.1. Attribution errors

An attribution error is made when the line-of-sight observation is completely attributed to e.g. a vertical displacement, using only a single viewing geometry, and without further justification. In such studies, no projection statements are given, and LoS observations are directly interpreted as vertical displacements ([7, 27–31]). This is erroneous, and results in a severe underestimation (bias) of vertical displacements of up to 40%. For a situation with only vertical displacements d_u (thus, $d_n = 0$ and $d_e = 0$), and $\theta = 45°$, we have $d_{\mathrm{LoS}} = \cos 40° d_{\mathrm{u}} \approx 0.71 \cdot d_{\mathrm{u}}$, which is a significant underestimation of the vertical displacements.

Typical examples of attribution errors found in literature include:

1. *"15 ascending Sentinel-1A TOPS SAR images […] were selected to estimate vertical average surface subsidence "* [30]
2. *"Vertical displacements […] has been drawn […] using the available data. "* [7]
3. *"The result from the IPTA processing is a surface velocity map […] the velocity map shows a slow subsidence."* [27]

Statement 1 is incorrect since it is not possible to estimate the vertical velocities from one data set only, without explicitly stating additional assumptions. Furthermore, without any projection statements, it remains unclear how the results were obtained, which does not satisfy the scientific principle of reproducibility. Perhaps, the LoS observations are projected but it could also be that the LoS data is directly interpreted as vertical displacements. The same holds for the second statement, here the 'available data' are LoS displacements. In the third statement, where only one viewing geometry is available, it is unclear what the published velocity map shows: LoS velocities or LoS velocities projected onto the vertical? The authors state that 'subsidence' results can be obtained from the map, this cannot be stated from one viewing geometry only.

Several studies use terminology inconsistently [28, 32]. Here, InSAR results are first presented unaltered as LoS displacements, while later the terms 'LoS displacements' and 'subsidence' or 'vertical displacements' are mixed up. It is evident that loose usage of terminology can easily lead to a misinterpretation.

To prevent attribution errors, one could present the LoS observations unaltered and avoid suggestive

words such as ‘subsidence’ and ‘vertical’, i.e., strictly use the term *LoS displacements* when results are discussed. Another option would be to project the LoS results onto any arbitrary direction, e.g., the vertical direction, as long as this is stated explicitly.

2.5.2. Projection errors

Projection errors occur when LoS displacement estimates are projected onto the vertical, but are subsequently presented as ‘vertical displacements’.[5] This type of error occurs, just like attribution errors, when only one single viewing geometry is available, and the actual direction of the displacement vector is unknown.

While *‘projection onto the vertical’* would be a perfectly correct statement, *‘vertical displacement’* is not, since the latter would necessarily rely on the assumption that any non-vertical displacement component of the 3D vector is non-existent. Since this assumption is in many cases incorrect, e.g. for landslides or even subsidence bowls, it leads to a biased estimate instead of a more noisy estimate. Frequently, a bias has a bigger impact and less chance of being detected, which is the case in [33–38].

Samiei-Esfahany et al. [39] showed that the bias Δd_u induced while projecting the LoS onto the vertical without assuming horizontal displacements is computed as:

$$\Delta d_u = \tan\theta \cdot [-d_e \sin\alpha_d - d_n \cos\alpha_d]. \tag{2.26}$$

Thus, when a horizontal displacement is directed in the zero-Doppler plane (in the look direction of the sensor) the bias is maximal and can be estimated with

$$\Delta d_{u,\max} = \tan\theta \cdot d_{\mathrm{ZDP}}, \tag{2.27}$$

where d_{ZDP} is the horizontal displacement in the ZDP. Thus, for larger incidence angles, the induced bias becomes larger. When d_{ZDP} is 5 m and $\theta = 35°$, the bias becomes 3.5 mm, which may be significant for many applications.

There are also studies where assumptions on the horizontal component are not made at all, e.g., [8, 40–42]. Examples include:

1. *“We converted the LoS displacements […] to vertical displacements using* $d_v = d_{LoS}/\cos\theta$. *”* [8]
2. *“The differential phase […] was converted from SAR LoS to vertical displacements using:* $d_u = \phi(\lambda/4\pi)/\cos\theta$.*”* [40]
3. *“Each of the PS points was projected into the vertical deformation according to their own incidence angle. ”* [42]

All three statements are incorrect since the words ‘converted’ and ‘transformed’ suggest that there is a one-on-one relation between the LoS displacements and the vertical displacements. However, it is not possible to convert or transform the LoS displacements directly to vertical displacements. Other verbs, such as ‘computed’, ‘calculated’, ‘estimated’, and ‘determined’ would also be wrong.

To prevent projection errors, we suggest (i) to mention the assumption of a non-existent horizontal component (when this valid) or (ii) use the safe projection operation and write: *‘We projected the LoS displacements onto the vertical direction along ...’*. However, to prevent a misinterpretation we suggest to add a statement or caveat that a projection onto the vertical is not the same as the vertical displacements. Added to this, when an oblique projection is used following Eq. (2.23) (as is almost ever the case) it should be made clear that the LoS displacements are projected onto the vertical *along* the plane orthogonal to the LoS vector.

Added to this, we suggest a consequent use of the term ‘projection onto the vertical’ in all figures, tables, and throughout the whole paper. This would be especially recommended for the captions of

[5] Obviously this also holds for equivalent situations in a particular horizontal direction.

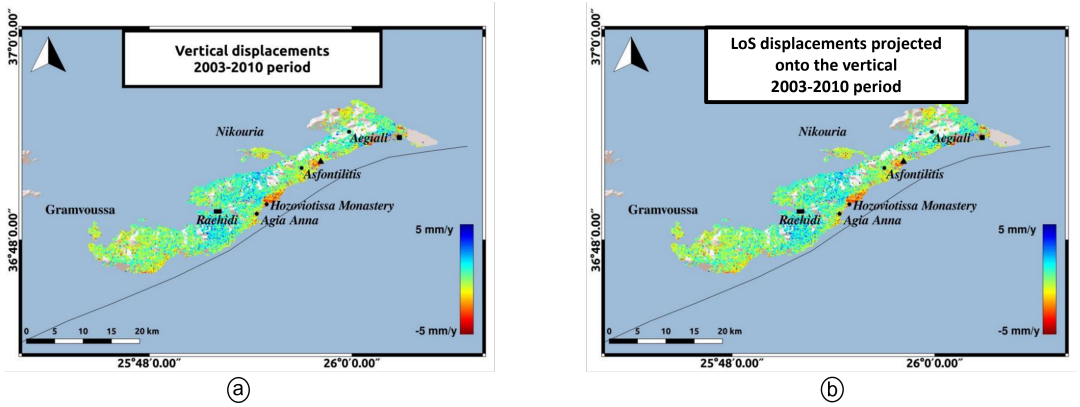

Figure 2.21: Projection errors can be corrected by changing the semantics. In (a), the caption of the figure reads *'Vertical displacements'* whereas the results shown are LoS observations projected onto the vertical direction. To obtain a correct figure, we therefore advise to change the caption of the figure in *'LoS observations projection onto the vertical'* to prevent misinterpretations as in (b).

colorbars of InSAR products, which all too frequently simply state 'vertical displacements'. As stated above, a *displacement projected onto the vertical* is not identical to a *vertical displacement*. In Fig. 2.21 we show changing the semantics can help in achieving a correct result.

2.5.3. Decomposition errors

Decomposition errors occur when the null-space in the 3D solution space—using only one or two viewing geometries, i.e., ascending and descending—is ignored, and subsequently a 'non-measurable' displacement vector component is equated to a 'non-existing' displacement vector component. In such cases, it is assumed that the *lack of sensitivity* in the north-component for near-polar orbits is equivalent to the *absence* of a north-south component by simply removing the component from the decomposition equation, e.g., [9, 43–52]. This assumption fails since the solution space for two observations is a line which is never orthogonal to the east-up (EU) plane, see section 2.4.1. Neglecting the north-component results in biased estimates mostly for the vertical component but depending on the latitude of the target it may also influence the east-component, see section 2.4.1. Therefore, these approaches are very dependent on the actual magnitude of the north-south displacements and on the location on earth where they occur.

Typical examples of decomposition errors include statements such as:

- *"By combining an ascending and a descending time-series, it is possible to disentangle east-west horizontal deformation from vertical deformation."* [44]
- *"Whenever two data sets of InSAR images are available, […] the PS-InSAR results can be used successfully to estimate the vertical and east-west components of the local displacement fields."* [46]
- *"The combination of ascending and descending satellite passes allows the decomposition of the light of sight velocities into horizontal east-west and vertical components."* [9]
- *"Reconstructing vertical and horizontal components […] using two interferograms, one from an ascending and the other from a descending orbit."* [47]

All these statements suggest that it is possible to 'disentangle', 'estimate', or 'reconstruct' two displacements components, usually the vertical and east component, with two LoS observations. However, in general this is not possible due to the dimensionality of the solution space when two observations are available. There are also approaches where authors try to decompose the observations into the plane spanned by the up direction and the azimuth look direction of one of the satellites, see [8, 51].

However, this approach is still incorrect since the plane that is used has not the same orientation as the plane orthogonal to the null line, and therefore the results are still biased.

To prevent decomposition errors we suggest two solutions. The first option would be to project the two LoS observations onto the EU plane as in Eq. (2.22), and solving for the displacements in the east and up direction in this plane. However, it should be stressed that the results of the voluntary projection are not the same as the unknown displacement components. Another option is to solve for the two displacements components that are in the directions of the vectors that span the plane orthogonal to the null line.

2.5.4. Flawed assumptions

The problem of estimating 3D displacement vectors observed by only one or two viewing geometries can only be solved by adding additional information (conditions) in the form of assumptions. Thus, these need to be explicitly stated, both in the documentation of the approach as well as in the final information products, such as maps. Yet, in many cases, these assumptions are either *lacking, misstated, incorrect, or implausible.* The consequence of *flawed assumptions* typically results in biased results rather than noisy results.

When an approach is incorrect due to flawed assumptions, it is often related to an attribution, projection, or decomposition error. We observed lacking assumptions in both the projection error and the decomposition error. Regarding the projection error, it is possible to only solve for the vertical displacements under the assumption that the horizontal components are zero. However, in many studies this assumption was not explicitly mentioned. The same holds for the decomposition error: one could potentially solve for two displacement components with two Los observations, however this requires additional conditions, which are often lacking.

Studies where the assumptions are misstated are mainly found for the decomposition error, e.g.:

- *"Assuming that the orbital path of the satellite is approximately parallel to the meridian, the LOS sensitivity to motion in the north-south direction is negligible, hence the equation can be rewrite to solve for d_e and d_u."* [50]
- *"The north-south component can be neglected due to the low sensitivity of SAR sensors along that direction."* [52]
- *"The sensitivity to a target motion along the north-south direction is usually quite low."* [46]

It is indeed correct that near-polar radar satellites have a low sensitivity for the north-component. However, simply removing d_n from the decomposition equation under the assumption of the low sensitivity for that component is not permissible without any knowledge or explicit statements on the expected magnitude of the north-component. Thus, this is typically a Signal-to-Noise Ratio (SNR) consideration. As long as the real world displacement into the north-direction is large enough, e.g., larger than the noise level of the projected LoS observations, it can still be discriminated from the observations.

Examples of assumptions that are implausible are:

- *"The north component is insensitive […] consequently, we add the additional constraint that the north-south motion is assumed to be zero. In this way, we calculate the velocity in east-west and up-down direction."*[9]
- *"Sentinel-1 data are insensitive to north-south displacements direction […] Therefore, we assumed that $d_n = 0$, and this allowed us to find the other two components of the deformation vector."* [48]
- *"It is also assumed that horizontal velocities are mainly due to east–west motion, owing to InSAR low sensitivity to the north component."* [51]

Here is is assumed that $d_n = 0$ since the radar is insensitive for displacements into the north-south direction. However, the assumption of $d_n = 0$ is an assumption on the actual size of the physical signal, which is the unknown parameter and evidently *not* correlated to the sensitivity of the radar instrument!

Examples of incorrect assumptions are:

- *"However, […] results obtained from two different acquisition geometries (i.e. ascending and descending), […], allows one to estimate 2D measurements."* [53]

- *"Using data from both ascending and descending orbits, it is possible to determine the vertical displacement and one component of horizontal displacement."* [47]

As discussed, those statements are incorrect since the solution space of this underdetermined problem is a line, so with two observations only it is never possible to unambiguously solve for two displacement components, since the solution space is never orthogonal to the plane spanned by the two displacement components.

2.5.5. Discussion

When discussing the sensitivity of the north-south component and subsequently removing it from the decomposition equations, an argument that is often used, is that the sensitivity for the north-south component is only valid for exceptional cases with large north-south displacements. Yet, we argue that the argumentation should be exactly opposite: one should describe the decomposition problem in a generic sense, both for small and large displacements. Initially, the stochastic model plays no role, as only the geometry of the observations should be taken into account, as captured in the A-matrix. Once the *generic* model is known, it is possible to deduce *particular* cases, e.g., cases with either small displacements or very high or low observation precision. We have shown that there are several factors that can influence particular cases, such as the location (latitude) of the area of interest, or the magnitude of the event. Deductions from the generic to the particular are more valuable than the other way around, where authors start with the exceptional (particular) case, stating that the precision of the observations is low or that the displacements are small, and from there try to deduce the generic model.

In Appendix E we discuss some fallacious propositions that we encountered in this literature study.

Finally, we would like to stress that our attempt to identify and classify common errors (fallacies) in InSAR studies, based on a thorough review of publications, does not imply any position on the level of understanding of the authors of those studies. Instead, we respectfully assume that the majority of authors is well-aware of the geometric limitations of InSAR, and that the different fallacies cited are not a consequence of a lack of mathematical understanding, but rather a loose usage of semantics. Yet, for the general public, we observed that a rather loose and non-strict communication easily leads to misinterpretation, misunderstanding or confusion, which can have a high impact in several cases.

2.6. Suggestions for handling the underdetermined problem

While the underdetermined nature of the problem cannot be formally solved, we propose some practical solutions.

2.6.1. LoS unaltered as the final product

Presenting the LoS observations unaltered as the final product is obviously correct, as it does not attempt to do any projection, attribution, or decomposition. The approach can be seen in [43, 54–56]. The drawback of the LoS product is that it is typically hard to interpret, especially for untrained end-users. As potential vertical and horizontal displacement components are projected into the LoS and superposed, it remains 'invisible' what happens in the real world.

2.6.2. “Projection-onto” products

When only one LoS observation is available, a correct option is to present the projection of the LoS onto the, e.g., vertical direction. In this case, it must be made clear that the results are displacement projections and not the vertical displacements themselves to avoid misinterpretation. Moreover, the projection type should be made clear, since the oblique projection provides different results compared to the orthogonal projection.

The results should also be communicated consistently. In all figures, tables, and the entire written text it should be mentioned that the estimates are projections on the vertical rather than the vertical displacements itself. When two LoS observations are available, it is possible to project the observations on any arbitrary plane and solve for two displacement directions in the plane. However, the estimated displacements are not equal to the true displacements.

2.6.3. 2D Decomposition with valid, plausible, and explicit assumptions

While assumptions that east-west displacements are more likely than north-south displacements are implausible in most cases, there are several assumptions for which plausibility would be hardly disputed. For example, for gravity-induced down slope displacements, it is near-impossible that there is a displacement component parallel to the elevation contours, it is near-impossible that for a subsidence-bowl, there is a displacement component parallel to the LoS displacement contours. It is very unlikely to have significant secular displacements in the longitudinal direction of horizontal line infrastructure [16, 57]. For such cases, the displacement vector can be described as a 2D displacement vector, and as a result, it is possible to solve for the two unknown displacement components with only two LoS observations. More on this approach is described in chapter 3.

A complete overview of all the different approaches even with their impact can be found in Appendix C. In Appendix D we present fallacious statements for the different InSAR approaches and our proposal on how approach can be made correct.

3

The strap-down approach

Using the ENU system is only one of the infinitely many possibilities for the parameterization of the inverse problem. However, in many cases it is a choice that is not optimally tuned to the user needs, and in chapter 2 we have seen that it often results in an underdetermined problem. One solution to the underdetermined problem would be to choose the parameterization such that there are only two unknown displacement parameters which are into the direction of the two vectors that span the plane orthogonal to the null line unit vector[1].

Here we developed a new alternative solution to the underdeterminancy problem, in the form of a 'strap-down' approach, which uses a local strap-down reference system that is fixed to the deformation phenomenon with transversal, longitudinal, and normal (TLN) components. This approach results in better interpretable results compared to the conventional method where displacements are estimated in the east-up (EU) plane. In sections 3.1 and 3.2 we first discuss the strap-down approach and the different deformation phenomena for which it can be used. In sections 3.4 and 3.5 we analyze the impact of the uncertainty of the alignment of the TLN-frame on the final estimates, resulting in the final mathematical model which we discuss in section 3.6. Finally, in section 3.7, we discuss when particular displacements can be detected.

3.1. LoS-Vector decomposition using a local strap-down coordinate system

For most deformation phenomena we propose to work with a local, '*strap-down*', right-handed Cartesian coordinate system that is fixed to the deformation phenomenon with transversal, longitudinal, and normal components, see e.g., Fig. 3.1. The term *local* implies that the orientation of the TLN frame may differ for each location in the image. A displacement in those three directions is projected onto the LoS with Eq. (2.7) as [57]:

$$d_{\mathrm{LoS}} = P_{\mathrm{LoS}}\, d_{\mathrm{ENU}}, \tag{2.7}$$

$$= P_{\mathrm{LoS}}\, R_1\, R_2\, R_3\, d_{\mathrm{TLN}}, \tag{3.1}$$

where d_{TLN} is the vector containing the displacement components in the local strap-down system, with $d_{\mathrm{TLN}} = [d_T, d_L, d_N]^T$, containing the transversal, longitudinal, and normal displacement components,

[1] For every parameterization it is furthermore important that no information is lost. This happens for instance when the decomposition is done in the east-up plane: information is lost on the north component resulting in biased estimates. Once this information is 'lost' it is not possible to go back at another parameterization.

respectively. R_1, R_2, and R_3 are rotation matrices which are expressed as

$$R_1 = \begin{bmatrix} \cos\beta & \sin\beta & 0 \\ -\sin\beta & \cos\beta & 0 \\ 0 & 0 & 1 \end{bmatrix},$$
$$R_2 = \begin{bmatrix} 1 & 0 & 0 \\ 0 & \cos\gamma_l & -\sin\gamma_l \\ 0 & \sin\gamma_l & \cos\gamma_l \end{bmatrix},$$
$$R_3 = \begin{bmatrix} \cos\gamma_t & 0 & \sin\gamma_t \\ 0 & 1 & 0 \\ -\sin\gamma_t & 0 & \cos\gamma_t \end{bmatrix}, \tag{3.2}$$

where $\beta \in [0°, 360°)$ is the azimuth of the longitudinal direction relative to the north. Note that the longitudinal direction has a 180° ambiguity. Therefore, in case of a topographic slope or a subsidence slope, the longitudinal direction is defined tangential to the local iso-elevation or iso-deformation lines, such that the positive transversal direction is always directed down-slope. In the absence of a clear slope, we use the smallest angle w.r.t. the north, i.e. $\beta \in (-90°, +90°]$, following [57]. The slope in the longitudinal direction is $\gamma_l \in (-90°, +90°]$, where up-hill is positive. The slope in the transversal direction is $\gamma_t \in (0°, +90°]$. The normal direction completes the right-handed system. The angles γ_t and γ_l represent the elevation angles of the slope relative to the horizontal.

While Eq. (3.1) does not solve the problem of underdeterminancy, for many practical cases, e.g., line infrastructure, landslides, or subsidence bowls, analysis of the main driving forces supports the assumption that significant displacements in the longitudinal direction are unlikely. Under this assumption, Eq. (3.1) can be solved with two sets of STCI LoS observations from sufficiently different viewing geometries.

Below, we will address the application, and implications, of the strap-down system for different practical situations.

3.2. Deformation Phenomena

In practice, we can distinguish two main categories of InSAR deformation cases. First, there are cases where the deformation mechanism is known, where a TLN system can be well-defined, and where we can assume that there are no displacements in the longitudinal direction ($d_L = 0$). This holds, e.g., when the main driving mechanisms and forces are gravity or a volume change underneath the Earth's surface. Second, there are cases in which it is not known whether deformation is occurring, or when the deformation mechanism is unknown. For such cases, it is obviously not possible to distinguish a primary driving force for the displacements. As a result, it is impossible to define 'main' orientations for the displacements, and we cannot use the TLN frame. This is the case for, e.g., nationwide InSAR displacement products, see e.g. [5]. For such cases, the ENU system be used for the decomposition and three sets of STCI LoS observations are required.

Here we discuss three typical types of deformation phenomena from the first category: downslope displacement, subsidence and uplift, and infrastructure.

3.2.1. Gravity induced downslope displacement

Landslides, moving glaciers, or slope instability of a dike are examples of phenomena where the main deformation occurs along the slope, with gravity as the main driving force. When the longitudinal axis is parallel to the iso-elevation lines of the slope of the occurring landslide, we can safely assume that displacements in the longitudinal direction are (close to) zero, i.e., all displacements occur in the vertical plane spanned by the d_T and d_U vectors, see Fig. 3.1a. Hence, in Eq. (3.2), $\gamma_L = 0°$ by definition.

The slope *aspect*, i.e., the compass direction that a terrain surface faces, determines the values for the angles β and γ_t, see Fig. 3.1b. We define the orientation angle β as the direction of the longitudinal axis relative to the north. Hence, perhaps counterintuitively, for a north-east facing slope (first quadrant

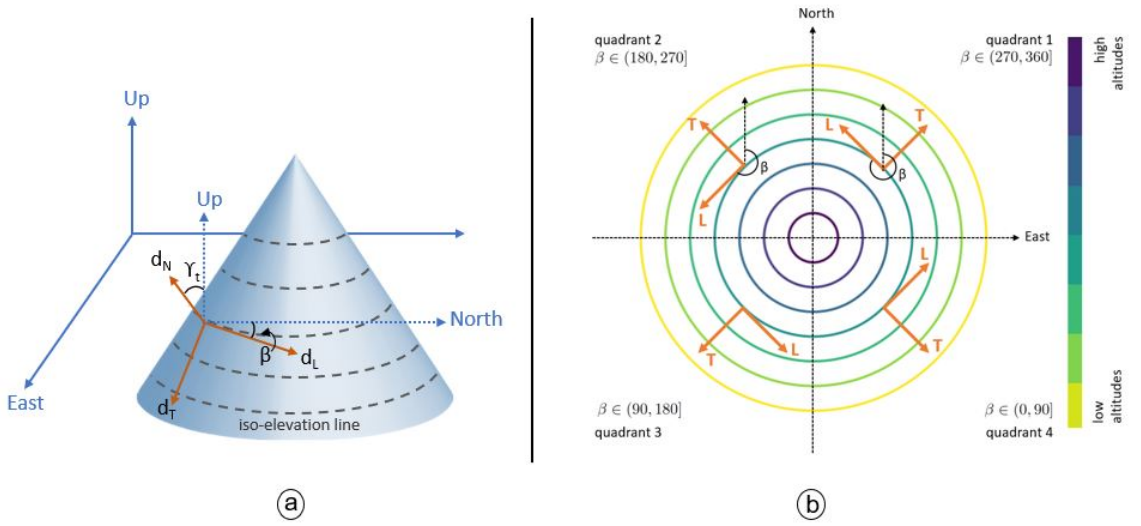

Figure 3.1: Orientation of the TLN reference system for slopes. (a) shows how the TLN reference system is oriented to the ENU reference system for gravity-induced downslope deformation phenomena. (b) A top view of a schematized mountain, where the highest elevation is located at the center of the figure. The slope aspect determines in further detail the boundaries within which β should lie.

in Fig. 3.1b), $\beta \in (-90°, 0°]$ such that the positive transversal direction is downslope. The (angle of the) slope is γ_t, and is always referred to as a positive number.

3.2.2. Subsidence and uplift

Subsidence bowls and uplift domes are caused by a change in volume underneath the Earth's surface. They exhibit vertical and horizontal displacement components. The horizontal component is orthogonal to the iso-deformation lines: centripetal for subsidence [58], and centrifugal for uplift. Thus, the longitudinal direction is oriented parallel to the iso-deformation lines, and the transversal direction is downslope (centripetal) for subsidence, see Fig. 3.2. For uplift, the transversal direction is centrifugal. Caused by the the gravitational force, and the driving mechanisms involved, it is safe to assume that no displacements in the longitudinal direction may occur. The normal displacements are the largest in the center of the field, where there is almost no vertical displacement at the edge of the field. Considering a perfect circular subsidence field as in Fig 3.2, the poss β values depend on the quadrant.

3.2.3. Line-infrastructure

Line infrastructure is characterized by an extended spatial dimension in one direction (the longitudinal direction), where the spatial extent in the other two directions is limited, as e.g. roads, railways, dikes, and pipelines. The slope of the asset is given by γ_l, and γ_t represents the cant of the asset or the slope in the transversal direction, which is usually small. Often, it is possible to assume that no significant displacements occur in the longitudinal direction [16, 57]. For cases where γ_t equals zero, there is a directional ambiguity for β, and the smallest azimuth angle should be chosen, i.e., $\beta \in (-90°, 90°]$.

3.3. Estimating displacements using the strap-down system

Given the definition of the TLN-frame, there are several options for estimating the displacements in the transversal and normal direction using the assumption of zero longitudinal displacements. One option is to estimate d_T and d_N by adding a pseudo observation for d_L, where the pseudo observation is chosen to be $d_L = 0$ as in [57] and [16]. However, the drawback of this approach is that it is likely that the estimates for the transversal and normal displacements components are biased, which happens when the assumption of $d_L = 0$ fails. The assumption of zero longitudinal displacements fails when the orientation of TLN frame is chosen incorrectly.

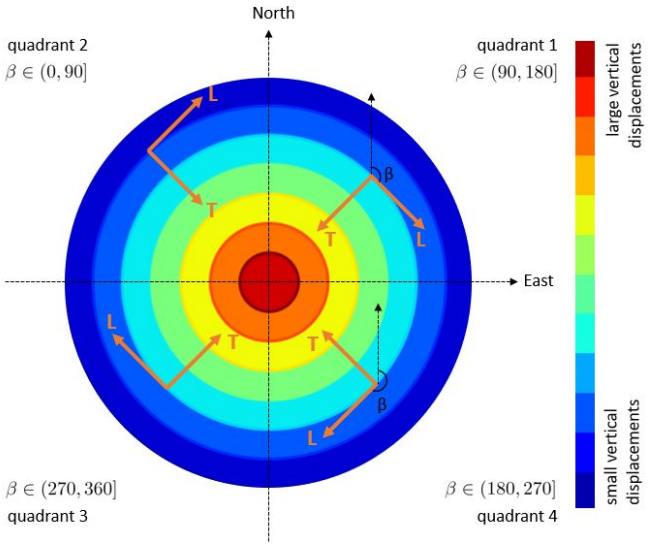

Figure 3.2: Orientation of the TLN reference system for subsidence bowl. The transversal direction is always directed towards the centre of the subsidence bowl. It differs per quadrant what can be the possible β values.

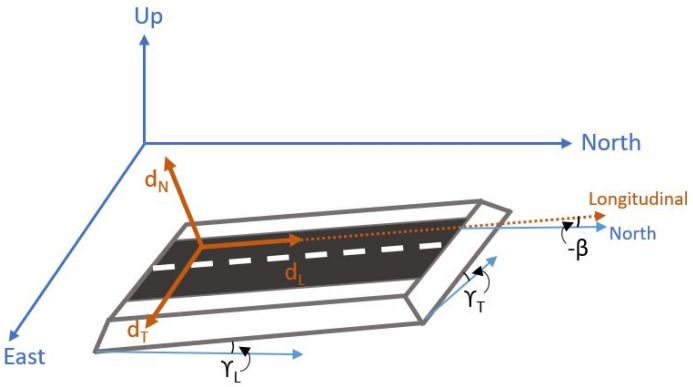

Figure 3.3: The orientation of the TLN reference system for line-infrastructure.

Table 3.1: Viewing characteristics of a satellite in an ascending and a descending orbit

Geometry type	Incidence angle θ	Azimuth angle of the ZDP α_d
ascending	30°	260°
descending	35°	92°

For every displacement vector in the conventional ENU system there exist an infinite number of 2D planes that contain the displacement vector by definition. When this plane is the plane spanned by the transversal and the normal direction (TN plane)[2], the longitudinal direction points in the direction of the normal vector of this TN plane. When we know the exact orientation of the TN plane, an approach with a pseudo-observation for the longitudinal displacement will result in proper unbiased estimates for the three displacement components. However, the problem is that the exact orientation of the TN plane is not known. We can only estimate the orientation by means of the direction of the displacement vector, but this is the unknown of the inverse problem. There are deformation phenomena for which we can make a good estimate of the orientation (see section 3.2) but the exact orientation remains unknown.

In section 3.3.1 we will show that a misalignment of the TLN frame results in a biased estimate. Then, in section 3.4 we study the effect of the frame alignment uncertainties on the estimated displacement parameters from which we will conclude that the alignment uncertainty should be considered in the mathematical model. Therefore, in section 3.6, this leads to the final approach where we added the frame uncertainty to the mathematical model to arrive at proper estimates for d_T and d_N.

3.3.1. A misalignment of the TLN frame

The assumption of $d_L = 0$ is likely to fail when the orientation of the TLN reference frame is chosen incorrectly. So for a decomposition, optimal estimates for β, γ_t, and γ_l are required. Let β^0, γ_t^0, and γ_l^0 represent the initial estimates for the orientation of the TLN frame. When the orientation estimate is incorrect, e.g., $\beta^0 \neq \beta$, we make a mistake in the design matrix A and the functional model is incorrect, i.e., the assumption of $d_L = 0$ fails resulting in biased estimates. Consequently, we may view the biased estimation problem in terms of the uncertainty of the estimates for the orientation angles. During the rest of this section we only focus on the uncertainty for β^0 but the approach is identical for the other two angles γ_t^0 and γ_l^0. With an uncertainty of $\beta^0 \pm \varepsilon_\beta$ we have

$$\mathrm{B} = |d(\beta^0 - \varepsilon_{\beta^0}) - d(\beta^0 + \varepsilon_{\beta^0})|, \tag{3.3}$$

where B represents the bias introduced by an imperfect alignment of the reference frame, d is the estimated displacement (in the transversal or normal direction) and ε_{β^0} represents the uncertainty of the value of β^0 in degrees. The bias is the absolute difference between the estimated displacement calculated with an angle of $\beta^0 - \varepsilon_{\beta^0}$ and $\beta^0 + \varepsilon_{\beta^0}$. The better we can estimate the initial value for the angle of β^0, the smaller the bias we create on our final estimates.

We simulated unit displacements in the transversal and normal direction. With $\gamma_t = 10°$ and $\gamma_l = 0°$ we computed two STCI LoS observations for varying values of $\beta \in (0°, 360°]$, following the satellite geometry shown in Table 3.1. The LoS observations were computed using the forward model as in Eq. (3.1). We choose the uncertainty for the azimuth angle to be $\varepsilon_\beta = 10°$ and we set the value for σ_{d_L} to 0.0001 mm, and for $\sigma^2_{\mathrm{LoS},1}$ and $\sigma^2_{\mathrm{LoS},2}$ to 0.3 mm, even though this has no consequence for the alignment bias estimation. The results for the misalignment-induced bias for both the transversal and normal direction are shown in Fig. 3.4.

The normalized bias is calculated by dividing B by the simulated displacement signal. A zero-value implies a non-biased result, while a value of one implies that the B is equal to the simulated displacement component, i.e., a significant error. The value of B depends on the azimuth orientation β of the TLN system. This follows from the fact that we simulated two LoS observations from almost near-polar orbits. As a result, the null space is oriented almost in the north-south direction. When the transver-

[2]In most practical cases, this plane will be the (near-)vertical plane

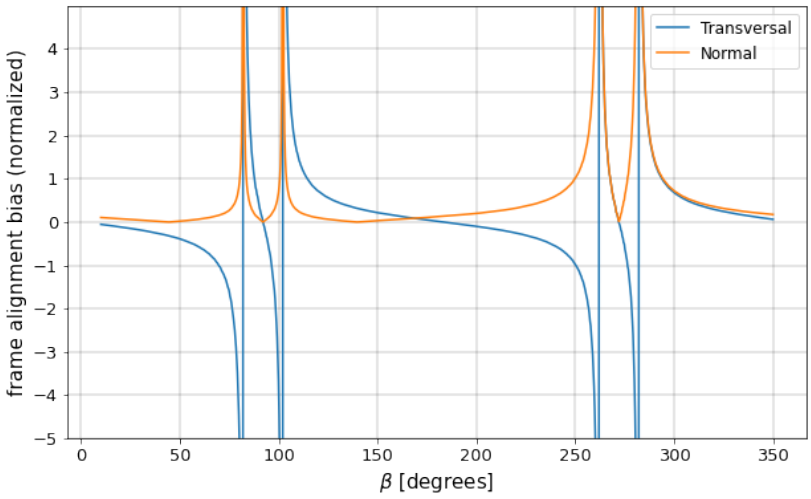

Figure 3.4: Normalized bias induced by a frame misalignment of $\varepsilon_\beta = 10°$, as a function of β, for the normal and transversal component. This shows that a unit displacement in the transversal direction, given a misalignment of 10 degrees, may give a bias of more 3 times the true displacement value for $\beta \approx 80°$. The two 'peaks' in the curve follow from the fact that the transversal direction is directed into the direction of the null line for that particular orientation of the TLN frame.

sal direction is exactly in the direction of the null line[3], it cannot be retrieved. Furthermore, when the transversal direction near the direction of the null line, the estimates can be significantly biased, which is the case when β has values around $80°$, $100°$, $220°$, and $260°$. For such cases, Fig. 3.4 shows that there is also leakage to the normal component.

3.4. Uncertainty for the TLN frame alignment

The application of the strap-down approach is subject to the correct alignment of the TLN frame. In this section we will investigate the effect of misalignments, i.e., the alignment uncertainty, of the TLN frame on the precision of the final estimates for the transversal and normal displacements. For deformation phenomena, where $d_L = 0$ by definition, any displacement vector can be unambiguously represented in a 2D plane, the (d_T, d_N) system, as long as the orientation of the TLN reference frame over the RUM is well chosen. Therefore, the mathematical model can be written as

$$E\{\underbrace{\begin{bmatrix} \underline{d}_{\mathrm{LoS}}^{(1)} \\ \vdots \\ \underline{d}_{\mathrm{LoS}}^{(m)} \end{bmatrix}}_{\underline{y}}\} = \underbrace{\begin{bmatrix} p_{1T} & p_{1N} \\ \vdots & \vdots \\ p_{mT} & p_{mN} \end{bmatrix}}_{A} \underbrace{\begin{bmatrix} d_T \\ d_N \end{bmatrix}}_{x} \tag{3.4}$$

$$D\{\underbrace{\begin{bmatrix} \underline{d}_{\mathrm{LoS}}^{(1)} \\ \vdots \\ \underline{d}_{\mathrm{LoS}}^{(m)} \end{bmatrix}}_{\underline{y}}\} = \underbrace{\begin{bmatrix} Q_{\mathrm{LoS},1} & 0 & 0 \\ 0 & \ddots & \vdots \\ 0 & \dots & Q_{\mathrm{LoS},m} \end{bmatrix}}_{Q_{yy}}, \tag{3.5}$$

where $E\{.\}$ expresses the expectation of the model, which can be solved with two sets of STCI LoS observations: $\underline{d}_{\mathrm{LoS}}^{(1)}$ and $\underline{d}_{\mathrm{LoS}}^{(2)}$, each having a different viewing geometry and consisting of a positive number of scatterers. Each set is dependent of the unknown parameters via $[p_{1T}d_T + p_{1N}d_N]$ which corresponds to $P_{\mathrm{LoS},1}R_1R_2R_3[d_T, d_L, d_N]^T$, where the component related to the longitudinal direction d_L is removed by definition. $D\{.\}$ is the dispersion of the model, where $Q_{\mathrm{LoS},i}$ is the covariance matrix of the LoS observations for set i. This covariance matrix is a diagonal matrix containing the variances of displacement for each scatterer within the set.

[3]See section 2.3.3 for a definition of the null line.

The A matrix contains the important information on the orientation of the TLN frame. Thus, for estimating d_T and d_N also estimates for the orientation angles β, γ_t, and γ_l are actually required, which are described by stochastic variables $\underline{\beta}$, $\underline{\gamma}_t$, and $\underline{\gamma}_l$ which have initial values β^0, γ_t^0, and γ_l^0 and standard deviations σ_β, σ_{γ_t}, and σ_{γ_l} respectively. Thus, $\underline{\beta} \sim \mathcal{N}(\beta^0, \sigma_\beta^2)$, $\underline{\gamma_t} \sim \mathcal{N}(\gamma_t^0, \sigma_{\gamma_t}^2)$, and $\underline{\gamma_l} \sim \mathcal{N}(\gamma_l^0, \sigma_{\gamma_l}^2)$. With these distributions, using a Monte Carlo (MC) approach, we can get insight in how the alignment uncertainty affects the distribution and uncertainty of the estimated parameters d_T and d_N.

For a particular RUM it is possible to compute N realizations from the distributions $\underline{\beta}$, $\underline{\gamma}_t$, and $\underline{\gamma}_l$. For every realization $n \in [1, N]$, we can compute estimates for d_T and d_N, where every estimate $\hat{d}_{T,n}$ and $\hat{d}_{N,n}$ would be unique due to the different realizations for the orientation angles and consequently different A matrices used in the inverse model. The Monte Carlo procedure contains the following steps.

1. Simulate a displacement signal in the transversal and normal direction (d_T and d_N) for a specific orientation of the TLN frame with β, γ_t, and γ_l (the true frame orientation).
2. With (i) the displacement signal, (ii) the characteristics of the satellite viewing geometries of an ascending and a descending acquisition, and (iii) the correct orientation of the TLN frame it is possible to compute two LoS observations, using the forward model in Eq. (3.4). This results in $d_{\text{LoS-asc}}$ and $d_{\text{LoS-dsc}}$.
3. To estimate d_T and d_N we use the inverse model. Within the inverse model, the true orientation of the TLN frame is not known, and therefore estimates are required as initial values for (β^0 γ_t^0, and γ_l^0) as well as their uncertainty (σ_β, σ_{γ_t}, and σ_{γ_l}). We simulate N realizations for $\underline{\beta}$, $\underline{\gamma}_t$, and $\underline{\gamma}_l$.
4. With the LoS observations $d_{\text{LoS-asc}}$ and $d_{\text{LoS-dsc}}$, we also simulate N different realizations of the LoS observations from normal distributions which are defined as: $\underline{d}_{\text{LoS-asc}} \sim \mathcal{N}(d_{\text{LoS-asc}}, \sigma_{\text{LoS-asc}}^2)$, and $\underline{d}_{\text{LoS-dsc}} \sim \mathcal{N}(d_{\text{LoS-dsc}}, \sigma_{\text{LoS-dsc}}^2)$.
5. For every realization $n \in [0, N]$ we estimate $\hat{d}_{T,n}$ and $\hat{d}_{N,n}$, where every estimate $\hat{d}_{T,n}$ and $\hat{d}_{N,n}$ is unique due to the different realizations for the LoS observations and orientation angles.

3.4.1. Results from the Monte Carlo approach

We did different Monte Carlo simulations to study the impact of the uncertainty in the alignment of the frame on $\hat{d}_T$ and $\hat{d}_N$. We started with simulating a displacement signal of $d_T = 5$ mm and $d_N = 10$ mm. For all Monte Carlo simulations, the displacements are observed from an ascending and descending orbit with viewing characteristics as presented in Table 3.1.

Impact of uncertainty β (for $\beta = 10°$)

For the first simulation we only took into account an uncertainty for $\underline{\beta}$, i.e., we assumed no uncertainty for $\underline{\gamma_t}$ and $\underline{\gamma_l}$. We set $N = 3000$, $\sigma_\beta = 5°$, and $\sigma_{\text{LoS}} = 10^{-4}$ i.e., we simulated noise-free LoS observations at first. This allows us to study purely the effect of the uncertainty of $\underline{\beta}$ on the distribution for the estimated displacement components $\hat{d}_T$ and $\hat{d}_N$. For the first simulation, we choose the orientation of the TLN frame such that $\beta = 10°$, $\gamma_t = 0°$, and $\gamma_l = 0°$, see the blue histograms in Fig. 3.5. The blue histogram at the top left (Fig. 3.5A) shows the distribution of the transversal component, $\hat{d}_T$, the blue histogram in the middle (Fig. 3.5C) shows the distribution of the normal component, $\hat{d}_N$ and the histogram at the bottom right (Fig. 3.5F) shows the distribution of $\underline{\beta}$ where $\underline{\beta} \sim \mathcal{N}(\beta^0, \sigma_\beta^2)$ and where we choose $\beta^0 = \beta$.

From the blue histogram in Fig. 3.5A, we see that the estimates for the transversal component, $\hat{d}_T$, are not normally distributed. The tail at the right side of the simulated value ($d_T = 5$ mm) is broader compared to the tail at the left side, which follows from the direction of the null line of the two LoS observations. The orientation of the null line in the TLN reference system is described by ϕ_{TLN} and ζ_{TLN}, where ϕ_{TLN} is the angle between the null line and the longitudinal axis and ζ_{TLN} is the angle

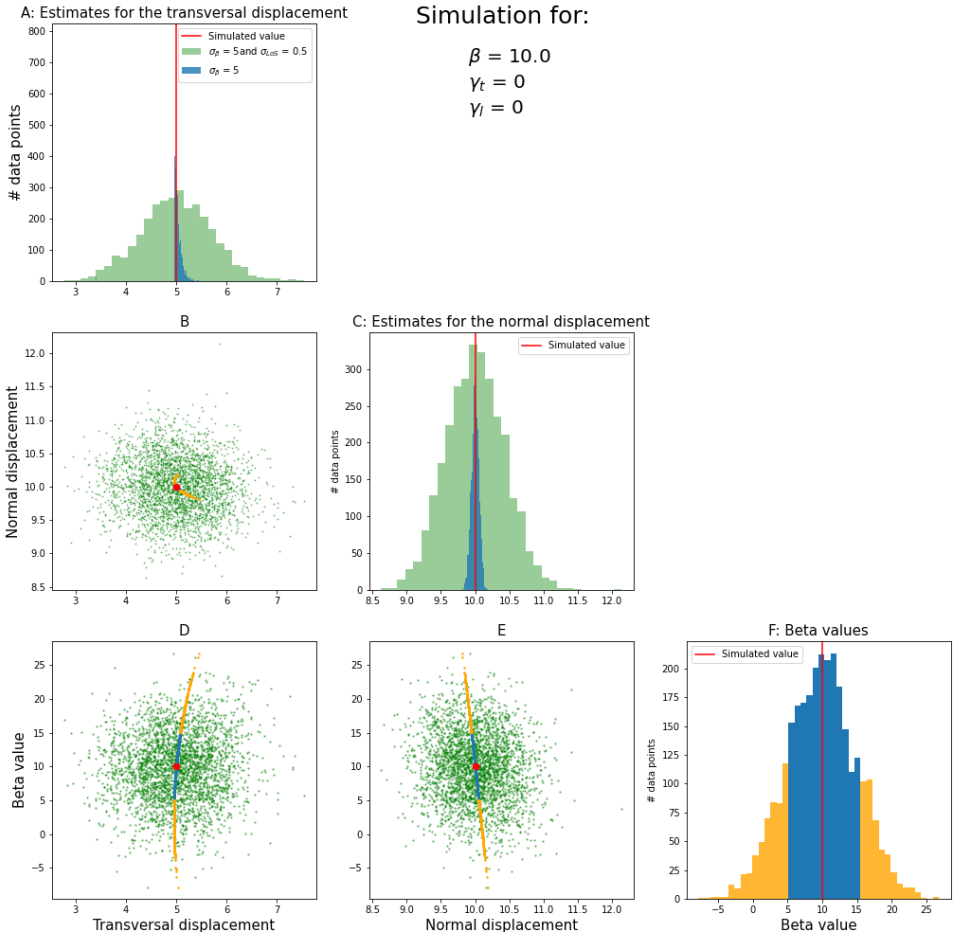

Figure 3.5: Results from the Monte Carlo analysis using 3000 realizations for β, where the TLN frame is oriented such that $\beta = 10^\circ$, $\gamma_t = 0^\circ$, and $\gamma_l = 0^\circ$. (A and B): distributions of the estimates for the transversal $\hat{d}_T$ and normal $\hat{d}_N$ displacement component. The blue histograms show the results form the simulation with noise-free LoS observations. The green histograms show the results from the situation where we simulated noisy LoS observations ($\sigma_{\text{LoS}} = 0.5$ mm). (B, D, and E) the noise-free results with the blue and yellow dots and the noisy results with the green dots. In F, the different realizations for β are shown. The blue values are closer to the true values and the yellow values are further apart. In D and E, different estimates for the transversal and normal displacements are shown versus the realizations for β. The blue dots correspond to the blue β values in F, we see that the larger the difference between β_r and β, the larger the bias for $\hat{d}_T$ and $\hat{d}_N$. The red dot in D and E shows the simulated displacement.

between the plane spanned by the longitudinal and transversal axis and the null line, see Eqs (2.15) and (2.16) in section 2.3.3. For $\beta = 10°$ we find $\phi_{\text{TLN}} = -8°$ and $\zeta_{\text{TLN}} = 7°$. Therefore, the orientation of the null lineis almost in the longitudinal direction. When $\phi_{\text{TLN}} = 0°$, the longitudinal direction would be insensitive, and the sensitivity for the transversal component would be maximal. If we then use a realization β_r for $\underline{\beta}$ such that $\beta_r \neq \beta$ in the inverse model, this only results in an overestimation of the transversal displacement component. Since for β_r that is used, the sensitivity for the transversal component is smaller compared to the β that corresponds to the deformation phenomena and thus the LoS observation. We see this effect also for the simulated case at $\beta = 10°$, where the null line in the TLN frame is almost fully in the longitudinal and normal direction. For this particular case, there are lot of realizations for β_r that result in a lower sensitivity for the transversal displacement compared to the correct orientation of the frame, for all those values $\hat{d}_T \leq d_T$.

Above, we only discussed the results for the noise free case (the blue histograms). However, the noise level of the LoS observations also has an effect on the uncertainty for $\hat{d}_T$ and $\hat{d}_N$. The green histograms in Fig. 3.5 show the results when we also take into account the noise level of the observations. We took realizations for the LoS observations from $\underline{d}_{\text{LoS-asc}} \sim \mathcal{N}(d_{\text{LoS-asc}}, \sigma^2_{\text{LoS-asc}})$ and $\underline{d}_{\text{LoS-dsc}} \sim \mathcal{N}(d_{\text{LoS-dsc}}, \sigma^2_{\text{LoS-dsc}})$, where $\sigma_{\text{LoS-asc}} = 0.5$ mm and $\sigma_{\text{LoS-dsc}} = 0.5$ mm. It can be seen that for the case where $\beta = 10°$, the uncertainty of the LoS observations has a larger impact on the uncertainty for $\hat{d}_T$ and $\hat{d}_N$ compared with the frame uncertainty.

Impact of uncertainty β (for $\beta = 70°$)
We did the same simulations for an orientation of the TLN frame with $\beta = 70°, \gamma_t = 0°$, and $\gamma_l = 0°$. The results are shown in Fig. 3.6. In this case, the orientation of the null line is such that $\phi_{\text{TLN}} = -68°$ and $\zeta_{\text{TLN}} = 7°$, meaning that it is almost directed in the transversal direction, resulting in an ill-posed problem. For the case where $\beta = 70°$ and $\sigma_\beta = 5°$ there are some realizations β_r for $\underline{\beta}$ that result in the the null line fully directed in the transversal direction, making it impossible to find a solution for $\hat{d}_T$. We indeed see that the spread of the estimates for the transversal component is larger compared to the simulation where $\beta = 10°$. This follows from the fact that the satellites are less sensitive for displacements in the transversal direction for this situation, resulting in a lower reliability of the estimates.

Also, for $\beta = 70°$, we did the simulation with and without noise for the LoS observations. Again, the blue histograms show the noise-free results, and the green histograms show the noisy results. Compared to the situation where $\beta = 10°$ we see that the uncertainty of the frame alignment has a more significant effect compared to the noisy observations, since (especially for $\hat{d}_T$) the difference between the blue and green histogram became smaller.

From Figs. 3.5 and 3.6 we also conclude that the uncertainty for $\underline{\beta}$ has a larger effect on the uncertainty for $\hat{d}_T$ compared to $\hat{d}_N$ (for the situation where $\gamma_t = 0°$ and $\gamma_l = 0°$). However, when $\gamma_t \neq 0°$ and/or $\gamma_l \neq 0°$ we find that the uncertainty for $\hat{d}_N$ becomes larger since the sensitivity for $\hat{d}_N$ becomes smaller.

Impact of uncertainty γ_t and γ_l
So far, we only took into account the uncertainty for $\underline{\beta}$. However, $\underline{\gamma}_t$ and $\underline{\gamma}_l$ do also have an uncertainty that should be taken into account, so we also performed simulations where we simulated realizations from $\underline{\gamma}_t \sim \mathcal{N}(\gamma_t^0, \sigma^2_{\gamma_t})$ and $\underline{\gamma}_l \sim \mathcal{N}(\gamma_l^0, \sigma^2_{\gamma_l})$ where $\sigma^2_{\gamma_t} \neq 0°$ and $\sigma^2_{\gamma_l} \neq 0°$. We found that we were able to create the same figures as shown in Figs. 3.5 and 3.6, with β being replaced by γ_t or γ_l. We find that not only the uncertainty for $\underline{\beta}$ has an impact on the uncertainty for $\hat{d}_T$ and $\hat{d}_N$, the uncertainty for $\underline{\gamma_t}$ and $\underline{\gamma_l}$ is also important.

3.5. Factors of influence on the uncertainty of $\hat{d}_T$ and $\hat{d}_N$

From the Monte Carlo analyses, we can conclude that the two parameters of interest, d_T and d_N, suffer from two types of errors: (i) the random or measurement error in the original LoS observations and

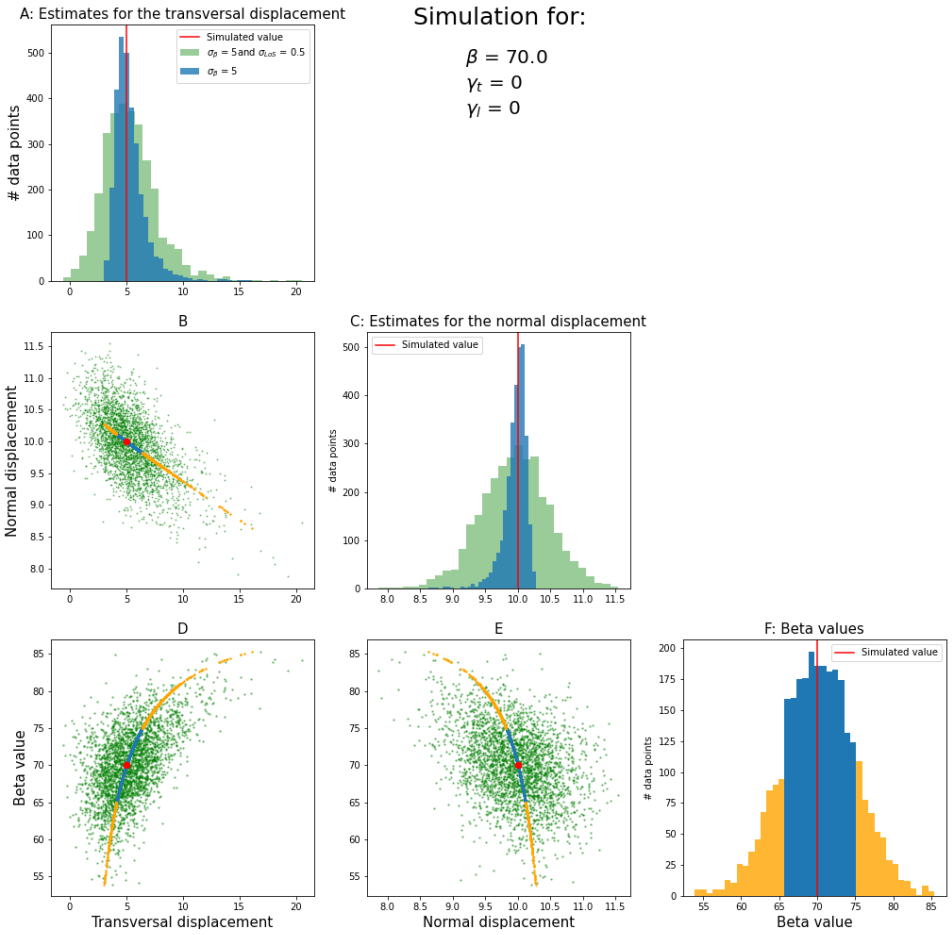

Figure 3.6: Results from the Monte Carlo analysis with 3000 realizations for β, where the TLN frame is oriented such that $\beta = 70^\circ$, $\gamma_t = 0^\circ$, and $\gamma_l = 0^\circ$. (A and B) distributions of the estimates for the transversal $\hat{d}_T$ and normal $\hat{d}_N$ displacement component. The blue histograms show the results from the simulation with noise-free LoS observations. The green histograms show the results from the situation where we simulated noisy LoS observations ($\sigma_{\text{LoS}} = 0.5$ mm). (B, D, and E) noise-free results with the blue and yellow dots and the noisy results with the green dots. In F, the different realizations for β are shown. The blue values are closer to the true values and the yellow values are further apart. In D and E, different estimates for the transversal and normal displacements are shown versus the realizations for β. The blue dots correspond to the blue β values in F, we see that the larger the difference between β_r and β, the larger the bias for $\hat{d}_T$ and $\hat{d}_N$. The red dot in D and E shows the simulated displacement.

(ii) a potential misalignment of the TLN frame. However, the latter only introduces a bias for the final estimates $\hat{d}_T$ and $\hat{d}_N$ in the case that there is deformation. It is possible to define four factors of influence on the uncertainty of the estimated parameters:

1. The precision of the LoS observations
2. The orientation of the TLN reference frame
3. For the case that there is actual deformation:
   (a) The potential misalignment of the frame
   (b) The magnitude of the displacements

Below, these four factors of influence are discussed.

3.5.1. The precision of the LoS observations

The LoS observations are assumed to be[4] described by a Probability Density Function (PDF) of a Gaussian distribution, i.e. $\underline{d}_{\mathrm{LoS}}^{(m)} \sim \mathcal{N}(d_{\mathrm{LoS}}^{(m)}, \sigma_{d_{\mathrm{LoS}}}^2)$, where the precision of the LoS observation is described by the variance of the normal distribution, σ_{LoS}^2. It can be seen that the uncertainty of the estimates is a direct result from the precision of the LoS observations using the error propagation law

$$Q_{\hat{x}} = (A^T Q_{yy}^{-1} A)^{-1} = \begin{bmatrix} \sigma_T^2 & \sigma_{TN} \\ \sigma_{NT} & \sigma_N^2 \end{bmatrix}. \tag{3.6}$$

Where Q_{yy} is the variance-covariance matrix as described in Eq. (3.5) and A is the design matrix as in Eq. (3.4). The effect of σ_{LoS} could also be seen in Figs. 3.5 and 3.6.

3.5.2. The orientation of the TLN reference frame

As described in section 2.3, the combination of two sets of LoS observations results in a null space which is described by a line, the null line, and it is impossible to find a solution for displacements that have the same direction as the line. In section 2.4.1 we parameterized the orientation of the null line in the ENU system, see Eqs. (2.15) and (2.16) in section 2.3.3. It is also possible describe the orientation of the line in the TLN system by azimuth angle ϕ_{TLN} (to the longitudinal direction) and elevation angle ζ_{TLN} (to the plane spanned by the transversal and longitudinal axis).

The inverse problem estimates the two unknown displacements parameters d_T and d_N. The sensitivity for one of those parameters is the highest when the two unknown parameters span the plane normal to the null line. Thus, the uncertainty for displacement estimate becomes larger when the sensitivity for the displacement direction becomes smaller.

So, for example, when $\phi_{\mathrm{TLN}} = 0°$ and $\zeta_{\mathrm{TLN}} = 0°$ the sensitivity for the transversal component would be maximal (given the two viewing geometries). When $\phi_{\mathrm{TLN}} = 90°$ and $\zeta_{\mathrm{TLN}} = 0°$ it would be minimal. For the latter case, the transversal direction is in the null space and it is impossible to find reliable estimates for $\hat{d}_T$. This effect was also visible in Figs. 3.5 and 3.6.

The influence of the orientation of the frame on the uncertainty for the $\hat{d}_T$ and $\hat{d}_N$ could also be seen from Eq. (3.6), where $Q_{\hat{x}}$ is a function of the design matrix A and the variance-covariance matrix Q_{yy}. A contains information on the orientation of the frame. In Fig. 3.7 we visualized two realizations for $Q_{\hat{x}}$. Both matrices are obtained by simulating one observation from an ascending and one observation from a descending acquisition with the viewing geometry as presented in Table 3.1. The standard deviation of the LoS observations was set to one, i.e. $\sigma_{\mathrm{LoS}} = 1$, resulting in Q_{yy} being the identity matrix. The orientation of the TLN reference frame for Fig. 3.7a was chosen such that $\beta = 0°, \gamma_t = 0°$, and $\gamma_l = 0°$.

[4] Note that the PDF for the LoS displacement follows from the original phase observations, which are not Gaussian distributed, but follow a Von Mises distribution. A deeper analysis of including this alternative PDF falls outside the scope of this study, but is recommended in future research.

By taking the square root of the diagonal elements of $Q_{\hat{x}}$ we compute the standard deviations for $\hat{d}_T$ and $\hat{d}_N$, this resulted in $\sigma_{d_T} = 1.32$ and $\sigma_{d_N} = 0.84$. Fig. 3.7b shows the result for $Q_{\hat{x}}$ when the orientation of the TLN frame was chosen such that $\beta = 90°, \gamma_t = 0°$, and $\gamma_l = 0°$. Again, we were able to compute σ_{d_T} and σ_{d_N}, this resulted in 20.91 and 1.22 respectively. It could be seen that for the second case, the uncertainty for d_T is much worse compared to the first case.

Lastly, from the Monte Carlo simulations, we can conclude that the orientation of the TLN frame does not only affect the width of the distribution of $\hat{d}_T$ and $\hat{d}_N$ but *also* the shape. From Figs. 3.5 and 3.6 it follows that a Gaussian distribution could not describe the distribution of the estimated parameters and that the shape of the distribution depends on the orientation of the TLN frame.

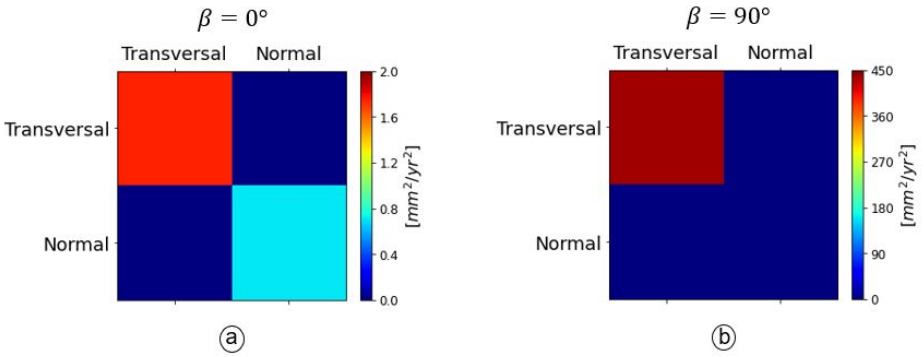

Figure 3.7: Visualizations for $Q_{\hat{x}}$ for two different orientations of the TLN reference frame. In both cases (a and b) $\gamma_t = 0°, \gamma_l = 0°$ and σ_{LoS}, the angle β differs. It can be seen that the uncertainty for $\hat{d}_T$ and $\hat{d}_N$ depends on the orientation of the TLN frame

3.5.3. The uncertainty of the frame alignment

Suppose there is an actual deformation signal (i.e. $d_T > 0$ and/or $d_N > 0$). In that case, the uncertainty of the frame alignment also plays a role in the accuracy, i.e., the deviation from the truth, for the estimated displacement parameters. We will now show the effect of a misalignment in the TLN frame. Consider a situation where we do have a displacement signal which equals $x = [d_T, d_N]^T$. Using the forward model, this results in

$$y_{\text{LoS}} = A(\beta, \gamma_t, \gamma_l) \begin{bmatrix} d_T \\ d_N \end{bmatrix} = \begin{bmatrix} d_{\text{LoS}}^{(1)} \\ d_{\text{LoS}}^{(2)} \end{bmatrix}, \tag{3.7}$$

where $A(\beta, \gamma_t, \gamma_l)$ is the design matrix (as in Eq. (3.4)) with correct values for β, γ_t, and γ_l. With two LoS observations and estimates for the orientation angles we can estimate the unknown parameters with

$$\begin{bmatrix} \hat{\underline{d}}_T \\ \hat{\underline{d}}_N \end{bmatrix} = (A(\beta_r, \gamma_{t,r}, \gamma_{l,r})^T Q_{yy}^{-1} A(\beta_r, \gamma_{t,r}, \gamma_{l,r}))^{-1} A(\beta_r, \gamma_{t,r}, \gamma_{l,r})^T Q_{yy}^{-1} \underline{y}_{\text{LoS}} \tag{3.8}$$

Where $\beta_r, \gamma_{t,r}$ and $\gamma_{l,r}$ are realizations from $\underline{\beta} \sim \mathcal{N}(\beta^0, \sigma_\beta^2)$, $\underline{\gamma}_t \sim \mathcal{N}(\gamma_t^0, \sigma_{\gamma_t}^2)$, and $\underline{\gamma}_l \sim \mathcal{N}(\gamma_l^0, \sigma_{\gamma_l}^2)$. When $\beta_r = \beta$, $\gamma_{t,r} = \gamma_t$, and $\gamma_{l,r} = \gamma_l$ the estimates for the transversal and normal displacement components are unbiased, i.e. $E\{\hat{d}_T\} = d_N$ and $E\{\hat{d}_N\} = d_N$. However, if we make a mistake in our estimates for the orientation angles and $\beta_r \neq \beta$ and/or $\gamma_{t,r} \neq \gamma_t$ and/or $\gamma_{l,r} \neq \gamma_l$ we make a mistake in the functional model resulting in biased estimates, i.e., $E\{\hat{d}_T\} \neq d_T$ and $E\{\hat{d}_N\} \neq d_N$. From Eq. (3.8) it can further be seen that the larger the difference between the true orientation angles and the realizations, the larger the bias for the estimated parameters d_T and d_N. This effect was also visible in Figs. 3.5 and 3.6. E.g., subfigure E shows the effect for incorrect values for β_r on $\hat{d}_T$. It can be seen that the larger the difference between β_r and β, the larger the bias in the estimate for $\hat{d}_T$, the red dot shows the true simulated values. Subfigure F shows the relation between the estimated value for β_r and only now for the normal component.

3.5.4. Magnitude of displacements

The size of the bias also depends on the displacement magnitude. First consider the trivial case of zero displacements, i.e. $d_T = 0$ and $d_N = 0$. Using the forward model, this results in LoS observations which are zero: $d_{\mathrm{LoS}}^{(1)} = 0$ and $d_{\mathrm{LoS}}^{(2)} = 0$. Obviously, from Eq. (3.8) it follows that $E\{\hat{d}_T\} = d_T = 0$ and $E\{\hat{d}_N\} = d_N = 0$, resulting in unbiased estimates. The estimates are independent from the size of the misalignment in the frame. However, there is a special case when one of the unknown parameters is (almost) in the direction of the null line, the solution for the unknown parameter is totally unreliable and can be totally incorrect.

For cases with (i) nonzero displacements (i.e. $d_T > 0$ and/or $d_N > 0$) *and* (ii) when we make an error in the alignment of the TLN frame, the size of the bias depends on the size of the displacements. For larger displacements, y_{LoS} becomes larger, resulting in more extensive biases. We will elaborate on this in section 3.6.1.

3.6. The alignment uncertainty in the mathematical model

We can give reliable estimates for d_T and d_N for deformation phenomena where we can assume that $d_L = 0$ when the following conditions are fulfilled: (i) At least two sets of STCI LoS observations over one RUM are available, (ii) the direction of d_T and d_N is not into the direction of the null line, and (iii) the alignment of the TLN frame is well chosen. However, for the the latter, we have shown with a Monte Carlo approach in section 3.4 that the uncertainty of the orientation angles ($\sigma_\beta, \sigma_{\gamma_t}$, and $\sigma_{\gamma,l}$) has an effect on the uncertainty and distribution of $\hat{d}_T$ and $\hat{d}_N$. Therefore, the uncertainty of the frame alignment ($\sigma_\beta, \sigma_{\gamma_t}, \sigma_{\gamma_l}$) should be taken into account by adding pseudo-observations $\underline{\beta}$, $\underline{\gamma}_t$, and $\underline{\gamma}_l$ for the orientation angles to the mathematical model resulting in

$$E\{\underbrace{\begin{bmatrix} \underline{d}_{\mathrm{LoS}}^{(1)} \\ \vdots \\ \underline{d}_{\mathrm{LoS}}^{(m)} \\ \underline{\beta} \\ \underline{\gamma}_t \\ \underline{\gamma}_l \end{bmatrix}}_{\underline{y}}\} = \underbrace{\begin{bmatrix} a_1(x) \\ \vdots \\ a_m(x) \\ a_{m+1}(x) \\ a_{m+2}(x) \\ a_{m+3}(x) \end{bmatrix}}_{A(x)} = \underbrace{\begin{bmatrix} p_{1T}d_T + p_{1N}d_N \\ \vdots \\ p_{mT}d_T + p_{mN}d_N \\ \beta \\ \gamma_t \\ \gamma_l \end{bmatrix}}_{A(x)} \tag{3.9}$$

$$D\{\underbrace{\begin{bmatrix} \underline{d}_{\mathrm{LoS}}^{(1)} \\ \vdots \\ \underline{d}_{\mathrm{LoS}}^{(m)} \\ \underline{\beta} \\ \underline{\gamma}_t \\ \underline{\gamma}_l \end{bmatrix}}_{\underline{y}}\} = \underbrace{\begin{bmatrix} Q_{\mathrm{LoS},i} & \dots & 0 & 0 & 0 & 0 \\ \vdots & \ddots & \vdots & \vdots & \vdots & \vdots \\ 0 & \dots & Q_{\mathrm{LoS},i} & 0 & 0 & 0 \\ 0 & \dots & 0 & \sigma_\beta^2 & 0 & 0 \\ 0 & \dots & 0 & 0 & \sigma_{\gamma_t}^2 & 0 \\ 0 & \dots & 0 & 0 & 0 & \sigma_{\gamma_l}^2 \end{bmatrix}}_{Q_{yy}}, \tag{3.10}$$

where the unknowns of the model are $d_T, d_N, \beta, \gamma_t$ and γ_l. $E\{.\}$ expresses the expectation of the model, which can be solved with two sets of STCI LoS observations: $\underline{d}_{\mathrm{LoS}}^{(1)}$ and $\underline{d}_{\mathrm{LoS}}^{(2)}$, each having a different viewing geometry and consisting of a positive number of scatterers. To overcome rank deficiency, pseudo observations for $\underline{\beta}$, $\underline{\gamma}_t$, and $\underline{\gamma}_l$ are added. $D\{.\}$ is the dispersion of the model, where $Q_{\mathrm{LoS},i}$ is the covariance matrix of the LoS observations for set i. This covariance matrix is a diagonal matrix containing the variances of displacement for each scatterer within the set. σ_β^2, $\sigma_{\gamma_t}^2$, and $\sigma_{\gamma_l}^2$ are the variances for the pseudo observations for the estimates of the orientation angles. Rows 1–m in the A matrix are non-linear equations that consist of $d_T, d_N, \beta, \gamma_t$, and γ_l, where p_{mT} and p_{mN} are defined as:

$$\begin{aligned} p_{mT} =& (\sin\theta_m \sin\alpha_{d,m} \cos\beta - \sin\theta_m \cos\alpha_{d,m} \sin\beta)\cos\gamma_t - \\ & (-(\sin\theta_m \sin\alpha_{d,m} \sin\beta + \sin\theta_m \cos\alpha_{d,m} \cos\beta)\sin\gamma_l + \cos\theta_m \cos\gamma_l)\sin\gamma_t \end{aligned} \tag{3.11}$$

$$\begin{aligned} p_{mN} =& (\sin\theta_m \sin\alpha_{d,m} \cos\beta - \sin\theta_m \cos\alpha_{d,m} \sin\beta)\sin\gamma_t + \\ & (-(\sin\theta_m \sin\alpha_{d,m} \sin\beta + \sin\theta_m \cos\alpha_{d,m} \cos\beta)\sin\gamma_l + \cos\theta_m \cos\gamma_l)\cos\gamma_t. \end{aligned} \tag{3.12}$$

Every set of STCI LoS observation has unique values for p_{mT} and p_{mN} due to the different incidence angles and the azimuth angles of the zero-Doppler plane (ZDP) at the RUM. To estimate the five unknown parameters, we need to linearize the system of equations. The linearized system of equations is defined as

$$\underbrace{\begin{bmatrix} \Delta\underline{d}_{\mathrm{LoS}}^{(1)} \\ \vdots \\ \Delta\underline{d}_{\mathrm{LoS}}^{(m)} \\ \Delta\underline{\beta} \\ \Delta\underline{\gamma_t} \\ \Delta\underline{\gamma_l} \end{bmatrix}}_{\Delta\underline{y}_{[0]}} \approx \underbrace{\begin{bmatrix} \frac{\partial}{\partial d_T}a_1(x_{[0]}) & \frac{\partial}{\partial d_N}a_1(x_{[0]}) & \frac{\partial}{\partial \beta}a_1(x_{[0]}) & \frac{\partial}{\partial \gamma_t}a_1(x_{[0]}) & \frac{\partial}{\partial \gamma_l}a_1(x_{[0]}) \\ \vdots & \vdots & \vdots & \vdots & \vdots \\ \frac{\partial}{\partial d_T}a_{m+3}(x_{[0]}) & \frac{\partial}{\partial d_N}a_{m+3}(x_{[0]}) & \frac{\partial}{\partial \beta}a_{m+3}(x_{[0]}) & \frac{\partial}{\partial \gamma_t}a_{m+3}(x_{[0]}) & \frac{\partial}{\partial \gamma_l}a_{m+3}(x_{[0]}) \end{bmatrix}}_{J_{[0]}} \underbrace{\begin{bmatrix} \Delta d_T \\ \Delta d_N \\ \Delta\beta \\ \Delta\gamma_t \\ \Delta\gamma_l \end{bmatrix}_{[0]}}_{\Delta x_{[0]}}, \tag{3.13}$$

where $J_{[0]}$ is the Jacobian matrix which is a function of $x_{[0]}$ (the initial estimate for the unknown parameters), where $x_{[0]} = [d_{T[0]}, d_{N[0]}, \beta_{[0]}, \gamma_{t[0]}, \gamma_{l[0]}]^T$. $\Delta\underline{y}_{[1]}$ is the difference between the observed observations and the computed observations for the initial estimate $x_{[0]}$: $\Delta\underline{y}_{[0]} = \underline{y} - A(x_{[0]})$. With $\Delta\underline{y}_{[0]}$ and $J_{[0]}$ we can estimate $\Delta x_{[0]}$ by using least-squares estimation:

$$\Delta\underline{\hat{x}}_{[0]} = (J_{[0]}^T Q_{yy}^{-1} J_{[0]})^{-1} J_{[0]}^T Q_{yy}^{-1} \Delta\underline{y}_{[0]}. \tag{3.14}$$

The estimate for the unknown parameters $\underline{\hat{x}}$ now becomes $\underline{\hat{x}}_{[1]} = x_{[0]} + \Delta\underline{\hat{x}}_{[0]}$. We can iterate this process by using $\underline{\hat{x}}_{[1]}$ again to compute $J_{[1]}$ and $\Delta\underline{y}_{[1]}$, following the iteration scheme presented in Fig. 3.8. It is needed to define a stop criterion. For converging solutions we choose $\Delta\underline{\hat{x}}_{[0]} < \epsilon$ where ϵ is the tolerance level. Once $\underline{\hat{x}}$ approaches x the increment $\Delta\underline{\hat{x}}_{[0]}$ becomes very small. Furthermore, we need an initial estimate $x_{[0]}$ for the unknown parameters.

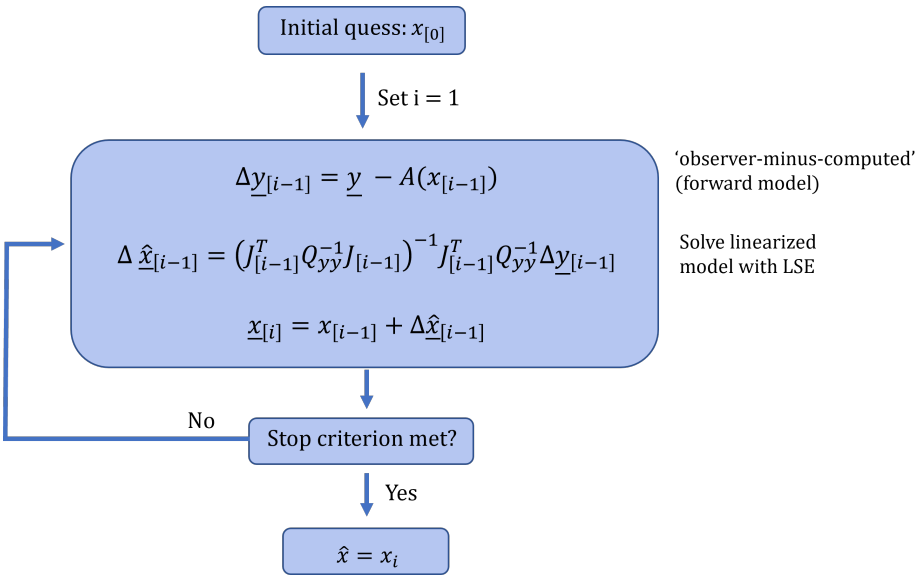

Figure 3.8: The iteration scheme for non-linear least-squares estimation (after [59])

To linearize the model in Eq. (3.9) and apply the Jacobian matrix J, partial derivatives for the functions a_1 until a_m are needed. When i corresponds to a particular LoS observation and $i \in [1, m]$, the partial derivatives are defined as

$$\frac{\partial}{\partial d_T}a_i = (\sin\theta_i \sin\alpha_{d,i}\cos\beta - \sin\theta_i \cos\alpha_{d,i}\sin\beta)\cos\gamma_t - (-(\sin\theta_i \sin\alpha_{d,i}\sin\beta + \sin\theta_i \cos\alpha_{d,i}\cos\beta)\sin\gamma_l + \cos\theta_i \cos\gamma_l)\sin\gamma_t \quad (3.15)$$

$$\frac{\partial}{\partial d_N}a_i = (\sin\theta_i) sin\alpha_{d,i}\cos\beta - \sin\theta_i \cos\alpha_{d,i}\sin\beta)\sin\gamma_t + (-(\sin\theta_i \sin\alpha_{d,i}\sin\beta + \sin\theta_i \cos\alpha_{d,i}\cos\beta)\sin\gamma_l + \cos\theta_i \cos\gamma_l)\cos\gamma_t \quad (3.16)$$

$$\frac{\partial}{\partial \beta}a_i = ((-\sin\theta_i \cos\alpha_{d,i}\cos\beta - \sin\theta_i \sin\alpha_{d,i}\sin\beta)\cos\gamma_t + (\sin\theta_i \sin\alpha_{d,i}\cos\beta - \sin\theta_i \cos\alpha_{d,i}\sin\beta)\sin\gamma_l \sin\gamma_t)d_T + ((-\sin\theta_i \cos\alpha_{d,i}\cos\beta - \sin\theta_i \sin\alpha_{d,i}\cos\beta)\sin\gamma_t - (\sin\theta \sin\alpha_{d,i}\cos\beta - \sin\theta_i \cos\alpha_{d,i}\sin\beta)\sin\gamma_l \cos\gamma_t)d_N \quad (3.17)$$

$$\frac{\partial}{\partial \gamma_t}a_i = (-(\sin\theta_i \sin\alpha_{d,i}\cos\beta - \sin\theta_i \cos\alpha_{d,i}\sin\beta)\sin\gamma_t - (-(\sin\theta_i \sin\alpha_{d,i}\sin\beta + \sin\theta_i \cos\alpha_{d,i}\cos\beta)\sin\gamma_l + \cos\theta_i \cos\gamma_l)\cos\gamma_t)d_T + ((\sin\theta_i \sin\alpha_{d,i}\cos\beta - \sin\theta_i \cos\alpha_{d,i}\sin\beta)\cos\gamma_t - (-(\sin\theta_i \sin\alpha_{d,i}\sin\beta + \sin\theta_i \cos\alpha_{d,i}\cos\beta)\sin\gamma_l + cos\theta_i \cos\gamma_l)\sin\gamma_t)d_N \quad (3.18)$$

$$\frac{\partial}{\partial \gamma_l}a_i = -(-\sin(\theta_i \sin\alpha_{d,i}\sin\beta + \sin\theta_i \cos\alpha_{d,i}\cos\beta)\cos\gamma_l - \cos\theta_i \sin\gamma_l)\sin\gamma_t d_T + (-(\sin\theta_i \sin\alpha_{d,i}\sin(\beta) + \sin\theta_i \cos\alpha_{d,i}\cos\beta)\cos\gamma_l - \cos\theta_i \sin\gamma_l)\cos\gamma_t d_N \quad (3.19)$$

The rows j_{m+1} until j_{m+3} of the Jacobian matrix J in Eq. (3.13) are defined as

$$\begin{bmatrix} j_{m+1} \\ j_{m+2} \\ j_{m+3} \end{bmatrix} = \begin{bmatrix} 0 & 0 & 1 & 0 & 0 \\ 0 & 0 & 0 & 1 & 0 \\ 0 & 0 & 0 & 0 & 1 \end{bmatrix}. \quad (3.20)$$

The uncertainty of the final estimates for $d_T, d_N, \beta, \gamma_t$, and γ_l can be computed with

$$Q_{\hat{x}} = \left(J_{[i]}^T Q_{yy}^{-1} J_{[i]}\right)^{-1}, \quad (3.21)$$

where J_i is the Jacobian matrix for the point when convergence is reached, i.e., the last iteration step.

3.6.1. Impact of the size of the deformation signal

As discussed in section 3.5, the size of the displacement signal affects the magnitude of the uncertainty for the estimated displacements in the transversal and normal direction. With Eq. (3.21) we are able to validate this. We simulated both a small and a large displacement signal and for both cases we computed $Q_{\hat{x}}$. We also tested the effect of the orientation of the frame for both cases. In Table 3.2 the characteristics for the different cases are presented. We simulated one LoS observation from an ascending and one LoS observation from a descending satellite with a viewing geometry as presented in Table 3.1, p. 39. We set $\sigma_\beta = 5°$, $\sigma_{\gamma_t} = 5°$, and $\sigma_{\gamma_l} = 5°$, we choose σ_{LoS} to be 1 mm for both the LoS observations.

Case 1 and 2

In case 1 and 2 the orientation of the TLN frame was chosen such that $\beta = 10°$, $\gamma_t = 0°$, and $\gamma_l = 0°$. For the first case, we simulated a displacement signal where $d_T = 1$ mm and $d_N = 1$ mm. The result for $Q_{\hat{x}}$ for only the upper four elements is presented in Fig. 3.9a. We find $\sigma_{d_T} = 1.36$ mm and $\sigma_{d_N} = 0.85$ mm. In the second case, we estimated $Q_{\hat{x}}$ but now we simulated a larger displacement signal, consisting of $d_T = 10$ mm and $d_N = 10$ mm, which resulted in $\sigma_{d_T} = 1.64$ mm and $\sigma_{d_N} = 1.21$ mm, see Fig. 3.9b.

Table 3.2: Simulated orientations of the TLN reference frame and displacements in the transversal and normal direction. Case 1 and 3 represent small displacements, Case 2 and 4 large displacements. The orientation of the frame differs between cases 1/2 and 3/4.

	Case 1	Case 2	Case 3	Case 4
β	10°	10°	80°	80°
γ_t	0°	0°	0°	0°
γ_l	0°	0°	0°	0°
d_T	1 mm	10 mm	1 mm	10 mm
d_N	1 mm	10 mm	1 mm	10 mm

Case 3 and 4
For cases 3 and 4, we repeated the same simulations as in cases 1 and 2 but now for another orientation of the TLN frame. For cases 3 and 4 $\beta = 80°$. With the simulated near-polar orbits of the satellites this means that for those two cases we are less sensitive for the transversal direction. Within case 3 we simulated a small displacement signal ($d_T = d_N = 1$ mm) and within case 4 we simulated a larger displacement signal ($d_T = d_N = 10$ mm). The results are shown in Fig. 3.9c and d respectively. For case 3 we estimated $\sigma_{d_T} = 11.59$ mm and $\sigma_{d_N} = 1.16$ mm, and for case 4 we estimated $\sigma_{d_T} = 15.76$ mm and $\sigma_{d_N} = 1.61$ mm.

When comparing the results of these four cases, we conclude that the larger the displacement signal, the larger the uncertainty for the unknown parameters σ_{d_T} and σ_{d_N}. This can be understood by the following. If we make a mistake in the alignment of the frame, we introduce a bias for the final estimates, see section 3.5. The bias scales with the displacement signal. With the mathematical model as in Eqs. (3.9) and (3.10) we take into account the potential misalignment of the frame, and also the effects of this. We try to capture the potential bias for the displacement estimates into uncertainties for those estimates. Therefore it is apparent that the uncertainties for the displacement estimates become larger when the displacement signal becomes larger too, since the biases becomes also larger. It can also be explained by Eq. (3.21): for the different displacement signals we used other values for the Jacobian matrix $J_{[i]}$. E.g., for case 1 and 3 we used $d_{T[i]} = d_{N[i]} = 1$ mm and for case 2 and 4 we used $d_{T[i]} = d_{N[i]} = 10$ mm, therefore the realizations for $Q_{\hat{x}}$ were different.

3.7. Detectability of displacements

It is possible to use the mathematical model described in section 3.6 to comment on the detectability of displacements. When InSAR is used to monitor the displacements of a RUM, we want to detect displacements that are significantly different from the displacement history. A stakeholder may want to be warned when the RUM starts behaving differently. Therefore, the question is: “When is the new observation significantly different from the observations before?” It is possible to use the standard deviations of $\hat{d}_T$ and $\hat{d}_N$ as a metric for the detectability of displacements. We will elaborate on this in this section.

Assume that we have estimated a decomposed time series in the transversal and in the normal direction from t_0 until t_{m-2}, see Figs. 3.10a and c. Both time series are obtained by performing a decomposition over the RUM per epoch $t \in [0, m-2]$, using the iterative approach described in section 3.6. Both time series have a negative trend. Due to the observation noise and a potential misalignment of the TLN frame, the decomposed time series have a particular noise level. We also plotted dashed lines for $+\sigma$ and $-\sigma$ for the estimated linear trends.

When we estimate the displacement at t_{m-1} (the orange dot), we want to test whether this estimated displacement is significantly different from the deformation history of the RUM. At first sight, the estimate for t_{m-1} does not seem to be significantly different. However, the estimate at t_m (red dot) seems to be different from the observations before. Thus, the question is: ‘When do we state that a displacement is significantly different from a given deformation history?’ To answer this question, we need to test a null hypothesis H_0 against an alternative hypothesis H_a.

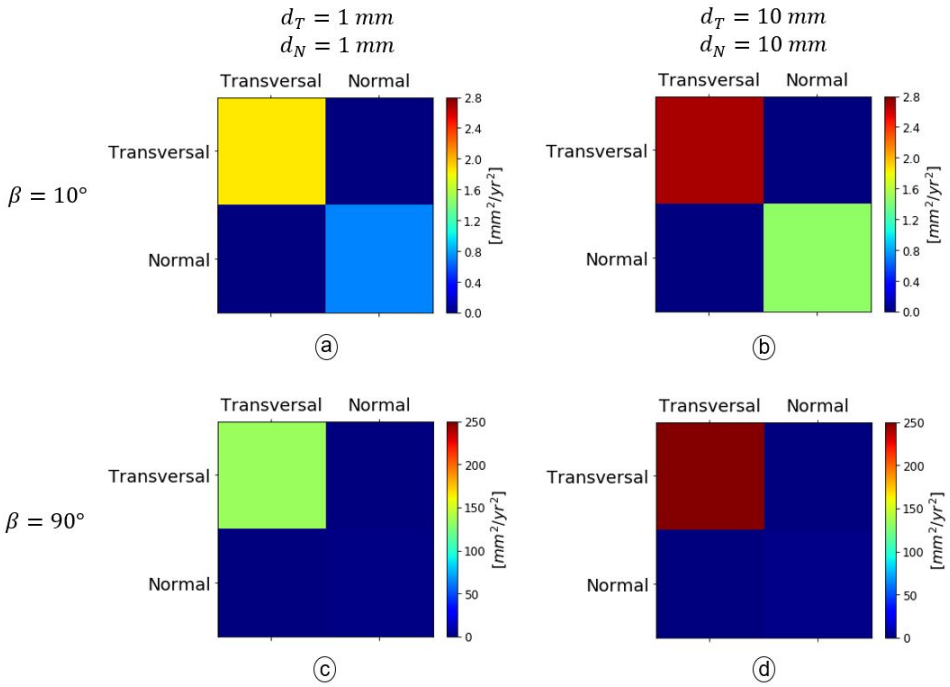

Figure 3.9: Visualizations of the upper four elements of $Q_{\hat{x}}$ estimated with Eq. (3.21). Fig. a and b are a result from simulations were $\beta = 10°$. For Fig. c and d we changed to orientation to $\beta = 80°$. We also simulated different displacement signals. It can be seen that the larger the displacement signal, the larger the uncertainty for the displacement parameters d_T and d_N (diagonal elements of $Q_{\hat{x}}$)

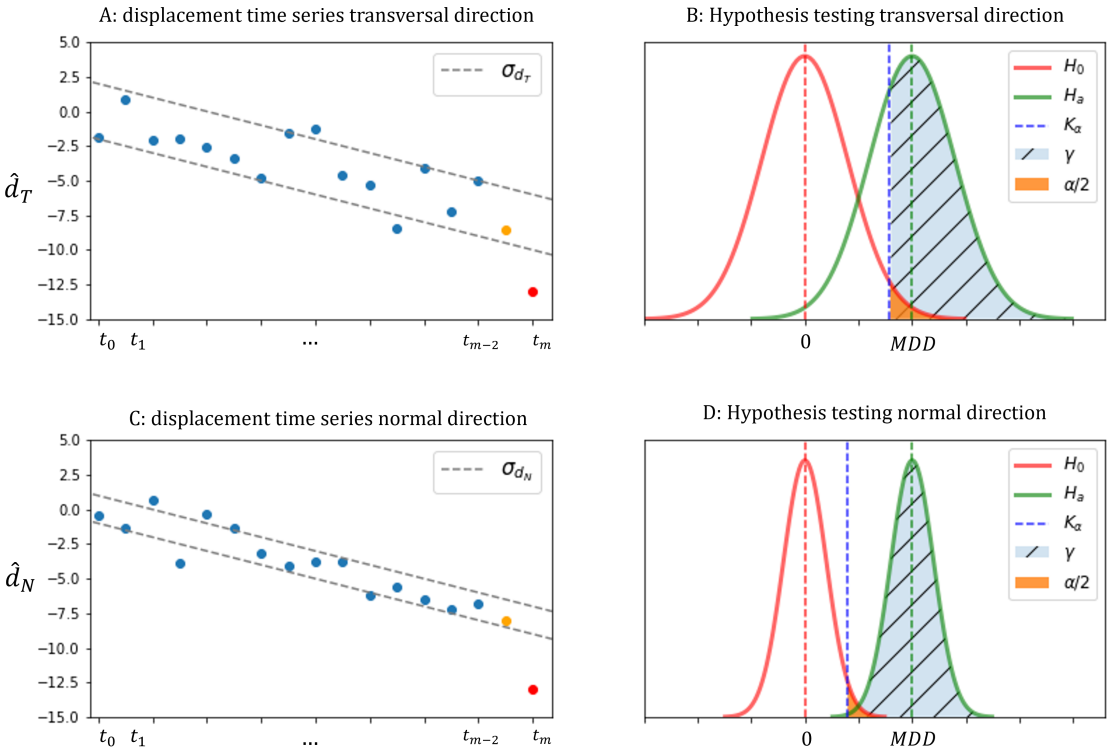

Figure 3.10: (a) and (c) show simulated displacement time series in the transversal and normal direction respectively. For new estimates $\hat{d}_T$ and $\hat{d}_N$ we want to test whether it is likely that the RUM starts behaving differently from the deformation history or that there is no change in deformation behavior. (b) and (d) show the hypothesis test to answer that question. The probability density functions under H_0 (no displacement) and under H_a (a displacement of MDD) are shown. The MDD can be estimated when the detectability power γ and significance level α are known.

In the following, we will discuss the procedure for the transversal component. Obviously, the same procedure belongs to the normal component.

3.7.1. Hypothesis for the functional model

When we use a functional model where we have a displacement time series in the transversal direction, and we want to estimate the displacement velocity, the null hypothesis is defined as

$$H_0 : E\{\underbrace{\begin{bmatrix} \underline{d}_T^{(1)} \\ \underline{d}_T^{(2)} \\ \vdots \\ \underline{d}_T^{(m)} \end{bmatrix}}_{\underline{y}'}\} = \underbrace{\begin{bmatrix} 1 & t_0 - t_1 \\ 1 & t_0 - t_2 \\ \vdots & \vdots \\ 1 & t_0 - t_m \end{bmatrix}}_{A} \underbrace{\begin{bmatrix} d_{T_0} \\ v_T \end{bmatrix}}_{x}, \tag{3.22}$$

where $\underline{y}'$ is the vector with estimates for the transversal component for epoch 1 until m. Those estimates can be obtained by using the method described in section 3.6 per epoch $t \in [0, m]$. The hypothesis is that the displacement behavior of the RUM is described by a linear model with an initial value d_{T_0} and velocity v_T. The vector of unknowns x is therefore defined as $x = [d_{T_0}, v_T]^T$. All displacements $\underline{d}_T^{(1)}$ until $\underline{d}_T^{(m)}$ are referenced to epoch t_0 and to a stable reference point outside the RUM. The stochastic model is defined as

$$D\{\underbrace{\begin{bmatrix} \underline{d}_T^{(1)} \\ \underline{d}_T^{(2)} \\ \vdots \\ \underline{d}_T^{(m)} \end{bmatrix}}_{\underline{y}'}\} = \underbrace{\begin{bmatrix} \sigma^2_{d_T^1} & 0 & 0 & 0 \\ 0 & \sigma^2_{d_T^2} & 0 & 0 \\ 0 & 0 & \ddots & 0 \\ 0 & 0 & 0 & \sigma^2_{d_T^m} \end{bmatrix}}_{Q_{yy}}, \tag{3.23}$$

where $\sigma^2_{d_T^1}$ until $\sigma^2_{d_T^m}$ are estimated with Eq. (3.21) for every epoch separately since the values depend on the size of the displacement signal which can differ per epoch.

We test the null hypothesis against an alternative hypothesis where we assume that something has changed for the last observation at epoch m:

$$H_a : E\{\underbrace{\begin{bmatrix} \underline{d}_T^{(1)} \\ \underline{d}_T^{(2)} \\ \vdots \\ \underline{d}_T^{(m)} \end{bmatrix}}_{\underline{y}'}\} = \underbrace{\begin{bmatrix} 1 & t_0 - t_1 \\ 1 & t_0 - t_2 \\ \vdots & \vdots \\ 1 & t_0 - t_m \end{bmatrix}}_{A} \underbrace{\begin{bmatrix} d_{T_0} \\ v_T \end{bmatrix}}_{x} + \underbrace{\begin{bmatrix} 0 \\ \vdots \\ 0 \\ 1 \end{bmatrix}}_{c_y} \nabla, \tag{3.24}$$

where c_y is an $m \times 1$ column vector with all zeros except for the last value, which equals one.

3.7.2. Hypothesis for the model of condition equations

We can also approach the problem following a different rationale. With the observations from t_0 until t_{m-1} we can estimate the initial value for the transversal displacement d_{T_0} and velocity v_T with $\underline{\hat{x}} = (A^T Q_{yy}^{-1} A)^{-1} A^T Q_{yy}^{-1} \underline{y}'$, where A is the design matrix from Eq. (3.22), $\underline{y}'$ is a column vector containing the estimated values for the transversal component and Q_{yy} is the variance-covariance matrix as in Eq. (3.23). The uncertainty for $\underline{\hat{x}}$ is estimated with $Q_{\hat{x}} = (A^T Q_{yy}^{-1} A)^{-1}$.

With the estimate for initial value d_{T_0} and velocity v_T, it is possible to compute a predicted value for the transversal displacement at epoch m, $\underline{d}_{T,p}^{(m)}$ with

$$\underline{d}_{T,p}^{(m)} = \underbrace{\begin{bmatrix} 1 & t_0 - t_m \end{bmatrix}}_{A_p} \begin{bmatrix} \hat{d}_{T_0} \\ \hat{v}_T \end{bmatrix}, \tag{3.25}$$

where $[\hat{d}_{T_0},\ \hat{v}_T]^T = \hat{x}$. The precision for $\underline{d}_{T,p}^{(m)}$ is computed with

$$\sigma_{d_{T,p}}^2 = A_p Q_{\hat{x}} A_p^T, \tag{3.26}$$

where A_p is the design matrix as in Eq. (3.25) [60]. For RUMs where the displacement behavior is not changing, we expect the predicted value to be equal to the measured value at t_m, i.e., $E[\underline{d}_{T,p}^{(m)} - \underline{d}_T^{(m)}] = 0$. We can therefore write the null hypothesis H_0 as

$$H_0 : B^T E[\underline{y}] = 0, \tag{3.27}$$

where $B^T = [1\ \ -1]$ and $\underline{y} = [\underline{d}_{T,p}^{(m)}, \underline{d}_T^{(m)}]^T$. The dispersion of the model is defined as

$$D\left\{\underline{y}\right\} = \begin{bmatrix} \sigma_{d_{T,p}}^2 & 0 \\ 0 & \sigma_{d_{T,m}}^2 \end{bmatrix}, \tag{3.28}$$

where $\sigma_{d_{T,m}}^2$ is the precision of the measured parameter, which is in this case the estimate for the transversal component at epoch m which is $\underline{d}_T^{(m)}$. $\sigma_{d_{T,p}}^2$ is the uncertainty of the predicted value for the transversal component at epoch m. The longer the historical time series, the smaller the uncertainty for the predicted parameter.

If the displacement behavior of the RUM changed in the last epoch, the predicted value will no longer be equal to the measured value. The alternative hypothesis H_a is therefore defined as

$$H_a : B^T E[\underline{y}] = c_t \nabla, \tag{3.29}$$

where c_t is a 1×1 scalar and ∇ is the change in displacement behavior.

3.7.3. Minimal Detectable Displacement

Given the hypotheses in section 3.7.2 and selected values for the significance level and the detectability power, we can test whether the deformation behavior of the RUM changes, which is of interest from a monitoring perspective. Equally important is it to know a priori, for each point, how likely it is to detect a displacement with a particular magnitude.

If we choose a confidence level $1-\alpha$, where α is the significance level, it is possible to compute a critical value K_α, see Figs. 3.10b and d. Displacements greater than K_α are considered significantly different from the null hypothesis H_0, and H_0 is rejected. The significance level α determines the probability of a 'false alarm', which is the probability that H_0 is rejected while it is correct.

Additionally, we can test how large a displacement should be before it is detected with a predefined detectability power (DP) γ, where γ is the likelihood that the alternative hypothesis is correctly sustained. A displacement detected with a likelihood of γ is called the Minimal Detectable Bias (MDB) [60], or, in this specific context, the Minimal Detectable Displacement (MDD). The MDD corresponds to a particular alternative hypothesis H_a, where we test whether we can significantly detect a displacement with a magnitude of MDD.

From Figs.3.10b and d, it can be seen that the smaller the uncertainty for $\hat{d}_T$ and $\hat{d}_N$, the larger the detectability power γ for a particular MDD. In Figs. 3.10b and d, the distribution for the null hypothesis H_0 and the alternative hypothesis H_a are visualized where H_a is a displacement of the size of the MDD in the transversal and normal direction, respectively (the MDD has the same magnitude for both cases). The width of the distributions depends on the precision of $\hat{d}_T$ and $\hat{d}_N$. Thus, the more precise we can estimate the unknown parameters, the more narrow the distributions, and the higher the power γ for detecting a particular MDD.

MDD for model of condition equations

When an overall model test (OMT) is used to test whether H_0 should be sustained or rejected, a significance level α is required. Subsequently, a w-test can be used to estimate the MDD when γ, α_1 (the

significance level for the w-test) and the dispersion $D\{y\}$ are known. When H_0 and H_a are specified as in the linear model of condition equations in Eqs. (3.27) and (3.29) the MDD is estimated with [60]

$$|\mathrm{MDD}| = \sqrt{\frac{\lambda_0}{c_t^T Q_t^{-1} c_t}}, \tag{3.30}$$

where λ_0 is the non-centrality parameter, which couples the OMT and the w-test, with

$$\lambda_0 = \lambda(\alpha,\ q = m - n,\ \gamma = \gamma_0) = \lambda(\alpha_1,\ q = 1,\ \gamma = \gamma_0), \tag{3.31}$$

where α is the significance value of the OMT test which has a redundancy of $m - n$, where m is the number of observations and n the number of unknowns. The w-test has a significance level α_1 and has a redundancy of $q = 1$. When $\lambda_0 = \lambda$, a model error can be found with the same probability in the OMT and the w-test. Both tests also have the same reliability and therefore the same MDD. When the model of condition equations is used, c_t is a scalar that has a value of 1. Q_t can be estimated with

$$Q_t = B^T Q_{\hat{x}} B. \tag{3.32}$$

It can be seen that with this method, we can a priori (i.e., before the InSAR investigation started) estimate the MDD as long as we know the viewing geometry of the LoS observations, the precision of the LoS observations, and the precision of the predicted parameter.

MDD for the functional model
When H_0 and H_a are specified using the functional model as in Eqs. (3.22) and (3.24), the MDD is estimated with

$$|\mathrm{MDD}| = \sqrt{\frac{\lambda_0}{c_y^T Q_{yy}^{-1} Q_{\hat{e}\hat{e}} Q_{yy}^{-1} c_y}}, \tag{3.33}$$

where Q_{yy} is defined in Eq. (3.23) and c_y in Eq. (3.24), $Q_{\hat{e}\hat{e}}$ is specified as:

$$Q_{\hat{e}\hat{e}} = Q_{yy} - Q_{\hat{y}\hat{y}} = Q_{yy} - A Q_{\hat{x}} A^T = Q_{yy} - A(A^T Q_{yy}^{-1} A)^{-1} A^T. \tag{3.34}$$

Practical implementation
In order to make an a priori assessment on the applicability of InSAR for a particular application, stakeholders need to decide on the confidence level $1 - \alpha$. A higher confidence level means that displacements need to be more significant to be detected. Yet, as a consequence, smaller signals will be missed. Alternatively, choosing a lower confidence level will result in more false warnings, which can be unfavorable.

Stakeholders can also choose to select a particular detectability power γ. With γ given, values for the MDD can be estimated. It may be that the MDD in the transversal direction differs from the MDD in the normal direction (due to the different Q_{yy} matrices in Eq. (3.28)). Stakeholders often want high values for the detectability power γ, as this implies that true displacement anomalies will be detected. Hence this results in unfavorable MDDs.

In other cases, the MDD is predefined by stakeholders, where the maximum allowable displacement can determine the MDD to ensure the surroundings' safety. Given the MDD, the detectability power γ can be estimated, and stakeholders can consider whether it is large enough for the particular situation.

3.8. Summary and Discussion

We developed a new alternative approach for the underdetermined problem often encountered in InSAR studies (see section 2.4 p. 22) that we call the 'strap-down' approach. The approach makes use of

a local TLN reference frame. For lot of deformation phenomena it is possible to make the assumption that the displacements in the longitudinal direction are zero. Therefore the inverse problem can be solved with two sets of STCI LoS observations.

However, we have found that the approach requires that the orientation of the TLN frame is well chosen and that in the case of a misalignment of the frame, the estimated transversal and normal displacements are biased. We therefore came with a mathematical model that also takes into account the frame alignment uncertainty, see section 3.6.

In section 3.5 we have seen that there are multiple factors that affect the precision and accuracy for the displacement estimates: (i) the precision of the LoS observations, (ii) the orientation of the TLN frame, and for cases where there is a displacement signal, also (iii) the uncertainty of the frame alignment, and (iv) the magnitude of the displacements. With the method we developed, we were able to take into account all those factors while estimating the displacements in the transversal and normal direction.

However, stakeholders are often not only interested in the displacements itself but also in detecting a change in the displacement behavior of a RUM. In section 3.7 we developed a methodology to estimate the Minimal Detectable Displacements given a Detectability Power, significance level and the stochastic model of the LoS observations. We found that we could also use the strap-down approach for this.

3.8.1. Discussion

From the Monte Carlo analysis in section 3.4, we found that the uncertainty of the TLN frame orientation results in an uncertainty for the estimated parameters. For the case of noise-free LoS observations, we found that the distributions of the different estimates for d_T and d_N were not normally distributed. However, the estimates are still described by a variance, or standard deviation.

When we review the situation with noisy LoS observations (using $\sigma_{\text{LoS}} = 0.5$ mm) we see that the estimates for d_T and d_N have an (almost) normal distribution, at least for $\beta \in (-60°, 60°)$. For $\beta \sim 90°$, we still found that the estimates were not normally distributed. However, in most cases, the noise of the LoS observations is larger than 0.5 mm, more likely around 2 mm. Therefore we expect that normal distributions can then describe the distribution of the estimates for most of the orientations of the TLN frame.

To estimate the MDD with the model of condition equations, it is required to have initial displacement values and displacement velocities. It is also required to know the corresponding standard deviations, which can be estimated when the standard deviations of the estimated displacements per epoch are known. The latter can be estimated with Eq. (3.21). The only remark here is that the distribution of the standard deviations per epoch is unknown (it depends on the noise level of the observations and the frame orientation). However, estimating the MDD requires normally distributed data since it is a modification of the w-test. Nevertheless, as we mentioned before, in most cases, it is possible to assume that the estimates will normally be distributed due to the larger noise level of the LoS observations.

4

Practical considerations: feasibility, applicability, and impact

InSAR investigations are typically complex. We define different perspectives on how we can 'look' at the InSAR problem described by Eqs. (3.9) and (3.10). In section 4.1, we first review the different InSAR factors related to the perspectives which we use for the different perspectives. In section 4.2.1, we discuss the stakeholder's perspective followed by the perspective of the user of a pre-existing InSAR information product which is discussed in section 4.2.2. Finally, we discuss the space perspective in section 4.2.3.

4.1. InSAR influence factors

We distinguish five factors influencing the feasibility, applicability, and impact of InSAR analysis, i.e., (i) the space segment, (ii) the location of the Area of Interest (AoI) on Earth, (iii), the particular deformation phenomenon at hand, (iv) the location-specific part, and (v) the (requested) characteristics of final InSAR product. We discuss different factors below.

4.1.1. Space segment

Many SAR satellite missions can be considered within the space segment, each with a unique viewing geometry, affecting the LoS direction from a target towards the satellite. Moreover, the different radars use different wavelengths affecting the precision of the LoS observations, and therefore the minimal detectable displacement will differ per mission. Finally, the ground resolution differs per mission. Often, with finer resolutions, displacements can be detected earlier.

4.1.2. Location on Earth

For every location on Earth, the LoS direction towards the satellite is different, e.g., the incidence angle and the azimuth angle of the zero-Doppler plane (ZDP) change from near to far range within an InSAR image, see section 2.1.5. Furthermore, the revisit time, and thus the number of available observations and independent viewing geometries is different for different locations on Earth. For example, for Sentinel-1, the revisit times are around six days near the equator but significantly smaller for higher latitudes [61]. Note that we use the term *revisit* to indicate how frequent a particular location on earth is observed by the same satellite mission, even if it is from different viewing geometries. We use the term *repeat* to indicate how frequent a particular area is observed from the same orbital position in space.

4.1.3. Deformation phenomenon

Each deformation phenomenon can be characterized by its own unique spatial and temporal characteristics, including the spatio-temporal extent and spatio-temporal smoothness, a certain magnitude and the direction of the displacements. The direction of the displacements determines how the displacements are projected onto the LoS. Also, the spatial magnitude of the signal is of relevance. Larger displacement signals can be detected with a higher detectability power (see section 3.7). To be detected, it is the particular SNR that is of importance: the signal needs to be significantly greater than the noise level. We found that the orientation of the TLN reference frame affects the detectability for the transversal and normal directions.

The smoothness of a signal in space is essential for detecting displacements. A higher spatial sampling is required for highly local deformation signals compared to smooth and wide signals. The temporal extent provides information on the duration of the deformation and is essential for the required length of the InSAR investigation. Lastly, the temporal smoothness determines how often measurements are needed, e.g., temporally smooth signals can be monitored with reduced temporal sampling rates.

4.1.4. Location-specific part

The location-specific part differs per case, and is the part that influences the spatial distribution of the LoS observations. Given the land cover, for every location on Earth the distribution of observations will different, which is a defining characteristic of InSAR. Typically, InSAR does not work over water bodies or in the middle of the tropical rain forest. Consequently, the quality of the observations is captured within the location-specific part. Before we can decompose the LoS signals, we require observations with sufficient quality that remain coherent in time.

4.1.5. InSAR product

There is no single unique InSAR product. The final product often is a result of the stakeholder's requirements. In some cases the stakeholder may want a full representation of the deformation phenomenon and a decomposition is required, while in other cases, the LoS observations themselves may already be sufficient.

Per case, it will differ what product can be delivered. Suppose only observations from one viewing geometry are available (given the space segment). In that case, it is impossible to decompose the LoS observations, and only the LoS observations themselves or projections of the LoS observations can be delivered. Furthermore, the deformation phenomenon affects the final product since smooth signals in space require fewer RUMs compared to non-smooth signals in space.

The final product should be delivered with an uncertainty: how reasonable are the final estimates?. Within section 3.5 we found that the uncertainty depends on the viewing geometry (space segment and location on Earth) and the orientation of the TLN frame (deformation phenomenon).

4.2. InSAR perspectives

We require two sets of STCI LoS observations over the RUM to be able to decompose the LoS observations in the TLN system, i.e., for deformation phenomena with no longitudinal displacements, see chapter 3. This requires coherent scatterers which are well distributed over the RUM to successfully decompose the LoS observations. Thus, considering the five influence factors discussed above, we can state that the location-specific part needs to 'sufficient', as we need observations from a sufficient quality. Since we cannot influence the way the Earth looks at a particular location, from now on, we need to assume that the location-specific factor is satisfactory, i.e., we assume that there are enough observations available over the RUM and that these are coherent and well distributed.

Under this assumption, there are four influence factors left. With these four InSAR factors, we define three different InSAR perspectives: three unique ways of looking at InSAR studies, see Fig. 4.1. These are the perspectives from a prospective user, from a user of a pre-existing product, and from a provider of InSAR services or data. Each perspective results in a different set of questions that can be asked.

	Who	Question	What is known?	A priori or a posteriori
Perspective 1	Stakeholder	What can I get from InSAR? What can InSAR do for me?	1. Space segment 2. Location on Earth 3. Deformation phenomenon	A priori
Perspective 2	User of pre-existing InSAR product	What deformation phenomenon can be significantly estimated from the product?	1. Space segment 2. Location on Earth 3. InSAR product	A posteriori
Perspective 3a	Value adding companies	What satellite mission(s) should be used to meet the product requirements for monitoring a specific deformation phenomenon?	1. Location on Earth 2. Deformation phenomenon 3. InSAR product	A priori
Perspective 3b	Space agencies	What satellite mission would be needed to optimally monitor a specific deformation phenomenon?	1. Location on Earth 2. Deformation phenomenon 3. InSAR product	A priori

Figure 4.1: Within every InSAR perspective there is one questioner who is interested in one InSAR factor. There are always three InSAR factors known.

The different perspectives have in common that there are always three InSAR influence factors considered to be known, while a statement on the fourth one is required. We will further discuss the different perspectives in the following.

4.2.1. Perspective 1: The stakeholder's perspective

The first perspective to look at the problem is the perspective of a (prospective) end-user. For example, suppose an asset manager considers to use InSAR to monitor a deformation phenomenon of a bridge. Even though the asset manager has minimal knowledge about satellites, radars, and the InSAR technology in general, he should still make difficult decisions, e.g., regarding what satellite mission(s) to use, or on feasibility in general. The typical questions of the stakeholder are: *"What can InSAR do for me in this particular situation?"* and *"Is InSAR able to detect displacements of a particular size in a particular direction for my bridge with InSAR?"*

After the choice for a particular satellite mission is made, this will lead to particular product requirements, i.e., *"how precise can we estimate the unknown displacement parameters?"*, *"can we disentangle (estimate) the three displacement parameters?"*, and *"what is the magnitude of the displacement (i.e., the MDD) that can be detected in a particular direction?"* It should be possible to answer the stakeholders questions before starting with the InSAR study because the answers to the questions above determine whether it is worth investing in choosing the InSAR technology, over alternatives.

Especially the MDD and the DP values can help the stakeholder to make a decision, whether it is worth investing in InSAR. For example, when a stakeholder wants to use InSAR to monitor a landslide-prone area, the MDD can be predefined. In section 3.7.3, we have seen that, when the viewing geometries and precision of the LoS observations of the available acquisitions are known, and we define a value for the significance level, we can estimate the DP corresponding to this MDD. The stakeholder should now decide on whether this DP satisfies his requirements. When the stakeholder is just interested in what InSAR can do for him, the MDD can serve as an answer to that question. In that case, the stakeholder should a priori decide on the DP, and we can estimate the corresponding MDD. Afterward, the stakeholder can decide whether this MDD value is sufficient. Obviously, to be able to answer those questions, the deformation phenomena that needs to be monitored should be known.

Considering these two examples, we see that the first perspective is actually an *a priori* perspective, since the answers to the questions can serve as a metric to help in making a decision on whether is it worth to invest in applying the InSAR methodology. In this first perspective, three InSAR influence factors are known: the space segment, the location on Earth, and the deformation phenomenon. The stakeholder's questions are related to the product requirements, which is the unknown InSAR influence

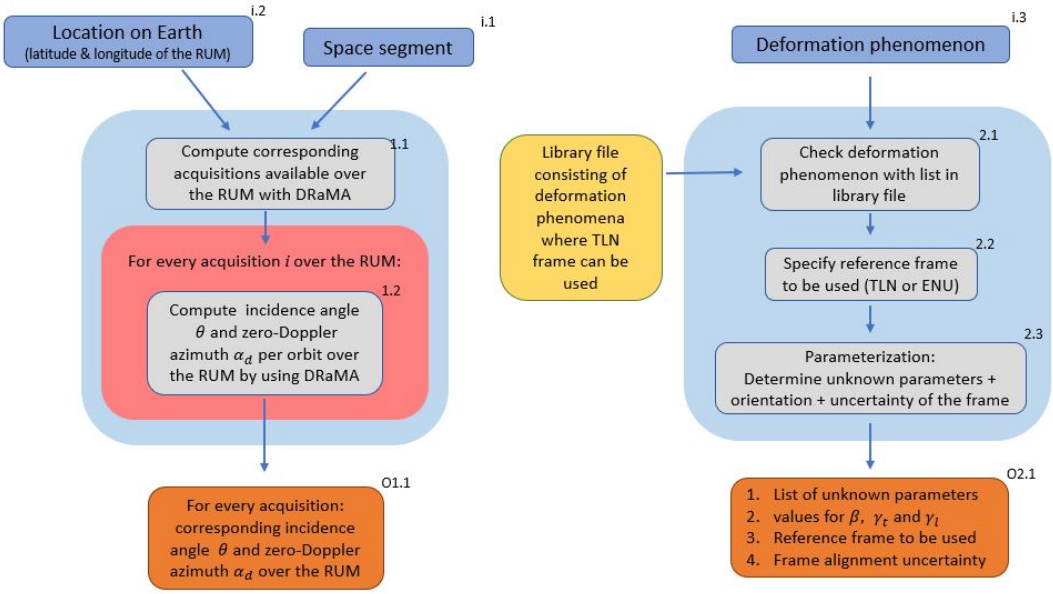

Figure 4.2: Workflow for Module 1: LoS geometry (left) where the viewing geometry for a particular satellite mission at a location on Earth is estimated using DRaMA and Module 2: Parameterization of the deformation phenomenon (right) where the unknown parameters for the deformation phenomenon are determined.

factor. The workflow for this perspective consists of four modules, which have been developed and implemented in software routines in the framework of this study, i.e., (i) Module 1: LoS geometry, (ii) Module 2: Parameterization of the deformation phenomenon, (iii) Module 3: The functional model and the Q_{yy} matrix, and iv) Module 4: Hypothesis testing.

Module 1: LoS geometry
Given the space segment and the location on Earth, the first module aims to estimate the viewing geometry for the space segment for a specific location on Earth, see Fig. 4.2. In the first step, the available acquisitions are computed with the simulation toolbox DRaMA [19]. It could be the case that multiple acquisitions are available over the RUM. Therefore, in step 1.2 the corresponding incidence angles θ and azimuth angles of the ZDP α_d are computed. The output of the first module is per acquisition the incidence angle θ and the azimuth angle of the ZDP α_d per RUM.

Module 2: Parameterization of the deformation phenomenon
Within module 2, the unknown parameters for the deformation phenomenon are defined. The first step is to test whether it is possible to assume that there are no longitudinal displacements and whether the TLN system can be used, and subsequently the unknown parameters can be determined. When the TLN frame can be used, the orientation of the frame needs to be estimated even as this has a certain uncertainty, see Fig. 4.2. For deformation phenomena without a main driving mechanism or where the deformation phenomena is unknown, the ENU reference system should be used, resulting in three unknown displacement parameters.

Module 3: Functional model and Q_{yy}
The third module aims to define, per RUM, the functional model and the Q_{yy} matrix that should be used to solve for the unknown parameters. With the viewing geometry of the available satellite mission (output module 1), the orientation of the reference frame, and the unknown parameters (output module 2), it is possible to define the functional model. In step 3.2, the number of available sets of STCI observations m is compared with the number of unknown displacement parameters n. It is important to mention that sufficient angular diversity is required to solve for the unknown parameters, see section 2.3.4. When $m < n$, the output of Module 3 is the following statement: *'There are not enough observations to give*

estimates for all unknown parameters.' When $m \geq n$, the design matrix A in Eq. (3.9) can be filled. As a last step, the variance-covariance matrix Q_{yy}, see Eq. (3.10), should be defined. Given the satellite mission and the location on Earth, a rough a priori estimate of the uncertainty of the LoS observations needs to be made. The output of module 3 is the design matrix A and the Q_{yy} for the RUM for the case where $m \geq n$. For an overview of the third module, see Fig. 4.3

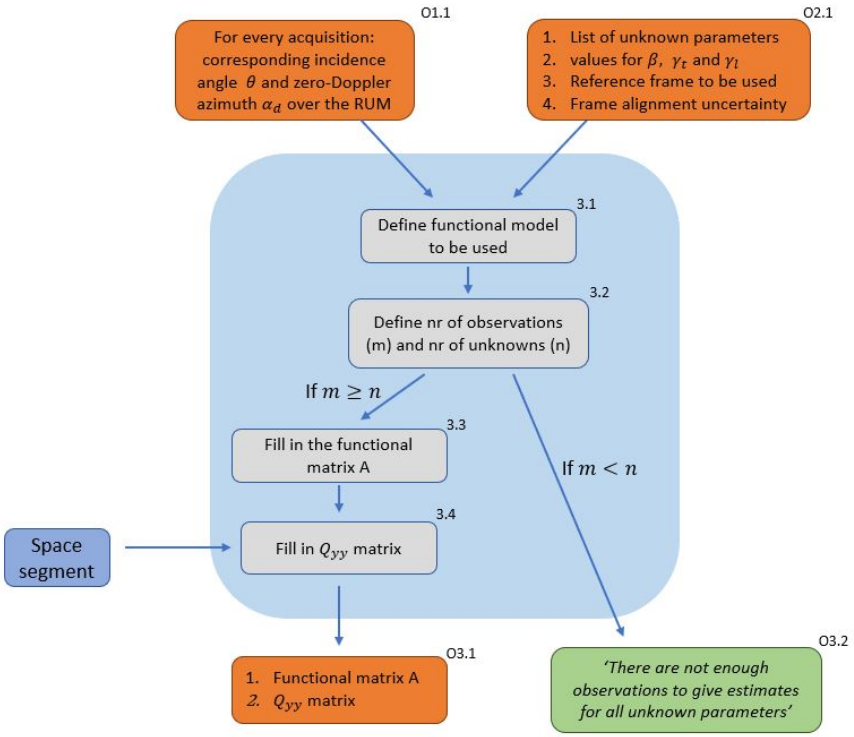

Figure 4.3: Workflow for Module 3: Functional model and Q_yy where the mathematical model that should be used is formed. It is also checked whether the inverse model can be solved with the observation (geometry) available.

Module 4: Hypothesis testing

The aim of Module 4 is to estimate the MDD or DP, see Fig. 4.4. The first step is to check which of the two is predefined. If the DP, γ, is predefined, step 4.3 needs to be performed, where $Q_{\hat{x}}$ is estimated using Eq. (3.14). $Q_{\hat{x}}$ contains information regarding how precise the unknown parameters can be estimated with the available viewing geometries, the orientation of the TLN frame, and the frame uncertainty. Consequently, σ_{d_T} and σ_{d_N} (the diagonal elements of $Q_{\hat{x}}$) are estimated and the linear model of condition equations (see section 3.7.2) should be defined (step 4.4), followed by computing the corresponding Q_{yy} matrix (see Eq. (3.28)). It is now possible to define a null hypothesis H_0 and an alternative hypothesis H_a in step 4.6. These two hypotheses are needed to compute the value for the MDD with Eq. (3.30) in step 4.7, which is the output of this module.

If the MDD is predefined, step 4.2 is needed first, i.e., making a first estimate for the DP γ_i. With this value for γ_i we can estimate MDD_i, if $\mathrm{MDD} = \mathrm{MDD}_i$, the value for γ_i is the the DP that corresponds to the value for MDD. When $\mathrm{MDD} \neq \mathrm{MDD}_i$, we should make a new estimate for γ_i. We repeat this process until we find the correct value for γ such that $\mathrm{MDD} = \mathrm{MDD}_i$.

4.2.2. Perspective 2: User of a pre-existing InSAR information product

Within this second perspective from an end-user, the InSAR information product does already exist. Note that this is different from the first perspective, in which the information product still needs to be acquired or computed. Suppose the end user of this information product, e.g., a displacement map that shows colored dots, where the colored dots represent the LoS displacement rates, as in Fig. 1.1, p. 1.

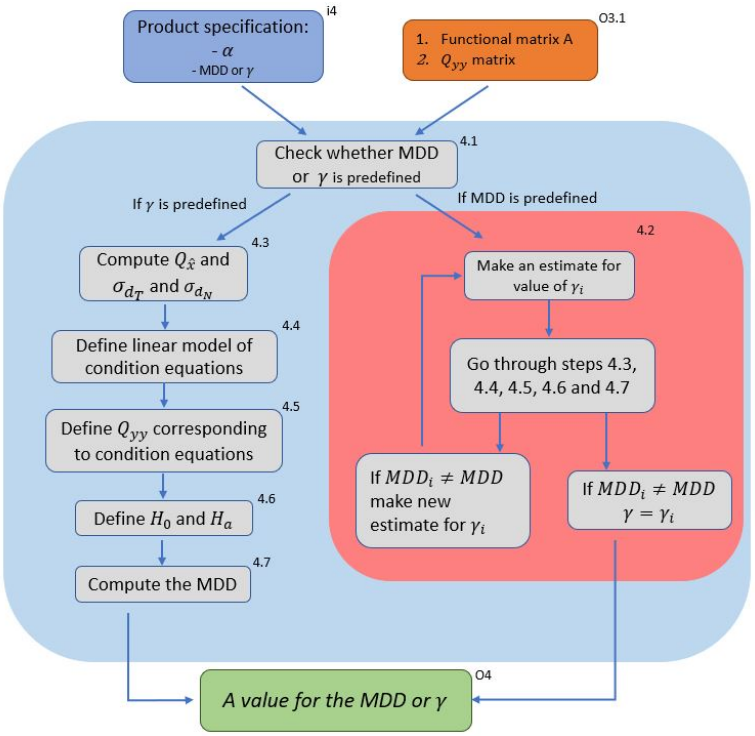

Figure 4.4: Workflow for Module 4: Hypothesis testing. This module aims to estimate the MDD or the DP, given the mathematical model and the product specifications defined by the stakeholder.

Obviously, the user is not particularly interested in the colored dots. Most likely, he is interested in what happens with the asset, or deformation phenomenon, that he should monitor. He wants to know what the product tells him about the deformation phenomenon. So the question related to this perspective is: *"What can we get from the product?"*, or, in other words: *"What deformation phenomenon can be significantly estimated from the product?"* Since the InSAR data is already processed, this is an a posteriori perspective.

The workflow developed for this perspective is divided into (i) module 5: RUM observations and unknown parameters, (ii) module 6: RUM parameter estimation, and (iii) module 7: Deformation phenomenon visualization.

Module 5: RUM observations and unknown parameters
The input for this module is the displacement product, for instance, a LoS displacement time series for different scatterers. Within step 5.1, it is first needed to identify different RUMs from the product. The next step is to make an estimate for the deformation phenomenon for every RUM r, which serves as the input for step 5.2 where the orientation angles and their uncertainties are estimated. Consequently, within step 5.3, the number of unknowns n related to the deformation phenomenon, e.g., d_T and d_N, are determined. Afterwards, the number of sets of STCI observations m that have sufficient angular diversity over the RUM should be defined from the product (step 5.4).

It is essential to check whether the angular diversity of the different LoS observations is large enough to have a full-rank functional model. Within step 5.5, the number of unknowns n are compared with the number of sets of STCI observations m. If $m < n$, the output of module 5 for that particular RUM is: 'There are not enough sets of STCI observations to solve for the unknowns for RUM rh.' For every RUM where $m \geq n$ the output is as follows: (i) Available (LoS) observations over the RUM, (ii) list of n unknown parameters, and (iii) values for β, γ_t and γ_l and for $\sigma_\beta, \sigma_{\gamma_t}$ and σ_{γ_l}, see Fig.4.5

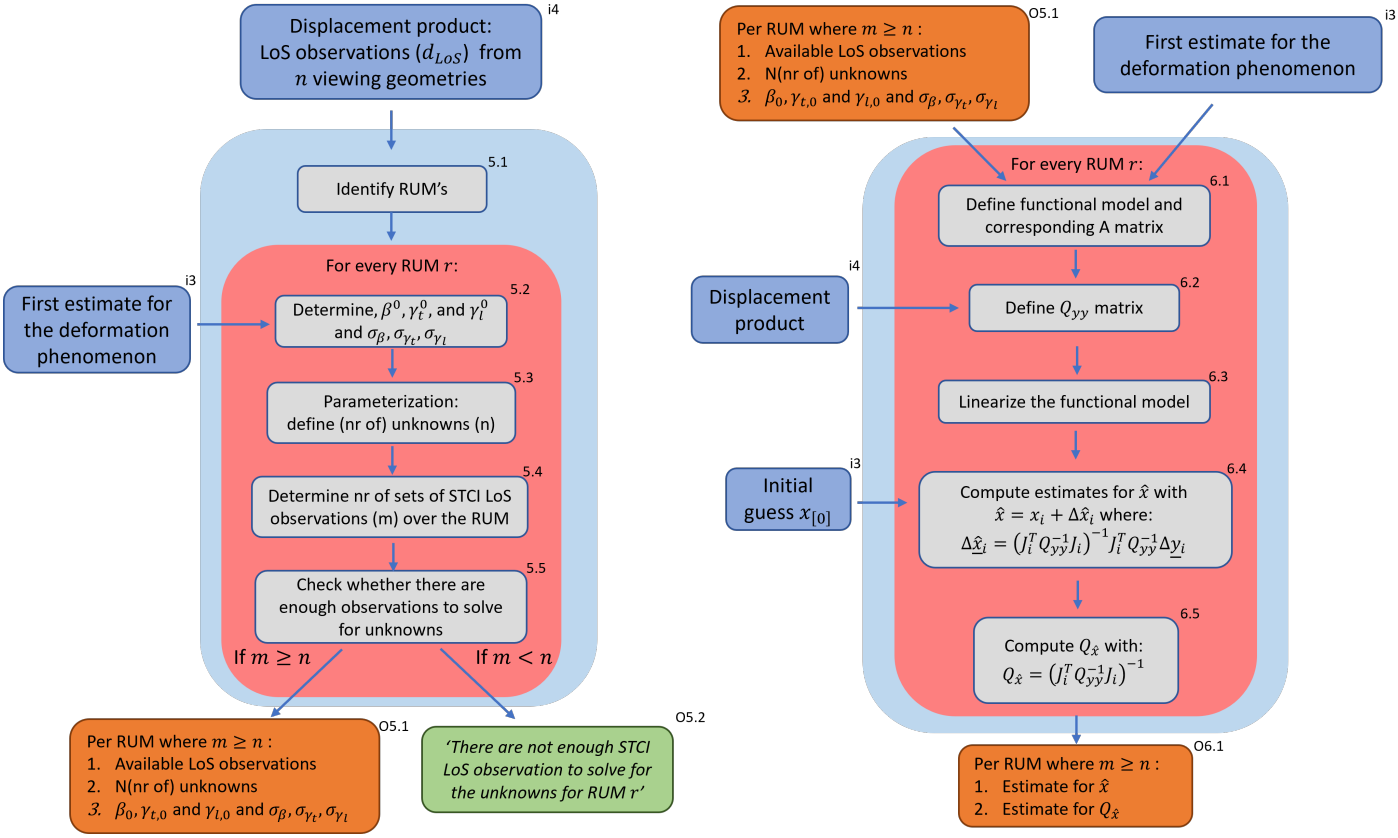

Figure 4.5: Workflow for Module 5: RUM observations and unknown parameters (left) and Module 6: RUM parameter estimation (right). In Module 5, per RUM the deformation phenomenon is estimated and it is verified whether there are enough observations to solve for the unknowns. Subsequently, in module 6, the unknown displacements are estimated using the STCI observations.

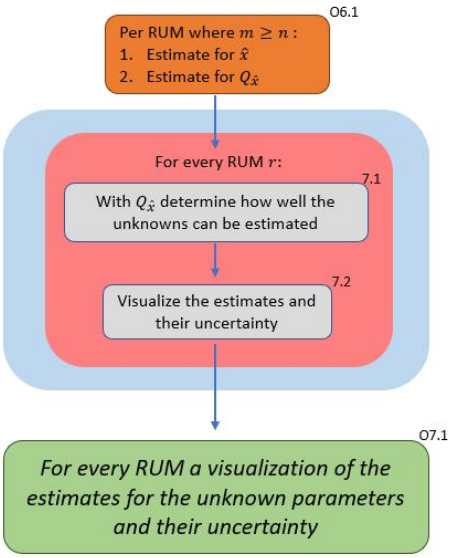

Figure 4.6: Workflow for Module 7: Deformation phenomenon visualization where the estimates for the deformation phenomenon are visualized.

Module 6: RUM parameter estimation
With the output of module 5 and the estimate for the deformation phenomenon, it is possible to loop through all the RUMs and define the functional model that should be used per RUM (step 6.1). A decision should be made about the reference frame that should be used (TLN or ENU) and whether it is possible to assume $d_L = 0$. With the geometry of the observations it is possible to define the design matrix A. Within step 6.2, one should define the Q_{yy} matrix, which consists of the precision of the product (which are, for instance, the LoS observations). With the functional model and Q_{yy}, the system needs to be linearized if the TLN frame is used. With the linearized model and the observations, the next step is to estimate the unknowns with Eq. (3.14) and the iteration scheme as in Fig. **??**. As a last step, in 6.5 we compute $Q_{\hat{x}}$ by using Eq. (3.21). The output for module 6 is an estimate for the unknowns $\hat{x}$ and $Q_{\hat{x}}$. For an overview of module 6, see Fig. 4.5.

Module 7: Deformation phenomenon visualization
The defining question related to the second perspective was, *'What deformation phenomenon can be significantly estimated?'*. The result from module 6 was an estimate per RUM for the unknown parameters and their uncertainty. Within module 7, we try to visualize those results to answer the question related to this perspective. When we observe that the uncertainty for one of the final estimates is low, our conclusion should be that it is impossible to significantly conclude something about the deformation phenomenon from the product, see Fig. 4.6.

4.2.3. Perspective 3: The InSAR service provider

The last perspective reviews the problem from the space segment. On the one hand, the stakeholders within this perspective can be 'value-adding service' providers. These are companies that are using InSAR data to create end products that stakeholders can use. These companies have to meet the product requirements set by their customers. E.g., the stakeholders can require that a particular MDD is always detected with a DP of 80%, or they may ask for a decomposed displacement map where the uncertainty falls below a particular level. The question that such parties typically ask is *"with which (combination) of satellite mission(s) can we meet the product requirements asked by the client?"*

Another category of stakeholders are the data providers, such as space agencies. Space agencies and other space companies providing InSAR satellites want to create missions (or systems) that deliver what is needed and have highest added value. As they want to know what the viewing geometry of a new InSAR satellite should be, they may ask: *"what should be the viewing geometry of a new operating satellite to deliver an InSAR product that has a high added value?"*

Within this perspective we consider the location on Earth, the deformation phenomenon, and the product requirements to be known. We want to state something about the space segment. Module 8 and Module 9 correspond to the space perspective from the value adding services, where module 10 corresponds to the perspective of the space agencies.

Module 8: MDD for different missions
Within module 8, the aim is to select the satellite mission that fits the client's product requirements. Due to the difference in viewing geometry and resolution between different missions, it differs per satellite mission, whether displacements can be detected or not. In step 8.1, Module 2: parameterization of the deformation phenomenon is executed. Afterward, it is needed to loop trough all available satellite missions. Per satellite mission, first the LoS geometry is estimated with Module 1. With the LoS geometry and the parameterization of the deformation phenomenon, the functional model and Q_{yy} are computed with Module 3. Afterward, the MDD for a particular satellite is estimated for a predefined γ (step 8.4). The module's output is a list with values for the MDD and the corresponding satellite mission. When the computed MDDs are compared with the predefined MDDs of the client, the satellite mission can be chosen that satisfies the client's requirements, see Fig. 4.7.

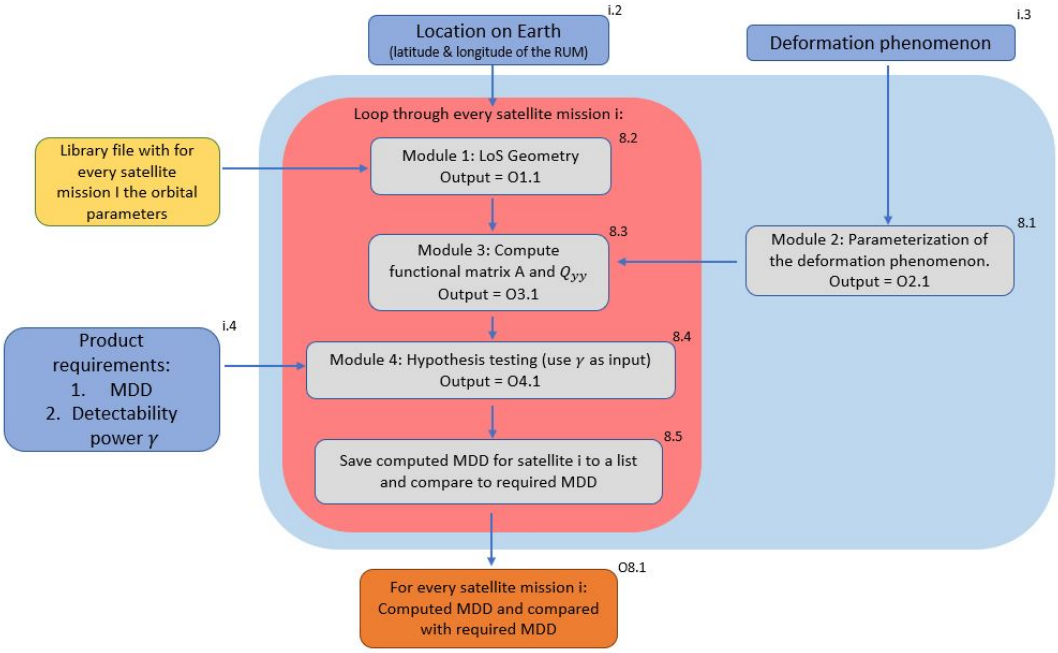

Figure 4.7: Workflow for Module 8: MDD for different missions. The module aims to select the satellite mission that fits the client's product requirements given a particular location on Earth and the deformation phenomenon

Module 9: MDD for combinations of missions
For some cases, to reach higher values for the MDD, combinations of satellite missions are used and needed to monitor displacements. To assess the satellite combination that satisfies the requirements, we can run Module 9. The only difference with module 8 is that Module 9 loops trough combinations of missions instead of missions.

Module 10: New mission design
Within Module 10, a deformation phenomenon at a particular location on Earth is monitored. There are already LoS observations of one (or more) satellite acquisitions available. However, space agencies may be looking for the geometry of a mission under design such that the results for monitoring the deformation phenomenon are optimal, see Fig. 4.8.

The input for module 10 consists of (i) the location on Earth, (ii) the space segment, which consists of the already available satellite observation(s), and (iii) the deformation phenomenon. The first step is to run module 2 to obtain a parameterization of the deformation phenomenon (10.1). Afterward, p potential incidence angles and q potential azimuth angles of the ZDP values are defined (10.2). The next step is to loop trough all angles, resulting in $p \times q$ potential LoS directions. Per potential LoS direction, the design matrix A is defined even as the Q_{yy} matrix with Module 3. In step 10.4, $Q_{\hat{x}}$ is computed with Eq. (3.21) followed by 10.5 where the standard deviation for the estimates for d_T and d_N are computed, and the values are saved in a $p \times q$ matrix. Lastly, we find the potential viewing geometry that provides the smallest standard deviations for the transversal and normal components. This is the optimal viewing geometry for monitoring the deformation phenomenon under consideration and the output for module 10.

4.2.4. Software
Together, all modules that we discuss above form so called 'building blocks' to answer the questions that are asked in the three InSAR perspectives. We also incorporated the modules in software that can answer the InSAR questions. For the software we refer to Appendix F. In Chapter 5 we will test whether the software we created can help in answering the questions asked by the different stakeholders.

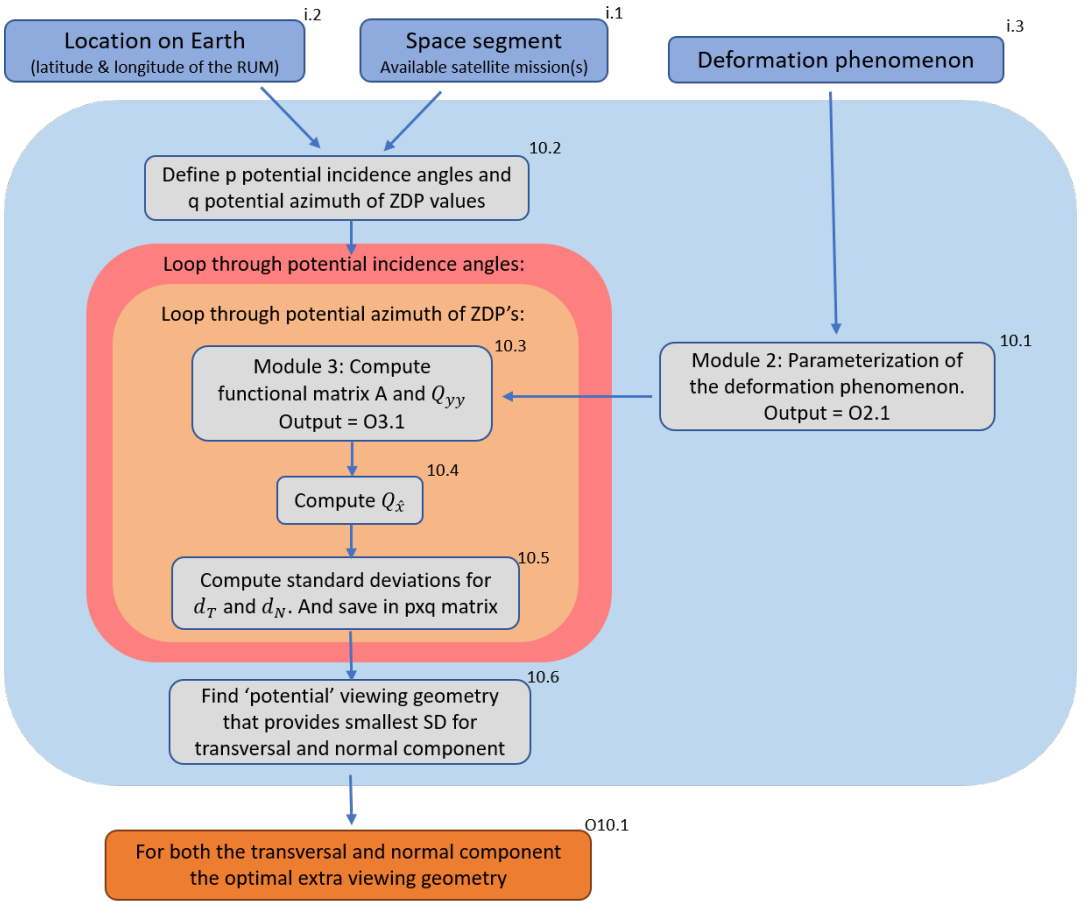

Figure 4.8: Workflow for Module 10: Optimal viewing geometry. The module is used to help space agencies to design a new satellite mission such that the results for monitoring a deformation phenomenon at a particular location on Earth are optimal.

5

Case studies

We performed different case studies related to the three InSAR perspectives as described in Chapter 4. First, in section 5.1 we discuss the perspective of a stakeholder that is considering to use InSAR to monitor the A6 highway in Switzerland. Subsequently, we analyze two deformation phenomena in two existing InSAR products: a subsidence case due to salt production in Groningen, the Netherlands, in section 5.2 and displacements resulting from coal mining after-effects in Limburg, the Netherlands, in section 5.3. This covers the second perspective of extracting information from a pre-existing product. Finally, in section 5.4 we discuss the optimal viewing geometry for monitoring strike-slip motion at faults, which is an example of the perspective of a product or service provider.

5.1. Stakeholder's perspective: A6 highway, Switzerland

We applied the approach for the first perspective at a case study on the A6, a highway that runs between Bern and Thun in Switzerland, see Fig. 5.1. Between the villages Muri and Rubigen, the road runs along a river on sloped terrain, resulting in down-slope displacements that need to be monitored. In this case, the stakeholder wants to know whether it is worth investing in the application of InSAR technology. He is interested in the magnitude of the displacements that can be detected, i.e., the MDDs. To answer the question, we use the workflow, and written software, as described in section 4.2.1.

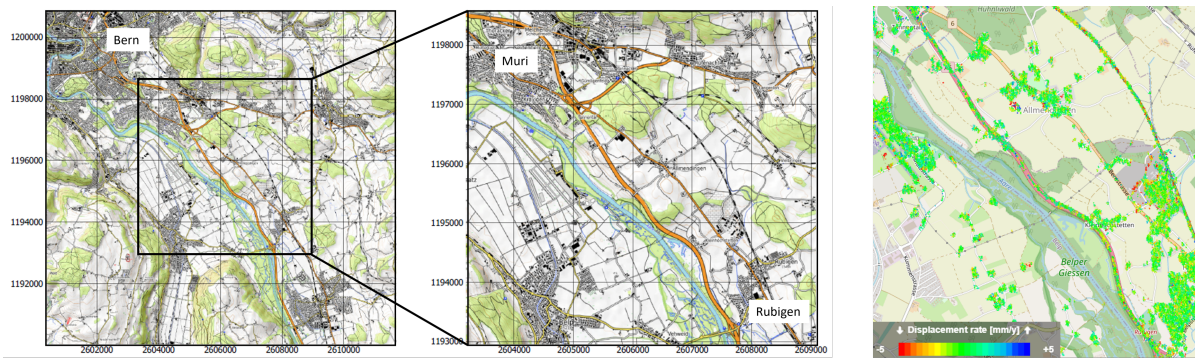

Figure 5.1: The A6 highway between Bern and Thun in Switzerland. Close to the villages Muri and Rubigen, the road runs along the river Aare on a slope. (c) shows InSAR LoS displacements estimated projected onto the vertical obtained over the road with an ascending and an descending acquisition. From the estimates shown in the visualization, no significant displacements can be seen (data from SkyGeo).

Table 5.1: Acquisition details for Sentinel-1 track 15 and track 66 available over the A6 highway between Muri and Rubigen

	Sentinel-1 track 15	Sentinel-1 track 66
Acquisition	ascending	descending
Mean θ	31°	43°
Mean α_d	261°	98°
Start	May 16, 2016	May 20, 2016
End	June 30, 2020	June 28, 2020

5.1.1. Deformation phenomenon and RUMs

Since the road runs along a slope, we assume that it is most likely that the road may deform along the slope with gravity as the main driving force. Thus, we mainly assumed gravity-induced downslope displacements. We use the strap-down approach and use the iso-elevation lines to define the orientation of the TLN frame. The longitudinal direction is directed parallel to the iso-elevation lines and the transversal direction downslope (see section 3.2.1). Since the road has a varying orientation, the orientation of the TLN frame is location-dependent as well. Therefore we need to make sure that we define the RUMs such that the orientation of the frame remains consistent within one RUM. In total we defined 36 RUMs, see Fig 5.2. We used a Digital Elevation Model (DEM) to estimate the value for γ_t (the slope in the transversal direction), and to extract iso-elevation lines which are used to estimate β (the azimuth of the longitudinal direction)[1]. Per RUM, the values for β and γ_t can be seen in Figs 5.2a and 5.2b respectively. We set $\gamma_l = 0°$ for every RUM, meaning that the slope in the longitudinal direciton is 0°. Further we estimated $\sigma_\beta = 7°$, $\sigma_{\gamma_t} = 5°$, and $\sigma_{\gamma_l} = 3°$.

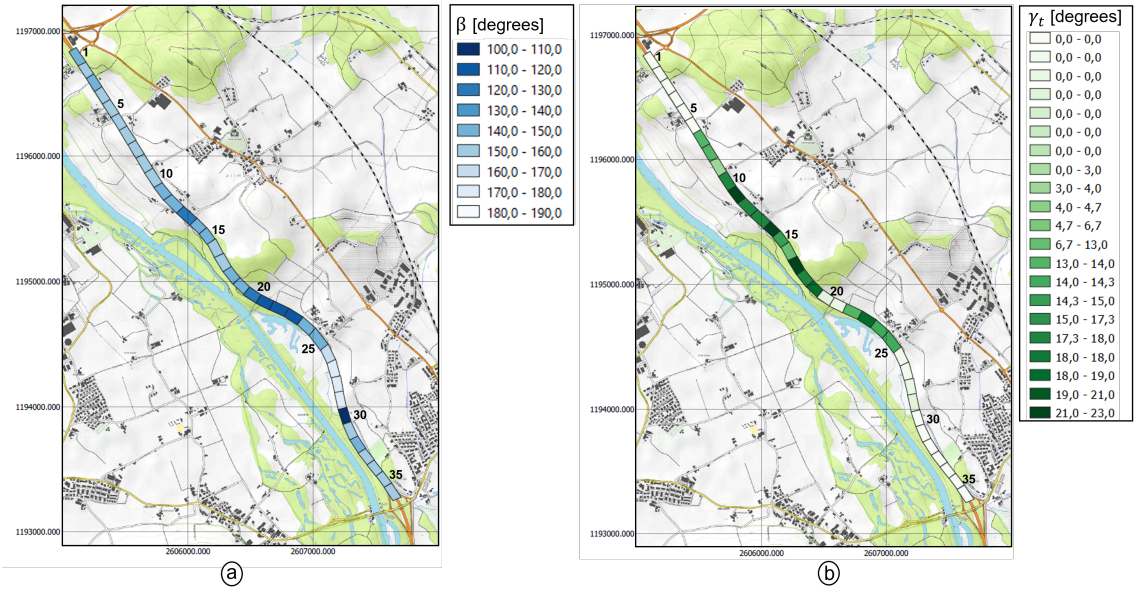

Figure 5.2: The A6 is divided in 36 RUMs, where the DEM is used to determine the orientation of the TLN frame for each RUM. (a) shows the azimuth value β per RUM. (b) shows the slope values γ_t. The value for γ_l was set to 0° for all RUMs, as the road largely follows the iso-heightlines.

5.1.2. Satellite characteristics

Per RUM, there are two unknown parameters (d_T and d_N). Thus, to estimate the MDDs in those two directions, observations from at least two viewing geometries are required. The area is monitored with observations from Sentinel-1 from both an ascending orbit (track 15) and a descending orbit (track 66). In Tab 5.1 we presented the viewing characteristics.

[1] In Fig. 3.1 at p. 37 the definition of the orientation angles for gravity induces downslope displacements can be found

Table 5.2: Relation between the β value of a RUM and estimated MDD in the transversal direction

# RUM	β [degrees]	MDD (transversal direction) [mm]
6	143°	5.4
28	170°	5.2
29	170°	4.1
36	147°	4.9
21	115°	14.9
22	115°	16.8
30	100°	83.4

5.1.3. Minimal Detectable Displacements

To estimate the MDD in the transversal and normal direction, we need to define the null hypothesis for both the displacements in the transversal and the normal direction. We assume that the displacement behavior of every RUM is stable, i.e., we do not expect accelerations or velocity changes in the displacement behavior. With the LoS observations available over the area (Fig. 5.1c), we can estimate the displacement time series in the transversal and normal direction for epochs t_0 until t_m. Based on those time series, we can estimate the mean velocities, and we can predict the displacement value for epoch t_{m+1}. The null hypothesis, i.e. no change in displacement behavior, is defined as in Eq. (3.27) on p. 53, where the predicted value equals the new measurement update. The alternative hypothesis is defined such that there is a change in displacement, see Eq. (3.29).

We can estimate the MDDs with Eq. (3.30) on p. 54, where Q_t is computed with Eq. (3.32). We need to know $Q_{\hat{x}}$ which is defined as:

$$Q_{\hat{x}} = \begin{bmatrix} \sigma^2_{\hat{d}_{T,p}} & 0 \\ 0 & \sigma^2_{\hat{d}_{T,m}} \end{bmatrix}, \tag{5.1}$$

where $\sigma^2_{\hat{d}_{T,p}}$ is the variance of the predicted displacement at epoch t_{m+1} and $\sigma^2_{\hat{d}_{T,m}}$ the variance for the measured value at epoch t_{m+1}.

We can estimate the predicted displacement based on the displacement history of the RUM by estimating the displacement velocity and the initial displacement value. Therefore, the longer the displacement time series, the better the estimate of the velocity and the initial value. Also, the number of scatterers available within one RUM and the noise level of the corresponding LoS displacement times series play a role. First we estimate the mean LoS displacement time series for the ascending and the descending track per RUM. Consequently, we can estimate the displacement in the transversal and normal direction per epoch, using Eqs. (3.9) and (3.10) on p. 47, resulting in displacement time series in the transversal and normal direction. Afterward, we estimate the velocities and the initial values. The more scatterers (and thus LoS displacement time series) available within one RUM, the smaller the noise level of the mean LoS displacement time series and consequently, the smaller the variance of the estimated displacements in the transversal and normal direction and therefore, the smaller $\sigma^2_{\hat{d}_{T,p}}$. Obviously, the exact value of $\sigma^2_{\hat{d}_{T,m}}$ is unknown. However, we can estimate it by computing the noise level of the estimated displacement time series in the transversal or normal direction.

To estimate the MDDs for the transversal and normal direction, we need to define a significance level α (the percentage of false warnings) and the detectability power, γ, which were set to 5% and 90% respectively. The results for the MDDs in both directions can be seen in Fig.5.3. We see that the MDD in the transversal direction depends largely on the orientation angle of β for the TLN frame, see Table 5.2. For β values around 180°, the MDD is smaller, and when β is close to 90°, the MDD is larger. This relation follows from the direction of the null line. For orientations of the TLN frame where $\beta \approx 280°$, the transversal direction is directed almost in the north direction, and therefore, for near polar orbiting satellites, very close to the direction of the null line.

The MDD in the transversal direction also depends on the number of scatterers at the RUM. E.g, RUMs 9 and 10 have high MDDs in the transversal direction: 15.1 mm and 15.3 mm respectively,

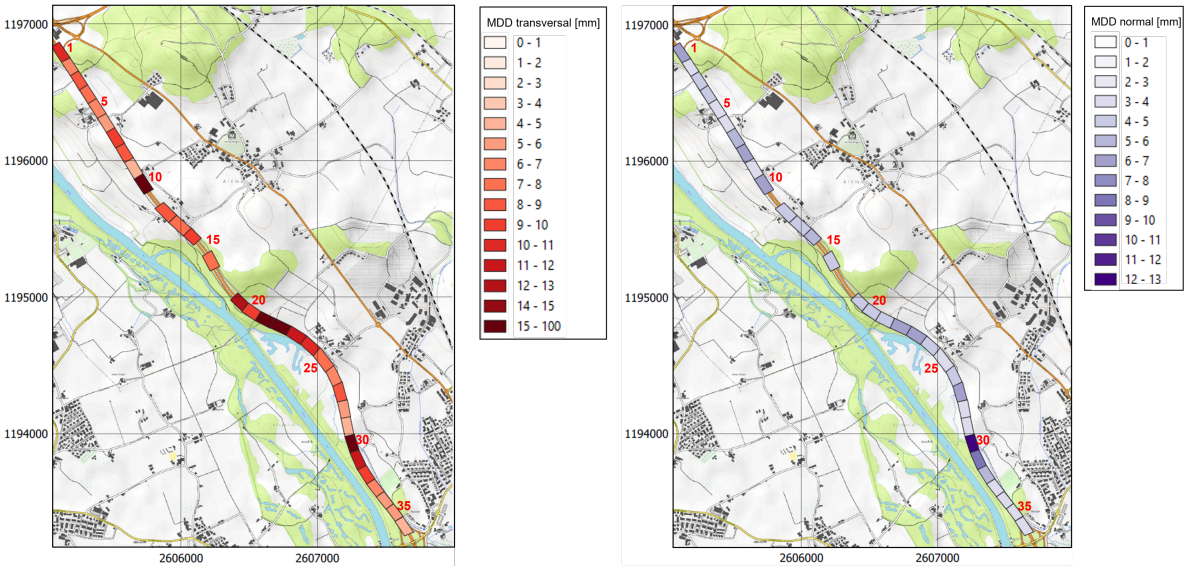

Figure 5.3: The MDDs in the transversal and normal direction per RUM over the A6. A high value, indicates that large displacement needs to occur before the displacement is detected. E.g., a MDD value of 10 mm means that the magnitude of the displacement between to observations epochs (which is 6 days) needs to occur before it can be detected. For RUM 11, 15, 18, and 19 there were no LoS time series available, and therefore it was not possible to estimate the MDD. We found that the value of the MDD for the other RUMs depends on the orientation of the TLN frame, even as the number of available LoS time series.

where $\beta = 146°$ and $\beta = 144°$ respectively. But because there are only 2 and 1 scatterer for the ascending acquisition, respectively, the uncertainty for the estimated normal and transversal displacement time series is high. Therefore, the variance for the predicted observation at t_{m+1} will be high, and consequently, the MDD is high as well.

We can also see that the MDD for the normal direction depends on γ_t. The larger γ_t, the larger the MDD in the normal direction. E.g., for RUMs 22 and 23, the MDDs in the normal direction are 6.7 mm and 6.4 mm, corresponding to slopes of $14°$ and $19°$ respectively. Moreover, we see that for RUM 30, the high value for the MDD results from the unstable solution for that RUM. The MDD for RUM 10 is high due to the low amount of available LoS time series.

5.1.4. Comparison with estimated time-series

From the InSAR LoS displacements estimations (Fig. 5.1c), it seems that there are no significant displacements observed by the satellites. However, the question related to the stakeholder's perspective, is not on getting insight in whether we see 'something' happening. The question is, 'when something *would* happen, are we able to see it?'

So with the displacement time series available over the RUM, we can validate whether the estimated MDDs are reasonable. Since it seems that there are no significant displacements, we would expect that the displacement time series are 'smaller' than the MDD. In Fig. 5.4 we show the estimated time-series for RUM 4 and RUM 25 together with the estimated velocities and the values for the MDDs. For both RUMs, it can be seen that the estimated velocities are low and that both do not show unexpected deformation behavior since the estimated decomposed time series falls in between the MDD range. We computed those figures for all RUMs and found that all RUMs have small estimated displacement rates and none of them had a significantly different behavior from the predicted behavior.

5.1.5. Changing the MDD

In some situations, the stakeholder may like to decrease the MDD. As discussed in section 3.5 at p. 43, multiple parameters affect the size of the MDD: (i) the orientation of the TLN frame, (ii) the standard deviation of the LoS observations, (iii) the viewing geometry of the satellites, (iv) the deformation signal, and (v) the length of the observations time-series. Here we show the effect of changing those param-

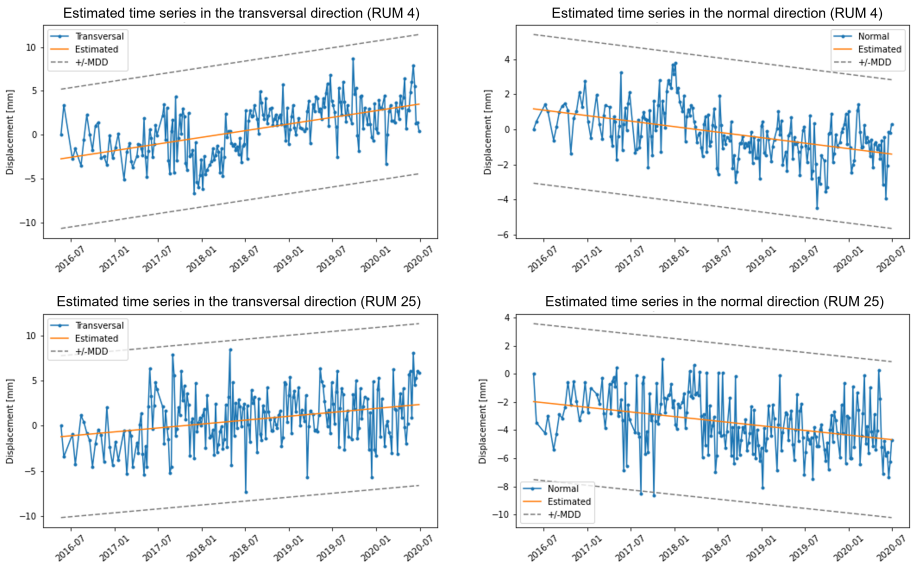

Figure 5.4: Decomposed time series in the transversal and normal direction for RUM 4 and 25. The estimated displacement velocities are shown in orange and the MDD by the striped grey lines. Both RUMs do not show a displacement behavior that differs from the expected behavior.

Table 5.3: RUM characteristics for RUM 27

	Value
$\beta,\ \gamma_t,\ \gamma_l$	$354°,\ 3.2°,\ 0°$
$\sigma_\beta,\ \sigma_{\gamma_t},\ \sigma_{\gamma_l}$	$7°,\ 5°,\ 3°$
$\theta_{\text{asc}},\ \theta_{\text{dsc}}$	$31°,\ 44°$
$\alpha_{d,\text{asc}}\alpha_{d,\text{dsc}}$	$261°,\ 98°$
v_T	-0.8 mm/yr
v_N	-0.7 mm/yr
# observations epochs	210

eters on the MDD. We take RUM 27 as an example, with characteristics as presented in Table 5.3, the MDD in the transversal direction was 8.6 mm, and 6.1 mm in the normal direction. When we change (i) the number of available observations (the epochs), (ii) the uncertainty of the alignment of the frame, (iii) the deformation signal, or (iv) the precision of the observations, we see that the MDD in both directions changes, see Fig. 5.5. Interesting is the figure that shows the MDD as an effect of the number of available epochs. First, we see that having more extended LoS time series is valuable since the MDDs are decreasing. However, when more than 250 observation epochs are available, we see that the MDDs are increasing. This can be understood from the fact that when $v_t \neq 0$ or $v_t \neq 0$, the estimated displacements become larger when having longer LoS time series. We have seen before, that for larger displacement signals the MDDs are larger as well. Moreover, we see that when we enlarge the uncertainty for the frame alignment and the precision of the observations, the MDDs also become larger.

5.1.6. Discussion

One can argue that the case we describe here is not a perfect example of the stakeholder's perspective as described in Chapter4, where we write that the perspective an a priori perspective where no satellite data is available. We have satellite data available in this example, and we estimate the MDDs based on those data. However, we choose to show the results for a case with real data to be able to compare our results with what was observed, see Fig. 5.5. For a situation where the MDDs are used as a metric to decide whether the stakeholder should invest in InSAR, there are a few differences with what we

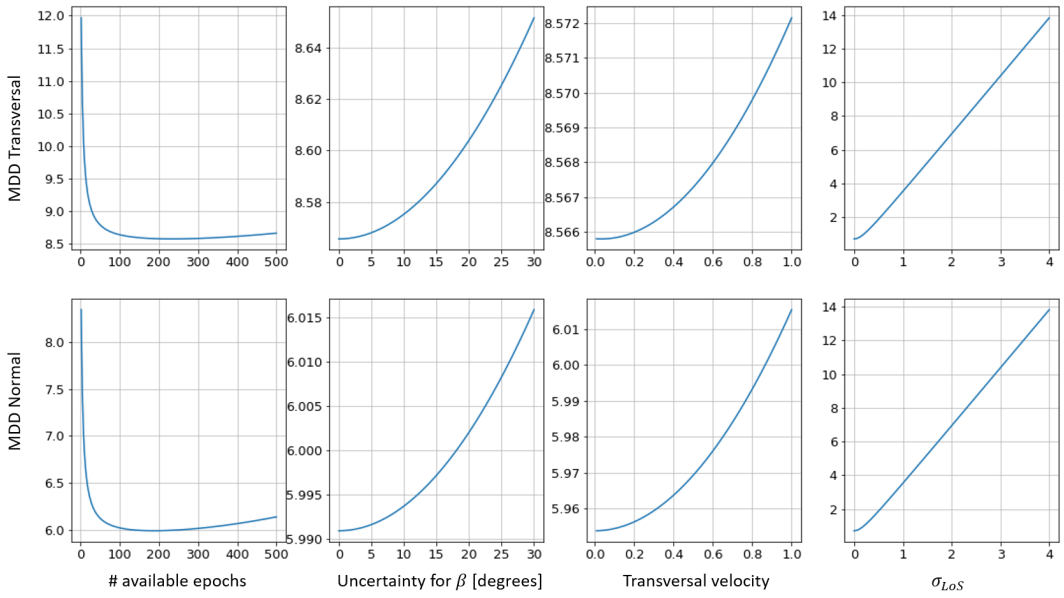

Figure 5.5: The effect of (i) the length of the LoS displacement time series, (ii) the uncertainty for the alignment of the frame, (iii) the displacement velocities and (iv) the precision of the LoS observations on the MDDs in the transversal and normal direction.

have shown here. Obviously, information on the amount of available scatterers and their location and quality is needed to be able to make a quantitative statement on the values for the MDD. An option would be to estimate those values, however that is very difficult. Therefore an existing data set could help.

For the case we described in this section, we estimated the precision for every estimated displacement in the transversal and normal direction per epoch (σ_{d_T} and σ_{d_N}). We estimated those values from the estimated time series in the transversal and normal directions. Another method is to estimate the standard deviation for every available LoS displacement time series per RUM, which we still need to do from the data since the actual values are not known. The next step is to estimate the mean value LoS displacement time series per acquisition, and corresponding uncertainty. Those time series can be used to estimate the precision for $\hat{d}_T$ and $\hat{d}_N$ for every epoch. This method probably gives a smaller standard deviation and is less conservative than the way we did it.

We also have to make an assumption on the occurring deformation phenomenon, where we assume that displacements only occur in the downslope direction. We use the iso-elevation lines for the orientation of the TLN system. However, we are studying a road, so one could argue that we should also consider the deformation phenomenon of the road (line infrastructure) and take the road for the orientation of the TLN system. Nevertheless, for most of the RUMs, the road runs parallel to the iso-elevation lines. Only for RUMs 21 and 29, there is a significant difference in orientation. For these two RUMs, the assumption of zero longitudinal displacements in the direction perpendicular to the slope is probably not valid, and therefore, the estimated MDDs are also less reliable.

5.2. User of a pre-existing InSAR product: Magnesium extracting in Veendam

In Veendam (north of the Netherlands) magnesium is extracted at a depth of approximately 1500 meters. As an undesired consequence, this leads to subsidence, resulting in a subsidence bowl. Wells are injected with water and as a result, the magnesium salts resolve and can be extracted. Through this process, caverns start to form and at locations where the cavern's pressure is lower than the pressure in the surrounding salt layers, salt flows towards to cavern[62]. Resulting in overlaying rock layers moving towards the downwards and to the center, and resulting in a subsidence bowl [62]. The vertical displacements are largest near the center of the bowl, which is at the location of the wells. There are

Table 5.4: Acquisition details for Sentinel-1 track 15 and track 139 available at Veendam

	Sentinel-1 track 15	Sentinel-1 track 139
Acquisition	ascending	descending
Mean θ	36.3°	44.2°
Mean α_d	261°	98°
Start	January 29, 2016	January 14, 2016
End	March 8, 2020	February 16, 2020

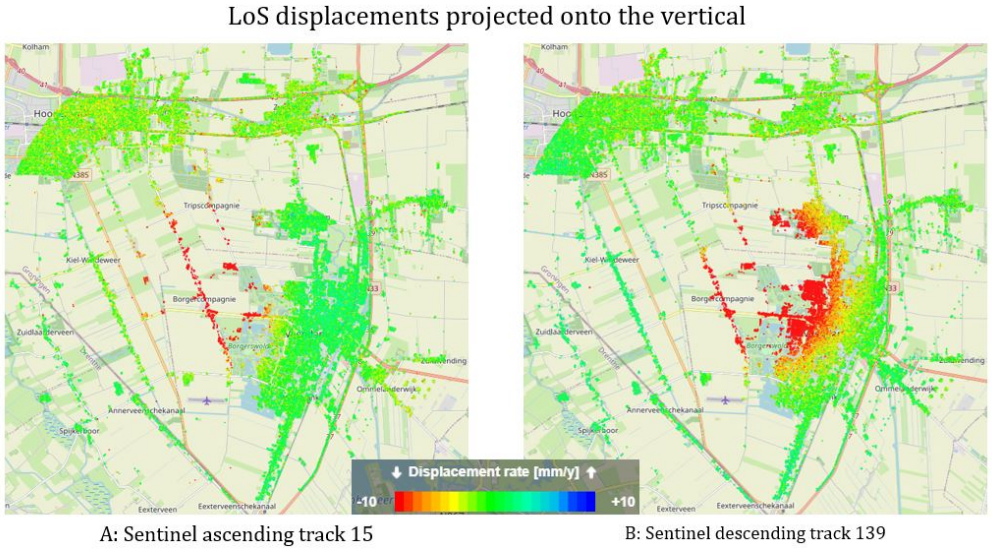

Figure 5.6: LoS displacement rates projected onto the vertical for an ascending and descending track over the subsidence bowl which is a result of the magnesium extraction near Norg, the Netherlands (data: SkyGeo).

also horizontal displacements directed towards the center of the subsidence bowl.

5.2.1. The InSAR product

The area is monitored with Sentinel-1 data from ascending and descending acquisitions, we refer to Tab 5.4 for the acquisition details. The estimated LoS displacement rates projected onto the vertical for both acquisitions are shown in Fig. 5.6. It appears that the location with the most extensive displacement is different for both acquisitions. E.g., Fig. 5.6a shows the results from the ascending acquisition where the location with maximum LoS displacements is located more towards the west compared to the results obtained from the descending acquisition, Fig. 5.6b. This is a first indication for the presence of horizontal displacements [63].

From the two LoS datasets, the vertical and east-west (EW) velocities are also estimated (see Fig 5.7) under the commonly made assumption that 'the north component can be neglected'. This is typically a decomposition error but also an approach that is used a lot in InSAR literature, see section 2.5 at p. 29. We address a few points regarding the results. First, the NS component is simply neglected and not shown, which results in a bias for the vertical component. Second, why would an end-user be interested in the EW component, and not in any other direction?. Obviously the decomposed estimated are not tuned to the needs of the end-user and the complete deformation behavior remains unclear from the EW-Up decomposed results. Third, the choice for the decomposition direction is arbitrary. With the two viewing geometries available, there is also a sensitivity for other directions instead of only the EW and Up direction. The sensitivity may be less, but we argue that that should not be leading for the decomposition direction. Moreover, the figures give no indication of the quality of the estimated parameters, which makes interpretation difficult. And finally, we already have information about the location that we are observing: we know we are looking at a salt mining case, and therefore we know that we have a subsidence bowl, so we know that there is also a NS component.

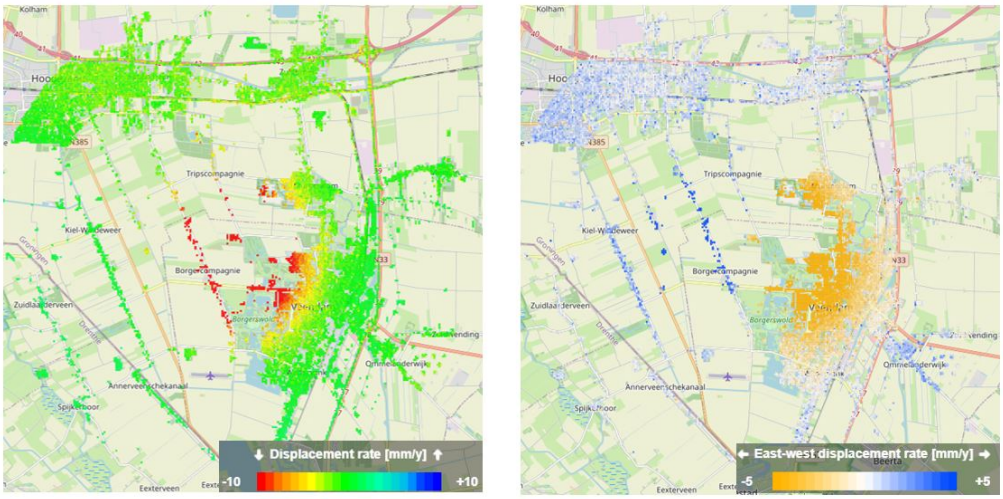

A: Vertical displacement rate B: East-West displacement rate

Figure 5.7: Estimated vertical (A) and east-west (B) displacement rates for the area around Veendam from the two available LoS data sets.

Table 5.5: Angles for β^0 per segment

Segment #	β^0	Segment #	β^0
1	105°	7	285°
2	135°	8	315°
3	165°	9	345°
4	195°	10	15°
5	225°	11	45°
6	255°	12	75°

Nedmag, the company that produces the salt may be interested in the complete deformation phenomenon, with a proper error description. To discover the complete deformation phenomenon we can use the workflow as described in section 4.2.2.

5.2.2. Deformation phenomenon and RUMs

As already described, the deformation phenomenon related to this case is a subsidence bowl, and displacements parallel to the iso-deformation lines are note expected (see section 3.2.2). Thus, we can use the TLN frame and assume $d_L = 0$.

For different locations at the subsidence bowl, the orientation of the TLN frame is different. Therefore, we divided the full subsidence bowl into different RUMs, see Fig. 5.9, and we assumed that all scatterers within one RUM behave according to the same deformation phenomenon. For every RUM, we estimated β^0 (see Table 5.5) and we set $\sigma_\beta = 5°$. We estimated $\gamma_t^0 = 0°$ and $\gamma_l^0 = 0°$ due to the absence of significant topography, and we set $\sigma_{\gamma_t} = 2°$ and $\sigma_{\gamma_l} = 2°$.

5.2.3. Parameter estimation per RUM

We have two unknown parameters per RUM: the displacement velocity in the transversal direction, v_T, and the displacement velocity in the normal direction v_N. With the LoS observations and pseudo-

observations for the orientation angles we have

$$E\{\underbrace{\begin{bmatrix} \underline{v}_{\text{LoS}}^{\text{asc}} \\ \underline{v}_{\text{LoS}}^{\text{dsc}} \\ \underline{\beta} \\ \underline{\gamma_t} \\ \underline{\gamma_l} \end{bmatrix}}_{y}\} = \underbrace{\begin{bmatrix} a_1(x) \\ a_2(x) \\ a_3(x) \\ a_4(x) \\ a_5(x) \end{bmatrix}}_{A(x)} = \underbrace{\begin{bmatrix} p_{1T}v_T + p_{1N}v_N \\ p_{2T}v_T + p_{2N}v_N \\ \beta \\ \gamma_t \\ \gamma_l \end{bmatrix}}_{A(x)} \tag{5.2}$$

$$D\{\underbrace{\begin{bmatrix} \underline{v}_{\text{LoS}}^{\text{asc}} \\ \underline{v}_{\text{LoS}}^{\text{dsc}} \\ \underline{\beta} \\ \underline{\gamma_t} \\ \underline{\gamma_l} \end{bmatrix}}_{y}\} = \underbrace{\begin{bmatrix} \sigma^2_{v_{\text{LoS-asc}}} & 0 & 0 & 0 & 0 \\ 0 & \sigma^2_{v_{\text{LoS-dsc}}} & 0 & 0 & 0 \\ 0 & 0 & \sigma^2_{\beta} & 0 & 0 \\ 0 & 0 & 0 & \sigma^2_{\gamma_t} & 0 \\ 0 & 0 & 0 & 0 & \sigma^2_{\gamma_l} \end{bmatrix}}_{Q_{yy}}, \tag{5.3}$$

where $\underline{v}_{\text{LoS}}^{\text{asc}}$ and $\underline{v}_{\text{LoS}}^{\text{dsc}}$ are the displacement velocities in the LoS direction for the ascending and descending acquisition. The unknowns of the model are $v_T, v_N, \beta, \gamma_t$ and γ_l. The first row in the A matrix is $[p_{1T}v_T + p_{1N}v_N]$ which corresponds to $P_{\text{LoS},1}R_1R_2R_3[v_T, v_L, d_N]^T$, with the component related to the longitudinal direction v_L removed. The last three rows of $A(x)$ correspond to the pseudo-observations for the orientation angles. $D\{.\}$ is the dispersion of the model, where $\sigma^2_{\text{LoS},1}$ and $\sigma^2_{\text{LoS},2}$ are the variances for the estimated LoS displacement rates. σ^2_{β}, $\sigma^2_{\gamma_t}$, and $\sigma^2_{\gamma_l}$ are the uncertainties for the orientation estimates.

The LoS velocities can be estimated from the mean LoS displacements time series per RUM with

$$E\{\underbrace{\begin{bmatrix} \underline{d}_{\text{LoS}}^{(1)} \\ \underline{d}_{\text{LoS}}^{(2)} \\ \vdots \\ \underline{d}_{\text{LoS}}^{(m)} \end{bmatrix}}_{\underline{y}'}\} = \underbrace{\begin{bmatrix} 1 & t_1 - t_0 \\ 1 & t_1 - t_2 \\ \vdots & \vdots \\ 1 & t_1 - t_m \end{bmatrix}}_{A} \underbrace{\begin{bmatrix} d_{LoS}^{(t_0)} \\ v_{\text{LoS}} \end{bmatrix}}_{x} \tag{5.4}$$

$$D\{\underbrace{\begin{bmatrix} \underline{d}_{\text{LoS}}^{(1)} \\ \underline{d}_{\text{LoS}}^{(2)} \\ \vdots \\ \underline{d}_{\text{LoS}}^{(m)} \end{bmatrix}}_{\underline{y}'}\} = \underbrace{\begin{bmatrix} \sigma^2_{\text{LoS},1} & 0 & 0 & 0 \\ 0 & \sigma^2_{\text{LoS},1} & \cdots & 0 \\ 0 & \vdots & \ddots & 0 \\ 0 & 0 & 0 & \sigma^2_{\text{LoS},m} \end{bmatrix}}_{Q_{yy}}, \tag{5.5}$$

where $\underline{d}_{\text{LoS}}^{(1)}$ until $\underline{d}_{\text{LoS}}^{(m)}$ are the mean LoS displacements from epoch 1 until m, $d_{\text{LoS}}^{(t_0)}$ is the unknown initial displacement and v_{LoS} is the displacement velocity in the LoS direction. $\sigma_{\text{LoS},1}$ until $\sigma_{\text{LoS},m}$ are the variances for the mean LoS displacements over the RUM.

Per RUM, we can estimate the velocity in the transversal and normal direction from from mean LoS displacements time series. In Fig. 5.8 the mean LoS displacement time series projected onto the vertical for RUMs D9 and E2 are shown. It can be seen that from January 2016 until March 2018, the displacement can be described by a linear trend. In March 2018, there is an acceleration in the displacement, which stabilizes more or less in August 2018. From August 2018 until the end of the time series, the displacements can again be described by a linear model. Therefore, we decided to estimate the displacement velocities over the period from August 2018 until March 2020.

Since the LoS displacements are not provided with a standard deviation (σ), we assumed that Q_{yy} in Eq. (5.5) equals the identity matrix. Thus, all mean displacement estimates have the same weight. The precision for the estimated LoS velocity $\sigma^2_{v_{\text{LoS}}}$ can be estimated by computing the residuals between the LoS observations and the estimated linear trend. With the velocities and corresponding precision for both acquisitions per RUM, it is possible to estimate the velocity in the transversal v_T and normal v_N direction with Eq. (5.2). With $Q_{\hat{x}} = (A^T Q_{yy}^{-1} A)^{-1}$ we can estimate the precision of both velocities.

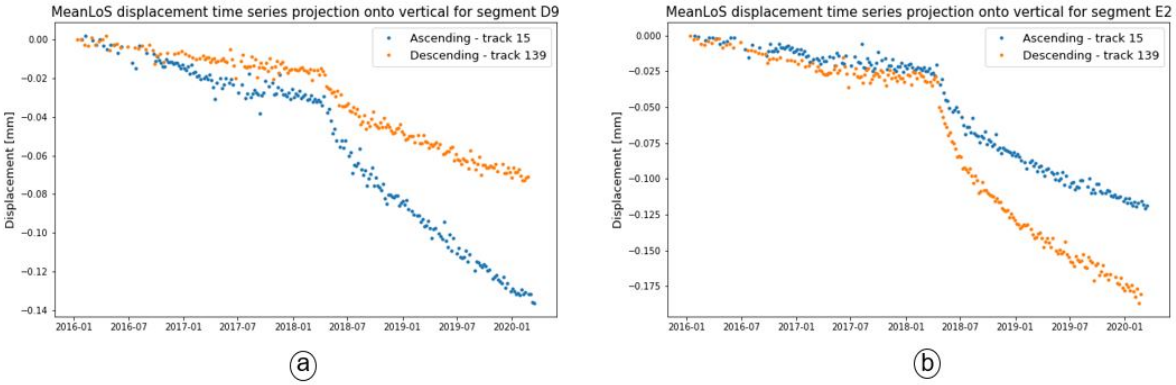

Figure 5.8: Mean LoS displacements rates projected onto the vertical for RUM D9 (a) and RUM E2 (b). In March 2018 an acceleration in the LoS displacements rates takes place which stabilizes more or less in August 2018.

5.2.4. Final results

In Fig. 5.9 the estimated velocities in the transversal (centripetal) and normal (near vertical) direction can be seen. For RUMs A4, A6, A7, and A8, only observations from one viewing geometry were available and we were not able to estimate the transversal and normal velocities. It can be seen that indeed the largest vertical displacements occur at the center of the subsidence bowl. We also found that all displacements are directed towards the center of the bowl, excepting RUM D12. At the center of the bowl, we found significant vertical displacements up to 40 mm/yr. When we compare those results with the results from the the east-west-up decomposition (Fig 5.7), we argue that we convey significantly more intelligible information, including the uncertainty estimates. Moreover, using the strap-down approach and the concept of RUMs resulted in figure where we could show both the vertical as well as the horizontal displacements. With this approach we were able to give a three dimensional representation of the full deformation phenomenon with only one figure.

To give good proper geodetic results, we also need to add uncertainties, what we did by adding error ellipses for the transversal component and error bars for the normal component. The short axis of the ellipse follows from error propagation given the uncertainty in the orientation of the frame. The long axis of the ellipse gives the uncertainty for the estimated transversal displacements. Immediately we can see that the estimates for the transversal components that are in the NS direction are less reliable compared to the estimated transversal displacements that are in the east direction, which follows from the near-polar orbit of Sentinel-1. For some RUMs, transversal displacement vector is situated entirely in the 2σ confidence error ellipse.

5.2.5. Discussion

The most significant discussion point here is whether we defined the RUMs the optimal way. In our approach, we divided the subsidence bowl into equal segments. However, to optimally estimate the displacements corresponding to the deformation phenomenon, it may probably be more optimal to define the RUMs based on the number of available observations. For locations with many observations, as is the case in the city of Veendam, the RUMs could be made smaller to map the deformation phenomenon optimally.

5.3. User of a pre-existing InSAR product: Coal mining after-effects near Brunssum

Because of the coal mining history in Limburg, there are some after-effects present in Limburg. There are three main effects, (i) differential ground heave induced by rising mine water, (ii) potential ground instability as the failure of a shaft may cause subsidence of a sinkhole, and (iii) at the near-surface mine voids, the hanging wall can collapse into the mine void [64]. Heitfeld et al. [64] document three major ground heave zones (based on InSAR data), where one of the zones is situated near Brunssum

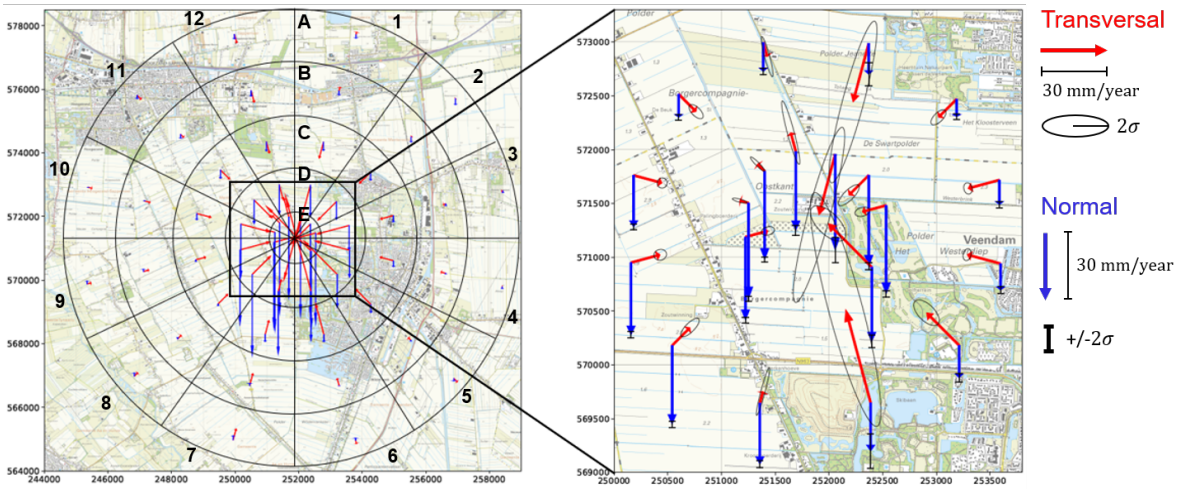

Figure 5.9: Results for strap-down approach at a subsidence bowl which is the result of magnesium extraction at Norg. The red arrows represent the estimated displacement velocities in the transversal direction (near horizontal), and their uncertainty is visualized by an ellipse. The blue arrows are the displacement velocities in the normal direction (near vertical), which have an error bar.

Table 5.6: Acquisition details for Radarsat-2 track 109 and track 302

	Radarsat-2 track 109	Radarsat-2 track 302
Acquisition	ascending	descending
Mean θ	37.3°	33.4°
Mean α_d	259.2°	100.9°
Start	December 14, 2016	December 4, 2016
End	September 12, 2020	September 26, 2020

along the Feldbiss fault. Within this case study, we have a closer look at the displacements near the Feldbiss fault in Brunssum caused by the rising mine water, see Fig. 5.10.

5.3.1. The InSAR product

The area around Brunssum is monitored with an ascending and a descending acquisition from Radarsat-2, see Tab 5.6 for the acquisition details. The estimated LoS displacement rates projected onto the vertical for both acquisitions are shown in Fig. 5.11. Around the Feldbiss fault, the two acquisitions show different results for the projected LoS displacements onto the vertical, indicating significant horizontal displacements.

With the observations from the two acquisitions, the vertical and EW velocities are also estimated while neglecting the displacements directed into the north, resulting in biased estimates (due to the decomposition error, see section 2.5 at p. 29). Nevertheless, the (biased) estimated vertical, and EW displacement rates are presented in Fig. 5.12a and b, respectively. It seems that the area is moving upward at the southwest side of the fault, while at the northeast side, it seems that the vertical displacements are minimal. When we review the estimated EW displacement rates, the interpretation of the signal is too ambiguous, especially for a non-export stakeholder. This lack of intelligible information is a consequence of the choice of the visual representation, rather than a lack of meaningful observations.

5.3.2. Deformation phenomenon and RUMs

From the LoS displacement estimates and the (biased) decomposed estimates, we hypothesize that the surface moves upward southwest of the Feldbiss fault. We also hypothesize that the horizontal displacements are directed away from the fault, rather than parallel to the fault, since the driving mechanism is most likely related to the redistribution of subsruface water pressure. There is no in-

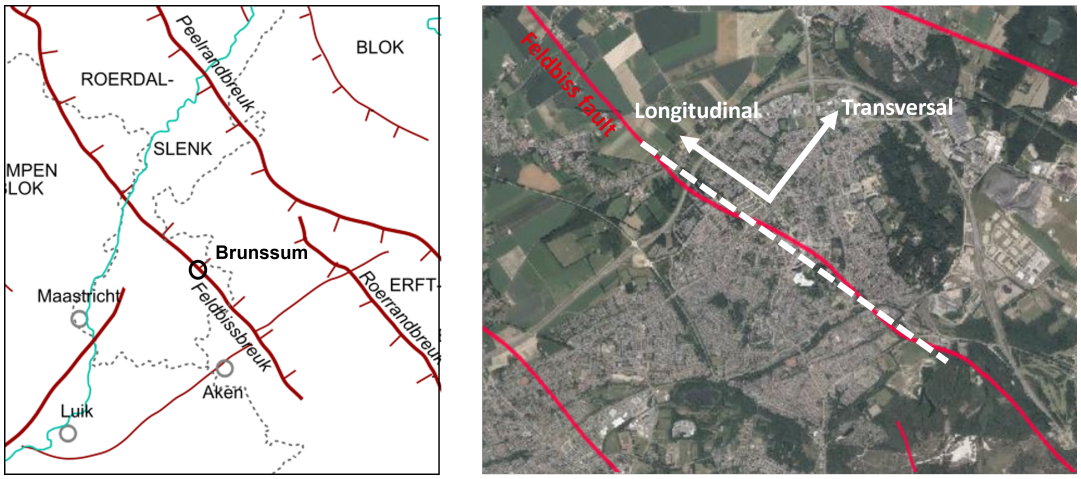

Figure 5.10: Left: the Feldbiss fault runs approximately northwest to southeast through Limburg. Source: [65]. Right: The alignment of the TLN reference system for displacements around the Feldbiss fault near Brunssum. The longitudinal axis is parallel to the fault and the transversal direction perpendicular to it. Since the two sides of the fault move away, we can assume that there are no longitudinal displacements. The normal direction is near vertical.

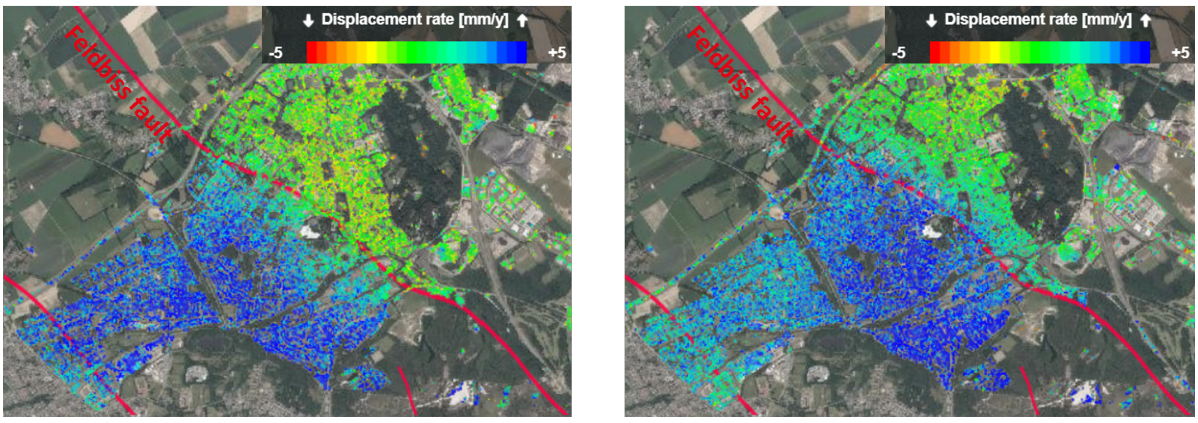

A: Ascending data

B: Descending data

Figure 5.11: Estimated LoS displacement rates projected onto the vertical for an ascending (a) and descending (b) track over the area of Brunssum in Limburg, the Netherlands. The feldbiss fault runs trough the midle of the city from approximately north-west to south-east (data: SkyGeo).

dication to assume a strike-slip component parallel to the fault direction. Therefore, we can use the strap-down approach, where the longitudinal axis is defined parallel to the Feldbiss fault. We assume that there are no longitudinal displacements, see Fig. 5.10.

We assume that the whole area for Brunssum shows the same behavior and that the orientation of the TLN frame is the same everywhere. Therefore we divide the area into grid cells of 70×70 meter were we estimate that $\beta^0 = -55°$ and $\gamma_t^0 = \gamma_l^0 = 0°$, and we set $\sigma_\beta = 10°$ and $\sigma_{\gamma_t} = \sigma_{\gamma_l} = 5°$ for every grid cell.

5.3.3. Parameter estimation

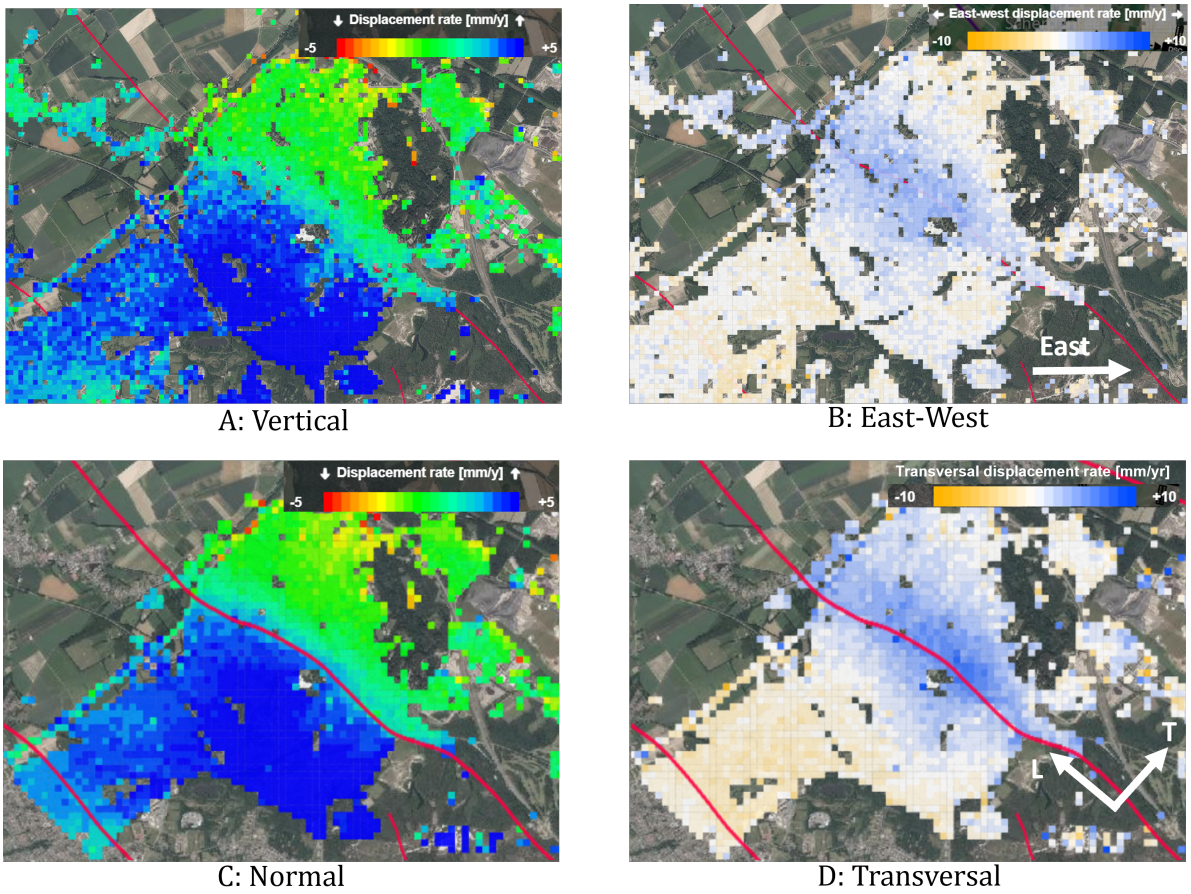

A: Vertical B: East-West

C: Normal D: Transversal

Figure 5.12: Estimated decomposed displacement rates for Brunssum. A and B show the biased vertical and EW displacements rates (estimated while neglecting the NS displacements). A blue value in figure B indicates an eastbound motion and orange a westbound motion. C and D show the estimated normal and transversal displacement rates estimated with the strap-down approach. A blue value in C means that there is an upward motion. A blue value in D means that there the displacements in the transversal direction are positive and an orange value means a negative transversal displacement.

Per grid cell (i.e., RUM), the workflow is as follows:

1. Estimate the mean LoS displacement rate for both the ascending and descending acquisition
2. Estimate σ_{LoS} for both the ascending and descending acquisition by estimating the spread of the LoS displacement rates around the estimated average value.
3. Compute the mean incidence angles and azimuth angles of the ZDP per acquisition.
4. Solve for the unknown normal and transversal displacement rates using Eqs. (5.2) and (5.5). The system of equations needs to be linearized.

The estimated transversal and normal displacement rates per grid cell are shown in Fig. 5.12c and d. At the southwest, we find positive normal displacements, meaning that the area moves upward relatively, which is in line with expected vertical displacements [66]. At the norteast, the normal displacements are almost zero but there are significant transversal displacements. Northeast of the fault, we see positive transversal displacements, while at the southwest of the fault, the transversal displacements are negative, meaning that the two sides of the fault move away.

Moreover, we find that the largest transversal displacements are ≈ 6 mm/yr. Since the length of the displacement time-series has a length of almost four years, the total displacement (over four years) is approximately 2.3 cm. With the width of the area with the largest transversal displacements being 400 m, the results in approximately 23 micro-strain, which is quit significant.

When we compare the decomposed estimates with the vertical and EW displacements rate, we can state that the strap-down results are much better interpretable. Especially for the estimated horizontal components. Based on the estimated EW components, the magnitude of the horizontal displacements seems smaller compared to the estimated horizontal dispacements from the strap-down approach. Thus, the estimated EW displacements are actually an underestimation of the horizontal displacements which can be unfavorable.

5.4. The InSAR service provider: Monitoring displacements near strike-slip faults

Around fault zones, large displacements may occur. This section discusses the optimal viewing geometry to monitor displacements at the North Anatolian Fault (NAF) in Turkey and the San Andreas Fault (SAF) in North America. Both faults are strike-slip faults, which means that both sides of the fault move horizontally relative to each other in opposite directions, see Fig. 5.13. Displacements are assumed to occur only parallel to the fault. When the TLN frame is used, the transversal direction is directed along the fault and the longitudinal direction perpendicular to the fault. For strike-slip faults, we can therefore assume that $d_L = 0$.

Within this section, we study the problem from the perspective of product providers, such as space-agencies, who are particularly interested in answering the following question: *"What should be the viewing geometry of a new satellite mission to deliver an InSAR product that has a high added value?"*. Note that we do not limit ourselves to feasible orbits and look angles, as we focus on the optimal geometry.

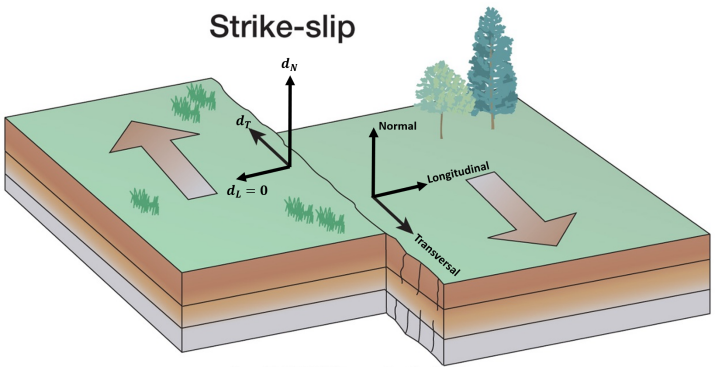

Figure 5.13: At a strike-slip fault, both sides of the fault move horizontally in opposite directions. The TLN frame is aligned such that the transversal direction is along the fault and longitudinal direction is perpendicular to the fault direction, therefore $d_L = 0$, [67].

5.4.1. North Anatolian Fault

The North Anatolian Fault (NAF) is a 1200 km long fault that runs along the northern part of Turkey. It separates the Eurasian and Anatolian plates. The East Anatolian Fault (EAF) is the separation between

Table 5.7: Viewing geometry of the available Sentinel-1 acquisitions at the NAF

	θ	α_d
Ascending 1 (A1)	31.8°	259.1°
Ascending 2 (A2)	42.7°	260.4°
Descending 1 (D1)	34.8°	100.6°
Descending 2 (D2)	45.1°	99.3°

the Anatolian plate and the Arabian plate. Due to the motion of the Arabian plate, which is northbound, the region of Anatolia moves westward relative to Eurasia, resulting in a right-lateral strike-slip fault motion along the NAF, see Fig. 5.14. Due to the large displacements and potential earthquakes, it is crucial to monitor the displacements.

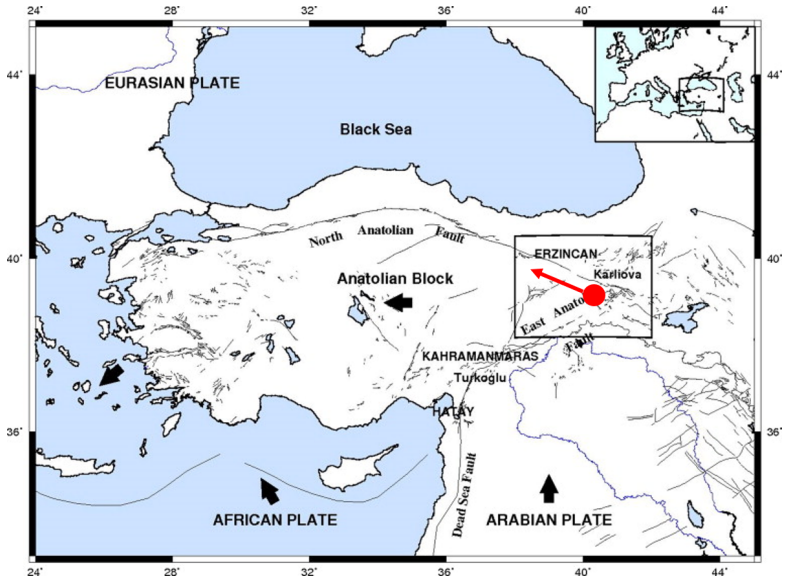

Figure 5.14: The NAF seperates the Eurasian and Anatolian plates and runs along the northern part of Turkey. The red dot is the location under consideration close to Karliova, which moves in the transversal direction. Figure from [68]

Here we focus on a location close to Karliova at a latitude of 39.215°and a longitude of 40.515°, see Fig. 5.14. At this location, four Sentinel-1 satellite acquisitions are available, see Table 5.7. We are interested in the optimal viewing geometry to add for this particular case? To answer that question, we can use the workflow as described in section 4.2.3.

We first need to align the TLN reference frame at the location. Ozener et al. [68] monitored the area with a GPS campaign and found that the motion near Karliova is -18.00 mm/yr towards the east and 5.45 mm/yr towards the north. We can therefore use $\beta^0 = \tan^{-1}(-v_n/v_e) + 180° = 196.8°$. Moreover, $\gamma_t^0 = 0°$ and $\gamma_l^0 = 0°$, and we estimate $\sigma_\beta = 7°$, and $\sigma_{\gamma_t} = \sigma_{\gamma_l} = 5°$.

We first consider the situation when only ascending acquisition A1 is available and we investigate what would be the viewing geometry of a new satellite mission such that the results for monitoring displacements around the fault are optimal. We constrained that $\alpha_d \in [0°, 360°)$ and $\theta \in [10°, 80°]$, although we know that some values within those ranges are not feasible. For both the available ascending acquisition and the new, non-existent mission, we assumed that $\sigma_{\text{LoS}} = 1$ mm, i.e., the LoS observations from both missions have a standard deviation of 1 mm.

To estimate the optimal additional viewing geometry, we define potential values for θ and α_d and loop trough all possible combinations. One combination of θ and α_d gives the viewing geometry for the additional mission which we can use to estimate $Q_{\hat{x}}$ with Eq. (3.21), since the viewing geometry of the existing geometry is also known. Consequently, we can estimate the uncertainties for $\hat{d}_T$ and $\hat{d}_N$ from

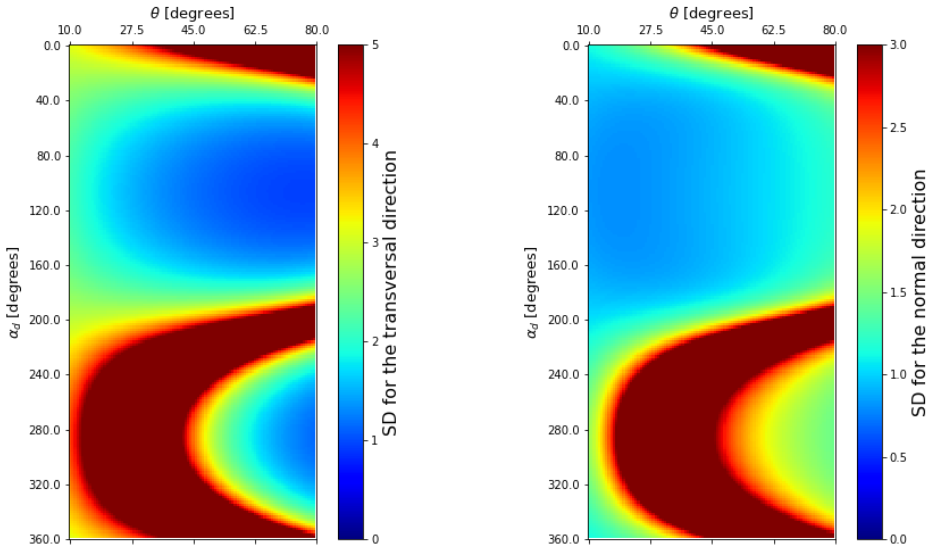

Figure 5.15: Estimated standard deviations for the transversal and normal displacement component when a potential viewing geometry is combined with ascending acquisition A1. The horizontal axis represents potential values for the azimuth angle of the ZDP. The vertical axis contains possible incidence angles. The optimal viewing geometry differs per direction that should be monitored.

the diagonal elements. To estimate $Q_{\hat{x}}$, we first need estimates $d_{T,0}$ and $d_{N,0}$, which we set to $d_{T,0} = 1$ and $d_{N,0} = 1$ since we are only interested in relative improvements for the precision for d_T and d_N.

In Fig. 5.15 the estimated standard deviations for the transversal and normal displacement components are visualized for all potential viewing geometries of the new mission in combination with the existing ascending acquisition A1. The optimal viewing geometry differs per displacement direction. For the transversal direction, we find that the optimal viewing geometry has incidence angle $\theta = 77.2°$ and the azimuth of the zero-Doppler plane is $\alpha_d = 106.7°$. Obviously, the optimal θ is large since the more the radar looks under an angle, the more the LoS is directed into the transversal direction. From Fig. 5.15 it can also be seen that when the viewing geometry of the new acquisition has the same geometry as A1, the standard deviations for both the transversal and normal direction become large. We find that the optimal viewing geometry for monitoring the normal direction results in $\theta = 17.8°$ and $\alpha_d = 106.7°$, so the same azimuth angles of the ZDP as for the transversal component but now a smaller incidence angle. It is interesting to observe that the optimal viewing geometries almost have an azimuth angle of the ZDP value that corresponds to a near-polar orbiting satellite.

Since multiple acquisitions are available, we can also estimate optimal viewing geometries for combinations of acquisitions. Since we are mainly interested in monitoring displacements in the transversal direction, we selected the optimal viewing geometry based on this direction, see Table 5.8 for the results. It can be seen that when also descending acquisitions are available the optimal viewing geometry has a different α_d compared to combinations where more ascending acquisitions are available. Actually, the estimated α_d corresponds to a left looking satellite in a near-polar orbit. With observations from A1 and an optimal geometry, the results are better compared to the case where we only have observations from excising acquisitions A1, A2 and D1. This can be seen by the smaller values for the standard deviation for the first case as presented in Tab. 5.8.

We also estimated the standard deviation for the transversal direction for the cases with five ascending acquisitions and five descending acquisitions. We let the azimuth angle of the ZDP for the ascending acquisitions vary from $259.05°$ to $260.38°$ and with the correlation between θ and α_d we can estimate the corresponding incidence angles, see Appendix B. For the descending acquisition α_d runs from $100.59°$ to $99.27°$. When those ten acquisitions are combined, we find that the standard deviation for the transversal direction is 0.58 mm.

Table 5.8: The optimal viewing geometries estimated for a combination of available acquisitions. The standard deviation for the transversal component before the optimal viewing geometry and with the optimal viewing geometries are shown.

Available mission(s)	standard deviation $\hat{d}_T$ [mm]	Optimal θ	Optimal α_d	standard deviation $\hat{d}_T$ (with optimal) [mm]
A1	–	77.2°	106.7°	0.95
A1 & D1	1.38	80°	287.64°	0.82
A1, A2 & D1	1.11	80°	106.7°	0.74
A1, A2, D1 & D2	0.87	80°	287.6°	0.66

Table 5.9: Viewing geometry of the available acquisitions at the SAF

	θ	α_d
Ascending 3 (A3)	37.4°	259.7°
Descending 3 (D3)	37.9°	100.2°

5.4.2. San Andreas Fault

For the San Andreas Fault (SAF), it is possible to do the same analysis. The major difference with the NAF is the orientation of the fault and location on Earth. For the analysis, we study the area around Point Reyes, just north of San Fransico, see Fig. 5.16. The latitudinal coordinate is 38.06°, and the longitudinal coordinate is −122.80°. The SAF, like the NAF, is a right-lateral strike-slip fault where at the west side of the SAF, the relative motion of the Pacific plate is northbound and at the east, the relative motion of the North American plate is southbound.

With DRaMA [19], we can compute the viewing geometry of the available Sentinel-1 acquisitions at Point Reyes. Two acquisitions are available: one ascending (A3) and one descending (D3), see Table 5.9. For different (combinations of) acquisitions, we investigate what what would be the viewing

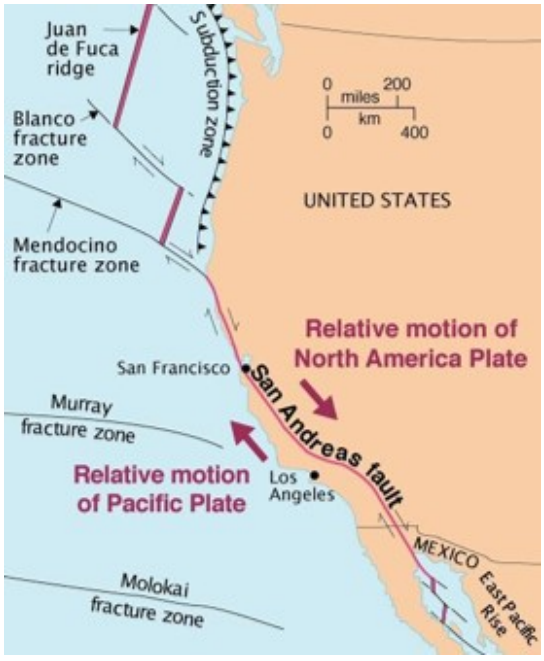

Figure 5.16: The SAF is a strike-slip fault. At the left of the SAF, the Pacific Plate has a relative northward motion, where at the right of the SAF the North American Plate as a relative southward motion. After [69]

geometry of a new satellite mission such that the results for monitoring displacements around the fault are optimal. First, we estimate the optimal viewing geometry of a new mission when we only have one ascending acquisition (A3). Again, the orientation of the TLN frame is needed. At point Reyes,

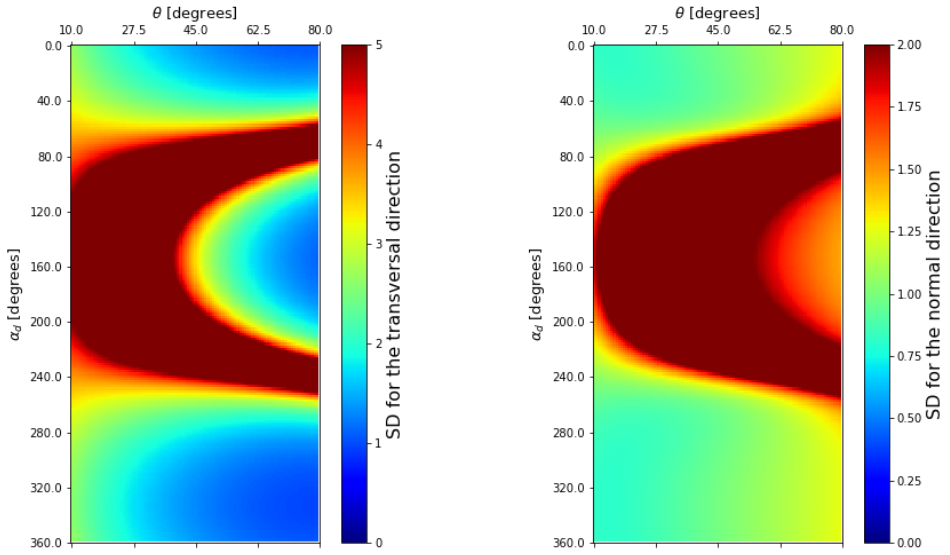

Figure 5.17: Estimated standard deviations for the transversal and normal displacement component when a potential viewing geometry is combined with ascending acquisition A3. The optimal viewing geometry differs per direction that should be monitored.

the fault runs from north-northwest to south-southeast, and therefore, we estimate $\beta^0 = 65°$. Again $\gamma_t^0 = \gamma_l^0 = 0°$ and $\sigma_\beta = 7°$ and $\sigma_{\gamma_t} = \sigma_{\gamma_l} = 5°$. The optimal geometry is estimated from the geometry that provides the smallest standard deviation for the unknown displacement components. We assume that σ_{LoS} for both the available acquisitions and the estimated optimal acquisitions equals 1 mm. We set $d_{T,0} = d_{N,0} = 1$ mm. The results for the standard deviations for the transversal and normal component for all potential viewing geometries are presented in Fig. 5.17.

As for the NAF, we also find for the SAF that the optimal incidence angle θ for monitoring the transversal component is large (80°). The optimal azimuth of the zero-Doppler plane α_d is in the direction of the SAF and is 155°. This corresponds to a satellite that has an inclination of approximately 25°. From Fig. 5.17 it can further be seen that a satellite that has $\alpha_d \approx 75°$ and $\alpha_d \approx 245°$ provides bad results, those angles correspond to right-looking near-polar orbiting satellites. For the normal direction, we again find that the optimal incidence angle is small: 10°.

We can also estimate the optimal viewing geometry of a new mission when there are aleardy multiple acquisitions available, see Table 5.10 for the estimated optimal viewing geometry that should be added. It can be seen that there is a major improvement when going from two existing acquisitions (A3 and D3) to a situation where there is only one existing acquisition and a new mission. The standard deviation for the transversal direction is more than halved.

We also study the imaginary case where there were already observations from five ascending acquisitions (from a near-polar orbiting satellite) and five descending observations. We varied the azimuth angles of the ZDP for the ascending acquisitions from 259.1°to 260.4°, and we estimated the corresponding incidence angles. The azimuth angles of the ZDP for the descending acquisitions were ranging from 99.7°to 100.6°. With those ten acquisitions, the standard deviation for the transversal component was 0.6 mm. So there is an improvement in the standard deviation compared to the case where we have A3, D3, and optimal viewing geometry.

Also, for monitoring displacements in the transversal direction, the SAF orientation is worse than the orientation of the NAF. For the SAF, the transversal direction is directed towards the north, where it is eastward for the NAF. Therefore, we see that when two Sentinel-1 acquisitions are combined, we find a value for the standard deviation for the NAF of 1.38 mm (based on A1 and D1). For the SAF, we find σ_T = 2.4 mm (based on A3 and D3), which is much worse. However, when we combine one ascending acquisition with the optimal viewing geometry for both cases, we find approximately the same values for the standard deviation, 0.95 mm, and 1.0 mm for the NAF and SAF, respectively. So we find a more

Table 5.10: The optimal viewing geometries estimated for a combination of available acquisitions for the SAF.

Available mission(s)	standard deviation $\hat{d}_T$ [mm]	Optimal θ	Optimal α_d	standard deviation $\hat{d}_T$ (with optimal) [mm]
A3	–	80°	155.6°	1.0
D3	–	80°	334.7°	0.97
A3 & D3	2.4	80°	334.7°	0.95

Table 5.11: The optimal viewing geometries estimated for a combination of available acquisitions for a strike-slip fault running perfectly north south.

Available mission(s)	standard deviation $\hat{d}_T$ [mm]	Optimal θ	Optimal α_d	standard deviation $\hat{d}_T$ (with optimal) [mm]
A3	–	80°	0°or 360°	1.1
D3	–	80°	0°or 360°	1.1
A3 & D3	1550.5	80°	334.7°	1
3 asc & 3 desc	0.9	–	–	–
5 asc & 5 desc	0.62	–	–	–

significant improvement for the SAF.

5.4.3. More observations vs optimal viewing geometry

To bring a new mission into operation, one may need to opt for either putting more satellites into near-polar orbit or putting several satellites into other special orbits. An argument for the first option is that the complete Earth can be studied with a near-polar orbiting satellite. However, we have seen that acquisitions in special orbits can significantly improve the precision of the estimated parameters. Moreover, there is no single best outcome to the above dilemma. The preferred option depends on the case which we will show with an example.

For a strike-slip fault that runs north-south, the transversal direction is also north-south directed. Thus for the TLN frame we have $\beta = 90°$ and $\gamma_t = \gamma_l = 0°$. If we further assume that the same acquisitions as for the SAF are available, see Table 5.9, and that $\sigma_\beta = 7°$ and $\sigma_{\gamma_t} = \sigma_{\gamma_l} = 5°$ we can again estimate optimal viewing geometries.

When we combine acquisition A3 with D3, this results in a high standard deviation for the transversal displacement component. We find σ_T = 1550.5 mm. However, when we only have acquisition A3, and we look for the optimal viewing geometry, we find $\theta = 80°$ and $\alpha_d = 0°$ or $\alpha_d = 360°$ resulting in σ_T = 1.1 mm. We see that we have a significant improvement with the optimal viewing geometry, whereas we have the same number of observations as with A3 and D3 only, see Table 5.11.

We can also look at the optimal viewing geometry that should be added when we have observations from three ascending and three descending acquisitions, with the same range for the azimuth angle of the ZDP as for the NAF. This results in a standard deviation of 0.9 mm, so in the same order of magnitude as A3, D3, and an optimal geometry. When we have five ascending and five descending acquisitions, the precision is improved to 0.62 mm.

When we compare the result to the NAF (where the transversal direction is almost in the EW direction), we can state that it depends on the situation whether it is preferred to add an optimal satellite or that the satellites available are already sufficient. For the NAF, the current viewing geometries are already in the right direction. When the results should be improved, it is helpful to add more observations by adding more satellites in the same orbit.

When deformation phenomena with the transversal direction directed NS are monitored, it is best to

add one satellite in a particular optimal orbit. We have seen that adding one satellite in an optimal orbit provides the same results as adding two ascending and two descending acquisitions.

5.4.4. Discussion

To estimate the optimal viewing geometries, we look for the viewing geometry that results in the smallest value for the standard deviation for the transversal and normal displacement components. To estimate the standard deviations we use Eq. (3.21), where Q_{yy} is needed, which contains σ^2_{LoS}, the variances of the LoS observations. We set σ^2_{LoS} for all acquisitions to 1. Obviously, those values are, not real values but estimated standard deviations. However, when we want to know the optimal viewing geometry, this is fine since we are only interested in the geometry that results in the smallest standard deviation for the transversal and normal displacement components and not in the absolute values.

To be able to compute the standard deviations we also need to provide initial estimates for the displacements since the standard deviations become larger for larger displacements, see section 3.5. Because both transversal and normal displacements may occur, we set both values to 1. Again, one could argue that these values are just some estimates and not based on any foreknowledge. However, we are not interested in the real standard deviation but in relative improvements based on varying geometries. So as long as the estimates remain the same during computations, it is a good approach.

We considered an extensive range of viewing geometries during the computations, and we ignored whether the viewing geometries were reasonable. A lot of the viewing geometries are impossible, e.g., all geometries with $\theta = 80°$. However, it is still possible to determine the optimal viewing geometry within the reasonable ranges with the figures we created.

6

Conclusions

This research aimed to provide a full and complete description of the decomposition problem and to analyze the consequences of particular choices. Moreover, the aim was to come with clear recommendation on how the underdetermined nature of the estimation problem should be handled. Furthermore, we wanted to develop a new approach that the provides physically more relevant estimates. The main research question to be answered was formulated as:

Can a better geometrical insight lead to a more optimal way of computing and communicating InSAR results?

We argue that this question can be answered affirmative. We analyzed the decomposition problem and formulated explicit conditions that need to be satisfied. Comparing those conditions with approaches typically encountered in literature, one main result is that many approaches are either incorrect or lack proper semantics, resulting in biased displacement estimates. We are well aware that this is a strict and firmly stand. However, we think that this helps in opening up the discussion on how results should be communicated.

Additionally, we found that the default displacement estimates in the ENU system are often not tuned to the needs of an InSAR product end-user, and are therefore sub-optimal. Therefore, we propose a new systematic approach that gives physically more relevant estimates and considers all uncertainties properly. We also developed a new taxonomy to label the different approaches that can help in evaluating InSAR results and InSAR papers. We argue that the next step lies with the InSAR community, to be aware of potential fallacious approaches. This will help the InSAR community to develop better and more informative information products and improve communication of InSAR results. In the following, we discuss the main conclusions of the research in more detail.

An analysis of the inverse problem
We found that uniquely estimating the three displacement components would require at least three sets of STCI LoS observations stemming from the same RUM. While fundamentally trivial, this condition, in particular explicitly expressing the need for STCI observations under an assumed region of uniform motion, is often not satisfied in reported InSAR studies. More importantly, the system of equations needs to have a full rank coefficient matrix, i.e., the different observations need to have sufficient angular diversity.

However, since almost all SAR satellites are near-polar orbiting satellites, there is limited angular diversity, and the sensitivity for the north-south displacement component is low, resulting in an ill-posed problem. Moreover, in most practical situations, two sets of STCI LoS observations (one ascending and one descending) are available at most, resulting in an underdetermined system with an infinite

amount of possible solutions.

With two observations, from different viewing geometries, there are two solution planes whose intersection is the *null line*. The direction of this line is given by azimuth angle ϕ and elevation angle ζ and depends on the viewing geometry of the two LoS observations, e.g., the incidence angles and azimuth angles of the zero-Doppler plane (ZDP). An essential finding in this study is that it is not the heading angle of the satellite, α_h, that is important, but it is the azimuth angle of the ZDP α_d that should be considered due to the convergence of the Earth meridians. In other words, the viewing geometry needs to be considered from the perspective of the target on the ground, rather than from the spacecraft perspective. Considering α_d instead of α_h also changes the projector of the forward model compared to what we commonly observe in InSAR literature.

In common literature, we often read that near-polar orbiting satellites are insensitive for displacements in the north direction due to the symmetric headings of the satellites. However, this statement is only valid when the null line is orthogonal to the plane spanned by the east and up direction which is (almost) never the case, see Fig. 2.17. First, asymmetric azimuth angles of the ZDP of the two observations result in $\phi \neq 0°$. Nevertheless, when the azimuth angles of the ZDP are symmetrical, the difference in incidence angles also results in $\phi \neq 0°$. Moreover, we fount that ζ is never equal to 0°and therefore, the satellites are always sensitive for displacements in the north direction and neglecting the north component leads to biased estimates for the east and up direction.

When d_n is removed from the inverse problem, the orientation of the null line also determines whether both the east and up estimates are biased. When $\phi = 0°$, only the up component is biased, and it is possible to solve unambiguously for the east component. We have seen that when observations from an ascending and a descending acquisition are combined, the azimuth angles of the ZDP are often not symmetrical relative to the north since α_d is range dependent. Therefore we would expect that $\phi \neq 0°$. Yet, for Sentinel-1, we have found a strong correlation between the incidence angle and α_d, which is latitude dependent, see Figs. 2.10 and 2.11. This correlation results in $\phi = 0°$. And therefore, for Sentinel-1 at the northern hemisphere, it is possible to give a proper (unbiased) estimate for the east component with only two LoS observations (one ascending and one descending). Only the estimate for the up component will be biased.

Approaches in common literature

Reviewing InSAR literature, we encounter different approaches to address the underdetermination problem, yet often with either mathematical or semantic flaws. We conclude that errors are made throughout the entire InSAR community and not only by people with limited InSAR knowledge, as some authors argue. The impact of the errors reaches from quantitative errors, mismatches in comparative studies with other geodetic techniques, to a lack of trust in the technology by end-users.

A recurring problem is the lack of distinction between a vector ‘projection’ and a vector ‘decomposition’. In InSAR, we often need to use both subsequently. First, the *attribution error* occurs when the LoS observation is attributed completely to the vertical, and the results are subsequently presented as vertical displacements. Then we found the *projection error*, where the LoS displacement estimations are projected onto the vertical but subsequently presented as ‘vertical displacements’. The *decomposition error* occurs when the null space in the 3D solution space is ignored, and only two viewing geometries are used in the decomposition. In such cases, it is assumed that the *lack of sensitivity* in the north-south component for near-polar orbits is equivalent to the *absence* of a north-south component by simply removing the component from the decomposition equation and only estimating the east and up components. The final error type is the case with *flawed assumptions*. Estimating 3D displacement vectors observed by one or two viewing geometries can only be solved by adding additional information in the form of assumptions, i.e., conditions. These need to be explicitly stated, both in the documentation and in the final products. Yet, in many cases, these assumptions are either lacking, misstated, incorrect, or implausible.

From the fallacious approaches mentioned above, we conclude that the way InSAR results are computed and communicated is often too loose and even wrong, resulting in misleading results. Often, there

is a lack of insight into the consequences of particular choices in terms of accuracy and precision. We argue that the InSAR community should refrain from 'hand-waving' argumentation when mentioning assumptions or final results, and that there is a need to streamline how the community communicates InSAR results. The developed taxonomy may help in evaluating InSAR results and publications.

In some cases, the fallacious approaches can be corrected by the use of proper semantics. E.g., considering the projection error it would be sufficient to present the results as 'displacement projected onto the vertical' instead of 'vertical displacements', see Fig. 2.21 at p. 31. The same holds for the attribution error. Approaches with a decomposition error are simply incorrect and cannot be solved with proper semantics. An argument that is often used when discussing the sensitivity of the north-south component and removing it from the decomposition equations is that the sensitivity for the north-south component is only valid for exceptional cases with large north-south displacements. However, we argue that it is exactly the other way around: one should describe the decomposition problem in a generic sense, both for small and large displacements. Initially, the stochastic model plays no role, as only the geometry of the observations should be taken into account, which is captured in the A matrix. Once the generic model is known, it is possible to deduce particular cases, e.g., cases with small displacements or very high or low observation precision. Thus not the other way around, where authors start with the exceptional (particular) case. They state that the precision of the observations is low or that the displacements are small, and from there, they try to deduce the generic model.

Added to this, a decomposition in up and east direction is often not tuned to the needs of the end-user of the InSAR product and results are difficult to interpret. For example, often there is no particular physical relevance of reporting an 'east-component'. Moreover, the results give no indication of the quality of the estimated parameters, which makes interpretation difficult.

Strap-down approach
As the decomposition error cannot be solved with proper semantics, the only solution would be to add additional information in the form of assumptions. We argue that working with a local, strap-down, right-handed Cartesian coordinate system fixed to the deformation phenomenon, with transversal, longitudinal and normal components is a straightforward and physics-based solution to the underdetermination problem. For many practical cases, such as line-infrastructure, landslides, or subsidence bowls, analysis of the main driving forces supports the assumption that significant deformations in the longitudinal direction are unlikely, effectively reducing the number of unknowns in the estimation.

However, this approach requires that the orientation of the TLN frame is well-chosen. Otherwise, the displacement estimates are still biased. We found that when the orientation of the frame is added to the mathematical model as an unknown, the uncertainty of the frame alignment can be taken into account. Therefore, it also affects the precision of the final estimates for the displacement components. We concluded that the frame's orientation uncertainty plays a more significant role for larger displacements.

Using the strap-down approach gives physically more relevant estimates and it results in more reliable estimates since it properly includes all uncertainties. From the results from a salt mining case in the Netherlands we further conclude that the conventional way of communicating (PS)-InSAR results by means of a *'dot distribution map'* is sub-optimal when considering the quality of the estimates, in particular for products with a decomposition in two (or three) orthogonal directions. For such InSAR information products, 'vector arrow maps', or traditional geodetic vector-based visualizations, including error ellipses are a viable and more optimal alternative in terms of information content.

InSAR perspectives
Discussions on InSAR studies, feasibility, and results suffer from differences in perspective. InSAR studies are complex studies in which different persons have different questions. There are stakeholders who want to know what InSAR can bring them for their particular case study, or users of existing InSAR products interested in what they can get from that product, and service providers and space agencies who want to design missions to be used optimally.

Thus, we defined three InSAR perspectives, all with their own parameters of interest. These different

perspectives require a unique sequence of operations to answer their typically relevant questions. They have in common that the question that is asked needs to be very clear. In other words, what is it exactly that the stakeholder is asking? Or, what requirements should the final product meet? Only then it is possible to make correct assumptions.

For every perspective, we developed a systematic sequence of operations as described in Chapter 4. From the results in Chapter 5, it is demonstrated that those methods worked to give a satisfying answer to the related questions. Moreover, by systematically following the methods described in Chapter 4, it is clear to everyone what is done and how the results should be interpreted.

6.1. Recommendations

Based on the results of this thesis, we suggest the following:

- The InSAR community should refrain from 'hand-waving' assumptions and descriptions while estimating the 3D displacement vector.
- The generic model, which requires three sets of STCI LoS observations available over the same RUM that provides a full rank system, should be used as a starting point in InSAR studies, and should be stated explicitly together with the quantitative results. From there, the particular cases can be solved (and not the other way around).
- The InSAR community should use proper semantics while presenting InSAR results both in written text and papers as in figures, maps, and tables. It is further important that authors remain consistent.
- We developed a taxonomy to label different approaches. We recommend the adoption of this taxonomy since it helps in evaluating InSAR results and publications.
- For deformation phenomena where significant displacements into the longitudinal direction are unlikely, we recommend the adoption of the strap-down approach since it provides physically more meaningful results compared to the approaches we see in current literature.
- We recommend to present InSAR results using the traditional geodetic vector-based visualizations with error-ellipses since it conveys more information than the standard dot-distribution maps used in the InSAR community.

6.2. Future directions

The results from this study lead to several directions for future studies.

- One of our main findings is that it is possible to give an unbiased estimate for the east displacement for large parts of the Northern Hemisphere with only two InSAR observations from Sentinel-1. This statement is based on viewing geometries for Sentinel-1 which are estimated with DRaMA [19]. It would be relevant to investigate whether the statements still holds for real viewing geometries. Moreover, it is important to investigate whether the statement also holds for satellite missions other than Sentinel-1 (e.g. TerraSAR-X or RADARSAT).
- Within this study we assumed that the LoS direction could be described by the incidence angle θ and azimuth of the zero-Doppler plane α_d. However, the zero-Doppler plane is not a perfectly flat plane but can be curved. This should be further investigated.
- Not for all missions the LoS direction can be described by θ and α_d, since not for all missions the observations are taken at zero-Doppler. It is important to investigate the error made when α_d is considered instead of the real azimuth of the plane spanned by the LoS unit vector and the gravity vector pointing from the Earth towards the satellite.

- Unfortunately, the strap-down approach is not a solution to the underdetermined problem for cases where the main deformation mechanism is unknown, as is the case for, e.g., nationwide InSAR displacement products, see e.g. [5]. For such problems the Harmony Earth Explorer 10 mission could potentially be a good solution. We recommend to investigate whether Harmony could bring a solution for the underdetermined problem in such cases.

Bibliography

[1] M. Crosetto, B. Crippa, E. Biescas, O. Monserrat, and M. Agudo, "State of the art of land deformation monitoring using differential sar interferometry," in *ISPRS Hannover Workshop*, pp. 17–20, 2005.

[2] R. Bürgmann, P. A. Rosen, and E. J. Fielding, "Synthetic aperture radar interferometry to measure earth's surface topography and its deformation," *Annual review of earth and planetary sciences*, vol. 28, no. 1, pp. 169–209, 2000.

[3] A. Ferretti, C. Prati, and F. Rocca, "Permanent scatterers in sar interferometry," *IEEE Transactions on geoscience and remote sensing*, vol. 39, no. 1, pp. 8–20, 2001.

[4] D. Massonnet and K. L. Feigl, "Radar interferometry and its application to changes in the earth's surface," *Reviews of geophysics*, vol. 36, no. 4, pp. 441–500, 1998.

[5] N. C. for Geodesy and G.-I. (NCG), *Bodemdalingskaart (BDK) Nederland* . 2020. Retrieved on: April 1, 2021, from.

[6] R. F. Hanssen, *Radar interferometry: data interpretation and error analysis*, vol. 2. Springer Science & Business Media, 2001.

[7] P. Teatini, L. Tosi, T. Strozzi, L. Carbognin, U. Wegmüller, and F. Rizzetto, "Mapping regional land displacements in the venice coastland by an integrated monitoring system," *Remote Sensing of Environment*, vol. 98, no. 4, pp. 403–413, 2005.

[8] S. Alatza, I. Papoutsis, D. Paradissis, C. Kontoes, and G. A. Papadopoulos, "Multi-temporal insar analysis for monitoring ground deformation in amorgos island, greece," *Sensors*, vol. 20, no. 2, p. 338, 2020.

[9] D. H. T. Minh, N. Yen-Nhi, T. T. Lê, T. C. Le, H. S. Bui, Q. V. Vuong, and T. Le Toan, "Quantifying horizontal and vertical movements in ho chi minh city by sentinel-1 radar interferometry," 2020.

[10] T. Carlà, E. Intrieri, F. Raspini, F. Bardi, P. Farina, A. Ferretti, D. Colombo, F. Novali, and N. Casagli, "Perspectives on the prediction of catastrophic slope failures from satellite insar," *Scientific reports*, vol. 9, no. 1, pp. 1–9, 2019.

[11] F. J. Van Leijen, "Persistent scatterer interferometry based on geodetic estimation theory," 2014.

[12] F. Hu, J. Wu, L. Chang, and R. F. Hanssen, "Incorporating temporary coherent scatterers in multi-temporal insar using adaptive temporal subsets," *IEEE transactions on geoscience and remote sensing*, vol. 57, no. 10, pp. 7658–7670, 2019.

[13] T. Eltoft, "The rician inverse gaussian distribution: a new model for non-rayleigh signal amplitude statistics," *IEEE Transactions on Image Processing*, vol. 14, no. 11, pp. 1722–1735, 2005.

[14] C. Tiberius, F. van Leijen, and A. Mousivand, *Physical principles of remote sensing: an introduction*. Faculty of Civil Engineering and Geosciences, Delft University of Technology, 2017.

[15] R. Czikhardt, H. van der Marel, F. J. van Leijen, and R. F. Hanssen, "Estimating signal-to-clutter ratio of insar corner reflectors from sar time series," *IEEE Geoscience and Remote Sensing Letters*, 2021.

[16] I. E. Özer, F. J. van Leijen, S. N. Jonkman, and R. F. Hanssen, "Applicability of satellite radar imaging to monitor the conditions of levees," *Journal of Flood Risk Management*, vol. 12, no. S2, p. e12509, 2019.

[17] D. O'Grady, M. Leblanc, and D. Gillieson, "Relationship of local incidence angle with satellite radar backscatter for different surface conditions," *International journal of applied earth observation and geoinformation*, vol. 24, pp. 42–53, 2013.

[18] E. S. A. (ESA), *Sentinel 1 SAR Acquisition Modes*. 2020. Retrieved on: February 19, 2021, from https://sentinel.esa.int/web/sentinel/technical-guides/sentinel-1-sar/sar-instrument/acquisition-modes.

[19] P. J. Lopez-Dekker and T. Andreas, *DRaMA software*. 2021. Retrieved on: July 14, 2021, from https://gitlab.tudelft.nl/drama/drama.

[20] H. Above, *Sentinel 1A - Ground track*. 2021. Retrieved on: July 14, 2021, from https://heavens-above.com/orbit.aspx?satid=39634.

[21] X. X. Zhu, S. Montazeri, C. Gisinger, R. Hanssen, and R. Bamler, "Geodetic tomosar—fusion of sar imaging geodesy and tomosar for 3d absolute scatterer positioning," in *2014 IEEE Geoscience and Remote Sensing Symposium*, pp. 1317–1320, IEEE, 2014.

[22] X. X. Zhu, S. Montazeri, C. Gisinger, R. F. Hanssen, and R. Bamler, "Geodetic sar tomography," *IEEE Transactions on Geoscience and Remote Sensing*, vol. 54, no. 1, pp. 18–35, 2015.

[23] R. F. Hanssen, "A radar retroreflector device and a method of preparing a radar retroflector device," 12 2018.

[24] T. J. Wright, B. E. Parsons, and Z. Lu, "Toward mapping surface deformation in three dimensions using insar," *Geophysical Research Letters*, vol. 31, no. 1, 2004.

[25] F. Rocca, "3d motion recovery with multi-angle and/or left right interferometry," in *Proceedings of the third International Workshop on ERS SAR*, Citeseer, 2003.

[26] ESA, *Sentinel-1 SAR User Guide*. 2021. Retrieved on: July 7, 2021, from https://sentinel.esa.int/web/sentinel/user-guides/sentinel-1-sar/acquisition-modes.

[27] S. Stramondo, F. Bozzano, F. Marra, U. Wegmuller, F. Cinti, M. Moro, and M. Saroli, "Subsidence induced by urbanisation in the city of rome detected by advanced insar technique and geotechnical investigations," *Remote Sensing of Environment*, vol. 112, no. 6, pp. 3160–3172, 2008.

[28] L. Solari, A. Ciampalini, F. Raspini, S. Bianchini, and S. Moretti, "Psinsar analysis in the pisa urban area (italy): a case study of subsidence related to stratigraphical factors and urbanization," *Remote Sensing*, vol. 8, no. 2, p. 120, 2016.

[29] M. Zheng, K. Deng, H. Fan, and S. Du, "Monitoring and analysis of surface deformation in mining area based on insar and grace," *Remote Sensing*, vol. 10, no. 9, p. 1392, 2018.

[30] L. Zhou, J. Guo, J. Hu, J. Li, Y. Xu, Y. Pan, and M. Shi, "Wuhan surface subsidence analysis in 2015–2016 based on sentinel-1a data by sbas-insar," *Remote Sensing*, vol. 9, no. 10, p. 982, 2017.

[31] M. Gao, H. Gong, B. Chen, X. Li, C. Zhou, M. Shi, Y. Si, Z. Chen, and G. Duan, "Regional land subsidence analysis in eastern beijing plain by insar time series and wavelet transforms," *Remote Sensing*, vol. 10, no. 3, p. 365, 2018.

[32] N. Svigkas, C. Loupasakis, P. Tsangaratos, I. Papoutsis, A. Kiratzi, and C. H. Kontoes, "A deformation study of anthemountas graben (northern greece) based on in situ data and new insar results," *Arabian Journal of Geosciences*, vol. 13, no. 13, pp. 1–13, 2020.

[33] W.-C. Hung, C. Hwang, Y.-A. Chen, L. Zhang, K.-H. Chen, S.-H. Wei, D.-R. Huang, and S.-H. Lin, "Land subsidence in chiayi, taiwan, from compaction well, leveling and alos/palsar: Aquaculture-induced relative sea level rise," *Remote Sensing*, vol. 10, no. 1, p. 40, 2018.

[34] A. H.-M. Ng, H. Wang, Y. Dai, C. Pagli, W. Chen, L. Ge, Z. Du, and K. Zhang, "Insar reveals land deformation at guangzhou and foshan, china between 2011 and 2017 with cosmo-skymed data," *Remote Sensing*, vol. 10, no. 6, p. 813, 2018.

[35] M. Haghshenas Haghighi and M. Motagh, “Sentinel-1 insar over germany: Large-scale interferometry, atmospheric effects, and ground deformation mapping,” *ZfV: Zeitschrift für Geodäsie, Geoinformation und Landmanagement*, vol. 2017, no. 4, pp. 245–256, 2017.

[36] R. Bonì, F. Cigna, S. Bricker, C. Meisina, and H. McCormack, “Characterisation of hydraulic head changes and aquifer properties in the london basin using persistent scatterer interferometry ground motion data,” *Journal of Hydrology*, vol. 540, pp. 835–849, 2016.

[37] W. Tang, P. Yuan, M. Liao, and T. Balz, “Investigation of ground deformation in taiyuan basin, china from 2003 to 2010, with atmosphere-corrected time series insar,” *Remote Sensing*, vol. 10, no. 9, p. 1499, 2018.

[38] R. N. Nof, G. Baer, A. Ziv, E. Raz, S. Atzori, and S. Salvi, “Sinkhole precursors along the dead sea, israel, revealed by sar interferometry,” *Geology*, vol. 41, no. 9, pp. 1019–1022, 2013.

[39] S. Samieie-Esfahany, R. Hanssen, K. van Thienen-Visser, and A. Muntendam-Bos, “On the effect of horizontal deformation on insar subsidence estimates,” in *Proceedings of the Fringe 2009 Workshop, Frascati, Italy*, vol. 30, 2009.

[40] N. Short, A.-M. LeBlanc, W. Sladen, G. Oldenborger, V. Mathon-Dufour, and B. Brisco, “Radarsat-2 d-insar for ground displacement in permafrost terrain, validation from iqaluit airport, baffin island, canada,” *Remote Sensing of Environment*, vol. 141, pp. 40–51, 2014.

[41] D. Raucoules, C. Maisons, C. Carnec, S. Le Mouelic, C. King, and S. Hosford, “Monitoring of slow ground deformation by ers radar interferometry on the vauvert salt mine (france): Comparison with ground-based measurement,” *Remote sensing of environment*, vol. 88, no. 4, pp. 468–478, 2003.

[42] H. Sun, Q. Zhang, C. Zhao, C. Yang, Q. Sun, and W. Chen, “Monitoring land subsidence in the southern part of the lower liaohe plain, china with a multi-track ps-insar technique,” *Remote sensing of environment*, vol. 188, pp. 73–84, 2017.

[43] B. V. Yazici and E. Tunc Gormus, “Investigating persistent scatterer insar (psinsar) technique efficiency for landslides mapping: a case study in artvin dam area, in turkey,” *Geocarto International*, pp. 1–19, 2020.

[44] H. Klemm, I. Quseimi, F. Novali, A. Ferretti, and A. Tamburini, “Monitoring horizontal and vertical surface deformation over a hydrocarbon reservoir by psinsar,” *First break*, vol. 28, no. 5, 2010.

[45] A. Rucci, D. Vasco, and F. Novali, “Monitoring the geologic storage of carbon dioxide using multicomponent sar interferometry,” *Geophysical Journal International*, vol. 193, no. 1, pp. 197–208, 2013.

[46] C. Janna, N. Castelletto, M. Ferronato, G. Gambolati, and P. Teatini, “A geomechanical transversely isotropic model of the po river basin using psinsar derived horizontal displacement,” *International Journal of Rock Mechanics and Mining Sciences*, vol. 51, pp. 105–118, 2012.

[47] S. Yun, P. Segall, and H. Zebker, “Constraints on magma chamber geometry at sierra negra volcano, galápagos islands, based on insar observations,” *Journal of Volcanology and geothermal research*, vol. 150, no. 1-3, pp. 232–243, 2006.

[48] K. Pawluszek-Filipiak and A. Borkowski, “Integration of dinsar and sbas techniques to determine mining-related deformations using sentinel-1 data: The case study of rydułtowy mine in poland,” *Remote Sensing*, vol. 12, no. 2, p. 242, 2020.

[49] P. Teatini, N. Castelletto, M. Ferronato, G. Gambolati, C. Janna, E. Cairo, D. Marzorati, D. Colombo, A. Ferretti, A. Bagliani, *et al.*, “Geomechanical response to seasonal gas storage in depleted reservoirs: A case study in the po river basin, italy,” *Journal of Geophysical Research: Earth Surface*, vol. 116, no. F2, 2011.

[50] A. Tamburini, M. Bianchi, C. Giannico, and F. Novali, “Retrieving surface deformation by psinsar™ technology: A powerful tool in reservoir monitoring,” *International Journal of Greenhouse Gas Control*, vol. 4, no. 6, pp. 928–937, 2010.

[51] S. Alatza, I. Papoutsis, D. Paradissis, C. Kontoes, G. A. Papadopoulos, and C. Raptakis, “Insar time-series analysis for monitoring ground displacement trends in the western hellenic arc: The kythira island, greece,” *Geosciences*, vol. 10, no. 8, p. 293, 2020.

[52] M. Imamoglu, F. Kahraman, Z. Cakir, and F. B. Sanli, “Ground deformation analysis of bolvadin (w. turkey) by means of multi-temporal insar techniques and sentinel-1 data,” *Remote Sensing*, vol. 11, no. 9, p. 1069, 2019.

[53] C. A. Bischoff, A. Ferretti, F. Novali, A. Uttini, C. Giannico, and F. Meloni, “Nationwide deformation monitoring with squeesar® using sentinel-1 data,” *Proceedings of the International Association of Hydrological Sciences*, vol. 382, pp. 31–37, 2020.

[54] N. Fatholahi, M. Akhoondzadeh, and A. Bahroudi, “An investigation of surface deformation over oilfield in southwest iran (2003–2010) using insar and physical modelling,” *International Journal of Remote Sensing*, vol. 41, no. 14, pp. 5355–5370, 2020.

[55] R. Guo, L. Sumin, Y. Chen, X. Li, and L. Yuan, “Identification and monitoring landslides in longitudinal range-gorge region with insar fusion integrated visibility analysis,” *Landslides*, pp. 1–18, 2020.

[56] L. Wang, K. Deng, and M. Zheng, “Research on ground deformation monitoring method in mining areas using the probability integral model fusion d-insar, sub-band insar and offset-tracking,” *International Journal of Applied Earth Observation and Geoinformation*, vol. 85, p. 101981, 2020.

[57] L. Chang, R. P. Dollevoet, and R. F. Hanssen, “Monitoring line-infrastructure with multisensor sar interferometry: Products and performance assessment metrics,” *IEEE journal of selected topics in applied earth observations and remote sensing*, vol. 11, no. 5, pp. 1593–1605, 2018.

[58] D. Müller and A. Preusse, “Use of the area of main influence to fix a relevant boundary for mining damages in germany,” *International Journal of Mining Science and Technology*, vol. 28, no. 1, pp. 79–83, 2018.

[59] S. Verhagen, *Lecture Slides - Non-linear least-squares - Geo-Measurement Processing*. Faculty of Civil Engineering and Geosciences, Delft University of Technology, 2020.

[60] P. J. Teunissen, *Testing theory*. VSSD Delft, 2006.

[61] E. S. A. (ESA), *Sentinel 1 User Guides Revisit and Coverage*. 2020. Retrieved on: April 27, 2021, from https://sentinel.esa.int/web/sentinel/user-guides/sentinel-1-sar/revisit-and-coverage.

[62] J. Brinkman, *Invloed van bodemdaling door zoutwinning Nedmag op bebouwing*. Deltares report, 2016.

[63] T. Fuhrmann and M. C. Garthwaite, “Resolving three-dimensional surface motion with insar: Constraints from multi-geometry data fusion,” *Remote Sensing*, vol. 11, no. 3, p. 241, 2019.

[64] M. Heitfeld and J. e. a. Klunker, *Na-ijlende gevolgen steenkolenwinning Zuid-Limburg - Summary report with integrated Bow-Tie-Analysis*, vol. 1. Projectgroep GS-SL, 2016.

[65] Wikipedia, *Feldbiss*. March 15, 2020. Retrieved on: July 11, 2021, from https://nl.wikipedia.org/wiki/Feldbiss.

[66] M. C. Cuenca, A. J. Hooper, and R. F. Hanssen, “Surface deformation induced by water influx in the abandoned coal mines in limburg, the netherlands observed by satellite radar interferometry,” *Journal of Applied Geophysics*, vol. 88, pp. 1–11, 2013.

[67] Geologypage, *How Strike-Slip Faults Form, the Origin of Earthquakes*. July 17, 2017. Retrieved on: June 28, 2021, from https://www.geologypage.com/2017/07/strike-slip-faults-form-origin-earthquakes.html.

[68] H. Ozener, E. Arpat, S. Ergintav, A. Dogru, R. Cakmak, B. Turgut, and U. Dogan, “Kinematics of the eastern part of the north anatolian fault zone,” *Journal of geodynamics*, vol. 49, no. 3-4, pp. 141–150, 2010.

[69] USGS, *Tectonic setting of the San Andreas Fault (transform plate boundary) in California*. 2017. Retrieved on: June 29, 2021, from https://www.geologypage.com/2017/07/strike-slip-faults-form-origin-earthquakes.html.

[70] CelesTrak, *NORAD Two-Line Element Set Format* . 2021. Retrieved on: August 27, 2021, from https://www.celestrak.com/NORAD/documentation/tle-fmt.php.

[71] D. A. Vallado, *Fundamentals of astrodynamics and applications*, vol. 12. Springer Science & Business Media, 2001.

[72] H. D. Curtis, *Orbital mechanics for engineering students*. Butterworth-Heinemann, 2013.

A

The signs of the projector in the decomposition formula

The positive LoS displacement d_{LoS} should be seen from the scatterers perspective, i.e. a scatterer moving towards the radar is moving in a positive LoS direction. We can now deduce the signs of the projector in Eq. (2.7), (page 16) in the ENU reference system. The terminology that we use is as follows: d_{LoS}, d_{east}, d_{north} and d_{up} are scalar displacement values in the LoS, east, north and up direction respectively, and u_{LoS}, u_{east}, $\mathrm{u}_{\text{north}}$ and u_{up} are unit vectors in the LoS, east, north and up direction respectively where

$$\mathrm{u}_{\text{LoS}} = \begin{bmatrix} \sin\theta \sin\alpha_d \\ \sin\theta \cos\alpha_d \\ \cos\theta \end{bmatrix}, \ \mathrm{u}_{\text{east}} = \begin{bmatrix} 1 \\ 0 \\ 0 \end{bmatrix}, \ \mathrm{u}_{\text{north}} = \begin{bmatrix} 0 \\ 1 \\ 0 \end{bmatrix}, \ \mathrm{u}_{\text{up}} = \begin{bmatrix} 0 \\ 0 \\ 1 \end{bmatrix}. \tag{A.1}$$

Given a purely vertical displacement signal d_{up}, the blue displacement vector in Fig. A.1 (which is equals $\mathrm{u}_{\text{up}} d_{\text{up}}$), the orthogonal projection of d_{up} onto the LoS direction is calculated with

$$d_{\text{LoS}} = \cos(\theta)\, d_{\text{up}}. \tag{A.2}$$

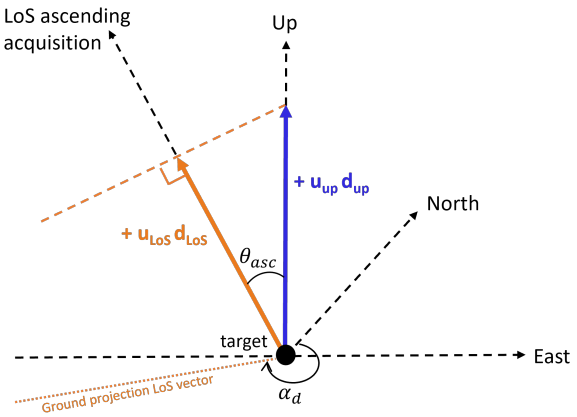

Figure A.1: The orthogonal projection of a purely vertical displacement signal onto the Los direction for an ascending acquisition. The striped orange line represents the null space.

In Figs. A.2 and A.3, the projection of a displacement purely in the eastern and northern direction, respectively, can be seen. However, to deduce the components for the projector, first the projection

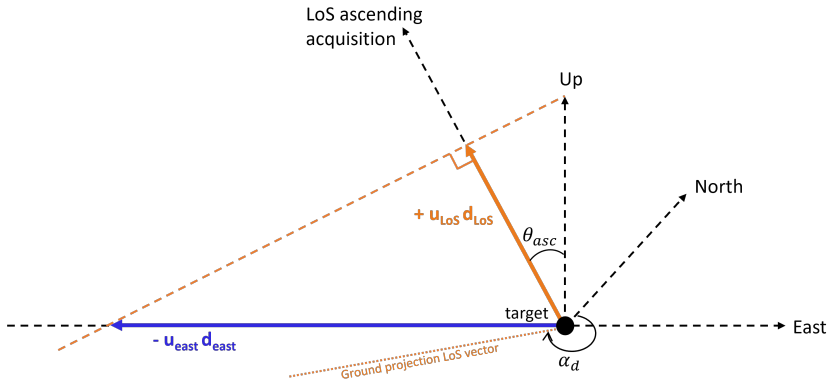

Figure A.2: The projection of displacement signal d_{east}, which only has a component in the east direction, onto the Los direction for an ascending acquisition.

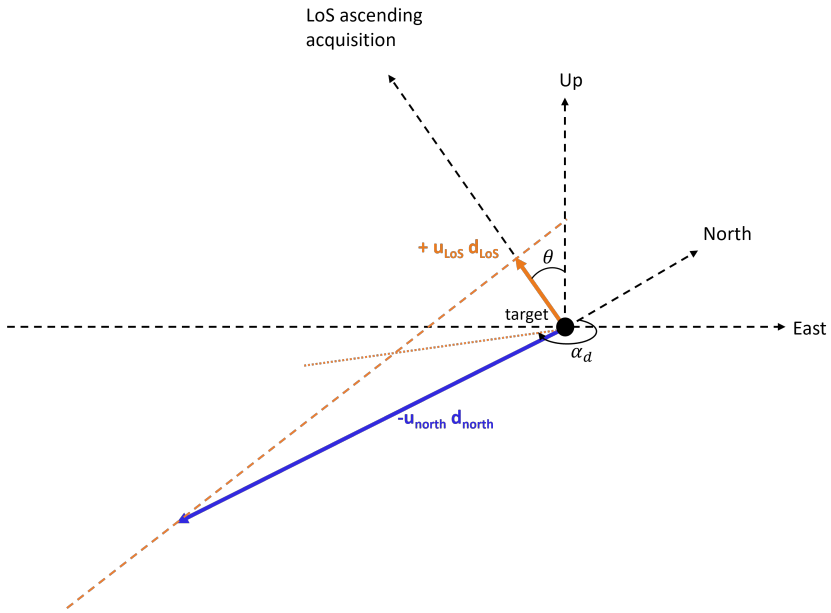

Figure A.3: The projection of displacement signal d_{north}, which only has a component in the northern direction, onto the Los direction for an ascending acquisition.

onto the zero-Doppler plane, $d_{\text{LoS, ZDP}}$ should be computed. The projection of the east component onto $d_{\text{LoS,ZDP}}$ is computed with

$$d_{\text{LoS,ZDP}} = -\sin(a)\, d_{\text{east}}.$$

With $a = \alpha_d - \pi$ (see Fig. A.4 for the top-view sketch) and $\sin(\alpha_d - \pi) = -\sin(\alpha_d)$ it is possible to write

$$d_{\text{LoS,ZDP}} = -\sin(\alpha_d - \pi)\, d_{\text{east}} = \sin(\alpha_d)\, d_{\text{east}}. \tag{A.3}$$

For the projection of the north component onto $d_{\text{LoS,ZDP}}$ we find (see Fig. A.4)

$$d_{\text{LoS,ZDP}} = -\cos(a)\, d_{\text{north}}.$$

With $a = \alpha_d - \pi$ and $\cos(\alpha_d - \pi) = -\cos(\alpha_d)$ it is possible to write

$$d_{\text{LoS,ZDP}} = -\cos(\alpha_d - \pi)\, d_{\text{north}} = \cos(\alpha_d)\, d_{\text{north}}.$$

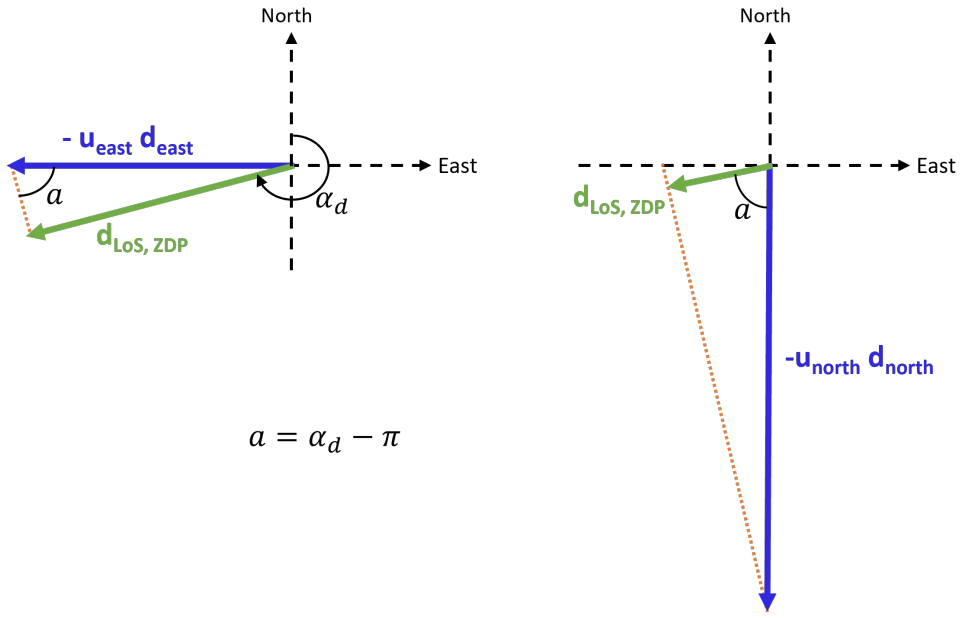

Figure A.4: The east (left) and north (right) displacement components, first need to be projected onto the Zero-Doppler plane, $d_{\mathrm{LoS},g}$.

Once the projection of the displacement components onto the zero-Doppler plane is known, we can compute the orthogonal projection of $d_{\mathrm{LoS,ZDP}}$ onto the LoS vector with

$$d_{\mathrm{LoS}} = \sin(\theta)\; d_{\mathrm{LoS,ZDP}},$$

see also Fig. A.5. So in the end, we find for the projection of a displacement in the east direction onto the LoS

$$d_{\mathrm{LoS}} = \sin(\theta)\sin(\alpha_d)\; d_{\mathrm{east}}, \tag{A.4}$$

and for a displacement in the north direction we find

$$d_{\mathrm{LoS}} = \sin(\theta)\cos(\alpha_d)\; d_{\mathrm{north}}, \tag{A.5}$$

With Eqs. (A.2), (A.4) and (A.5) we have shown that, when looking from a scatterer's perspective, the signs of the projector are indeed $[+,+,+]$ and that the LoS vector decomposition can be written as:

$$d_{\mathrm{LoS}} = \begin{bmatrix}\sin(\theta)\;\sin(\alpha_d) & \sin(\theta)\;\cos(\alpha_d) & \cos(\theta)\end{bmatrix}\begin{bmatrix}d_e\\ d_n\\ d_u\end{bmatrix}.$$

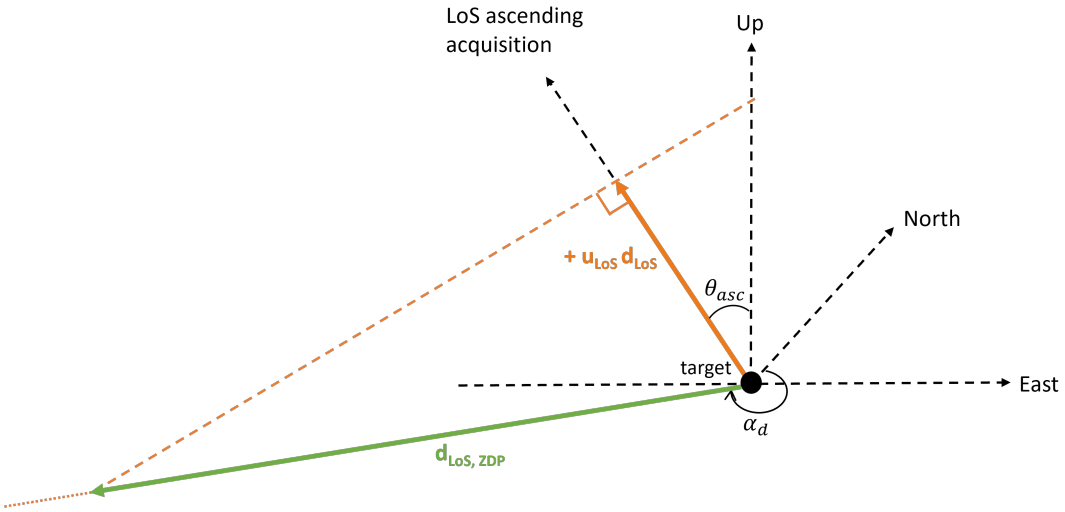

Figure A.5: Help triangles to compute the projections of d_{east} and d_{north} onto the ground component of the LoS vector $d_{\mathrm{LoS,\,g}}$

B

Sentinel-1 Viewing Geometry

B.1. Estimating the Sentinel-1 viewing geometry

The Delft Radar Modelling and performance Analysis (DRaMA) software [19] can be used to estimate the viewing geometries of the available Sentinel-1 acquisitions for locations on Earth. It gives an estimate for the incidence angle and the azimuth of the zero-Doppler plane (ZDP) at the position of the target of the available acquisitions. Here we discuss how the two angles are estimated.

First, the orbits of Sentinel-1 are estimated from the orbital parameters at a particular epoch (moment in time), extracted from the two-line-elements (TLE) file. The orbital parameters include i) the inclination, ii) the right ascension of the ascending node, iii) the argument of perigee, iv) the mean anomaly, and v) the mean motion [70]. For the particular epoch, the parameters are stored, and from there, the orbit is estimated for one orbital period using a J2 propagator. DRaMA estimates how the orbital parameters would change from the original epoch to the new ones, using the J2 perturbation algorithm of Vallado et al.[71] and Curtis et al.[72]. As the last step, the orbital parameters are converted into state vectors.

Then the viewing geometry can be estimated. From the state vectors, the LoS direction at the satellite in a satellite-centered coordinate system, is computed using state vectors and the fact that the observations are taken at zero-Doppler.

The incidence angle

1. With the LoS direction at the satellite, the position of the satellite, and assuming a WGS84 Earth, the point of intersection between the LoS direction and the location on Earth, which we call point P, is found.

2. At point P, compute the surface normal unit vector using the vector gradient of expression for an ellipsoid

3. Assuming a unit LoS vector, find the component of the LoS along the normal to the surface at P.

4. The arccosine of the result of step 3 is the incidence angle.

Azimuth of the ZDP

1. Define $z = [0, 0, 1]$. In an Earth-centered Earth-fixed (ECEF) system, z points from the center of the Earth to the north pole.

2. Find the rejection of z on the surface normal, which we call Q. Q now is tangential to the Earth's surface at point P. Normalize Q to make it a unit vector, and it points north.

3. Find the unit vector tangential to the Earth surface pointing in the east direction, which we call R. R is computed by the cross product of Q with the surface normal.
4. Find the component of the LoS that is normal to the surface normal, in the same way as step 2 (this component is tangential to the surface).
5. Project the LoS tangent component along with Q and R.
6. The arctangent of the projected LoS on Q and R is the azimuth of the ZDP at the target, towards the satellite.

B.2. Available observations

Due to the convergence of the meridians, different tracks overlap at higher latitudes. As a result, the number of observations per cycle per location on Earth differs, see Fig. B.1. For locations on Earth observed by multiple acquisitions, the geometric configuration of the observations differs since the range distance between the different satellite positions and the target is unique. Consequently, the incidence angles differ, but the azimuth of the ZDP varies as well.

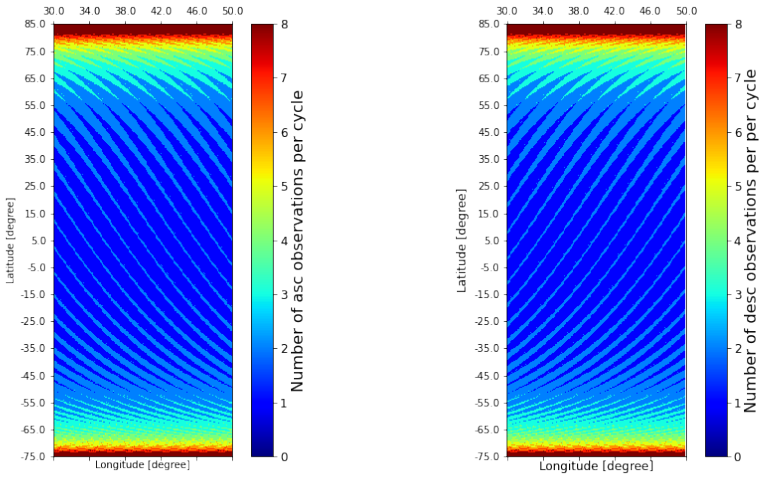

Figure B.1: Number of observations per cycle per location on Earth. Due to the convergence of the meridians, different tracks overlap at higher and lower latitudes. Around the equator, at most one ascending and one descending acquisition are available. Whereas at high latitudes some locations are observed by up to eight different ascending and descending acquisitions.

B.3. Ascending Acquisitions

With DRaMA, we computed the viewing geometries of all available ascending acquisitions for all locations on Earth. In Fig. B.2 we show per grid point (a location on Earth) the minimum and maximum available incidence angle θ (in the upper two figures) and the minimum and maximum azimuth of the ZDP α_d (in the lower two figures). It can be seen that around the equator—where often at most one ascending observation is available—the minimum and maximum incidence angle ranges from 30° to 45 °, which is in line with the near and far range incidence angles for Sentinel-1. The maximum available incidence angle at the poles is often around 45° and the minimum value is around 30° since often multiple observations are available.

For the minimum and maximum α_d, we find values around 260° for latitudes between $-35°$ and $+55°$. For other latitudes, we find that α_d is lower. For an ascending satellite, seen from the Earth's surface, the heading of the satellite α_h shifts more and more to the west as the satellite heads for the poles, see Fig. 2.9. Therefore, α_d shifts more north and becomes smaller compared to α_d around the equator

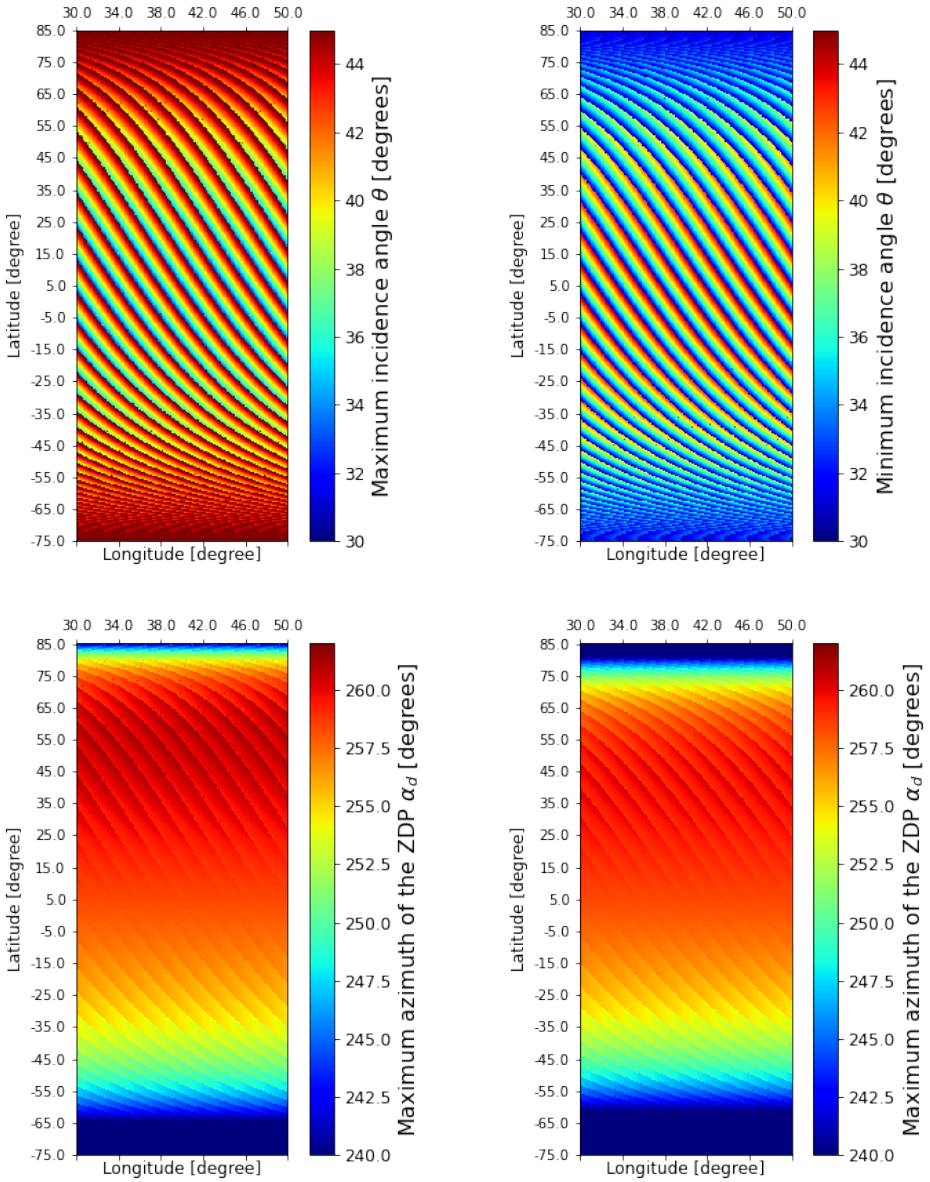

Figure B.2: The upper two plots show the maximum (left) and minimum (right) incidence angle of all ascending acquisitions that are available over a location on Earth. Around the equator, the incidence angle varies from 30° to 45°, which is in line with the near and far range incidence angle of Sentinel-1. The lower two plots show the maximum (left) and minimum (right) available azimuth angles of the ZDP's. Closer to the poles, α_d decreases.

(at the poles we find $\alpha_d < 260°$). As already mentioned, the incidence angle varies with range. But from Fig. B.3 it can be seen that also α_d varies with range. In blue, the position of the satellite is given, imaging two targets—indicated in red—at different ranges. As the range to the target increases, due to the meridian convergence the azimuth of the ZDP, α_d increases. Thus, for ascending acquisitions,

$\alpha_{d,\mathrm{nr}} < \alpha_{d,\mathrm{fr}}$ where $\alpha_{d,\mathrm{nr}}$ is the azimuth of the ZDP at the near range and $\alpha_{d,\mathrm{fr}}$ the azimuth of the ZDP at the far range. This implies that there is a positive correlation between the incidence angle and the azimuth of the ZDP.

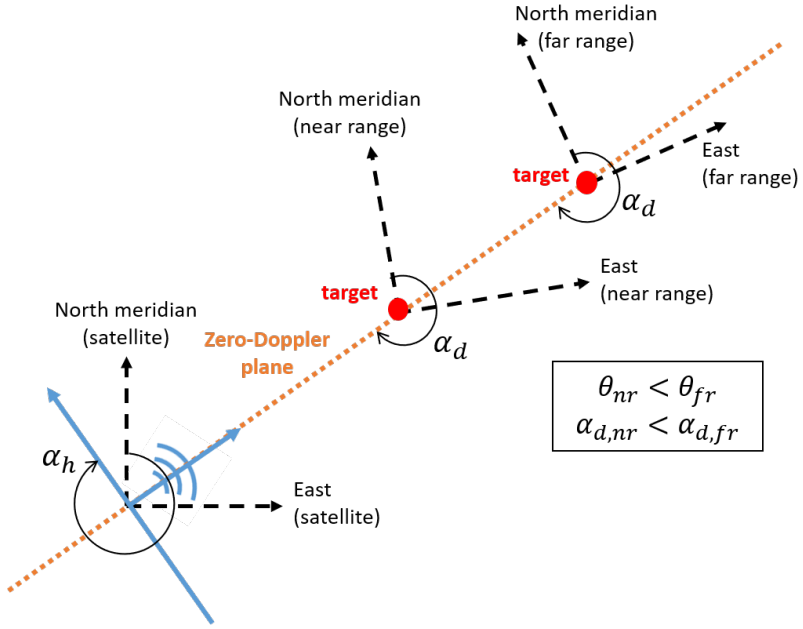

Figure B.3: Range dependency of the azimuth of the ZDP. In blue, the position and heading of the satellite. In red, two targets on the ground at different ranges. For the near range (nr), the north meridians at the Earth surface have a different orientation then the north meridians at the far range (fr). Therefore, for ascending acquisitions, $\alpha_{d,\mathrm{nr}} < \alpha_{d,\mathrm{fr}}$. As the incidence angle also varies with range, this results in a positive correlation between α_d and θ.

B.4. Descending Acquisitions

The results for the descending acquisitions are shown in Fig. B.4. Again, we show the minimum and maximum available incidence angle θ and azimuth of the ZDP α_d. It can be seen that the minimum and maximum α_d is around 110°, latitudes between −35° and +55°. It increases for other latitudes and can reach values of 120°.

For a descending satellite at the poles, just after the ascending acquisition changes into the descending acquisition, the heading α_h of the satellite is almost westward. As a result, α_h at the poles is larger than α_h at the equator which also holds for α_d. Further, α_d varies also for descending acquisitions with range, see Fig. B.5. As the range to the target increases, due to the meridian convergence the azimuth of the ZDP, α_d decreases. Thus, for descending acquisitions, $\alpha_{d,\mathrm{nr}} > \alpha_{d,\mathrm{fr}}$. This implies that there is a negative correlation between the incidence angle and the azimuth of the ZDP.

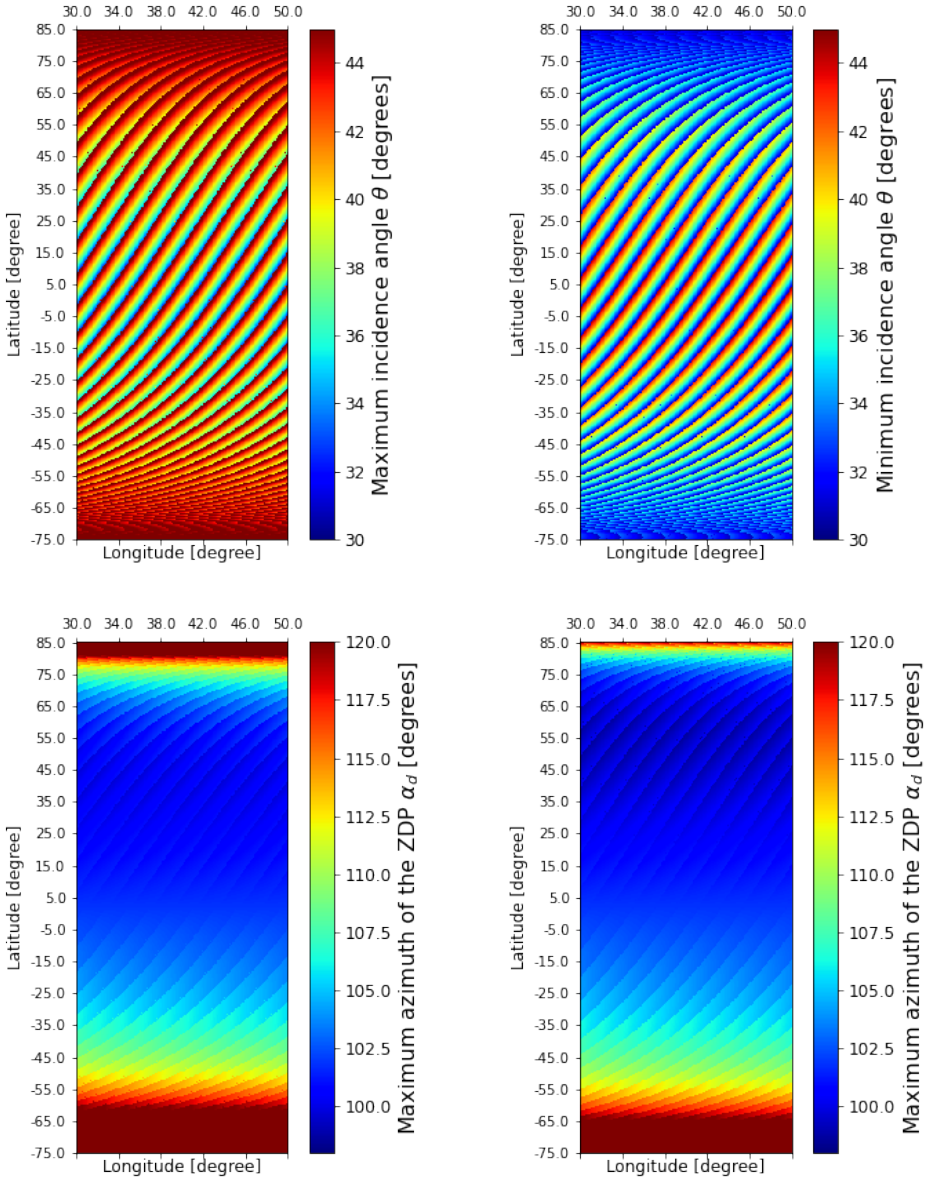

Figure B.4: The upper two plots show the maximum (left) and minimum (right) incidence angle of all descending acquisitions that are available over a location on Earth. Around the equator, the incidence angle varies from 30° to 45°, which is in line with the near and far range incidence angle of Sentinel-1. The lower two plots show the maximum (left) and minimum (right) available azimuth angles of the ZDP's. Closer to the poles, α_d increases.

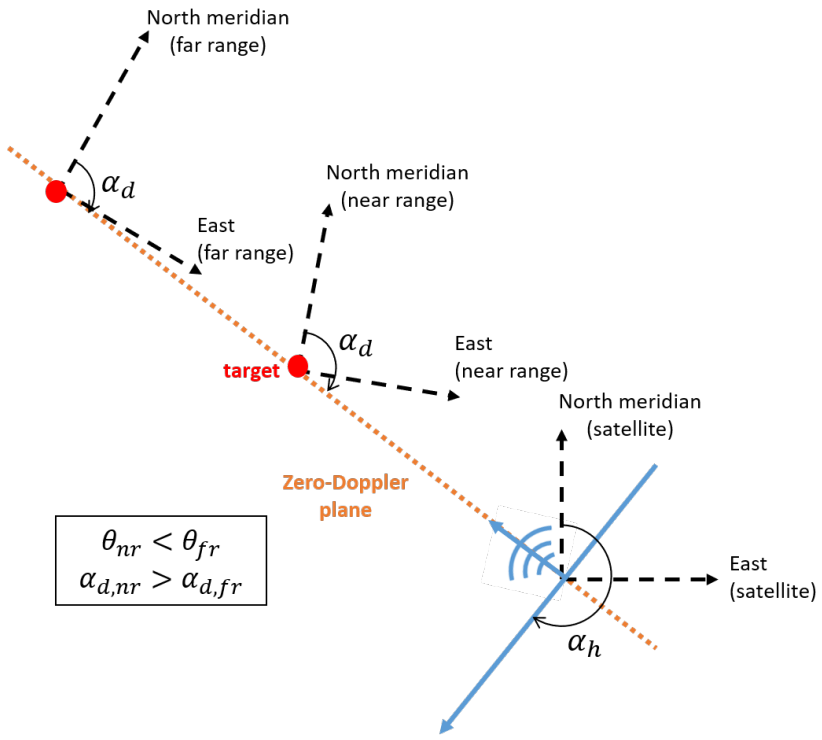

Figure B.5: Range dependency of the azimuth of the ZDP. In blue, the position and heading of the satellite. In red, two targets on the ground at different ranges. For the near range (nr), the north meridians at the Earth surface have a different orientation then the north meridians at the far range (fr). Therefore, for descending acquisitions, $\alpha_{d,\mathrm{nr}} > \alpha_{d,\mathrm{fr}}$. As the incidence angle also varies with range, this results in a negative correlation between α_d and θ.

B.5. Correlation between the incidence angle and azimuth of the ZDP

We tested whether these correlations were also visible in the viewing geometry from Sentinel that we computed with DRaMA. In Fig. B.6 the correlation between θ and α_d for all available ascending (left) and descending (right) acquisitions for a location at high latitude can be seen. There is a clear positive (linear) relation for the ascending acquisitions and a negative (linear) relation for the descending acquisitions. These relations are described by

$$\theta_{\text{asc}} = c_{a1}\alpha_{d,\text{asc}} + c_{a2} \tag{B.1}$$

$$\theta_{\text{desc}} = c_{d1}\alpha_{d,\text{desc}} + c_{d2} \tag{B.2}$$

where c_{a1} and c_{a2} are some constants related to the ascending acquisitions and c_{d1} and c_{d2} are the constants related to the descending acquisitions.

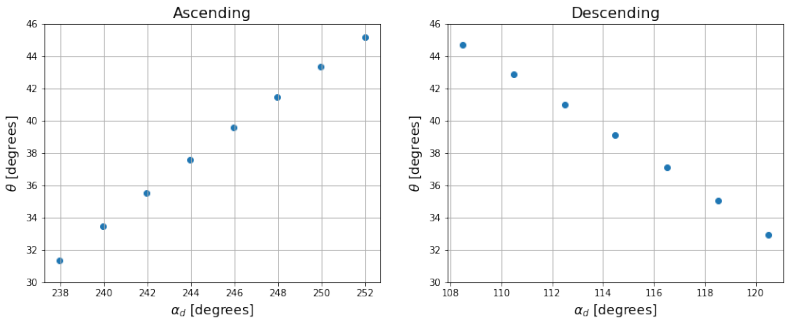

Figure B.6: In the left figure the positive correlation between α_d and θ for ascending acquisitions is shown. For descending acquisitions there is a negative correlation

For locations on Earth between $-75°$ and $+85°$ latitude and between 30° and 50° longitude we estimated the constants c_{a1}, c_{a2}, c_{d1} and c_{d2}. The results can be seen in Fig. B.7. There is indeed a positive correlation between θ and α_d for ascending acquisitions in the northern hemisphere and a negative correlation for descending acquisitions. It can further be seen that c_{a1} and c_{d1} change sign when going from the northern to the southern hemisphere. Near the equator, we expect to see enormous values for c_{a1} and c_{d1} since the incidence angles vary from near to far range. In contrast, the azimuths of the ZDP's only have a minor difference since the meridian convergence is minimal.

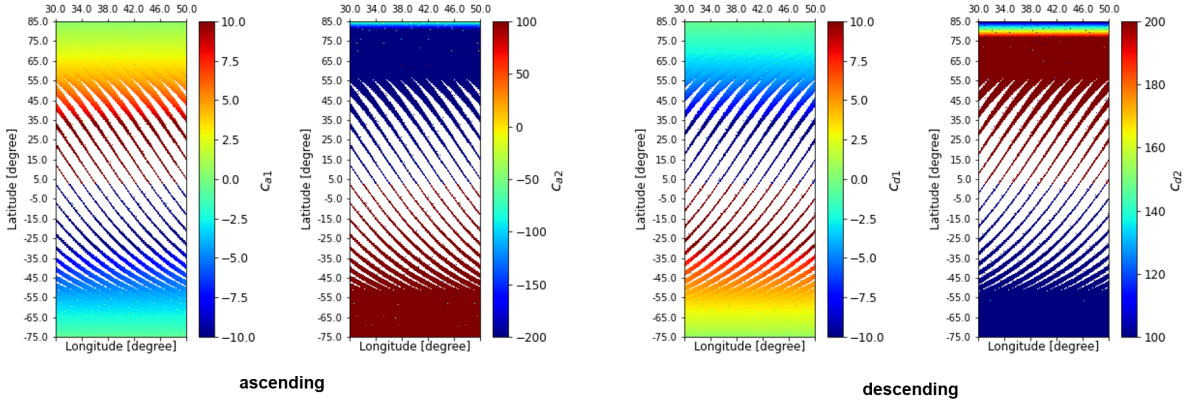

Figure B.7: For locations on Earth where multiple acquisitions were available, we computed the linear relation between the incidence angles and azimuth values of the ZDP's for both the ascending, (a) and (b) and the descending (c) and (d) acquisitions. The figures show the computed constants in Eqs. (2.4) and (2.5)

There is also a clear relation between the different constants c_{a1} and c_{d1} and c_{a2} and c_{d2}, see Fig. B.8 which is a scatter plot of all computed constants. So we plotted c_{a1} versus c_{d1} and c_{a2} versus c_{d2}. The

Table B.1: a and b values for the tangential relation between the latitudinal coordinate and constants c_{a1}, c_{d1}, c_{a2} or c_{d2} computed for the northern and southern hemisphere.

	c_{a1}	c_{d1}	c_{a2}	c_{d2}
a (lat $>5°$, North)	8.09	-8.15	-2091.26	826.45
b (lat $>5°$, North)	-1.71	1.78	477.91	-144.39
a (lat $<5°$, South)	4.70	-4.71	-1217.37	1.10
b (lat $<5°$, South)	-1.09	1.10	275.44	-115.63

high correlation between the constants shows that the viewing geometry of the ascending acquisitions is correlated to the viewing geometry of the descending acquisitions. Furthermore, it can be seen that $c_{a1} = -c_{d1}$

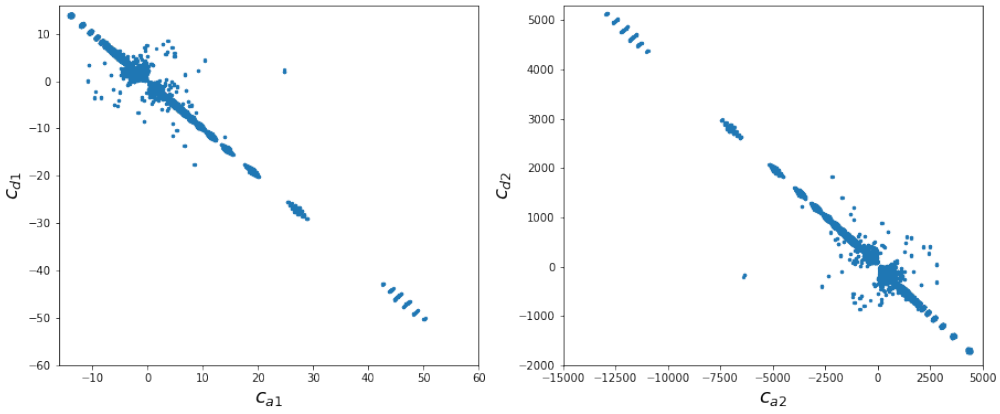

Figure B.8: In the left figure the correlation between c_{a1} and c_{d1} is shown, where we see that $c_{a1} = -c_{d1}$. The right figure shows the correlation between c_{a2} and c_{d2}

Additionally, there is a correlation between the latitude and the value of the different constants. First we computed the mean value for the four constants per latitude, afterwards it was possible to create a scatter plot for the four constants versus the latitude, see Fig. B.9. It can be seen that there is a clear relation between the constants and the latitudinal coordinate which we approximate with the following relation

$$c = \frac{a}{\tan(\Phi)} + b, \tag{B.3}$$

where c is the constant that we want to calculate (so c_{a1}, c_{d1}, c_{a2} or c_{d2}) and Φ the latitudinal coordinate. a and b are constants that are unique for every constant (c_{a1}, c_{d1}, c_{a2} or c_{d2}) that we want to estimate. In Fig. B.8, the red striped lines represent the fitted functions. The values that we found for a and b for the different constants for the northern and southern hemisphere, are shown in Tab. B.1.

With the values for a and b for every constant it is now possible to compute the corresponding incidence angle when only the azimuth of the ZDP and the latitudinal coordinate are known. As an example, at a latitude of 53° we have one ascending and one descending acquisition available where $\alpha_{d,\text{asc}} = 258°$ and $\alpha_{d,\text{desc}} = 99.7°$. To compute the corresponding incidence angles θ_{asc} and θ_{desc} we need the values for c_{a1}, c_{d1}, c_{a2} and c_{d2}, which we can find with Eq. (B.3). This way, we compute corresponding incidence angles of $\theta_{\text{asc}} = 33.1°$ and $\theta_{\text{desc}} = 42.5°$.

B.6. Orientation of the solution line for Sentinel-1

In section 2.3.3 we have seen that the solution line from the RUM's perspective could be described by azimuth angle ϕ and elevation angle ζ. Intuitively, it may make sense to think that $\phi = 0°$ when the azimuth of the ZDP of the ascending and descending acquisition are symmetrical around the north.

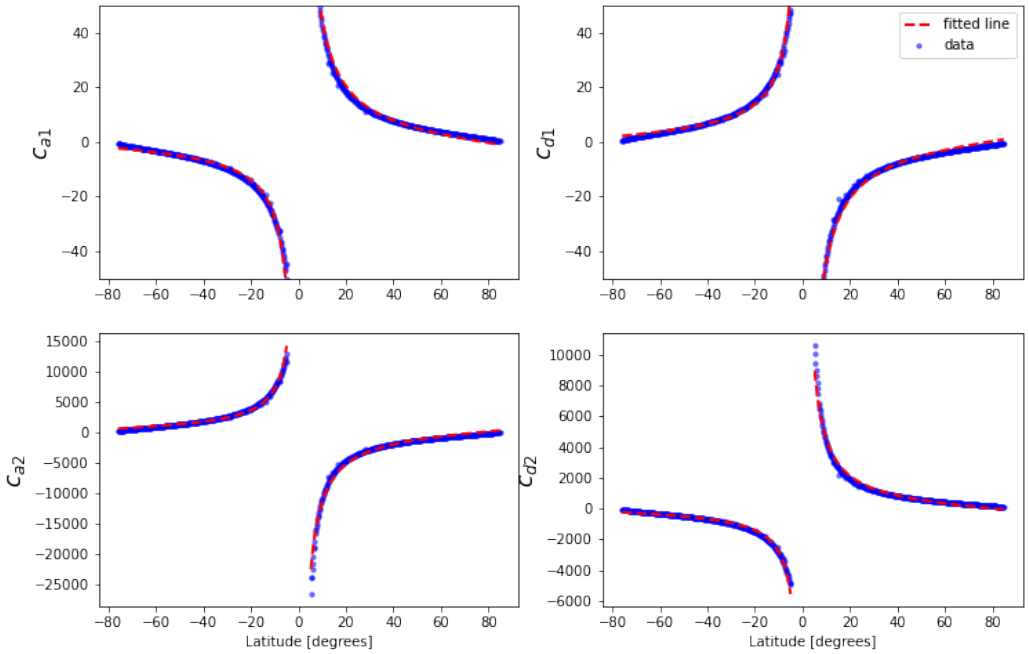

Figure B.9: The relation between α_d and θ can be described with a linear relation with constants c_{a1} and c_{a2} for ascending acquisitions and constants c_{d1} and c_{d2} for descending acquisitions. Those constants change with latitude where a tangential relation between the latitudinal coordinate and the constants is found.

Furthermore, we have seen that both the azimuth of the ZDP's and the incidence angles of both acquisitions play a significant role in the orientation of the solution line, cf. section 2.4.1.

For locations with multiple ascending and/or descending acquisitions, the extent of the asymmetry differs per combination. However, the asymmetry is maximal when for all locations, the acquisitions are chosen that have the maximal α_d, see Figs. B.2 and B.4. When we combine those two acquisitions, it is possible to compute the orientation of the solution line for all locations. The results can be seen in Fig. B.10a and b, where the values for ϕ and ζ are shown. A remarkable result is that $\phi \approx 0°$ for the Northern hemisphere, whereas the azimuths of the ZDP's are often not symmetrical. So due to the asymmetric azimuth of the ZDP's, the solution line has a $\phi \neq 0°$. However, the two corresponding incidence angles (which are not the same) are counteracting this result and thus $\phi = 0°$. For the Southern hemisphere, we find ϕ often not equal to 0°.

We have further seen that there is a correlation between α_d and θ. Therefore, it would be interesting to see whether $\phi = 0°$ is a general rule for the northern hemisphere for Sentinel-1. It is possible to compute ϕ and ζ for all combinations that we can make between ascending and descending acquisitions for different locations. Since we have found that the viewing geometry changes with latitude, we defined different locations, all with the same longitudinal coordinate but varying latitude (between $-75°$ and $+85°$). Around the equator, there are often only 1, 2, or 4 combinations to make since there are at most two ascending and two descending acquisitions available. However, with up to eight ascending and descending acquisitions at higher and lower latitudes, more combinations are made. In Fig. B.10c and d, we show values for ϕ and ζ for different combinations that we could make at a particular latitude (the longitudinal coordinate was set to 30°). We show up to 10 combinations per location. It can be seen that for the Northern hemisphere, all combinations result in $\phi = 0°$. So the result for one particular case shown in Fig. B.10a and b was not coincidentally. Also, we found that for the lowest latitudes, different combinations result in $\phi \neq 0°$. Further, for the elevation angle ζ, we find that it increases when approaching the poles.

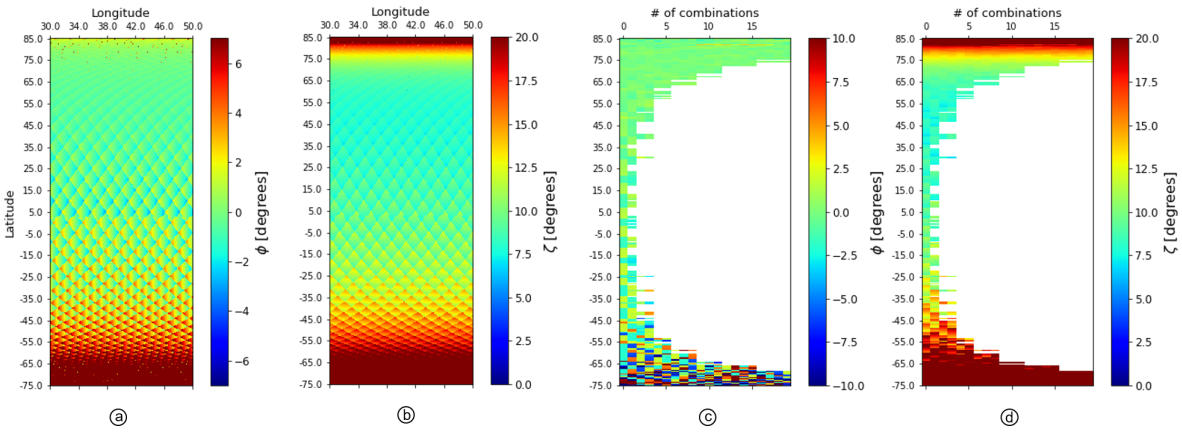

Figure B.10: In (a) and (b), we show ϕ and ζ values, which were computed by combining per location the ascending and descending observations that had a maximum azimuth of the ZDP. The asymmetry between the two ZDP's was maximal. However, this still results in $\phi = 0°$ for the Northern hemisphere due to the difference in incidence angles. In (c) and (d), we computed per location different ϕ and ζ values for all combinations that we could make between ascending and descending acquisitions. Again, we see at the Northern hemisphere that $\phi = 0°$.

B.6.1. Empirical orientation of the solution line

With the minimal and maximum values for the azimuth of the ZDP for the ascending and descending acquisitions (Figs. B.2 and B.4) available per location, it is possible to compute, per latitudinal coordinate, artificial potential azimuths of the ZDP for the ascending and descending acquisition. We computed, per latitude, six different potential azimuths of the ZDP for the ascending and the descending acquisitions. With Eqs. (B.3), (B.1) and(B.2), and the values from Tab. B.1, we could compute the corresponding incidence angles. Resulting in 6 artificial ascending viewing geometries and six artificial descending viewing geometries per location. Afterward, we could make 36 combinations between the ascending and descending viewing geometries, and we were able to compute corresponding values for ϕ and ζ per combination. The results can be seen in Fig. B.11.

It can be seen that for latitudes between $-35°$ and $+65°$ we find that all artificial combinations result in $\phi = 0°$. Only for higher and lower latitudes we find combinations that result in $\phi \neq 0°$. From this we can conclude that, when d_e and d_u are estimated with Eq. (2.20) with observations from one ascending and one descending Sentinel-1 acquisition, only the estimates for d_u are biased. The estimates for d_e will be unbiased.

For latitudes $< -35°$ and $> 65°$, the estimate for d_e is also biased since $\phi \neq 0°$. Further, we see that the bias on d_u will increase when moving away from the equator since ζ increases.

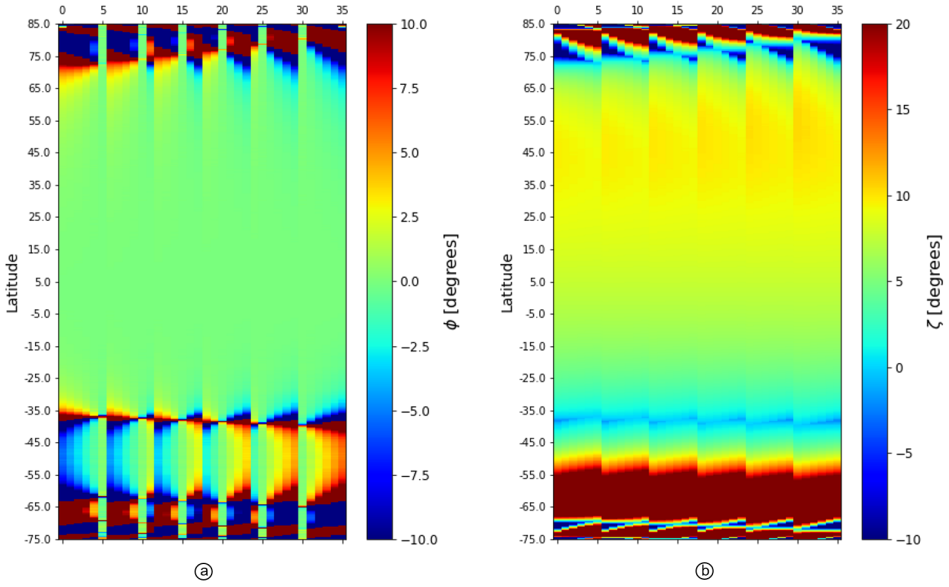

Figure B.11: Per latitude, we defined six artificial ascending acquisitions and 6 artificial descending acquisitions. Consequently, we were able to combine the different acquisitions, which resulted in 36 combinations. For all combinations we computed the orientation of the solution line. In the left figure, we show the results for ϕ, per latitude, per combination. The right figure shows the values for ζ.

C

Literature overview

On the next pages a table is presented consisting of all different approaches we found in the literature.

For every approach we give a short description. For some approaches there are different types of the approach, these types are indicated with the letter a), b), c) or d). Moreover, we weigh each approach according to its correctness, on a scale from 1 to 5. A value of 5 implies that the approach is completely incorrect, a value of 1 means that the approach is correct.

Approach 5, 6 and 7 are so-called correct approaches, which we weighted according to how practical they are (from 1 to 3). A value of 1 means that it is very practical and there are no drawbacks for the approach. A value of 3 means that the approach is not so practical to use and that there is a high likelihood of misinterpretations by readers.

	Approach	Description	Nr of obs.	Type	Impact	How incorrect?	How practical?	Correct for it
1	Attribution error	Attributing a LoS observation to a vertical displacement.	≥ 1	a) No projection statements are given, and LoS observations are directly interpreted as vertical displacements.	A systematic underestimation (bias) of vertical displacements of up to 30%	4	-	Researchers should rephrase the results to LoS observations (see approach 5) or project LoS observations (see approach 6)
				b) Inconsequent usage of terminology (mixing up 'LoS displacements' and 'Vertical displacements')	Potential mis interpretation by readers	3	-	Remain consistent throughout the whole research document and also in the figures and tables. Avoid using the term 'vertical displacements'
2	Projection error	Projecting the LoS displacement estimations onto the vertical, and presenting this as 'vertical displacements', or the equivalent situation in a particular horizontal direction.	≥ 1	a) Vertical displacements obtained by projecting LoS on vertical *without* mentioning assumptions on horizontal displacement component	When there are indeed horizontal displacements, this results in biased estimates for the vertical displacements which can be computed with: $\Delta d_u = \tan(\theta) \cdot [d_e \cos(\alpha_d) - d_n \sin(\alpha_d)]$	5	--	Use approach 6. So rename the *'vertical displacements*' to *'LoS observations projected onto the vertical'*
				b) Inconsequent usage of terminology in follow-up text and figures. First, the term *'projection onto the vertica*l' is used. Later the term *'Vertical displacements*' is used	Potential mis interpretation by readers	4	-	Remain consistent throughout the whole research document and also in the figures and tables. Avoid using the term 'vertical displacements'
				c) Vertical displacements obtained by projecting LoS on vertical *with* mentioning assumptions on horizontal displacement component. However, the assumption are questionable (e.g. for landslides, subsidence bowls)	Potential biased estimation instead of a more noisy estimation, which often has a bigger impact an less chance of being detected	3	-	Use approach 6. So rename the *'vertical displacements*' to *'LoS observations projected onto the vertical'*

	Approach	Description	Nr of obs.	Type	Impact	How incorrect?	How practical?	Correct for it
3	Decomposition error	Ignoring the null-space in the 3D solution space using only two viewing geometries, i.e., ascending and descending.	2	a) It is assumed that the lack of sensitivity in the north-south component for near-polar orbits is equivalent to the absence of a north-south component, by simply removing the component from the decomposition equation	Biased results for the east and vertical displacements in the case of existing NS displacements	4	-	Use approach 6 or 7
				b) Assumptions on the non-existence of the north-south displacement component.	Biased results for the east and vertical displacements in the case of existing NS displacements	4	-	Use approach 6 or 7
				c) When two LoS observations are available, it is possible to estimate two displacement components.	Biased results for the east and vertical displacements in the case of existing NS displacements	4	-	Use approach 6 or 7

	Approach	Description	Nr of obs.	Type	Impact	How incorrect?	How practical?	Correct for it
4	Flawed assumptions	In many cases we see lacking, misstated, incorrect, or implausible assumptions while estimating the 3D displacement components	≥ 1	a) Lacking assumptions (see 2a)	Potential biased estimation instead of a more noisy estimation, which often has a bigger impact an less chance of being detected	5	-	Check whether it is possible to add an assumption otherwise change to approach 5, 6 or 7
				b) Incorrect assumptions (see 2b or 3c)	Potential biased estimation instead of a more noisy estimation, which often has a bigger impact an less chance of being detected	4	-	Check whether it is possible to change the assumption otherwise change to approach 5, 6 or 7
				c) misstated assumptions (see 3a)	Potential biased estimation instead of a more noisy estimation, which often has a bigger impact an less chance of being detected	4	-	Check whether it is possible to change the assumption otherwise change to approach 5, 6 or 7
				d) implausible assumptions (see 3b)	Potential biased estimation instead of a more noisy estimation, which often has a bigger impact an less chance of being detected	4	-	Check whether it is possible to change the assumption otherwise change to approach 5, 6 or 7

	Approach	Description	Nr of obs.	Type	Impact	How incorrect?	How practical?	Correct for it
5	LoS unaltered as the final product	Approach is obviously correct, as it does not attempt to do any projection, attribution, or decomposition.	≥ 1		The drawback of the LoS product is that it is typically hard to interpret, especially for untrained end users.	-	2	
6	"Projection-onto" products	Present the projection of the LoS onto the, e.g., vertical direction.	≥ 1	a) Project LoS displacements onto the vertical (often an oblique projection)	It must be made clear that the results are displacement projections and not the vertical displacements itself to avoid misinterpretation. Moreover, make clear that an oblique projection is used.	-	2	
			≥ 2	b) Project the two LoS observations onto the EW-Up plane and estimate the displacement components into the EW and Up direction.	It must be made clear that the estimated displacements in the EW-Up plane are not the same as the displacement in the east and up direction. For Sentinel-1 in the Northern hemisphere, the up component is biased.	-	2	
7	2D Decomposition with valid, plausible, and explicit assumptions	There are several cases for which assumptions on displacement directions are hardly disputed.	≥ 2	When the displacement vector can be described as a 2D displacement vector, it is possible to estimate the two displacement components with only two LoS observations		-	1	

D

Fallacious statements

In the table within this Appendix, we show some fallacious statements and our proposal how the statements can be corrected. We also added a column where we describe why we think the statements are incorrect. The aim of this appendix is not to blame the authors that have written those statements. We respectfully assume that the majority of authors is well-aware of the geometric limitations of InSAR, and that the different fallacies cited are not a consequence of a lack of mathematical understanding, but rather a loose usage of semantics. Yet, we observed that a rather loose and non-strict communication easily leads to misinterpretation, misunderstanding or confusion. We therefore make a proposal on how to correct for the incorrect semantics.

Incorrect statement	*What should be written*	*Why incorrect?*
Attribution error		
15 ascending Sentinel-1A TOPS SAR images … were selected to **estimate vertical** average surface **subsidence**	15 ascending Sentinel-1A TOPS SAR images … were selected to **estimate the projection of the LoS displacements onto the vertical direction**	It is not possible to estimate the vertical velocities from one data set only. The LoS displacements are different from the vertical displacements. It is possible to project the LoS observations onto the vertical direction or to present the LoS observations unaltered.
Vertical displacements … has been drawn … using the available data	**LoS displacements projected onto the vertical** … are drawn … using the available data	
The result from the IPTA processing is a surface velocity map … the velocity map shows a slow subsidence	The result from the IPTA processing is a **LoS** surface velocity map … the velocity map shows a slow subsidence	
Projection error		
We **converted** the LoS displacements .. to vertical displacements	We **projected** the LoS displacements onto the vertical direction along…	Incorrect since the words ‘converted’ and ‘transformed’ suggest that there is a one-on-one relation between the LoS displacements and the vertical displacements. However, you cannot convert or transform the LoS displacements directly to vertical displacements with observations from one data set only. Other verbs as ‘computed’, ‘calculated’, ‘estimated’, and ‘determined’ would also be wrong.
The LoS deformation can be **transformed** into the required direction	The LoS deformation can be **projected** onto the required direction **with P the projection matrix**	
The differential phase … was **converted** from SAR LoS to vertical displacements	The differential phase … is **projected** from SAR LoS direction onto the vertical direction along …	

Incorrect statement	*What should be written*	*Why incorrect?*
Decomposition error		
Combining an ascending and a descending time-series, it is possible to **disentangle** east-west horizontal deformation from vertical deformation.	Combining an ascending and a descending time-series, it is possible to **project** both time series onto the EU plane and estimate the displacement components in that plane	Authors try to 'disentangle', 'estimate' or 'reconstruct' two displacements components, with two LoS observations. This is impossible regarding the solution space when two observations are available. In all cases described here, the authors try to estimate the displacements in east and up direction. This would only be possible when the null line would be orthogonal to the EU plane. However, we have seen that this is never the case.
Using data from both ascending and descending orbits, it is possible to **determine** the vertical displacement and one component of horizontal displacement.	Using data from both ascending and descending orbits, it is possible to **project** onto the EU plane and estimate the projected displacements.	
Whenever two data sets of InSAR images are available, ..., the PSInSAR results can be used **successfully to estimate** the vertical and east-west components of the local displacement fields	Whenever two data sets of InSAR images are available, ..., the PSInSAR results can be **projected onto the EU plane** and subsequently estimate the projected vertical and east-west components	
The combination of ascending and descending satellite passes allows the **decomposition** of the light of sight velocities into horizontal east-west and vertical components.	The combination of ascending and descending satellite passes allows **to project** both LoS vectors onto the EU plane, and estimate the displacement components in that plane.	
Reconstructing vertical and horizontal components … using two interferograms, one from an ascending and the other from a descending orbit.	Using two interferograms, one from an ascending and the other from a descending orbit makes it possible to **project** the LoS observations onto the EU plane, and estimate the displacement components in that plane.	

Incorrect statement	*What should be written*	*Why incorrect?*
Flawed assumptions		
The Nourth-south component can be neglected due to the **low sensitivity** of SAR sensors along that direction.	Change the reasoning to a deduction reasoning	As long as the signal is strong enough, the radar **is sensitive**. It is a SNR consideration but that should be written down.
Sentinel-1 data are **insensitive** to north-south displacements direction .... Therefore, we assumed that d_n = 0, and this allowed us to find the other two components of the deformation vector.	Change the reasoning to a deduction reasoning, e.g., write something in the line of: The two LoS observations are projected onto the EU plane, and estimate the displacement components in that plane.	Here the assumption is on the (physical) signal, not on the sensitivity of the measurements. It would not make sense to assume that $d\_n = 0$ while $d\_e \neq 0$.
The north component is **insensitive** … consequently, we add the additional constraint that the **north-south motion is assumed to be zer**o. In this way, we calculate the velocity in east-west and up-down direction.	Change the reasoning to a deduction reasoning, e.g., write something in the line of: The two LoS observations are projected onto the EU plane, and we estimated the displacement components in that plane.	Here the assumption is on the (physical) signal, not on the sensitivity of the measurement. It would not make sense to assume that $d\_n = 0$ while $d\_e \neq 0$.

E

Fallacious propositions

During the research, we had the opportunity to present our work on Fringe 2021, the 11th International Workshop on“Advances in the Science and Applications of SAR Interferometry and Sentinel-1 InSAR”. Here we obtained a reaction to our work. However, we also remarked that there were some fallacious propositions of people visiting the conference. Here we would like to discuss a few of them.

1. The EW component *can* be solved unambiguously from one ascending and one descending acquisition but NS & UD can’t be disentangled without assumptions due to the symmetric heading angles.

2. The north component is insensitive.

3. Taking the north component into account is in general not needed since it only plays a role when the displacements into the NS direction are relatively large.

4. The majority of the papers where InSAR fallacies as discussed in section 2.5 are observed are of non-SAR specialists. This means that there is a big communication gap between SAR experts and the users.

Generically, we think that the first proposition is incorrect. Let split the statement in two. The first part: *‘The EW component* can *be solved unambiguously from one ascending and one descending acquisition but NS & UD can’t be disentangled without assumptions’*, is in general not entirely correct. With one observation of an ascending acquisition and an observation of a descending acquisition, the solution space of the inverse problem is a line. The orientation of that line determines whether the estimates for d_e and d_u are biased and the potential magnitude. The solution line has an azimuth to the North, ϕ and elevation, ζ.

If and only if $\phi = 0°$, the estimate for d_e is unbiased. It is indeed correct that, for Sentinel-1, we often find $\phi = 0°$ (Fig. 2.17). However, the statement should be formulated more specifically. At the Northern hemisphere ϕ mostly equals $0°$ but for the Southern hemisphere we do find $\phi \neq 0°$.

Then, the second half of the statement: *‘due to the symmetric heading angles’*. Also, this part is incorrect. At the locations where we find $\phi = 0°$, this is not caused by the symmetric heading angle. We have seen that there are many locations where the azimuths of the ZDP’s can be asymmetric (Fig. 2.8). Nevertheless, the incidence angle and the azimuth of the ZDP are correlated. So when the azimuths of the ZDP’s are asymmetric, the correlation between θ and α_d causes the solution line to have an azimuth angle of 0°.

In the end, we propose to change the first proposition to: For the Northern hemisphere, the EW component *can* be solved unambiguously from one ascending and one descending acquisition, but NS & UD can't be disentangled without assumptions due to the viewing characteristics of Sentinel-1.

The second and third propositions are related, and we think in the generic sense not correct. As long as the solution line is not perpendicular to the EU plane, the NS component is measured and should be taken into account. For the third proposition, many authors argue that the sensitivity for the NS component is only valid for exceptional cases with large NS displacements. However, we argue that it is precisely the other way around. We think we should describe the decomposition problem in a generic sense for small and large displacements. Initially, the stochastic model plays no role, purely the geometry of the observations should be taken into account, which is captured in the A matrix. When the generic model is known, we can deduce particular cases, e.g., with small displacements or very high or low observation precision (deduction). Thus not the other way around, as is stated in proposition 3, where the authors start with the exceptional (particular) case. They state that the precision of the observations is low or that the displacements are small, and from there, they try to deduce the generic model. This is not possible (this method is called induction).

We think that the fourth statement is incorrect since, first of all, SAR specialists and non SAR specialists do not exist. There is no SAR diploma. Added to this, by making this point, the messenger of this point passes the problem away. After all, the InSAR community still reviews all those papers.